Vortex-Induced Fluidics Mixing for Control of Multi-Solvent Systems

By

Clarence Chuah
Bachelor of Engineering (Biomedical) (Honours)

Thesis
Submitted to Flinders University
for the degree of

Doctor of Philosophy
College of Science and Engineering
May 2025

TABLE OF CONTENTS

ABSTRACT

When solids or liquids undergo rotation, centrifugal and shear forces come into play, a phenomenon central to the continuous advancements in rotary systems such as dynamic thin-film flow technology. This cutting-edge technology plays a pivotal role in refining the structure-property relationships of materials at the nanoscale, marking a significant stride in the realm of green chemistry. Among the most notable innovations in this area is the vortex fluidic device (VFD), which offers distinct advantages over traditional batch processing methods. The VFD generates fluidic waves that produce intense shear forces, significantly increasing surface area for micro-mixing and thereby enhancing mass and heat transfer rates. This enables reactions to occur beyond the constraints of diffusion, fostering a novel, environmentally friendly approach to material modification across a variety of research and industrial applications by finely tuning small-scale flows and modulating chemical reactivity and self-organisation at the molecular and macromolecular levels.

Mixing immiscible liquids typically necessitates the use of auxiliary agents such as phase transfer catalysts and surfactants. However, the centrifugal separation of immiscible liquids of varying densities within a 45° tilted rotating tube can eliminate the need for these additives. In the VFD, micron- to submicron-scale topological flow regimes are established within thin films, significantly enhancing interfacial mass transfer. The hemispherical base of the tube generates a Coriolis force that allows the less dense liquid to penetrate the denser liquid layer, facilitating high-efficiency mass transfer without the need for additional catalysts. This approach offers innovative solutions for overcoming mass transfer limitations at liquid interfaces, enabling advanced extraction and separation processes while preventing the formation of emulsions.

Building on this understanding of immiscible liquids in the VFD, this thesis explores several examples of utilising the VFD to control various multi-solvent systems, demonstrating the state-of-the-art capabilities of this technology.

First, perfluorooctanoic acid (PFOA), part of the per- and poly-fluoroalkyl substances (PFAS) group, poses significant environmental and health risks due to its persistence and potential carcinogenicity. The VFD provides a cost-effective and efficient method for extracting PFOA from water. By utilising dynamic thin film microfluidic technology, the VFD enables intense micro-mixing and rapid extraction of PFOA, confirmed through liquid chromatography-mass spectrometry (LCMS). The device's scalability and efficiency make it suitable for large-scale production, highlighting its potential for environmental remediation.

Second, in fluorescent biosensing, achieving high signal sensitivity at low dosages is crucial. The VFD enhances the emission of a graphene oxide (GO)/fluorophore complex through intense micro-mixing. At a low rotational speed of 1500 rpm, the VFD achieves a fivefold increase in emission within five minutes, compared to conventional methods. This scalability and efficiency underscore the VFD's potential for large-scale production in advanced biosensing technologies. Understanding the mechanism of fluorophores' adherence to GO sheets is key to optimising this process.

Third, the formation of clathrates, such as those containing water and toluene, involves host molecules forming cage-like structures that trap guest molecules. While theoretically possible, the larger size of toluene molecules makes spontaneous clathrate formation with water unlikely under normal conditions. However, the VFD's high-pressure environment and shear stress might overcome these steric obstacles, promoting the formation of water cages that can encapsulate toluene. Further testing is required to confirm the feasibility of this unorthodox clathrate formation.

Overall, the VFD revolutionises material processing and environmental remediation through its innovative micro-mixing and high shear forces. Its efficiency and scalability enhance green chemistry applications, biosensing technologies, and complex material transformations. This technology offers a promising future for advanced scientific research, industrial advancements, and sustainable solutions to pressing environmental, health-related, and diverse industrial challenges worldwide, driving significant progress and innovation.

DECLARATION

I certify that this thesis:

1. does not incorporate without acknowledgment any material previously submitted for a degree or diploma in any university

2. and the research within will not be submitted for any other future degree or diploma without the permission of Flinders University; and

3. to the best of my knowledge and belief, does not contain any material previously published or written by another person except where due reference is made in the text.

Signed CLARENCE CHUAH

Date 07 / 04 / 2025

ACKNOWLEDGEMENTS

This thesis would not have been possible without the support and guidance of many incredible people. First and foremost, I am eternally grateful to my advisor, Professor Youhong Tang. His patience and insightful feedback were instrumental in navigating the challenges of this research.

I also owe a debt of gratitude to my co-advisor, Professor Colin L. Raston, for providing support, guidance, and willingness to share his wisdom. His observations and insights were enlightening.

To my fellow graduate students in both labs, thank you for the countless hours spent brainstorming, sharing resources, and offering moral support. Our late-night discussions were intellectually stimulating and a constant source of encouragement throughout this journey.

I would also like to express my sincere gratitude for the Research Training Program scholarship in providing the financial support that made this research possible.

Finally, to my dearest parents, brother, partner, and friends, thank you for your unwavering love and support. Your constant encouragement and belief in me motivated me during the most challenging moments. This accomplishment is truly a testament to your love.

LIST OF FIGURES

LIST OF TABLES

CHAPTER 1 : INTRODUCTION

1.1 General Overview

This thesis builds the essential knowledge for mixing multi-solvent systems within a microfluidic platform called a vortex fluidic device (VFD). Investigations into applications of this vortex-induced fluidics mixing will be discussed herein. This thesis will divide the work into two diverse parts. Many studies have demonstrated the potential of the VFD for a wide variety of applications. However, they investigated without reference to the specific fluidic flow involved. Thus, the main objective of this thesis is to explore the fluidic flow concerned and extend the VFD's applications. First, the thesis will examine the signature of mixed solvent systems in the VFD with varying speeds and tube geometries. The microfluidic platform forming thin films by confining liquid reagents during processing is vital to this thesis. Characterising the ability of the VFD to operate multi-solvent systems has led to swift optimisation of the system, allowing illumination for many advantages of VFD-based thin films. Secondly, the thesis will investigate and manipulate these multi-solvent systems in the VFD for advanced applications, such as inorganic-organic nanocomposites based on aggregation-induced emission lutinoes (AIEgens) and perfluorooctanoic acid (PFOA) extraction. This thesis lays a framework and delivers results for applications and future research.

Rotational motion and its associated effects pervade numerous facets of our existence, from shaping celestial bodies[1] to propelling vehicles and powering many pieces of machinery, including biological and molecular motors.[2, 3] Despite its omnipresence, the utilisation of rotational dynamics in controlling material systems remains limited. While the use of lathes to create solids of revolution or rifling to stabilise cannonballs in flight represent significant technological advances, historical applications like glassblowing and pottery wheel-throwing demonstrate the delicate balance between a material's cohesion and centrifugal forces to achieve axisymmetric shapes. However, they do not fully capture the essence of modern materials science.

Stationary architectures have often supplanted rotating systems due to ease of control and technological evolution. This tendency is best illustrated by the shift from gramophone records to magnetic tape recorders, CD-ROMs, and modern solid-state information storage devices without revolving parts.[4] However, prematurely dismissing rotary systems as antiquated would be misguided.

The central thesis presented herein posits that the strategic application of rotational motion to liquid or solid materials facilitates the imposition of forces—be they centrifugal or shear—that are arduous to replicate and sustain within stationary frameworks. By using these forces, one can obtain results that would be impossible otherwise, modifying the characteristics and internal structure of material systems and exerting precise control over processes.

This paradigm has applications in many contemporary technologies, such as separations, manufacturing defect-free silicon wafers, creating large telescope mirrors and high-performance solar cells, and the emerging field of lab-on-a-disc microfluidics.

These emerging findings unveil a landscape brimming with uncharted possibilities. The transplantation and assembly into rotating settings unveil exciting opportunities ripe for exploration.

This chapter explores situations where a single material or all constituent parts of a material system rotate uniformly and are subjected to shear and centrifugal forces. It refrains from examining instances where only specific internal elements within a broader system rotate, engendering localised vortex flows nearby. Typical examples are flagellar motors[2, 5] and their micro-motor counterparts,[3, 6] molecular machines,[7-9] or other assemblages of rotating particles involved in vortex collisions.[10 - 17]

1.2 Centrifuge

Due to his groundbreaking work in 1924, Svedberg was awarded the prestigious Nobel Prize in Chemistry in 1926 for creating the first ultracentrifuge, a marvel that changed colloidal separation procedures. His device, which could accelerate centrifugally up to 6,300 times the force of gravity, set the stage for further developments in the sector.[18]

Fast forward to the modern laboratory, where centrifuges have undergone remarkable evolution. Modern versions are capable of astounding speeds of up to 150,000 revolutions per minute (rpm), which results in centrifugal accelerations that can reach up to 10^6 times the force of gravity. That kind of powerful force makes it easier to separate molecules with a wide range of molecular weights: from the tiny few hundred grams per mole of glucose[19] to the massive millions of grams per mole of virus particles and organelles,[20] as well as the various components of biological importance such as proteins,[21] and nucleic acids.[22]

A notable refinement of this technique involves the creation of a stable density gradient within the rotating liquid medium. When a dense solute, usually a caesium salt, is added, various parts of the analyte mixture come into sedimentation equilibrium and gather in specific, well-defined zones where the surrounding density is similar to their own. This analytical technique is widely applicable in various fields, requiring minimal sample volumes and concentrations. It can be used to investigate diverse topics such as heterogeneity in samples,[23] macromolecular interactions,[24-26] protein conformational changes,[27] ligand binding dynamics,[28] nanoparticle separation,[29] and colloidal characterisation.[30]

Progressing into more specific domains, a series of centrifuges characterised by their combination of fast rotation and heat convection is used in isotope separation in the gaseous medium, [31, 32] most notably in separating 235U from its isotopic cousins. Moreover, centrifugation serves as a linchpin in the operation of rotating packed-bed (RPB) reactors, where acceleration surpassing terrestrial gravity engenders a potent counterflow mechanism, augmenting gas-liquid mass transfer by orders of magnitude[33] while curtailing reactor dimensions and weight.[34] This architectural ingenuity underpins a panoply of industrial processes, encompassing dehydration,[35] absorption,[36] seawater deaeration,[37] ozonation,[38] and a litany of gas-liquid catalytic reactions facilitated by the solid bed surfaces.[39 - 41]

Of particular importance is the burgeoning application of RPB reactors in the realm of CO_2 capture,[33, 42, 43] a salient endeavour in the current milieu of climate necessity. Moreover, the high-gravity reactive precipitation method, leveraging the swift micro-mixing capabilities inherent to RPBs, promises the production of nanoparticles at scale, endowed with exemplary mono-dispersity and spatial uniformity, heralding a new era of high-volume, cost-effective nanoparticle synthesis.[44]

Traditional centrifuges, while effective, present notable drawbacks, including their cost, bulkiness, and impracticality for deployment in resource-limited settings. These drawbacks impede their utility in point-of-care diagnostics, especially in underserved areas. Recognising this difficulty, several innovative solutions have emerged to democratise centrifugation technology, ushering in an era of portable devices tailored for field applications.[45, 46]

Among these innovations, perhaps none is as inventive as the low-cost centrifuge based on the humble whirligig concept.[47] This ingeniously basic concept (Figure 1.1) quickly rotates a centrally positioned paper disc perpendicular to the strings due to the manual winding and unwinding of paired strings. This ‘paperfuge’ is astonishingly fast, reaching up to 125,000 revolutions per minute (rpm), resulting in centrifugal accelerations that are 30,000 times faster than gravity. This homemade centrifuge shows excellent efficiency when equipped with capillaries that hold analytes; it can separate components of whole blood in only 1.5 minutes or isolate malaria parasites from blood samples in under 15 minutes. Impressively, the quality of separation achieved rivals that of conventional electrically powered devices.

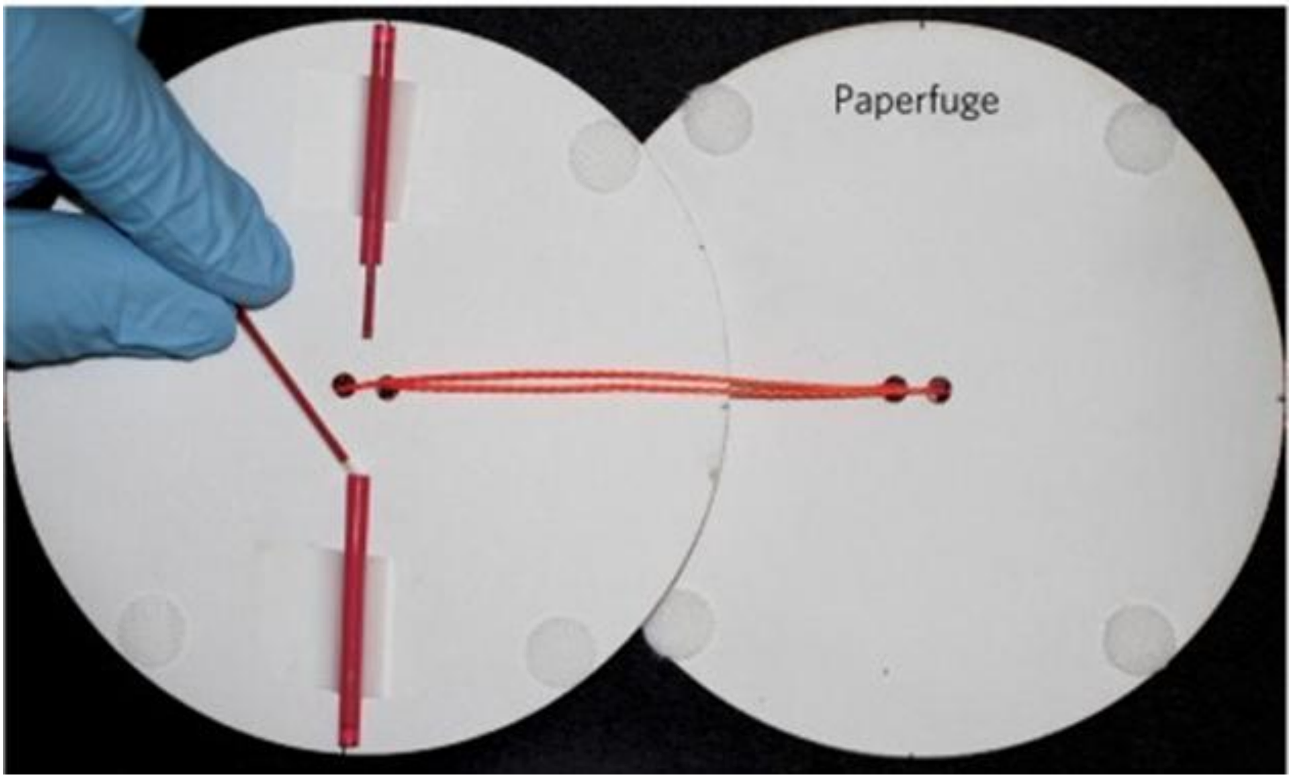

Figure 1.1 Unconventional centrifuges.

This illustration depicts a highly economical paper-based centrifuge designed for haematocrit analysis. It represents the insertion of a plastic capillary holding 20 µl of human blood into hollow plastic holders attached to the paper discs of the centrifuge. With this system, each capillary yields 8 µl of blood plasma separated from whole blood in less than 1.5 minutes. Reprinted from REF,[47] Springer Nature Limited.

However, it's crucial to note that the paperfuge's Achilles' heel lies in its inability to maintain a consistent and reproducible rotational speed over prolonged periods, thus limiting its applicability beyond simple centrifugal processes. Despite this caveat, the paperfuge is a remarkable testament to human ingenuity. It offers a hopeful glimpse into the potential of frugal innovation, a potential that could significantly impact and address pressing healthcare challenges in resource-constrained environments.

1.3 Lab-On-A-Disc

Fluids are propelled through outward-directed conduits by hydrostatic pressure differentials caused by centrifugal forces. 'Lab-on-a-disc' applications,[48 - 51] involves etching a microfluidic circuit onto a polymeric disc made of materials like polycarbonate[50, 52, 53] or polymethyl methacrylate.[54 - 56] This disc spins on its axis at speeds of 400 to 3,000 revolutions per minute (rpm), much like a CD-ROM[51] (see Figure 1.2). Centrifugal force expels fluid radially outward when a biological sample is delivered close to the rotational axis, eliminating the requirement for mechanical pumps – which have presented substantial fabrication and integration issues in lab-on-a-chip devices.[57, 58]

Figure 1.2 LabDisk for SAXS.

Each of the six segments involves aliquoting the three input liquids, combining them, and mixing them in various predefined concentrations. The resulting mixtures are then transferred to read-out chambers, designed to allow read-out on a disk using a synchrotron beamline. Reprinted from REF,[59] CC BY 3.0.

For example, centrifugal force modifies liquid flow over a chromatographic membrane in lateral flow strips similar to those used in pregnancy tests; if the sample is injected further from the rotating axis and moves towards it via capillarity, the flow is slowed down. By reducing flow sensitivity to manufacturing variations, this modulation improves strip-to-strip repeatability and prolongs incubation times.[60, 61] Moreover, centrifugation augments the buoyancy force, facilitating the facile removal of bubbles that might impede device performance.[48]

A variety of functions are made possible by valves-controlled sequences that, when necessary, allow fluids to move through the channels. These functions include mixing, sample partitioning, droplet production, separation based on different physical qualities, and detection. Notably, centrifugal force alone can trigger valves according to preset sequences internally controlled by on-chip events or externally controlled by a spinning-rate program.[62-65] This removes the requirement for external control.[48, 66 - 73]

The Coriolis force, which can outweigh centrifugal force for quickly flowing liquid segments in radial channels, can also be used to control flow and accomplish micro-mixing.[48, 49, 74, 75] An on-disc architecture designed for handling and analysing minuscule protein samples in a variety of liquid conditions are shown in Figures 1.2 and 1.3.[59] Here, 120 separated solutions are prepared automatically by combining six 2.5 µl protein stock solutions with different amounts of additional reagents. These samples are then subjected to small-angle X-ray scattering analysis, all within the same disc.

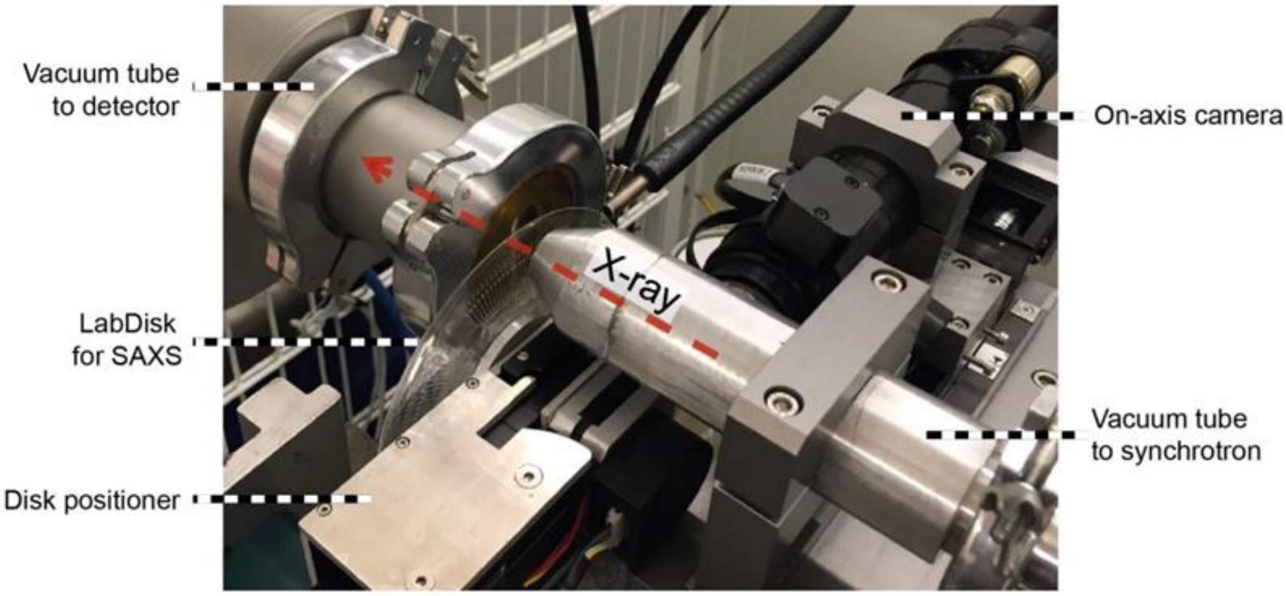

Figure 1.3 The LabDisk at the P12 beamline at EMBL Hamburg.

At the P12 beamline (PETRA III, DESY) at EMBL Hamburg, the LabDisk is used for small-angle X-ray scattering (SAXS) study of protein interactions under various chemical conditions. To create 20 alternative conditions for each protein sample, six ultralow-volume protein samples (2.5 µl each) are mixed with different buffers in varied quantities. An X-ray beam scans the disc holding these recently created aliquots after it has been set on a revolving positioner. Reprinted from REF,[59] CC BY 3.0.

Furthermore, these discs have intricate filtration and separation systems for processing patient-derived specimens. These discs provided a convincing illustration of how extracellular vesicles might be quickly separated from urine samples collected from cancer patients, exceeding traditional ultracentrifugation techniques regarding yield and efficiency.[77]

Another example involved testing for bacterial endotoxins using a single disc[78] to perform automated aliquoting, metering, and mixing for 104 reactions. This method required a lot less lysate per sample than standard procedures.

In a small-molecule detection setup, the target protein was ensconced in fluorescent antibodies and antibody-coupled paramagnetic particles. The self-assembly of beads into hexagonally packed monolayers was made possible by centrifugal force, which also allowed for single-bead resolution fluorescence detection.[79, 80] The sensitivity of the detection limit was significantly higher than that of traditional enzyme-linked immunosorbent tests, with an order of femtograms per millilitre.

One of the main advantages of lab-on-a-disc systems is their simplicity. They are sturdy in the field because the disc is the only moving portion. Prominent firms have commercialised some of these devices, which are used for various purposes, such as point-of-care blood analysis and water quality testing in swimming pools and aquaculture facilities.

Nevertheless, a barrier that prevents lab-on-a-disc systems from meeting the World Health Organisation's requirements for "extreme point-of-care diagnostics" in situations with limited resources is their dependence on an electric rotating motor with configurable speed.[81] However, there is hope on the horizon. A possible solution to this problem is the creation of manually powered [82, 83] devices similar to the paperfuge, opening up new possibilities for the future of these systems.

1.4 Centrifugal Casting

"Centrifugal casting" broadens the focus to include larger-scale manufacturing processes and procedures. This technique deposits hardening materials into a revolving mould using significant centripetal forces. The mould, which may take various forms such as pipes, flywheels, or engine cylinder liners, revolves around a fixed axis. Notably, while cylindrical shapes are commonplace, the technique accommodates non-cylindrical geometries.

Centrifugal casting distinguishes itself from static deposition methods by its capacity to reduce porosity and minimise the inclusion of impurities within the cast. Furthermore, it maintains axial symmetry in the distribution of crystallisation faults, thermal shrinkage zones, and internal characteristics. Despite its inception in the mid-nineteenth century, popularised by Alfred Krupp in mass industrial settings, centrifugal casting continues to evolve, finding novel applications in modern materials science.

These modern applications include the deposition of gradient nanoparticle films that facilitate directional charge carrier transport, often known as 'quantum funnels',[101] as well as graded composites,[84, 85] composites modified by magnetic fields,[86] and highly aligned nanosheets.[87] Centrifugal casting, however, runs into a bottleneck in industrial production since each mould can only produce one product at a time.

1.5 Spiral Separators

Centrifugal forces are evident when the spinning of a liquid results from the imposed geometric structure. An exemplary instance is found in spiral separators, also known as spiral concentrators, resembling colossal screws with a vertically oriented axis. These apparatuses facilitate the separation of liquids, liquid-particle mixtures (slurries), or powders descending in a spiral trajectory along a winding slope predicated upon density or particle size differences. The interaction of centrifugal, gravity, and drag forces created by the spiral path is what drives this separation process.

Smaller and lighter particles often migrate towards the spiral's outer periphery, whereas larger and denser particles typically tend towards the core axis. For quite some time, spiral separators have been acknowledged for achieving particle separation as fine as 30 µm while being economical, environmentally friendly, and requiring little energy in mineral[89] separation processes.

Despite their century-long use, comprehensive theoretical insights into the fluid dynamics governing spiral separators remained elusive until recently.[90] Such understanding necessitated sophisticated 3D multiphase flow and turbulence modelling techniques to elucidate the intricacies of fluid behaviour within these devices.

1.6 Spin Coating

The widely used spin-coating method is another situation where a liquid with a free top surface rotates. This method brings viscosity forces, solvent evaporation from a liquid film,[91] and centrifugal acceleration into delicate balance. Central to spin coating's utility is its capacity to generate smooth, thin films of photoresists with precise control over thickness,[92] a capability pivotal to photolithographic methodologies.[93]

In recent years, spin coating has garnered widespread adoption for fabricating high-quality thin films across diverse applications. Luminescent films for biosensing applications,[97] perovskite films for solar cell technologies,[94 - 96] nanoporous block copolymer films,[98] open-lattice colloidal crystals,[99] evenly doped graphene,[100] and composites with partially oriented nanotubes[101] are a few of these. Such versatile applications extend to potential uses in computing and beyond.[102]

1.7 Spinning Disc Reactors

The fundamental element of rotating tube reactors[103, 107] and spinning disc reactors (SDRs)[103 - 106] is the deployment of liquids onto revolving discs or inside of tubes. In SDRs, thin liquid films ranging from 25 to 200 µm thick are subjected to substantial shear forces due to centrifugal acceleration,[103 - 105] significantly augmenting heat and mass transfer rates.[108] This property helps to speed up exothermic reactions and other processes that would otherwise be impeded by slow mass transfer kinetics.[104]

The adaptability of rotating tube reactors and SDRs has been well-documented in several disciplines.[103, 109] Their applications include the manipulation of nanoparticles[103] and biotransformations.[110]

However, these devices are not without limitations. Short residence durations[103] are usually required for them, and a constant flow of liquids[111] is necessary to maintain a continuous shear intensity in the fluids interacting with the rotating surfaces.

1.8 Multilayered Rotating Systems

This discussion has focused on systems that support a single liquid phase thus far. On the other hand, centripetal pressures are applied to separate immiscible liquids into concentric layers based on density when the vessel is rotating. Notably, the density gradient ascends outwards,[112] with the densest liquid—subject to the most substantial centrifugal force—occupying the container's periphery (see Figure 1.4).

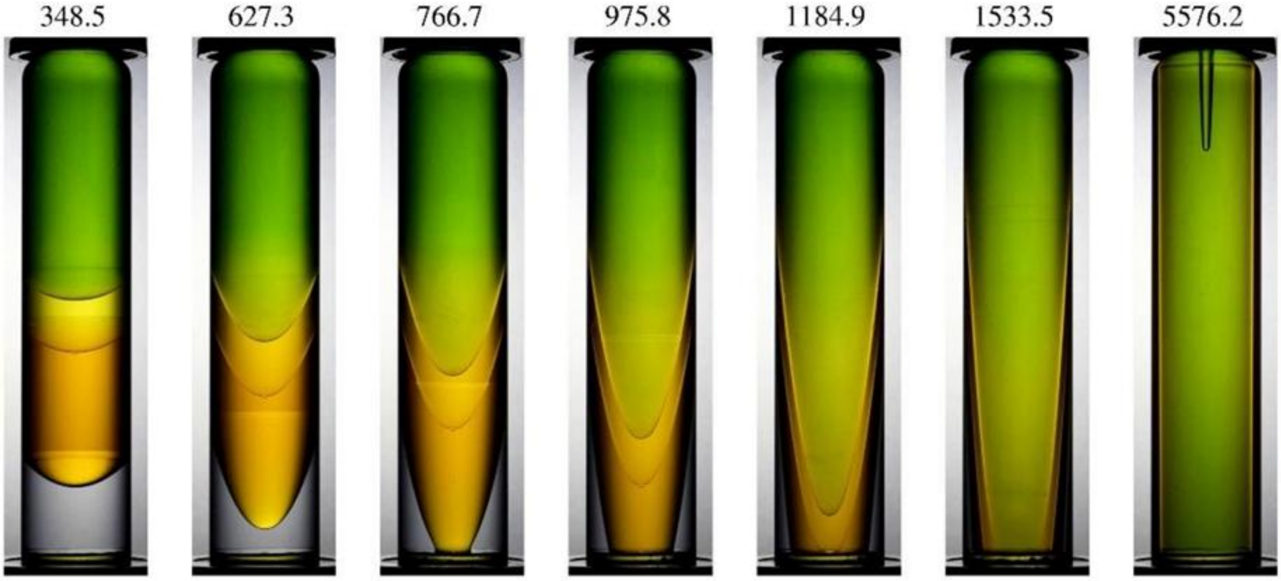

Figure 1.4 Continuous topological transformation of layers in elongated rotating tubes.

In the system's stationary state, mutually immiscible liquids are arranged from the densest to the lightest as the rotation speed (rpm) increases. Reprinted from REF,[112] Springer Nature Limited.

In a more intricate adaptation, liquids can be systematically introduced into an already rotating "stack." With careful execution, this method allows for stacking up to approximately 25 layers, including configurations where only adjacent layers exhibit pairwise immiscibility (such as alternating organic-aqueous stacks, as depicted in Figure 1.5).

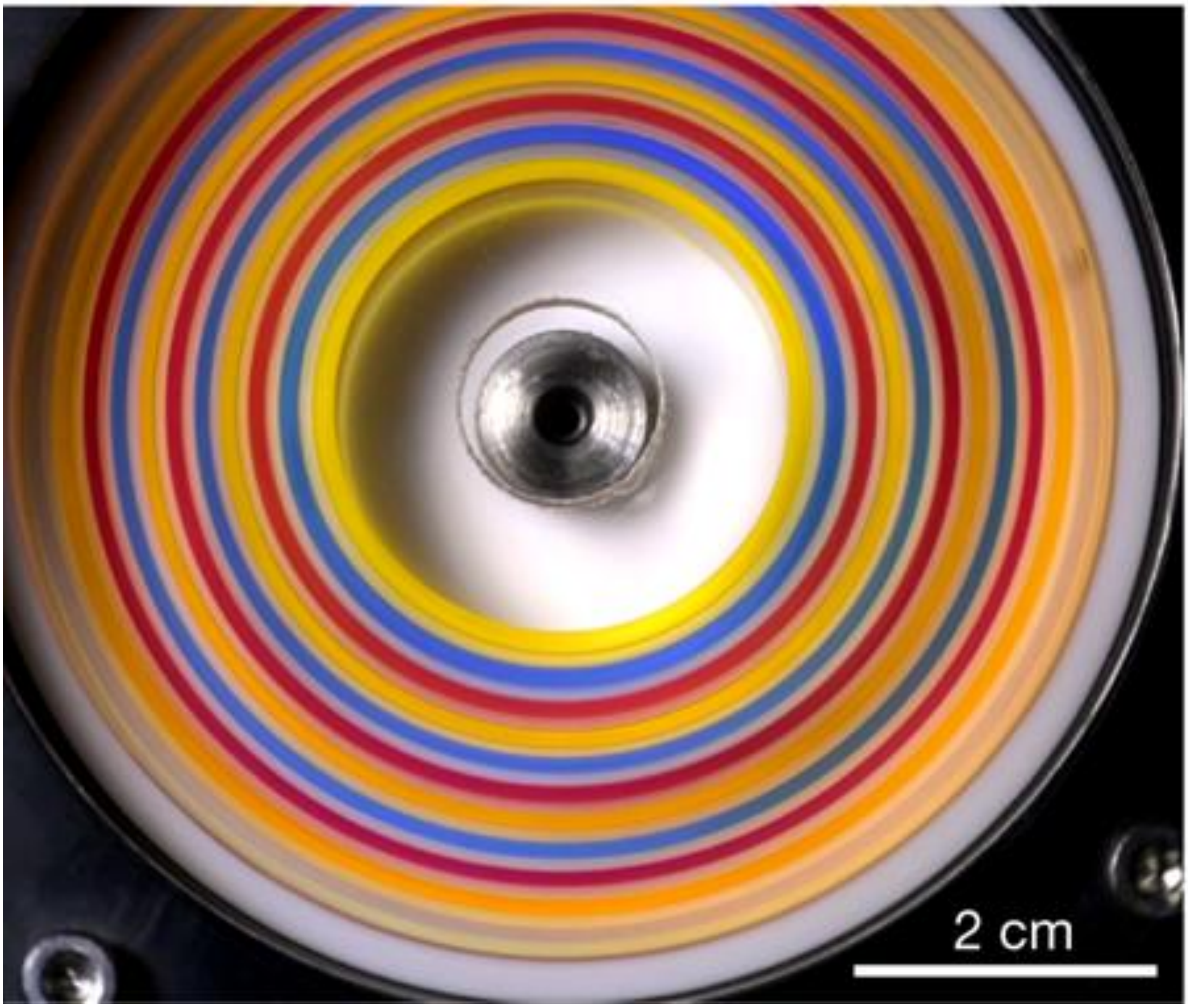

Figure 1.5 A stable, 22-layer discrete density ‘staircase.’

A stable, 22-layer discrete density ‘staircase’ is produced by certain ingredients and densities inside a chamber that rotates at 5,400 rpm. Over time, these layers remain stable and show no evidence of cross-contamination. Reprinted from REF,[112] Springer Nature Limited.

Two noteworthy observations merit attention. First, in containers of macroscopic dimensions, usually centimetres in size, and subjected to angular velocities in the range of single thousands of revolutions per minute, centrifugal forces dramatically outweigh surface tension effects. Consequently, the layers can be rendered exceptionally thin, reaching mere hundreds of micrometres in thickness (refer to Figure 1.6). Second, liquids circulate along both angular and radial coordinates due to cyclical acceleration and deceleration. This dynamic circulation fosters internal mixing within each layer, facilitating rapid stack transport. Notably, unlike static density columns,[113, 114] where transport is diffusion-limited, and layers must maintain considerable thickness to ensure stability, the rotating stack method enables thinner layers and efficient mixing without compromising structural integrity.

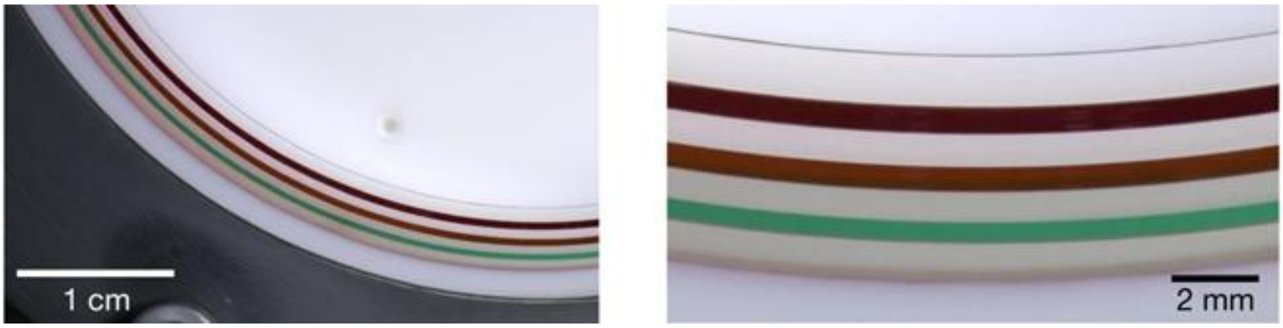

Figure 1.6 Layered system.

(Left) A seven-layer system with a total thickness of less than 5 mm made up of translucent mixtures of halocarbons and hydrocarbons and coloured water solutions of salts, starting with the densest green-coloured solution. **(Right)** A closer view of the system on the left. Reprinted from REF,[112] Springer Nature Limited.

Concentric-layer reactors leveraging rotational principles offer enhanced robustness and scalability compared to droplet-in-droplet emulsions, commonly called liquid emulsion membranes.[115 - 117] The commercial viability of the latter has been impeded by challenges related to emulsion instability and the need for intricate stirring mechanisms to sustain their integrity. Additionally, through the use of positively charged carriers – like long-chain aliphatic amines and their salts, which are employed in particular liquid emulsion membrane[118, 119] formulations – the application of concentric reactors may be extended to the specific extraction of negatively charged species from complex mixtures.

Beyond selective extraction processes, concentric liquid reactors find diverse applications across biotechnological domains. Their adaptability and usefulness in furthering numerous scientific activities are highlighted by their ability to facilitate bacterial communication across multiple layers and perform non-lethal extractions of bacteria.[112]

1.9 Vortex Fluidic Device (VFD) and Thesis Matrix

The vortex fluidic device (VFD) is another rotary reactor system that facilitates various processes. This device is the linchpin of this thesis and will be discussed further in Chapter 2.

This thesis has seven chapters, four of which focus on the investigations' outcomes, recommendations, and future work. Chapter 1 provides a general overview of the thesis and the investigation's goals. As noted, Chapter 2 is a literature review evaluating the most recent VFD data.

Chapter 3 will examine the signature of mixed solvent systems in the VFD with varying speeds and tube geometries. The microfluidic platform forms thin films by confining liquid reagents during processing, a vital aspect of this thesis. Characterising the ability of the VFD to operate mixed solvent systems has led to swift system optimisation, allowing the illumination of many advantages of VFD-based thin films.

The findings from Chapter 3 were then utilised to form Chapter 4, which investigated and manipulated these hybrid solvent systems in the VFD for perfluorooctanoic acid extraction. Chapter 5 establishes an alternative optimal processing parameter opposite the previous two chapters by investigating an inorganic-organic nanocomposite based on aggregation-induced emission probes. This thesis offers the basis for transforming these probes in the VFD, with results providing implications for biomedical applications and beyond.

Chapter 6 explores a previously discovered phenomenon and attempts to understand the mechanism based on the findings thus far. The closing chapter, Chapter 7, summarises the main conclusions of the experimental chapters and critically addresses the difficulties with this research. Significant avenues for future research are discussed in light of these.

1.10 Conclusion

A diverse array of systems exists wherein a macroscopic vessel's rotation governs its contents' transport or organisation. Although the fundamental principles of numerous systems, such as centrifuges, lab-on-a-disc apparatuses, or those propelling colloidal self-assembly, are widely recognised, innovative uses continue to be addressed. For example, although the physics of multilayered reactors, as shown in Figure 1.6, may appear simple, their ability to facilitate multistep extraction procedures calls for further investigation, opening up new study directions.

However, fundamental understanding remains elusive for certain systems, raising myriad questions. Some of the most fascinating questions posed by academics concern the complicated interactions of shear forces, highlighting the intricacy of these rotating systems and the stimulating prospects they offer for scientific study.

The timing of experiments involving rotating vessels now harmonises with technological advancements, enabling seamless interfacing with the external environment. Although slip rings (including mercury-wetted ones) for electrical connections, rotary unions that facilitate fluid supply to rotating systems, and fibre-optic rotary joints[120, 121] have long been known, their modular availability from reputable companies has only recently become widespread.

Furthermore, sensors and other electrical or electromechanical components contained within spinning vessels no longer require physical connections to the outside world via slip rings, thanks to the development of wireless communication standards. Such physical connections have always hampered precise measurements of weak signals.[122 - 126] For example, modern lab-on-a-disc technologies can have electrical layers with microcontrollers that can connect wirelessly to other systems. These microcontrollers are powered by revolving transformers to capture the rotary motion in an external magnetic field.[122, 127]

It's now possible to monitor and modify the conditions inside rotating reactors without implanting electrical components in the reactor itself. Although they're widely accessible, remote thermometers are only helpful for taking surface temperatures unless the materials are transparent to infrared light. Colorimetry can be used to facilitate bulk temperature measurements by employing thermochromic coatings or capsules that are commercially available. Furthermore, it's possible to monitor different ions and molecules using colorimetric[128, 129] or fluorescent sensors,[130] which are frequently found in sticky patches, foils, or coatings. Fluorescent sensors for pH[131] and dissolved gases[132] are also available.

However, direct use of these sensors and their remote readers presents difficulties since it frequently requires a line of sight through a moving observation window for a length of time that's incompatible with quickly rotating devices. Innovative technologies such as rotating mirrors or optical fibres that divert light from the moving observation window to a stationary detector could be used to solve this problem. Spinning mirrors and choppers, despite their complexity, are widely used in various devices, from benchtop spectrophotometers and confocal microscopes to laser printers and scanners. This provides valuable information for developing optical interfaces designed explicitly for rotating reactors.

1.11 References

1. Lynden-Bell, D., and J. E. Pringle. “The Evolution of Viscous Discs and the Origin of the Nebular Variables.” Monthly Notices of the Royal Astronomical Society 168, no. 3 (September 1, 1974): 603–37. https://doi.org/10.1093/mnras/168.3.603.
2. Berg, Howard C., and Robert A. Anderson. “Bacteria Swim by Rotating Their Flagellar Filaments.” Nature 245, no. 5425 (October 1, 1973): 380–82. https://doi.org/10.1038/245380a0.
3. Dreyfus, Rémi, Jean Baudry, Marcus L. Roper, Marc Fermigier, Howard A. Stone, and Jérôme Bibette. “Microscopic Artificial Swimmers.” Nature 437, no. 7060 (October 1, 2005): 862–65. https://doi.org/10.1038/nature04090.
4. Han, Su-Ting, Ye Zhou, and V. A. L. Roy. “Towards the Development of Flexible Non-Volatile Memories.” Advanced Materials 25, no. 38 (October 11, 2013): 5425–49. https://doi.org/10.1002/adma.201301361.
5. Noji, H., R. Yasuda, M. Yoshida, and K. Jr Kinosita. “Direct Observation of the Rotation of F1-ATPase.” Nature 386, no. 6622 (March 20, 1997): 299–302. https://doi.org/10.1038/386299a0.
6. Kay, Euan R., David A. Leigh, and Francesco Zerbetto. “Synthetic Molecular Motors and Mechanical Machines.” Angewandte Chemie (International Ed. in English) 46, no. 1–2 (2007): 72–191. https://doi.org/10.1002/anie.200504313.
7. Balzani, V. V., A. Credi, F. M. Raymo, and J. F. Stoddart. “Artificial Molecular Machines.” Angewandte Chemie (International Ed. in English) 39, no. 19 (October 2, 2000): 3348–91. https://doi.org/10.1002/1521-3773(20001002)39:19<3348::aid-anie3348>3.0.co;2-x.
8. Eelkema, Rienk, Michael M. Pollard, Javier Vicario, Nathalie Katsonis, Blanca Serrano Ramon, Cees W. M. Bastiaansen, Dirk J. Broer, and Ben L. Feringa. “Nanomotor Rotates Microscale Objects.” Nature 440, no. 7081 (March 1, 2006): 163–163. https://doi.org/10.1038/440163a.
9. Ruangsupapichat, Nopporn, Michael M. Pollard, Syuzanna R. Harutyunyan, and Ben L. Feringa. “Reversing the Direction in a Light-Driven Rotary Molecular Motor.” Nature Chemistry 3, no. 1 (January 2011): 53–60. https://doi.org/10.1038/nchem.872.
10. Grzybowski, Bartosz A., Howard A. Stone, and George M. Whitesides. “Dynamic Self-Assembly of Magnetized, Millimetre-Sized Objects Rotating at a Liquid–Air Interface.” Nature 405, no. 6790 (June 1, 2000): 1033–36. https://doi.org/10.1038/35016528.
11. Grzybowski, Bartosz A., and George M. Whitesides. “Dynamic Aggregation of Chiral Spinners.” Science (New York, N.Y.) 296, no. 5568 (April 26, 2002): 718–21. https://doi.org/10.1126/science.1068130.
12. Grzybowski, Bartosz A., and George M. Whitesides. “Directed Dynamic Self-Assembly of Objects Rotating on Two Parallel Fluid Interfaces.” The Journal of Chemical Physics 116, no. 19 (May 15, 2002): 8571–77. https://doi.org/10.1063/1.1462607.

13. Lenz, Peter, Jean-François Joanny, Frank Jülicher, and Jacques Prost. “Membranes with Rotating Motors.” Physical Review Letters 91, no. 10 (September 5, 2003): 108104. https://doi.org/10.1103/PhysRevLett.91.108104.
14. Goto, Yusuke, and Hajime Tanaka. “Purely Hydrodynamic Ordering of Rotating Disks at a Finite Reynolds Number.” Nature Communications 6, no. 1 (January 28, 2015): 5994. https://doi.org/10.1038/ncomms6994.
15. Yeo, Kyongmin, Enkeleida Lushi, and Petia M. Vlahovska. “Collective Dynamics in a Binary Mixture of Hydrodynamically Coupled Microrotors.” Physical Review Letters 114, no. 18 (May 5, 2015): 188301. https://doi.org/10.1103/PhysRevLett.114.188301.
16. Kokot, Gasper, Alexey Snezhko, and Igor S. Aranson. “Emergent Coherent States and Flow Rectification in Active Magnetic Colloidal Monolayers.” Soft Matter 9, no. 29 (2013): 6757–60. https://doi.org/10.1039/C3SM00136A.
17. Snezhko, Alexey, Eshel Ben Jacob, and Igor S Aranson. “Pulsating–Gliding Transition in the Dynamics of Levitating Liquid Nitrogen Droplets.” New Journal of Physics 10, no. 4 (April 21, 2008): 043034. https://doi.org/10.1088/1367-2630/10/4/043034.
18. Svedberg, The, and Herman Rinde. “THE ULTRA-CENTRIFUGE, A NEW INSTRUMENT FOR THE DETERMINATION OF SIZE AND DISTRIBUTION OF SIZE OF PARTICLE IN AMICROSCOPIC COLLOIDS.” Journal of the American Chemical Society 46, no. 12 (December 1, 1924): 2677–93. https://doi.org/10.1021/ja01677a011.
19. Van Holde, K. E., and R. L. Baldwin. “Rapid Attainment of Sedimentation Equilibrium.” The Journal of Physical Chemistry 62, no. 6 (June 1, 1958): 734–43. https://doi.org/10.1021/j150564a025.
20. Bancroft, Frank C., and David Freifelder. “Molecular Weights of Coliphages and Coliphage DNA: I. Measurement of the Molecular Weight of Bacteriophage T7 by High-Speed Equilibrium Centrifugation.” Journal of Molecular Biology 54, no. 3 (December 28, 1970): 537–46. https://doi.org/10.1016/0022-2836(70)90124-5.
21. Ghirlando, Rodolfo. “The Analysis of Macromolecular Interactions by Sedimentation Equilibrium.” Modern Analytical Ultracentrifugation 54, no. 1 (May 1, 2011): 145–56. https://doi.org/10.1016/j.ymeth.2010.12.005.
22. Schildkraut, Carl L., Julius Marmur, and Paul Doty. “Determination of the Base Composition of Deoxyribonucleic Acid from Its Buoyant Density in CsCl.” Journal of Molecular Biology 4, no. 6 (June 1, 1962): 430–43. https://doi.org/10.1016/S0022-2836(62)80100-4.
23. Stafford, W. F. 3rd. “Boundary Analysis in Sedimentation Transport Experiments: A Procedure for Obtaining Sedimentation Coefficient Distributions Using the Time Derivative of the Concentration Profile.” Analytical Biochemistry 203, no. 2 (June 1992): 295–301. https://doi.org/10.1016/0003-2697(92)90316-y.

24. Correia, J. J., S. Shire, D. A. Yphantis, and T. M. Schuster. “Sedimentation Equilibrium Measurements of the Intermediate-Size Tobacco Mosaic Virus Protein Polymers.” Biochemistry 24, no. 13 (June 18, 1985): 3292–97. https://doi.org/10.1021/bi00334a033.
25. Teller, David C. “[14] Characterization of Proteins by Sedimentation Equilibrium in the Analytical Ultracentrifuge.” In Methods in Enzymology, 27:346–441. Academic Press, 1973. https://doi.org/10.1016/S0076-6879(73)27017-9.
26. Vistica, Jennifer, Julie Dam, Andrea Balbo, Emine Yikilmaz, Roy A. Mariuzza, Tracey A. Rouault, and Peter Schuck. “Sedimentation Equilibrium Analysis of Protein Interactions with Global Implicit Mass Conservation Constraints and Systematic Noise Decomposition.” Analytical Biochemistry 326, no. 2 (March 15, 2004): 234–56. https://doi.org/10.1016/j.ab.2003.12.014.
27. Richards, E Glen, and Howard K. Schachman. “Ultracentrifuge Studies with Rayleigh Interference Optics.I. General Application.” The Journal of Physical Chemistry 63, no. 10 (October 1, 1959): 1578–91. https://doi.org/10.1021/j150580a008.
28. Prakash, V., and S. N. Timasheff. “Mechanism of Interaction of Vinca Alkaloids with Tubulin: Catharanthine and Vindoline.” Biochemistry 30, no. 3 (January 22, 1991): 873–80. https://doi.org/10.1021/bi00217a042.
29. Akbulut, Ozge, Charles R. Mace, Ramses V. Martinez, Ashok A. Kumar, Zhihong Nie, Matthew R. Patton, and George M. Whitesides. “Separation of Nanoparticles in Aqueous Multiphase Systems through Centrifugation.” Nano Letters 12, no. 8 (August 8, 2012): 4060–64. https://doi.org/10.1021/nl301452x.
30. Planken, Karel L., and Helmut Cölfen. “Analytical Ultracentrifugation of Colloids.” Nanoscale 2, no. 10 (2010): 1849–69. https://doi.org/10.1039/C0NR00215A.
31. Olander, Donald R. “The Theory of Uranium Enrichment by the Gas Centrifuge.” Progress in Nuclear Energy 8, no. 1 (January 1, 1981): 1–33. https://doi.org/10.1016/0149-1970(81)90026-3.
32. Whitley, Stanley. “Review of the Gas Centrifuge until 1962. Part I: Principles of Separation Physics.” Reviews of Modern Physics 56, no. 1 (January 1, 1984): 41–66. https://doi.org/10.1103/RevModPhys.56.41.
33. Lin, Chia-Chang, Wen-Tzong Liu, and Chung-Sung Tan. “Removal of Carbon Dioxide by Absorption in a Rotating Packed Bed.” Industrial & Engineering Chemistry Research 42, no. 11 (May 1, 2003): 2381–86. https://doi.org/10.1021/ie020669+.
34. Qian, Zhi, Zhen-Hu Li, and Kai Guo. “Industrial Applied and Modeling Research on Selective H2S Removal Using a Rotating Packed Bed.” Industrial & Engineering Chemistry Research 51, no. 23 (June 13, 2012): 8108–16. https://doi.org/10.1021/ie2027266.
35. Fowler, R., K.F. Gerdes, and H.F. Nygaard. “A Commercial-Scale Demonstration of Higee for Bulk CO2 Removal and Gas Dehydration,” OTC-6121-MS, 1989. https://doi.org/10.4043/6121-MS.

36. Munjal, Sarat, Milorad P. Dudukovć, and Palghat Ramachandran. “Mass-Transfer in Rotating Packed Beds—I. Development of Gas—Liquid and Liquid—Solid Mass-Transfer Correlations.” Chemical Engineering Science 44, no. 10 (January 1, 1989): 2245–56. https://doi.org/10.1016/0009-2509(89)85159-0.
37. Peel, J., C.R. Howarth, and C. Ramshaw. “Process Intensification: Higee Seawater Deaeration.” Oil and Natural Gas Production 76, no. 5 (July 1, 1998): 585–93. https://doi.org/10.1205/026387698525261.
38. Chang, Chia-Chi, Chun-Yu Chiu, Ching-Yuan Chang, Chiung-Fen Chang, Yi-Hung Chen, Dar-Ren Ji, Yue-Hwa Yu, and Pen-Chi Chiang. “Combined Photolysis and Catalytic Ozonation of Dimethyl Phthalate in a High-Gravity Rotating Packed Bed.” Journal of Hazardous Materials 161, no. 1 (January 15, 2009): 287–93. https://doi.org/10.1016/j.jhazmat.2008.03.085.
39. Cortes Garcia, German E, John van der Schaaf, and Anton A Kiss. “A Review on Process Intensification in HiGee Distillation.” Journal of Chemical Technology & Biotechnology 92, no. 6 (June 1, 2017): 1136–56. https://doi.org/10.1002/jctb.5206.
40. Kiss, Anton, and Megan Jobson. “Taking Reactive Distillation to the Next Level of Process Intensification.” Chemical Engineering Transactions 69 (October 1, 2018): 553–58. https://doi.org/10.3303/CET1869093.
41. Gudena, Krishna, G.P. Rangaiah, and S. Lakshminarayanan. “Modeling and Analysis of Solid Catalyzed Reactive HiGee Stripping.” Chemical Engineering Science 80 (October 1, 2012): 242–52. https://doi.org/10.1016/j.ces.2012.06.008.
42. Yu, Cheng-Hsiu, Chih-Hung Huang, and Chung-Sung Tan. “A Review of CO2 Capture by Absorption and Adsorption.” Aerosol and Air Quality Research 12, no. 5 (2012): 745–69. https://doi.org/10.4209/aaqr.2012.05.0132.
43. Oko, Eni, Meihong Wang, and Atuman S. Joel. “Current Status and Future Development of Solvent-Based Carbon Capture.” International Journal of Coal Science & Technology 4, no. 1 (March 1, 2017): 5–14. https://doi.org/10.1007/s40789-017-0159-0.
44. Chen, Jian-Feng, Yu-Hong Wang, Fen Guo, Xin-Ming Wang, and Chong Zheng. “Synthesis of Nanoparticles with Novel Technology: High-Gravity Reactive Precipitation.” Industrial & Engineering Chemistry Research 39, no. 4 (April 1, 2000): 948–54. https://doi.org/10.1021/ie990549a.
45. Brown, Jocelyn, Lauren Theis, Lila Kerr, Nazima Zakhidova, Kelly O’Connor, Margaret Uthman, Z. Maria Oden, and Rebecca Richards-Kortum. “A Hand-Powered, Portable, Low-Cost Centrifuge for Diagnosing Anemia in Low-Resource Settings.” The American Society of Tropical Medicine and Hygiene 85, no. 2 (August 1, 2011): 327–32. https://doi.org/10.4269/ajtmh.2011.10-0399.

46. Wong, Amy P., Malancha Gupta, Sergey S. Shevkoplyas, and George M. Whitesides. “Egg Beater as Centrifuge: Isolating Human Blood Plasma from Whole Blood in Resource-Poor Settings.” Lab on a Chip 8, no. 12 (2008): 2032–37. https://doi.org/10.1039/B809830C.
47. Bhamla, M. Saad, Brandon Benson, Chew Chai, Georgios Katsikis, Aanchal Johri, and Manu Prakash. “Hand-Powered Ultralow-Cost Paper Centrifuge.” Nature Biomedical Engineering 1, no. 1 (January 10, 2017): 0009. https://doi.org/10.1038/s41551-016-0009.
48. Strohmeier, O., M. Keller, F. Schwemmer, S. Zehnle, D. Mark, F. von Stetten, R. Zengerle, and N. Paust. “Centrifugal Microfluidic Platforms: Advanced Unit Operations and Applications.” Chemical Society Reviews 44, no. 17 (2015): 6187–6229. https://doi.org/10.1039/C4CS00371C.
49. Ducrée, Jens, Stefan Haeberle, Sascha Lutz, Sarah Pausch, Felix von Stetten, and Roland Zengerle. “The Centrifugal Microfluidic Bio-Disk Platform.” Journal of Micromechanics and Microengineering 17, no. 7 (June 28, 2007): S103. https://doi.org/10.1088/0960-1317/17/7/S07.
50. Gorkin, Robert, Jiwoon Park, Jonathan Siegrist, Mary Amasia, Beom Seok Lee, Jong-Myeon Park, Jintae Kim, Hanshin Kim, Marc Madou, and Yoon-Kyoung Cho. “Centrifugal Microfluidics for Biomedical Applications.” Lab on a Chip 10, no. 14 (2010): 1758–73. https://doi.org/10.1039/B924109D.
51. Kim, Nahui. “- LAB ON A CD.” - Annual Review of Biomedical Engineering 2006;8(1):601-628, n.d.
52. Siegrist, Jonathan, Robert Gorkin, Martine Bastien, Gale Stewart, Régis Peytavi, Horacio Kido, Michel Bergeron, and Marc Madou. “Validation of a Centrifugal Microfluidic Sample Lysis and Homogenization Platform for Nucleic Acid Extraction with Clinical Samples.” Lab on a Chip 10, no. 3 (2010): 363–71. https://doi.org/10.1039/B913219H.
53. Cho, Yoon-Kyoung, Jeong-Gun Lee, Jong-Myeon Park, Beom-Seok Lee, Youngsun Lee, and Christopher Ko. “One-Step Pathogen Specific DNA Extraction from Whole Blood on a Centrifugal Microfluidic Device.” Lab on a Chip 7, no. 5 (2007): 565–73. https://doi.org/10.1039/B616115D.
54. Schembri, C. T., T. L. Burd, A. R. Kopf-Sill, L. R. Shea, and B. Braynin. “Centrifugation and Capillarity Integrated into a Multiple Analyte Whole Blood Analyser.” Journal of Analytical Methods in Chemistry 17, no. 3 (January 1, 1995): 760816. https://doi.org/10.1155/S1463924695000174.
55. Lai, Siyi, Shengnian Wang, Jun Luo, L. James Lee, Shang-Tian Yang, and Marc J. Madou. “Design of a Compact Disk-like Microfluidic Platform for Enzyme-Linked Immunosorbent Assay.” Analytical Chemistry 76, no. 7 (April 1, 2004): 1832–37. https://doi.org/10.1021/ac0348322.

56. Lee, Beom Seok, Jung-Nam Lee, Jong-Myeon Park, Jeong-Gun Lee, Suhyeon Kim, Yoon-Kyoung Cho, and Christopher Ko. “A Fully Automated Immunoassay from Whole Blood on a Disc.” Lab on a Chip 9, no. 11 (2009): 1548–55. https://doi.org/10.1039/B820321K.
57. Sackmann, Eric K., Anna L. Fulton, and David J. Beebe. “The Present and Future Role of Microfluidics in Biomedical Research.” Nature 507, no. 7491 (March 1, 2014): 181–89. https://doi.org/10.1038/nature13118.
58. Walker, Glenn M., and David J. Beebe. “A Passive Pumping Method for Microfluidic Devices.” Lab on a Chip 2, no. 3 (2002): 131–34. https://doi.org/10.1039/B204381E.
59. Schwemmer, Frank, Clement E. Blanchet, Alessandro Spilotros, Dominique Kosse, Steffen Zehnle, Haydyn D. T. Mertens, Melissa A. Graewert, et al. “LabDisk for SAXS: A Centrifugal Microfluidic Sample Preparation Platform for Small-Angle X-Ray Scattering.” Lab on a Chip 16, no. 7 (2016): 1161–70. https://doi.org/10.1039/C5LC01580D.
60. Hwang, Hyundoo, Seung-Hoon Kim, Tae-Hyeong Kim, Je-Kyun Park, and Yoon-Kyoung Cho. “Paper on a Disc: Balancing the Capillary-Driven Flow with a Centrifugal Force.” Lab on a Chip 11, no. 20 (2011): 3404–6. https://doi.org/10.1039/C1LC20445A.
61. Kainz, Daniel M., Susanna M. Früh, Tobias Hutzenlaub, Roland Zengerle, and Nils Paust. “Flow Control for Lateral Flow Strips with Centrifugal Microfluidics.” Lab on a Chip 19, no. 16 (2019): 2718–27. https://doi.org/10.1039/C9LC00308H.
62. Thiha, Aung, and Fatimah Ibrahim. “A Colorimetric Enzyme-Linked Immunosorbent Assay (ELISA) Detection Platform for a Point-of-Care Dengue Detection System on a Lab-on-Compact-Disc.” Sensors (Basel, Switzerland) 15, no. 5 (May 18, 2015): 11431–41. https://doi.org/10.3390/s150511431.
63. Sayad, Abkar Ahmed, Fatimah Ibrahim, Shah Mukim Uddin, Koh Xiu Pei, Mas S. Mohktar, Marc Madou, and Kwai Lin Thong. “A Microfluidic Lab-on-a-Disc Integrated Loop Mediated Isothermal Amplification for Foodborne Pathogen Detection.” Sensors and Actuators B: Chemical 227 (May 1, 2016): 600–609. https://doi.org/10.1016/j.snb.2015.10.116.
64. Nwankire, Charles E., Anita Venkatanarayanan, Thomas Glennon, Tia E. Keyes, Robert J. Forster, and Jens Ducrée. “Label-Free Impedance Detection of Cancer Cells from Whole Blood on an Integrated Centrifugal Microfluidic Platform.” Biosensors & Bioelectronics 68 (June 15, 2015): 382–89. https://doi.org/10.1016/j.bios.2014.12.049.
65. Morais, Sergi, Jesús Tamarit-López, Javier Carrascosa, Rosa Puchades, and Angel Maquieira. “Analytical Prospect of Compact Disk Technology in Immunosensing.” Analytical and Bioanalytical Chemistry 391, no. 8 (August 2008): 2837–44. https://doi.org/10.1007/s00216-008-2224-4.
66. Kinahan, David J., Sinéad M. Kearney, Nikolay Dimov, Macdara T. Glynn, and Jens Ducrée. “Event-Triggered Logical Flow Control for Comprehensive Process Integration of Multi-Step Assays on Centrifugal Microfluidic Platforms.” Lab on a Chip 14, no. 13 (2014): 2249–58. https://doi.org/10.1039/C4LC00380B.

67. Miyazaki, Celina M., David J. Kinahan, Rohit Mishra, Faith Mangwanya, Niamh Kilcawley, Marystela Ferreira, and Jens Ducrée. “Label-Free, Spatially Multiplexed SPR Detection of Immunoassays on a Highly Integrated Centrifugal Lab-on-a-Disc Platform.” Biosensors and Bioelectronics 119 (November 15, 2018): 86–93. https://doi.org/10.1016/j.bios.2018.07.056.
68. Kinahan, David J., Sinéad M. Kearney, Olivier P. Faneuil, Macdara T. Glynn, Nikolay Dimov, and Jens Ducrée. “Paper Imbibition for Timing of Multi-Step Liquid Handling Protocols on Event-Triggered Centrifugal Microfluidic Lab-on-a-Disc Platforms.” RSC Advances 5, no. 3 (2015): 1818–26. https://doi.org/10.1039/C4RA14887H.
69. Kinahan, David J., Philip L. Early, Abhishek Vembadi, Eoghan MacNamara, Niamh A. Kilcawley, Thomas Glennon, Dermot Diamond, Dermot Brabazon, and Jens Ducrée. “Xurography Actuated Valving for Centrifugal Flow Control.” Lab on a Chip 16, no. 18 (2016): 3454–59. https://doi.org/10.1039/C6LC00568C.
70. Kinahan, David J., Marine Renou, Dirk Kurzbuch, Niamh A. Kilcawley, Éanna Bailey, Macdara T. Glynn, Colette McDonagh, and Jens Ducrée. “Baking Powder Actuated Centrifugo-Pneumatic Valving for Automation of Multi-Step Bioassays.” Micromachines 7, no. 10 (October 1, 2016). https://doi.org/10.3390/mi7100175.
71. McArdle, Hazel, Eva M. Jimenez-Mateos, Rana Raoof, Eadaoin Carthy, David Boyle, Hany ElNaggar, Norman Delanty, et al. “‘TORNADO’ – Theranostic One-Step RNA Detector; Microfluidic Disc for the Direct Detection of microRNA-134 in Plasma and Cerebrospinal Fluid.” Scientific Reports 7, no. 1 (May 11, 2017): 1750. https://doi.org/10.1038/s41598-017-01947-2.
72. Nwankire, Charles E., Di-Sien S. Chan, Jennifer Gaughran, Robert Burger, Robert 3rd Gorkin, and Jens Ducrée. “Fluidic Automation of Nitrate and Nitrite Bioassays in Whole Blood by Dissolvable-Film Based Centrifugo-Pneumatic Actuation.” Sensors (Basel, Switzerland) 13, no. 9 (August 26, 2013): 11336–49. https://doi.org/10.3390/s130911336.
73. Hess, J. F., S. Zehnle, P. Juelg, T. Hutzenlaub, R. Zengerle, and N. Paust. “Review on Pneumatic Operations in Centrifugal Microfluidics.” Lab on a Chip 19, no. 22 (2019): 3745–70. https://doi.org/10.1039/C9LC00441F.
74. Ducrée, J., T. Glatzel, T. Brenner, and R. Zengerle. “Coriolis-Induced Flow Control for Micro- and Nanofluidic Lab-on-a-Disk Technologies.” In MicroNano Integration, edited by Harald Knobloch and Yvette Kaminorz, 147–53. Berlin, Heidelberg: Springer Berlin Heidelberg, 2004.
75. Brenner, Thilo, Thomas Glatzel, Roland Zengerle, and Jens Ducrée. “Frequency-Dependent Transversal Flow Control in Centrifugal Microfluidics.” Lab on a Chip 5, no. 2 (2005): 146–50. https://doi.org/10.1039/B406699E.
76. Kassegne, Sam, Ajit Khosla, Dhruv Patel, Nithesh Paramesh, Nitin Harwood, and Bhuvnesh Arya. “Coriolis Force for Facilitating DNA Molecular Migration and Hybridization in Compact

Disk Microfluidic Platforms.” Microsystem Technologies 21, no. 4 (April 1, 2015): 719–32. https://doi.org/10.1007/s00542-014-2087-x.

77. Woo, Hyun-Kyung, Vijaya Sunkara, Juhee Park, Tae-Hyeong Kim, Ja-Ryoung Han, Chi-Ju Kim, Hyun-Il Choi, Yoon-Keun Kim, and Yoon-Kyoung Cho. “Exodisc for Rapid, Size-Selective, and Efficient Isolation and Analysis of Nanoscale Extracellular Vesicles from Biological Samples.” ACS Nano 11, no. 2 (February 28, 2017): 1360–70. https://doi.org/10.1021/acsnano.6b06131.
78. Klatt, Jan-Niklas, Ingmar Schwarz, Tobias Hutzenlaub, Roland Zengerle, Frank Schwemmer, Dominique Kosse, Jake Vincent, et al. “Miniaturization, Parallelization, and Automation of Endotoxin Detection by Centrifugal Microfluidics.” Analytical Chemistry 93, no. 24 (June 22, 2021): 8508–16. https://doi.org/10.1021/acs.analchem.1c01041.
79. Rissin, David M, Cheuk W Kan, Todd G Campbell, Stuart C Howes, David R Fournier, Linan Song, Tomasz Piech, et al. “Single-Molecule Enzyme-Linked Immunosorbent Assay Detects Serum Proteins at Subfemtomolar Concentrations.” Nature Biotechnology 28, no. 6 (June 1, 2010): 595–99. https://doi.org/10.1038/nbt.1641.
80. Rissin, David M., David R. Fournier, Tomasz Piech, Cheuk W. Kan, Todd G. Campbell, Linan Song, Lei Chang, et al. “Simultaneous Detection of Single Molecules and Singulated Ensembles of Molecules Enables Immunoassays with Broad Dynamic Range.” Analytical Chemistry 83, no. 6 (March 15, 2011): 2279–85. https://doi.org/10.1021/ac103161b.
81. Land, Kevin J., Debrah I. Boeras, Xiang-Sheng Chen, Andrew R. Ramsay, and Rosanna W. Peeling. “REASSURED Diagnostics to Inform Disease Control Strategies, Strengthen Health Systems and Improve Patient Outcomes.” Nature Microbiology 4, no. 1 (January 2019): 46–54. https://doi.org/10.1038/s41564-018-0295-3.
82. Zhang, Lu, Fei Tian, Chao Liu, Qiang Feng, Tingxuan Ma, Zishan Zhao, Tiejun Li, Xingyu Jiang, and Jiashu Sun. “Hand-Powered Centrifugal Microfluidic Platform Inspired by the Spinning Top for Sample-to-Answer Diagnostics of Nucleic Acids.” Lab on a Chip 18, no. 4 (2018): 610–19. https://doi.org/10.1039/C7LC01234A.
83. Michael, Issac, Dongyoung Kim, Oleksandra Gulenko, Sumit Kumar, Saravana Kumar, Jothi Clara, Dong Yeob Ki, et al. “A Fidget Spinner for the Point-of-Care Diagnosis of Urinary Tract Infection.” Nature Biomedical Engineering 4, no. 6 (June 1, 2020): 591–600. https://doi.org/10.1038/s41551-020-0557-2.
84. Pradeep, A.D., and T. Rameshkumar. “Review on Centrifugal Casting of Functionally Graded Materials.” International Conference on Advances in Materials Research - 2019 45 (January 1, 2021): 729–34. https://doi.org/10.1016/j.matpr.2020.02.764.
85. Saleh, Bassiouny, Jinghua Jiang, Aibin Ma, Dan Song, Donghui Yang, and Qiong Xu. “Review on the Influence of Different Reinforcements on the Microstructure and Wear Behavior of Functionally Graded Aluminum Matrix Composites by Centrifugal Casting.”

Metals and Materials International 26, no. 7 (July 1, 2020): 933–60. https://doi.org/10.1007/s12540-019-00491-0.

86. Zygmuntowicz, Justyna, Marcin Wachowski, Paulina Piotrkiewicz, Aleksandra Miazga, Waldemar Kaszuwara, and Katarzyna Konopka. “Investigation on Fabrication and Property of Graded Composites Obtained via Centrifugal Casting in the Magnetic Field.” Composites Part B: Engineering 173 (September 15, 2019): 106999. https://doi.org/10.1016/j.compositesb.2019.106999.
87. Zhong, Jing, Wei Sun, Qinwei Wei, Xitang Qian, Hui-Ming Cheng, and Wencai Ren. “Efficient and Scalable Synthesis of Highly Aligned and Compact Two-Dimensional Nanosheet Films with Record Performances.” Nature Communications 9, no. 1 (August 28, 2018): 3484. https://doi.org/10.1038/s41467-018-05723-2.
88. Kim, Jin Young, Valerio Adinolfi, Brandon R. Sutherland, Oleksandr Voznyy, S. Joon Kwon, Tae Wu Kim, Jeongho Kim, et al. “Single-Step Fabrication of Quantum Funnels via Centrifugal Colloidal Casting of Nanoparticle Films.” Nature Communications 6, no. 1 (July 13, 2015): 7772. https://doi.org/10.1038/ncomms8772.
89. Richards, R.G., D.M. MacHunter, P.J. Gates, and M.K. Palmer. “Gravity Separation of Ultra-Fine (−0.1mm) Minerals Using Spiral Separators.” Minerals Engineering 13, no. 1 (January 1, 2000): 65–77. https://doi.org/10.1016/S0892-6875(99)00150-8.
90. Matthews, B.W., C.A.J. Fletcher, and A.C. Partridge. “Computational Simulation of Fluid and Dilute Particulate Flows on Spiral Concentrators.” Applied Mathematical Modelling 22, no. 12 (December 1, 1998): 965–79. https://doi.org/10.1016/S0307-904X(98)10030-6.
91. Emslie, Alfred G., Francis T. Bonner, and Leslie G. Peck. “Flow of a Viscous Liquid on a Rotating Disk.” Journal of Applied Physics 29, no. 5 (May 1, 1958): 858–62. https://doi.org/10.1063/1.1723300.
92. WILSON, S. K., R. HUNT, and B. R. DUFFY. “The Rate of Spreading in Spin Coating.” Journal of Fluid Mechanics 413 (2000): 65–88. https://doi.org/10.1017/S0022112000008089.
93. Xia, Younan, and George M. Whitesides. “Soft Lithography.” Angewandte Chemie International Edition 37, no. 5 (March 16, 1998): 550–75. https://doi.org/10.1002/(SICI)1521-3773(19980316)37:5<550::AID-ANIE550>3.0.CO;2-G.
94. Ahn, Namyoung, Dae-Yong Son, In-Hyuk Jang, Seong Min Kang, Mansoo Choi, and Nam-Gyu Park. “Highly Reproducible Perovskite Solar Cells with Average Efficiency of 18.3% and Best Efficiency of 19.7% Fabricated via Lewis Base Adduct of Lead(II) Iodide.” Journal of the American Chemical Society 137, no. 27 (July 15, 2015): 8696–99. https://doi.org/10.1021/jacs.5b04930.
95. Kan, Bin, Miaomiao Li, Qian Zhang, Feng Liu, Xiangjian Wan, Yunchuang Wang, Wang Ni, et al. “A Series of Simple Oligomer-like Small Molecules Based on Oligothiophenes for Solution-Processed Solar Cells with High Efficiency.” Journal of the American Chemical Society 137, no. 11 (March 25, 2015): 3886–93. https://doi.org/10.1021/jacs.5b00305.

96. Chiang, Chien-Hung, Mohammad Khaja Nazeeruddin, Michael Grätzel, and Chun-Guey Wu. "The Synergistic Effect of H2O and DMF towards Stable and 20% Efficiency Inverted Perovskite Solar Cells." Energy & Environmental Science 10, no. 3 (2017): 808–17. https://doi.org/10.1039/C6EE03586H.

97. Guan, Weijiang, Wenjuan Zhou, Jun Lu, and Chao Lu. "Luminescent Films for Chemo- and Biosensing." Chemical Society Reviews 44, no. 19 (2015): 6981–7009. https://doi.org/10.1039/C5CS00246J.

98. Lee, Wonjoo, Xin Zhang, and R.M. Briber. "A Simple Method for Creating Nanoporous Block-Copolymer Thin Films." Polymer 51, no. 11 (May 14, 2010): 2376–82. https://doi.org/10.1016/j.polymer.2010.03.023.

99. Jiang, Peng, Tushar Prasad, Michael J. McFarland, and Vicki L. Colvin. "Two-Dimensional Nonclose-Packed Colloidal Crystals Formed by Spincoating." Applied Physics Letters 89, no. 1 (July 6, 2006): 011908. https://doi.org/10.1063/1.2218832.

100. He, Hans, Kyung Ho Kim, Andrey Danilov, Domenico Montemurro, Liyang Yu, Yung Woo Park, Floriana Lombardi, et al. "Uniform Doping of Graphene Close to the Dirac Point by Polymer-Assisted Assembly of Molecular Dopants." Nature Communications 9, no. 1 (September 27, 2018): 3956. https://doi.org/10.1038/s41467-018-06352-5.

101. Pradhan, Basudev, Ryan R. Kohlmeyer, and Jian Chen. "Fabrication of In-Plane Aligned Carbon Nanotube–Polymer Composite Thin Films." Carbon 48, no. 1 (January 1, 2010): 217–22. https://doi.org/10.1016/j.carbon.2009.09.006.

102. Shulaker, Max M., Gage Hills, Nishant Patil, Hai Wei, Hong-Yu Chen, H.-S. Philip Wong, and Subhasish Mitra. "Carbon Nanotube Computer." Nature 501, no. 7468 (September 1, 2013): 526–30. https://doi.org/10.1038/nature12502.

103. Chen, Xianjue, Nicole M. Smith, K. Swaminathan Iyer, and Colin L. Raston. "Controlling Nanomaterial Synthesis, Chemical Reactions and Self Assembly in Dynamic Thin Films." Chemical Society Reviews 43, no. 5 (2014): 1387–99. https://doi.org/10.1039/C3CS60247H.

104. Boodhoo, K.V.K., and R.J. Jachuck. "Process Intensification: Spinning Disk Reactor for Styrene Polymerisation." Applied Thermal Engineering 20, no. 12 (August 1, 2000): 1127–46. https://doi.org/10.1016/S1359-4311(99)00071-X.

105. Pask, Stephen D., Oskar Nuyken, and Zhizhong Cai. "The Spinning Disk Reactor: An Example of a Process Intensification Technology for Polymers and Particles." Polymer Chemistry 3, no. 10 (2012): 2698–2707. https://doi.org/10.1039/C2PY20237A.

106. Jacobsen, Nikolas C., and Olaf Hinrichsen. "Micromixing Efficiency of a Spinning Disk Reactor." Industrial & Engineering Chemistry Research 51, no. 36 (September 12, 2012): 11643–52. https://doi.org/10.1021/ie300411b.

107. Lodha, Himanshu, Roshan Jachuck, and Saravanan Suppiah Singaram. “Intensified Biodiesel Production Using a Rotating Tube Reactor.” Energy & Fuels 26, no. 11 (November 15, 2012): 7037–40. https://doi.org/10.1021/ef301235t.

108. Jachuck, R.J.J., and C. Ramshaw. “Process Intensification: Heat Transfer Characteristics of Tailored Rotating Surfaces.” Heat Recovery Systems and CHP 14, no. 5 (September 1, 1994): 475–91. https://doi.org/10.1016/0890-4332(94)90051-5.

109. Visscher, F., J. van der Schaaf, T.A. Nijhuis, and J.C. Schouten. “Rotating Reactors – A Review.” The 60th Anniversary of the European Federation of Chemical Engineering (EFCE) 91, no. 10 (October 1, 2013): 1923–40. https://doi.org/10.1016/j.cherd.2013.07.021.

110. Feng, Xudong, Darrell Alec Patterson, Murat Balaban, Guillaume Fauconnier, and Emma Anna Carolina Emanuelsson. “The Spinning Cloth Disc Reactor for Immobilized Enzymes: A New Process Intensification Technology for Enzymatic Reactions.” Chemical Engineering Journal 221 (April 1, 2013): 407–17. https://doi.org/10.1016/j.cej.2013.02.020.

111. Britton, Joshua, Keith A. Stubbs, Gregory A. Weiss, and Colin L. Raston. “Vortex Fluidic Chemical Transformations.” Chemistry – A European Journal 23, no. 54 (September 27, 2017): 13270–78. https://doi.org/10.1002/chem.201700888.

112. Cybulski, Olgierd, Miroslaw Dygas, Barbara Mikulak-Klucznik, Marta Siek, Tomasz Klucznik, Seong Yeol Choi, Robert J. Mitchell, Yaroslav I. Sobolev, and Bartosz A. Grzybowski. “Concentric Liquid Reactors for Chemical Synthesis and Separation.” Nature 586, no. 7827 (October 1, 2020): 57–63. https://doi.org/10.1038/s41586-020-2768-9.

113. Pattle, R. E. “Systems of Mutually Immiscible Liquid Layers.” Nature 165, no. 4188 (February 1, 1950): 203–4. https://doi.org/10.1038/165203a0.

114. Hildebrand, Joel H. “Seven Liquid Phases in Equilibrium.” The Journal of Physical and Colloid Chemistry 53, no. 6 (June 1, 1949): 944–47. https://doi.org/10.1021/j150471a021.

115. Itoh, H., M. P. Thien, T. A. Hatton, and D. I. Wang. “A Liquid Emulsion Membrane Process for the Separation of Amino Acids.” Biotechnology and Bioengineering 35, no. 9 (April 15, 1990): 853–60. https://doi.org/10.1002/bit.260350902.

116. Ahmad, A.L., A. Kusumastuti, C.J.C. Derek, and B.S. Ooi. “Emulsion Liquid Membrane for Heavy Metal Removal: An Overview on Emulsion Stabilization and Destabilization.” Special Section: Symposium on Post-Combustion Carbon Dioxide Capture 171, no. 3 (July 15, 2011): 870–82. https://doi.org/10.1016/j.cej.2011.05.102.

117. Kumar, Anil, Avinash Thakur, and Parmjit Singh Panesar. “A Review on Emulsion Liquid Membrane (ELM) for the Treatment of Various Industrial Effluent Streams.” Reviews in Environmental Science and Bio/Technology 18, no. 1 (March 1, 2019): 153–82. https://doi.org/10.1007/s11157-019-09492-2.

118. Schöller, C., J. B. Chaudhuri, and D. L. Pyle. “Emulsion Liquid Membrane Extraction of Lactic Acid from Aqueous Solutions and Fermentation Broth.” Biotechnology and Bioengineering 42, no. 1 (June 5, 1993): 50–58. https://doi.org/10.1002/bit.260420108.

119. Kumar, Anil, Avinash Thakur, and Parmjit Singh Panesar. “Lactic Acid and Its Separation and Purification Techniques: A Review.” Reviews in Environmental Science and Bio/Technology 18, no. 4 (December 1, 2019): 823–53. https://doi.org/10.1007/s11157-019-09517-w.

120. G. Dorsey. “Fiber Optic Rotary Joints-A Review.” IEEE Transactions on Components, Hybrids, and Manufacturing Technology 5, no. 1 (March 1982): 37–41. https://doi.org/10.1109/TCHMT.1982.1135951.

121. Shapar, Vladimir. “Principles of Compensation of Optical Rays’ Rotation and Multi-Channel Optical Rotary Connectors.” Applied Optics 57, no. 27 (September 20, 2018): 8023–33. https://doi.org/10.1364/AO.57.008023.

122. Höfflin, Jens, Saraí M. Torres Delgado, Fralett Suárez Sandoval, Jan G. Korvink, and Dario Mager. “Electrifying the Disk: A Modular Rotating Platform for Wireless Power and Data Transmission for Lab on a Disk Application.” Lab on a Chip 15, no. 12 (2015): 2584–87. https://doi.org/10.1039/C5LC00138B.

123. Martinez-Duarte, Rodrigo, Robert A. Gorkin III, Kameel Abi-Samra, and Marc J. Madou. “The Integration of 3D Carbon-Electrode Dielectrophoresis on a CD-like Centrifugal Microfluidic Platform.” Lab on a Chip 10, no. 8 (2010): 1030–43. https://doi.org/10.1039/B925456K.

124. Loo, J., H. C. Kwok, C. C. H. Leung, S. Y. Wu, I. L. G. Law, Y. K. Cheung, Y. Y. Cheung, et al. “Sample-to-Answer on Molecular Diagnosis of Bacterial Infection Using Integrated Lab--on--a--Disc.” Biosensors & Bioelectronics 93 (July 15, 2017): 212–19. https://doi.org/10.1016/j.bios.2016.09.001.

125. Torres Delgado, Saraí M., David J. Kinahan, Lourdes Albina Nirupa Julius, Adam Mallette, David Sáenz Ardila, Rohit Mishra, Celina M. Miyazaki, Jan G. Korvink, Jens Ducrée, and Dario Mager. “Wirelessly Powered and Remotely Controlled Valve-Array for Highly Multiplexed Analytical Assay Automation on a Centrifugal Microfluidic Platform.” Biosensors & Bioelectronics 109 (June 30, 2018): 214–23. https://doi.org/10.1016/j.bios.2018.03.012.

126. Torres Delgado, Saraí M., Jan G. Korvink, and Dario Mager. “The eLoaD Platform Endows Centrifugal Microfluidics with On-Disc Power and Communication.” Biosensors & Bioelectronics 117 (October 15, 2018): 464–73. https://doi.org/10.1016/j.bios.2018.05.056.

127. Delgado, Saraí M. Torres, David J. Kinahan, Fralett Suárez Sandoval, Lourdes Albina Nirupa Julius, Niamh A. Kilcawley, Jens Ducrée, and Dario Mager. “Fully Automated Chemiluminescence Detection Using an Electrified-Lab-on-a-Disc (eLoaD) Platform.” Lab on a Chip 16, no. 20 (2016): 4002–11. https://doi.org/10.1039/C6LC00973E.

128. Zhu, Danzhu, Bin Liu, and Gang Wei. “Two-Dimensional Material-Based Colorimetric Biosensors: A Review.” Biosensors 11, no. 8 (July 31, 2021). https://doi.org/10.3390/bios11080259.

129. Kaur, Baljeet, Navneet Kaur, and Subodh Kumar. “Colorimetric Metal Ion Sensors – A Comprehensive Review of the Years 2011–2016.” Coordination Chemistry Reviews 358 (March 1, 2018): 13–69. https://doi.org/10.1016/j.ccr.2017.12.002.

130. Wu, Di, Adam C. Sedgwick, Thorfinnur Gunnlaugsson, Engin U. Akkaya, Juyoung Yoon, and Tony D. James. “Fluorescent Chemosensors: The Past, Present and Future.” Chemical Society Reviews 46, no. 23 (2017): 7105–23. https://doi.org/10.1039/C7CS00240H.

131. Shamsipur, Mojtaba, Ali Barati, and Ziba Nematifar. “Fluorescent pH Nanosensors: Design Strategies and Applications.” Journal of Photochemistry and Photobiology C: Photochemistry Reviews 39 (June 1, 2019): 76–141. https://doi.org/10.1016/j.jphotochemrev.2019.03.001.

132. Wolfbeis, Otto S. “Luminescent Sensing and Imaging of Oxygen: Fierce Competition to the Clark Electrode.” BioEssays : News and Reviews in Molecular, Cellular and Developmental Biology 37, no. 8 (August 2015): 921–28. https://doi.org/10.1002/bies.201500002.

CHAPTER 2 : VORTEX FLUIDIC DEVICE (VFD)

Centrifugal and shear forces are produced when solids or liquids rotate. Rotary systems and devices that use these forces, such as dynamic thin-film flow technology, are evolving continuously, improving material structure-property relationships at the nanoscale, representing a rapidly thriving and expanding field of research high with green chemistry metrics consolidated at the inception of science. The VFD provides many advantages, with fluidic waves causing high shear and producing large surface areas for micro-mixing and rapid mass and heat transfer, enabling reactions beyond diffusion control in the processing. Combining these abilities allow for a green and innovative approach to altering materials for various research and industry applications by controlling small-scale flows and regulating molecular and macromolecular chemical reactivity, self-organisation phenomena, and synthesis of novel materials. This chapter highlights the aptitude of the VFD as a clean technology, with an increase in efficiency for a diversity of top-down, bottom-up, and novel material transformations benefiting from effective vortex-based processing for transforming material structure-property relationships.

This chapter was modified from the publication of “Clarence Chuah, Xuan Luo, Javad Tavakoli, Youhong Tang, Colin L. Raston, Thin-film flow technology in controlling the organization of materials and their properties, Aggregate, 2023, e433.”

Author contributions: CC performed the literature research, data summary, and analysis and wrote all the primary contents. JT and XL helped with some data collection and summary. YT and CR provided advice on the review directions to improve the quality of the manuscript. All the co-authors assisted with the revision of the manuscript before journal submission.

2.1 Abstract

Centrifugal and shear forces are produced when solids or liquids rotate. Rotary systems and devices that use these forces, such as dynamic thin-film flow technology, are evolving continuously, improve material structure-property relationships at the nanoscale, representing a rapidly thriving and expanding field of research high with green chemistry metrics, consolidated at the inception of science. The vortex fluidic device (VFD) provides many advantages over conventional batch processing, with fluidic waves causing high shear and producing large surface areas for micro-mixing as well as rapid mass and heat transfer, enabling reactions beyond diffusion control. Combining these abilities allows for a green and innovative approach to altering materials for various research and industry applications by controlling small-scale flows and regulating molecular and macromolecular chemical reactivity, self-organization phenomena, and the synthesis of novel materials. This review highlights the aptitude of the VFD as clean technology, with an increase in efficiency for a diversity of top-down, bottom-up, and novel material transformations which benefit from effective vortex-based processing to control material structure-property relationships.

2.2 Introduction

The field of nanotechnology has witnessed considerable progress in recent years, both in design and the scope of applications. As an interdisciplinary field, nanotechnology has undoubtedly led to industrial production of novel nanomaterials with designer properties such as being more robust, lighter, longer-lasting, anti-reflective, anti-microbial, electrically conductive, or becoming more luminous. In particular, nanoparticle (NP)-based medicine has gained traction, promising to revolutionize medical treatment with innovative therapeutics that are more potent and less toxic.[1]

Nanotechnology is revolutionary, and its hype is justified, especially for improving the quality of human life with novel consumer products through various materials and manufacturing methods. However, there are concerns on nanotechnology potentially creating delayed impacts on the environment and human health, especially where detrimental consequences are only noticed after commercialization has long begun. Thus, technologies being developed require cautionary measures to be upheld to avoid future predicaments for the environment and humanity, in tracking towards a sustainable future. This is to prevent history from repeating itself, such as petrol with lead, electronics with polychlorinated biphenyls, chlorofluorocarbons reducing upper atmosphere ozone dramatically, and the construction material asbestos, all of which led to environmental disasters.

Despite substantial research in the field and considerable progress, strategies for manufacturing nanoscale materials, through both top-down and bottom-up production processes, still face challenges. Top-down approaches for reducing materials to nanoscale dimensions often involve the use of harsh chemicals, leading to significant waste generation and raising environmental safety concerns[2]. Traditional assembly lines create products by building them up from the molecular level, the bottom-up strategy, which combines chemical synthesis and self-assembly. For current practical abilities, the main challenges are that the bottom-up strategy can be time-consuming, requiring extensive expertise and skill to control the size, morphology, and properties of the nanoscale products. Of paramount importance is the choice of synthetic method to finely control these features while circumventing uptake of impurities[2]. As such, the fundamental problem regarding the bottom-up strategy is developing the capability to exquisitely control the synthesis of the NPs while appropriately controlling size, morphology, and properties at nanoscale dimensions.

From a technological viewpoint, traditional methods abound in developing processes to control the growth and properties of materials. Such bottom-up material processing at the nanoscale dimension has been developed using channel-based microfluidic devices, albeit with some limitations. The main drawback is insufficient mixing resulting from laminar flows, often requiring sample dilution or reagent homogenization. The mixing process is usually restricted to diffusion control processing under such flows, denying the possibility of harnessing the advantages of turbulent mixing available in macro-scale systems[3]. While mixing enhancements can be achieved by incorporating multiple system parameters, including energy input, the velocity of flow, and the geometry of the mixers, these methods are time-consuming, leading to cost inefficiencies. In addition, channel-based microfluidic devices can suffer from clogging, specifically in the processing of macromolecules or at high reactant concentrations. Furthermore, incorporating external fields, such as electrical, magnetic, and laser fields, to control the processing is inherently complex for channel-based microfluidic platforms[4]. Although other mechanical energy forms, including sonication and grinding or milling, are effective in materials processing, they suffer from indiscriminate events in time and place, such as in cavitation and uneven energy transfer, resulting in non-uniform products under non-optimised processing conditions[5]. This can generate waste that, coupled with high energy usage, limits the sustainability metrics of such processing. A paradigm shift in microfluidics design is required to overcome such limits.

Thin film processing is an emerging technology where the liquid is subjected to centrifugal forces/shear stress or mechanical energy within dynamic thin films on a surface. These forces are useful in a range of thin film vortexing technologies, including for chemical synthesis and separations[6], material synthesis[7], material processing, lab-on-a-disc microfluidics[8] and enabling chiral selection[9]. Thin film processing offers several advantages, including accelerated reaction kinetics and improved control over chemical reactivity. The application of shear stress presents opportunities for enabling new types of chemical reactions and generating materials with new shapes, morphologies and sizes.[10] Thin film processing holds potential in situations where traditional batch processing is impractical or when conventional methods fail to provide access to unique forms of materials.[11]

Rotary devices that utilize centrifugal forces, pushing away from the rotation axis, are prime examples of how these forces can shape interfaces and effectively control material synthesis and chemical reactivity[10]. A diverse range of rotary devices have been reviewed and shown to achieve such performances, including lab-on-a-disc system[12], spiral seperators[13], spinning disc reactors[14], and vortex fluidic devices[15]. This review introduces the vortex fluidic device (VFD) as a paradigm shift in flow processing, with scalability factored in under the continuous-flow mode of operation of the device, along with its utility for tuning the size, morphology, and properties of materials at the nanoscale dimension. The VFD delivers high shear as a constant form of mechanical energy, with tunable control over the processing. The shear stress inside thin fluid films varies along the length of the tube reactor and has been calculated to range from 0.5246 to 0.5574 Pa when processed at 5 krpm in a 10 mm diameter tube reactor.[16] Processing in the device is not limited by diffusion control, providing a route to kinetically trapped novel forms of nanomaterials, and processing can also be facilitated by applied external fields for which the microfluidic platform is suited with the thin film of liquid approaching uniformity of treatment as such. Continuous-flow processing of the VFD is directly scalable, unlike batch processing which requires precise process engineering for upscaling, in overcoming uneven mixing and heat transfer. Whereas previous reviews of VFDs have focused on chemical transformations[17] and comparisons with other microfluidic devices[18], this review aims to deliver additional information about the significance of utilizing the VFD to control material structure-property relationships at the nanoscale with emphasis on its high green chemistry metrics.

2.3 Vortex Fluidic Technology

From manipulating single-cell organisms to processing advanced materials and small molecule synthesis, these processing capabilities and many more can be conducted through a VFD by accurately regulating the shear force experienced by the fluid, among various other parameters that affect the fluid dynamics. As shown in Figure 2.1, the VFD has noticeably unique features and capabilities relative to other processing platforms, in particular the ability to vary the tilt angle of the device. Typically a VFD has a glass or quartz tube with an external diameter of either 10 mm, 15 mm, or 20 mm, and can be spun at speeds from 1000 to 10000 rpm while inclined at an angle θ which can be varied from 90° to 0° with recent developments towards -45° processing[19]. The inclination angle and rotational speed control the management of shear rates along the tube reactor, with the fluid dynamics being inherently complex when $\theta >> 0°$[16,20]. The formation of a thin film from the liquid in the VFD witnesses high shear from the interaction between gravitational and centrifugal forces. These forces are accompanied by the appearance of Stewartson/Ekman layers as fluid flows upwards on the rotating tube's internal surface and downwards near the liquid's surface, parallel to the rotational axis of the rotating tube.

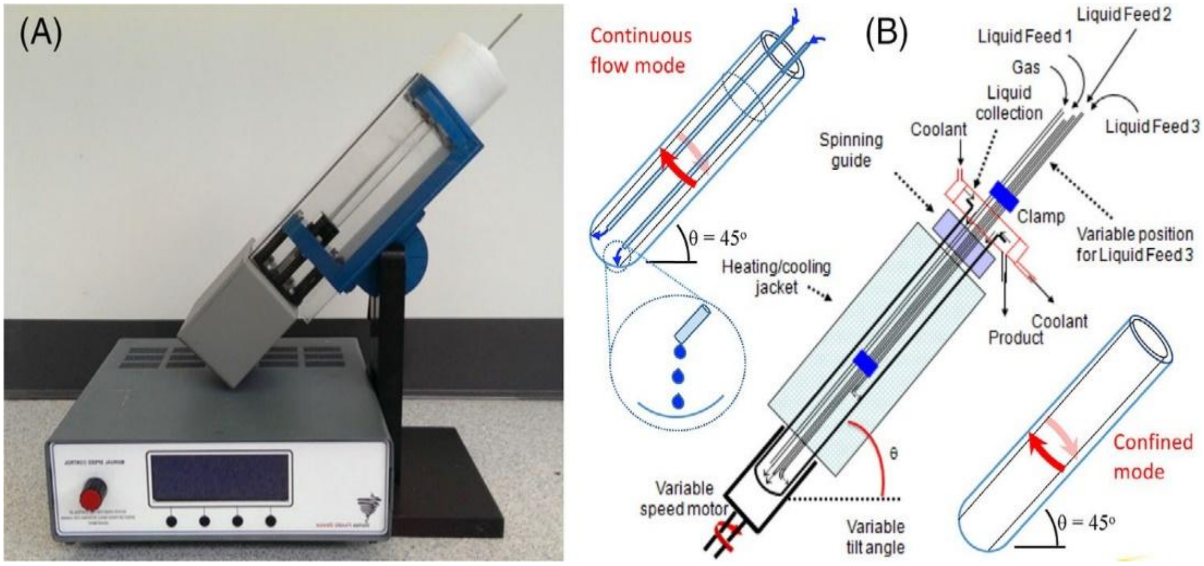

Figure 2.1 Vortex fluidic device (VFD).

(a) Front view of a VFD & (b) schematic diagram of the original VFD[21] with recent versions having the spinning guide replaced by a bearing with the other another bearing close to the base of the tube. (b) Reproduced under the terms of the CC BY 3.0 Unported license[21]. Copyright 2013, Springer Nature.

The VFD operates in two distinct modes: confined mode and continuous flow mode, each differing in sample handling. In confined mode, a fixed and finite volume of liquid is introduced into a sealed glass tube that is closed at one end and rapidly rotated, generating centrifugal forces that influence the liquid's behaviour. Since the system is closed, the liquid remains within the tube throughout the process, making this mode suitable for experiments requiring precise control over reaction conditions. In contrast, continuous flow mode allows for constant liquid exchange, with liquid continuously fed into the system, either at the base of the tube or at designated positions along the interior. Simultaneously, excess liquid exits from the top of the rotating tube. This mode is advantageous for prolonged operations, as it prevents sample depletion and enables the removal of reaction byproducts or unwanted components.

Although the capability for processing in continuous flow was the original purpose of the designed technology, processes in the confined mode can also be used for small quantities of liquid, with processing scalability being dependent on the amount of material required. As such, industrial applications with high volumes would require a single large unit[22] or multiple units in a parallel array for processing. In contrast, small volume niche applications, down to ~ 0.5 mL for a 10 mm diameter tube, for example in medicine, require only a single VFD unit. The VFD itself is relatively inexpensive, ~ $5,000US, and is a versatile microfluidic platform for controlling chemical reactivity and selectivity, material synthesis, and probing the structure of self-organized systems, offering a range of benefits over conventional processing[17,19]. Micro-mixing and high shear stress are imparted in the dynamic thin film on the surface of the rotating rapidly tube in the VFD, typically between 3,000 and 9,000 rpm. The VFD has been employed successfully for a remarkable diverse range of applications, such as in fabricating nanocarbons[23, 24], exfoliating of graphite and boron nitride[25], accelerating enzymatic reactions[26,27], manipulation of polymer networks[28], protein purification[16], and indeed protein folding[29].

The VFD is particularly useful for regulating the shape and size of NPs for both bottom-up and top-down processing. The rapidly evolving capabilities and innovative processing toolbox for the device allows mapping out synthetic strategies for seemingly endless research and industrial possibilities in the nanomaterials arena alone. Intense micro-mixing when liquids are added to the rotating tube in the VFD, and high shear stress associated with high mass topological fluid flows (see below) in the resulting thin film of liquid in the VFD, can be harnessed in a controlled way to discover and improve chemical reactivity beyond what is possible using batch processing where processing is limited by diffusion control. The VFD is proficient in probing the structure of self-organized systems, materials processing, instigating chemical reactions, and rapidly imparting organic modifications to a range of motifs in a controlled fashion. Despite the VFD being unlike typical microfluidics where channels are used with typically laminar fluid flow, it is acquiring distinction as a multipurpose microfluidic platform with novel operating characteristics. Modern-day chemistry focuses on the metrics of incorporating green chemistry into the science at its inception and in this context processing the VFD can be significantly improved for research and industrial applications.

Recent fundamental studies on fluid flow in the VFD have established an understanding that the fluid exhibits resonant behaviours from the constricting boundaries of the glass surface and the meniscus, which define the liquid film thickness. To overcome the inability to directly measure the unique fluid flow in the rotating reference frame in the VFD, materials processing strategies were employed which allowed identifying specific topological mass transport regimes[30], namely the spinning top flow normal to the surface of the tube, double-helical flow across the thin film, and spicular or spherical flow, and an area of transition whereby both effects are present. The presence of these topological fluid flows which have specific size and shape was further supported by determining mixing times, temperature profiles, and film thickness for increasing rotational speed. These flow patterns also possess distinctive signatures that make it possible to predict the morphology of nanomaterials processed in the VFD, for instance, in shear-stress induced recrystallization, crystallization, and polymerization, depending on the rotational speeds, thereby providing moulds of high-shear topologies, as ‘positive’ and ‘negative’ spicular flow behaviours, which are further detailed below. This is shown in Figure 2.2 along with “molecularly-drilling” of holes in thin films of preformed polysulfone which correspond to the spatial arrangement of double helical topological fluid flows. We note that optimal processing in the VFD for a myriad of applications is at θ 45° tilt angle and the aforementioned results for this angle uniquely provide the distinct behavioural topological fluid flow regimes, Figure 2.3. This model introduces a novel idea for creating unique nanomaterials and the organization of matter, now with the ability to have a high level of predictability for the optimal processing in tackling new applications of the VFD.

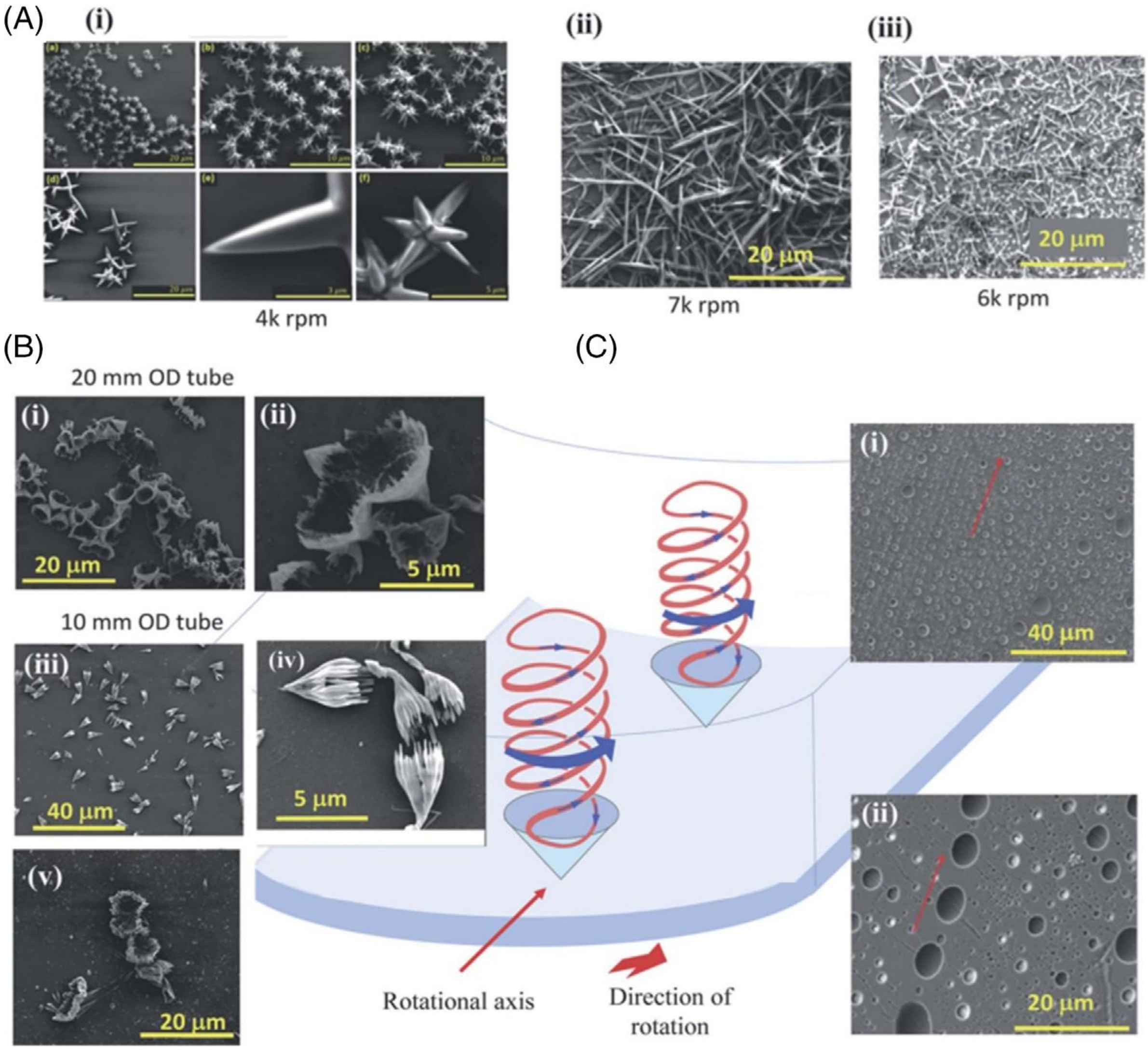

Figure 2.2 Polymer and nanocarbon materials melded in the VFD.

(a) Crystallization and self-assembly of C_{60} under shear stress in toluene at a concentration below saturation level, resulting in (i) spicules, (ii) rods, and (iii) mixes of spicules and rods formed at 4000, 7000 and 6000 rpm, corresponding to specular flow, transitions from specular to double-helical flow and helical flow, respectively. (b) Creating (i) regular and (ii) irregular cones of self-assembled C_{60} in a 20 mm OD tube, with (iii) and (iv) being sharper pitch cones with extended arms in a 10 mm OD tube, formed by micro-mixing a 1:1 solution of C_{60} in *o*-xylene and DMF, θ 45°, 20 mm OD tube, with (v) Cones fastened to the wall of the glass tube, 10 mm OD tube. (c) (i and ii) Patterns of the holes arising from double-helical flow, formed at the interface of the glass tube and a thin polysulfone film (~ 5 µm) formed in toluene at 20°C, θ 45°, 7000 rpm rotational speed, along the length of the tube, with the arrow designating the direction of the rotational axis of the tube[30]. (a-c) Reproduced under the terms of CC BY 3.0 license[30]. Copyright 2021, Royal Society of Chemistry.

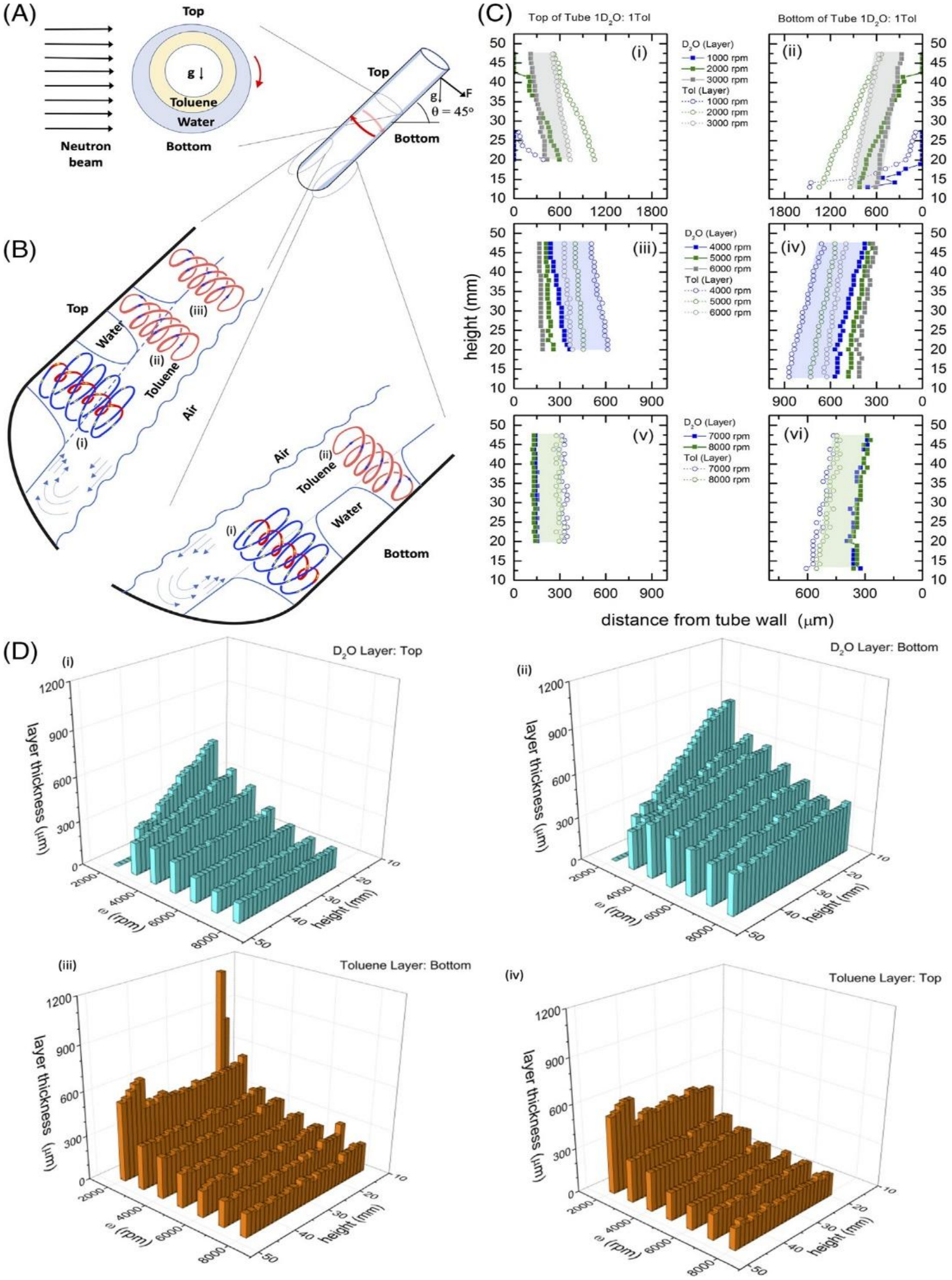

Figure 2.3 VFD biphasic processing.

(a) Cartoon of the relative film thickness on the upper and lower side of the rotating hemispherical based quartz tube (20 mm OD, 17.5 mm ID) when processing a mixture of water and toluene; two types of fluid flows presented in the thin film were spinning top and double helical topological fluid flows. (b) Film thickness derived from neutron imaging. (c) Layer thickness as a function of height up the tube and rotational speed. (a-c) Reproduced under the terms of Creative Commons Attribution 3.0 Unported License[15]. Copyright 2022, Royal Society of Chemistry.

We recently established that the VFD can centrifugally separate immiscible liquids of different densities in a θ 45° inclined rotating tube without using phase transfer catalysts, microgels, surfactants, complex polymers, nanoparticles, or micromixers. Depending on the properties of the two liquids, the micro to submicron size topological flow regimes in the thin films discussed previously caused substantial inter-phase mass transfer. A Coriolis force is produced from the hemispherical base of the tube which is the spinning top topological fluid flow. This is present in the less dense liquid but penetrates the denser layer of liquid, transporting liquid from the upper layer through the lower layer to the surface of the tube. In a similar way, double helical topological flow in the less dense fluid caused by Faraday wave eddy currents being twisted by Coriolis forces, also impact of the surface of the tube. Through the self-assembly of nanoparticles at the interface of the two liquids, the lateral dimensions of these topological flows have been identified, Figure 2.4a. When a threshold rotational speed is achieved, 7500 rpm in a 20 mm OD tube, double helical flow also occurs in the denser layer at high rotational speeds, which results in preformed emulsions of two immiscible liquids rapidly phase separating. By altering the shape of the base of the tube while maintaining rapid mass transfer between phases, it is possible to perturb the spinning top flow relative to double helical flow while avoiding the necessity for phase transfer catalysts, Figures 2.3 and 2.4b. The results discussed here have implications for overcoming mass transfer limitations at liquid interfaces and presenting innovative technologies for extraction and separation research, all while preventing the creation of emulsions.

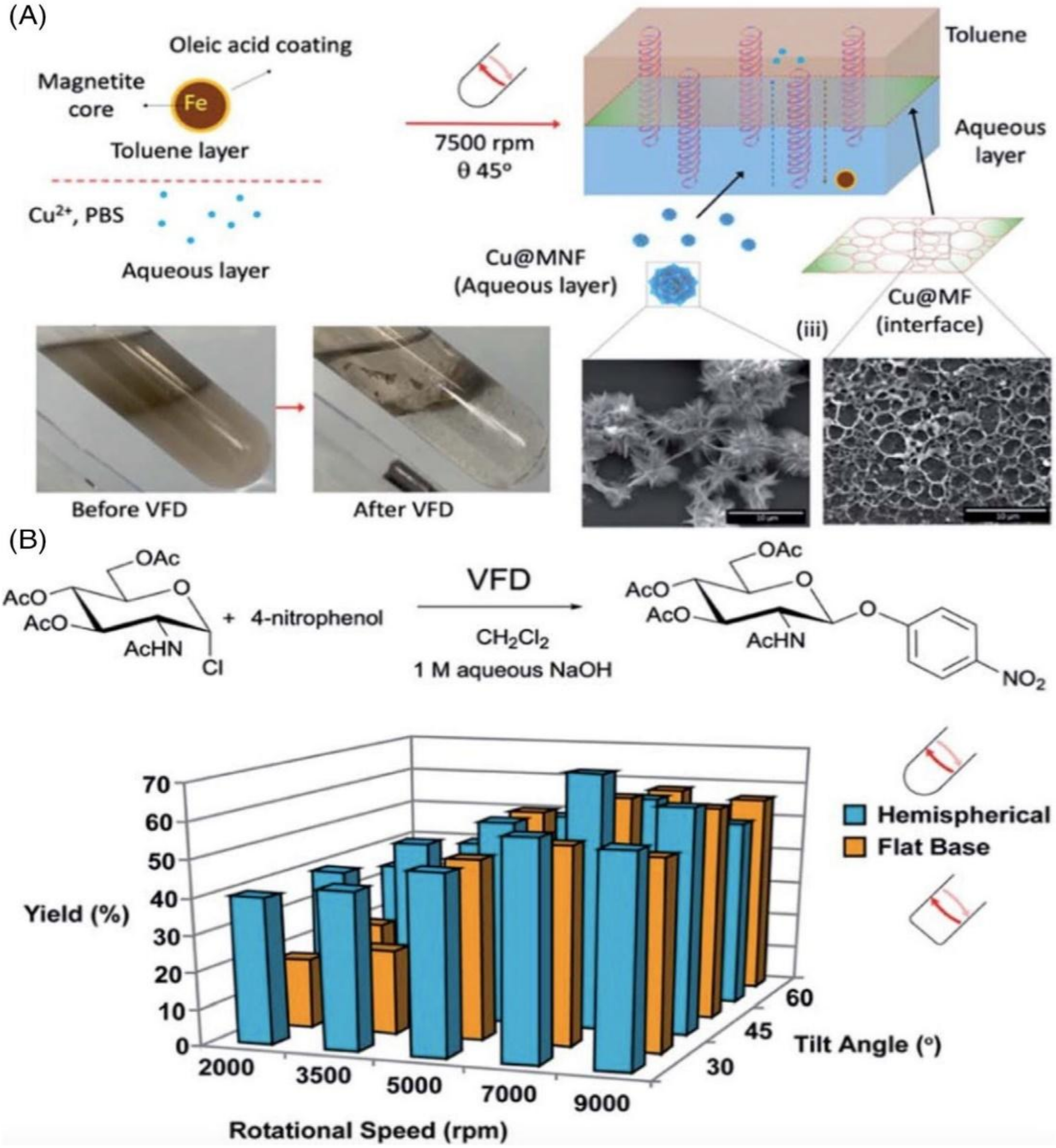

Figure 2.4 VFD biphasic fabrication.

(a) Fabrication of $Cu_3(PO_4)_2$@magnetite thin film (Cu@MF) and $Cu_3(PO_4)_2$@magnetite nanoflower (Cu@MNF) in a biphasic system of toluene and phosphate buffer saline (PBS) in a hemispherical base quartz tube, 20 mm OD, 17.5 mm ID. (i) Schematic for the creation of Cu@M composites in a VFD. Oleic acid-coated magnetite nanoparticles were disseminated in the toluene phase with all experiments using a 1:1 mixture of toluene and PBS, with $CuSO_4$ then added quickly, followed by VFD processing at 7500 rpm. (ii) SEM of Cu@MF formed at the toluene/PBS interface, while Cu@MFN present in the PBS phase. (b) The reaction of 2-acetamido-3,4,6-tri-O-acetyl-α-d-glucopyranosyl chloride with 4-nitrophenol in the absence of a phase transfer catalyst in an aqueous sodium hydroxide solution and dichloromethane, with the yield of the product plotted as a function of tilt angle and rotational speed of a quartz tube, for either a flat or hemispherical base[15]. (a-b) Reproduced under the terms of CC BY 3.0 license[15]. Copyright 2022, Royal Society of Chemistry.

2.4 Top-Down Nanomaterial Transformation

The pre-eminence of utilizing a VFD for top-down nanomaterial fabrication is evident by the shear stress within dynamic the thin film in the device being effective for controlled exfoliating of 2D laminar materials, in gaining access to material for use in a wide range of applications. For instance, hexagonal boron nitride (h-BN) and single-layered graphene sheets can be effectively exfoliated from bulk material by using VFD processing[25]. For specific applications it is essential to develop a simple and scalable approach to generate 2D material without uncontrollable chemical degradation or imparting defects, and for this the VFD can be effective. Graphene synthesis from graphite oxide or graphite, for example, using solution-based methods, such as high energy wet ball milling[31] or high power sonication[32,33], can deleteriously affect the properties of the resulting graphene. To this end, Chen *et al*. developed the VFD as device for imparting tunable mechanical energy simply by varying the rotational speed, ω, of the tube (3000 – 9000 rpm), to control the exfoliation of oxide-free graphene and also h-BN sheets from graphite and bulk h-BN respectively, in N-methyl-pyrrolidone, Figure 2.5. This work is the first report on using the VFD to essentially disassemble material, and indeed for the VFD in general, and is effectively a paradigm shift for the top-down fabrication of nanomaterials[25]. Continuous flow fabrication of green graphene oxide or gGO (20 mg/mL) was recently developed using only aqueous H_2O_2, achieving a yield of 40-50% at 8000 rpm with a flow rate of 0.5 mL/min[34]. The resulting gGO exhibits distinctive characteristics with controllable defects/oxidation of ~35% towards the edges rather than the basal plane of the sheets. These properties give rise to remarkable electrical and optical attributes, including purple to deep blue emission of narrow full width at half maximum (<35 nm).

The high shear stress (mechanical energy) in the VFD is also effective in exfoliating graphene from graphite as spheres confining self-assembled fullerene C_{60}[35]. The spheres form in essentially quantitative yield in the VFD through micro-mixing a *o*-xylene solution of C_{60} and a dispersion of graphite in DMF at room temperature, without the need for auxiliary substances and surfactants[35]. Interestingly their formation involves both top-down (graphene exfoliation) and bottom up (C_{60} self-assembly and simultaneous confinement) processes. The spheres are uniform in shape and have a size distribution of 1.5 to 3.5 µm with the ability to control their diameters by varying the VFD operating parameters, Figures 2.5e – j. As an electrode, the composite material has high cycle capacitance stability, with capacitance maintained at a high scan rate of 100 mV s^{-1} at 86.4 mF cm^{-2} (83.5%) and 24.7 F g^{-1}, and high areal capacitance of 103.4 mF cm^{-2}. These findings augur well in developing a range of all carbon material for energy storage applications. Moreover, the ability to prepare such material provides tantalizing possibilities for making composites of fullerene aggregates shrouded by other 2D materials, with different properties in general. In this context, a composite of graphene oxide shrouding self-assembled fullerene C_{70} has recently been reported[36].

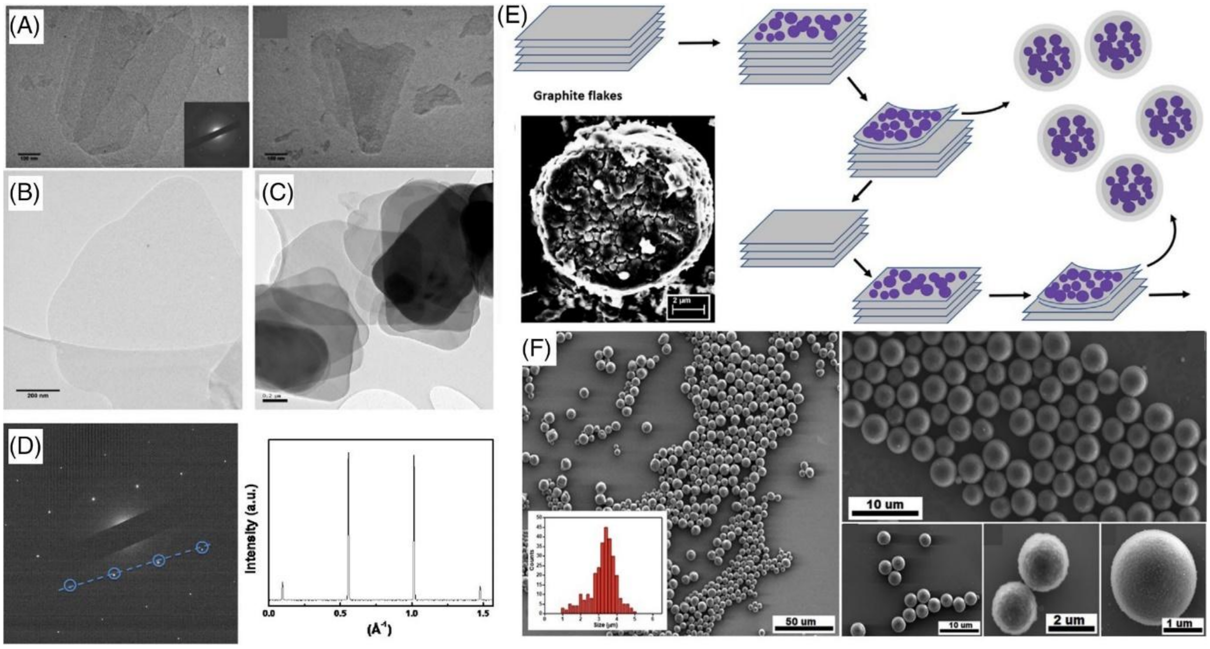

Figure 2.5 VFD top-down transformation.

TEM of (a) exfoliated graphene sheets with the inset SAED pattern, (b) a single sheet of h-BN, (c) adjacent h-BN layers, post processing, (d) BN sheets SAED pattern for (b) and intensity scan for the dashed line[25]. (e) The proposed mechanism for forming graphene spheres confining fullerene C_{60} within the VFD, (f-j) SEM images of composite spheres, with an inset size distribution35. (a-d) Reproduced under the terms of CC BY 3.0 license[25]. Copyright 2012, Royal Society of Chemistry. (e-j) Reproduced with permission[35]. Copyright 2019, American Chemical Society.

The precise slicing of carbon nanotubes to obtain a narrow length distribution with minimized defects except at the tube ends, holds tremendous potential for various applications, such as in solar cell technologies, sensors[37,38], electronic devices, and biomedical sciences.[39] Several methods have been reported for producing short carbon nanotubes using different physical,[40] electrical or chemical strategies[41]. The dynamic thin film of liquid in a VFD can laterally slice micron length BN and carbon nanotubes (BNNTs and CNTs respectively) with[19,23,39] and without the use of lasers[42], independent of the number of concentric rings making up the tubes. Notably, the process reduces the level of defects for sliced CNTs and occurs without the need for chemical stabilizers and surfactants, with scalability of the process using the continuous mode of operation of the VFD. In contrast, controlled lengths of shorter nanotubes were found to be more substantial in the confined mode for single-walled carbon nanotubes (SWCNTs), with potential for drug delivery applications due to the suitable length scale with narrow size distributions, Figures 2.6a-c[23]. Indeed, the availability of short single, double, or multi-walled carbon nanotubes (MWCNTs) down to 80 nm using VFD processing, where the side wall defects are minimal, as evident from Raman spectroscopy, further highlights the unique capabilities of the VFD and the prospect of uptake of the material in applications when specificity of the length scale is imperative.

As well as slicing CNTs, the VFD is also effective in fabricating coiled SWCNT nano-rings in high yield (80%) under continuous flow, with the processing devoid of surfactants, and without toxic chemicals[43]. The coiled nano-rings were fabricated with wall thicknesses from 3 to 70 nm, with 300 nm being the average diameter, Figures 2.6d-j. Importantly the rings are formed with more uniformity and without variation relative to the use of batch-to-batch processing. Magnetic force microscopy established that the thickness of the VFD fabricated SWCNT nano-rings affects their magnetic properties with the magnetic interactions stronger for the thicker nano-rings due to them being more efficiently packed, thus allowing electrons to tunnel more efficiently. Compared to straight SWCNTs, the curvature of coiled SWCNT nanoring influences their properties, endowing the coiled structures with potential in a range of applications, for example, electronic circuits and polymer composites as sensing devices, noting the scalability of their VFD mediated fabrication. In recent developments, there has been significant progress in understanding the high-shear topological fluid flow within submicron dimensions in the VFD, Figure 2.6o[30,15]. This understanding has enabled the control of the ring size of coiled single-walled carbon nanotube (SWCNT) toroids based on the solvent systems (water with toluene, *m*-xylene or *p*-xylene), diameter of the VFD tube (10, 15 and 20 mm outside diameter) and the shape characteristics of its reactor base (hemispherical or flat-base), all achieved under confined mode VFD processing[44]. By carefully manipulating these parameters, selective control over the diameter of the resulting toroids of SWCNTs down to about 35 nm in diameter has been established.

Aside from SWCNT transformations, the VFD thin film microfluidic platform can also decorate MWCNTs with superparamagnetic magnetite (Fe_3O_4) NPs[45]. This process was a three-step-in-one operation: (i) Bulk iron metal was ablated using a pulsed laser at 1064 nm to generate iron oxide superparamagnetic NPs *in situ*, (ii) MWCNTs were sliced, and finally, (iii) the surface of the MWCNTs was decorated with the NPs, as shown in Figures 2.6k-n. Generating this composite material directly from stock MWCNTs with minimal processing time and without the use of harsh chemicals further demonstrates the versatility of the VFD. The composite material was utilized for supercapacitor measurements as an electrode. At a scan rate of 10 mV s^{-1}, high areal capacitances and gravimetric of 1317.7 mF cm^{-2} and 834 F g^{-1}, respectively, was established, being superior to those reported using similar materials prepared using other methods[45]. Moreover, at the specific power of 2085 W kg^{-1}, the VFD fabricated material also had a substantially higher specific energy of 115.8 W h kg^{-1}, thus demonstrating potential as a material for next-generation energy storage devices.

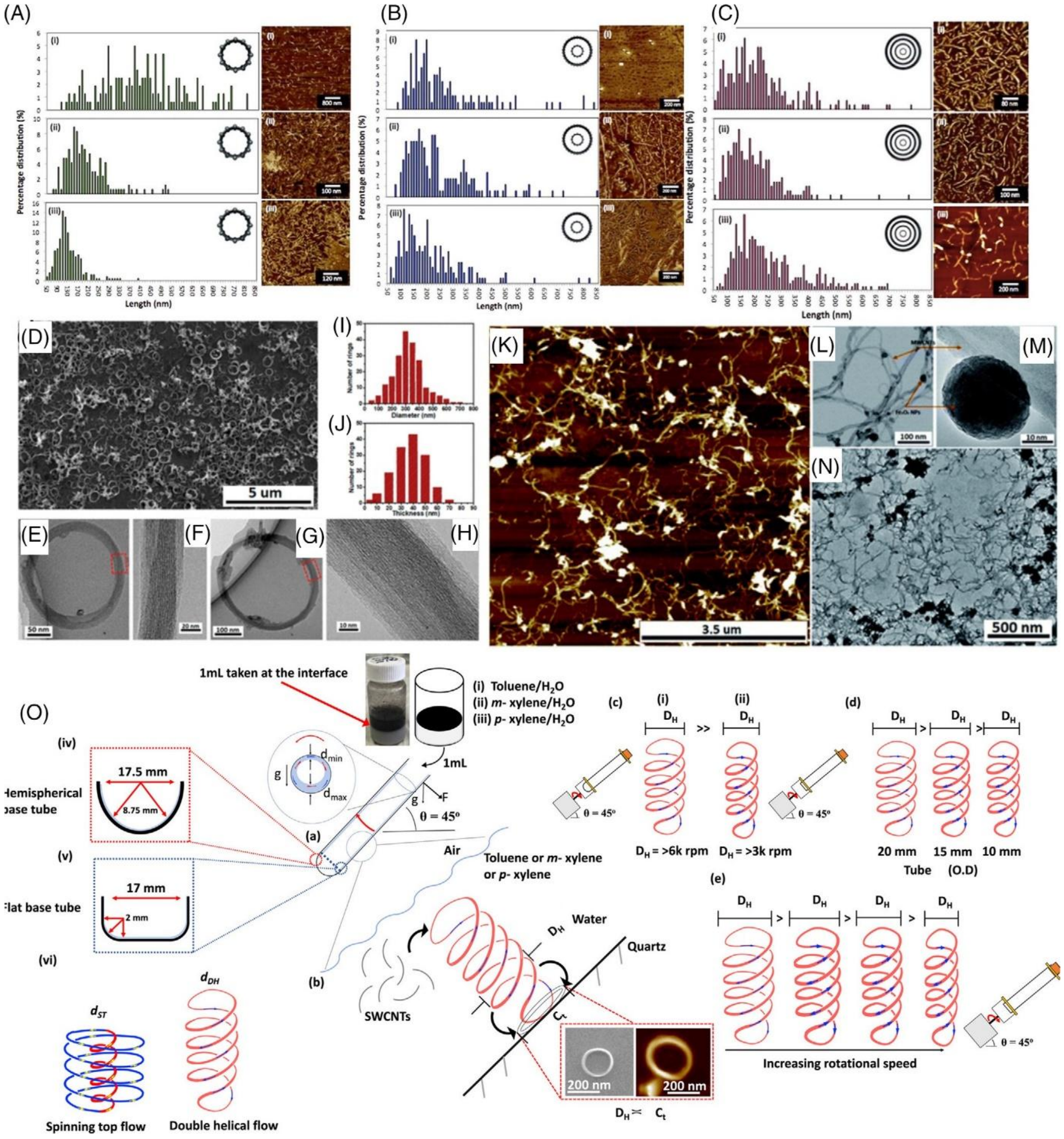

Figure 2.6 VFD CNT transformation.

Length distribution plots of laterally sliced (a) SWCNTs, (b) double walled CNTs, and (c) MWCNTs at = 45° with 7500 rpm rotational speed at reaction times of (i) 10 mins, (ii) 30 mins, and (iii) 60 mis, alongside their respective AFM height images[23]. Coiled SWCNT toroids (d) SEM image, (e) and (g) TEM images, (f) and (h) HRTEM for e and g, respectively, with (i) & (j) histograms for distribution of diameter and thickness, respectively[43]. (k) AFM, (l) STEM, (m) HRTEM, and (n) TEM image of composite materials with length distribution inset[45]. (o) Schematic for the processing of toroid from SWCNTs. The diameter of the double helix is compared between different tube types, including hemispherical and flat based tubes, and the effect of tube diameter and increasing rotational speed on the size of toroids and double helices. (a-c) Reproduced under the terms of the CC BY 3.0 Unported license[23]. Copyright 2016, Springer Nature. (d-j) Reprinted with permission[43]. Copyright 2019, American Chemical Society. (k-n) Reproduced under the terms of the CC BY 3.0 license[45]. Copyright 2019, Royal Society of Chemistry. (o) Reprint with permission[44]. Copyright 2022, American Chemical Society.

Luo *et al.* reported a tunable and effective procedure for preparing fluorescent polyethyleneimine-based NPs with controlled average particle sizes, as shown in Figure 2.7a-c, using the VFD operating under continuous mode[28]. Due to the high shear mechanical energy alongside the elevated temperature of the air (~160˚C) within the VFD, chain scission and polymer degradation cause the fragmented chains to reorganize into self-passivated NPs. Varying the flow rate of the liquid entering the VFD allows tuning the fluorescent properties of these NPs, all formed in the absence of any auxiliary reagents. The most favourable outcomes were achieved at flow rates of 0.1 mL.min^{-1} (lex = 325 nm, lem = 400 nm) and 0.2 mL.min^{-1} (lex = 447 nm, lem = 500 nm). 2D fluorescence maps revealed a more concentrated signal region, indicating a relatively higher level of sample homogeneity and a 1.7-fold increase in fluorescence intensity compared to samples prepared using the confined mode of operation of the VFD. Notably, processing conditions at 0.1 mL.min^{-1} resulted in more significant degradation of the polymer structure and a greater incorporation of -OH functionality than conditions at 0.2 mL.min^{-1}, primarily due to the extended residence time associated with the lower flow rate of 0.1 mL.min^{-1}. Enhancement of the auto-fluorescence and fluorescence intensity over an extensive range of excitation wavelength was possible by incorporating amide groups. Notably, cytotoxicity was significantly reduced in the resulting NPs after processing in the VFD compared to as-received materials, thus allowing the possibility of medical applications.

2.5 Bottom-Up Nanomaterial Transformation

Further advantages of the VFD include its ability to create self-assembly structures such as micelles[46], mesoporous nanomaterials[47,48], hydrogels[49], fullerene and its composites[50,35,30] and vesicles[51] and the potential to control the shape and size of NPs during formation and for regulating the thickness and strength of coating at the nanoscale.

The VFD has also been utilized as an innovative strategy for preparing mesoporous silica prior to the required calcining to remove the polymer template[46]. Tong *et al*. reported that the processing time of the VFD was less than an hour, with 5 hours being the overall duration for the synthesis involving 60 mL of solution, contrasting to the 48 hours required for the traditional materials involving hydrothermal batch processing[47]. Moreover, the VFD process operated at ambient pressure and temperature, significantly reducing energy consumption, and remarkably the pore size can now be controlled to fine-tune the properties of mesoporous silica. This is under continuous flow VFD processing such that there is potential for scaling up the synthesis of the pre-calcined material with uniformity of the product along with controlled pore wall thickness (at ~5 nm) and pore size (from 2.8 to 3.8 nm). The latter relates to the micelles being stretched by the shear forces in the thin film within the VFD. Consequentially, the increase in pore wall thickness increased the thermal stability of the calcines material, which is essential for high-temperature applications.

Tong *et al*. also developed an effective method for the nucleation and growth of palladium NPs *in situ* in the above micelle templated mesoporous silica synthesis, also as a continuous flow VFD process, then for calcining under batch processing, Figure 2.7e-g[48]. A mixture of Pluronic® P-123 and palladium(II) acetylacetonate mixture was continuously fed into the tube reactor spinning at 5000 rpm and then aqueous sodium fluoride was added. The solution mixture was then fed back into the VFD through one jet feed, and tetramethoxysilane (TMOS) simultaneously fed into the VFD through another jet feed, under a N_2/N_2 atmosphere, with the H_2 for reducing Pd(II), Figure 2.7g. The resulting Pd/SBA-15 composite calcined material is effective in a wastewater treatment process for removing nitrate-nitrogen, Figure 2.7m, with the maximum adsorption value for nitrate-nitrogen at 9.5 mgL^{-1} after 16 hours, upwards of 41% removal efficiency, with 36% removal efficiency upon recycling. Because Pd/SBA-15 is easily separated from the effluent, the relatively low nitrate-nitrogen adsorption is significant. Of particular note is that the Pd NPs in the composite material are entirely embedded within the pores rather than on the surface of the mesoporous silica particles, which is important in avoiding leaching of the NPs and for taking advantage of any catalytic process being enhanced within the confined space within the pores.

Silica hydrogel is readily formed in the VFD in water under continuous flow as a benign process, without the need for organic solvents or any other acids or bases, with significantly reduced processing times relative to batch processing[49]. Briefly, TMOS was fed into the VFD tube through one jet feed and MilliQ water was fed through another, with the flow rate in the range between 0.8 and 1.2 mL/min. This process is also effective in incorporating curcumin nanoparticles, with the silica hydrogel converting to an xerogel 3.5 hours post VFD processing. The use of VFD under scalable continuous flow conditions results in much faster kinetics, beyond the limits of diffusion control. The functional composite material showed improved inhibition of bacterial growth compared to bulk curcumin, Figure 2.7h-l. Here the xerogel silica network provides shielding for the curcumin particles for then slow leaching of the curcumin which becomes bioavailable. The xerogel silica has potential for drug delivery applications, noting that the overall process of incorporating drugs *in situ* is simple, without the need for auxiliary substances. In addition to *in situ* synthesis, Vortex fluidic-mediated shearing can also effectively manipulate the entanglement of three-dimensional self-assembled supramolecular gel networks[52]. This was achieved through the disruption of fluorous bis-urea derived gels and studied the local structure and aggregation with small angle neutron scattering (SANS).

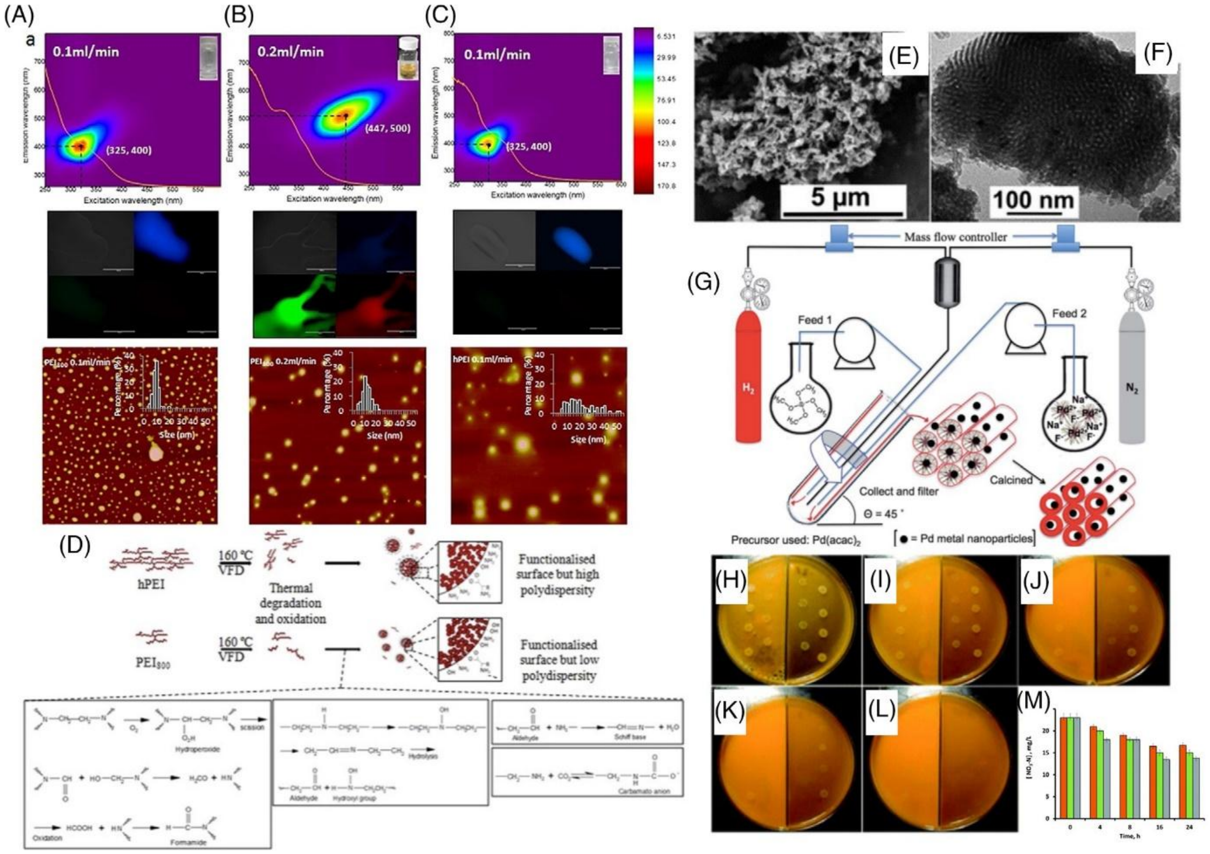

Figure 2.7 VFD bottom-up transformation.

VFD (20 mm O.D.) processed 2D fluorescence maps of PEIs formed at different flow rates at 160 alongside their corresponding sample images from AFM and inverted fluorescence microscopy for (a) PEI_{800} (8600 rpm, 0.1 $mL.min^{-1}$), (b) PEI_{800} (8600 rpm, 0.2 $mL.min^{-1}$), and (c) hPEI (8000 rpm, 0.1 $mL.min^{-1}$). (d) the proposed mechanism of the VFD-polymer reaction. Pd/SBA-15's (e) SEM and (f) TEM image, with (n) nitrate-nitrogen content for three different loading concentrations of 10, 25, and 50 mg adsorbent for brown, green, and grey, respectively[48]. (g) Schematic for the synthesis of Pd/SBA-15 using the VFD. Mueller Hinton agar plates for inhibition testing of bacterial growth with the addition of curcumin and curcumin/SiO_2 composite powder for right and left, respectively, for concentrations of (h) 209/60 $\mu g.mL^{-1}$, (i) 419/120 $\mu g.mL^{-1}$, (j) 628/180 $\mu g.mL^{-1}$, (k) 838/240 $\mu g.mL^{-1}$, and (l) 1047/300 $\mu g.mL^{-1}$. (a-d) Reproduced with permission[28]. Copyright 2015, John Wiley & Sons (e-g, m) Reproduced under the terms of the CC BY 3.0 license[48]. Copyright 2015, Royal Society of Chemistry. (h-l) Reproduced with permission[49]. Copyright 2015, Royal Society of Chemistry.

2.6 Innovative VFD Transformations

With its unique operating characteristics, vortex fluidic technology warrants consideration for preparing/transforming nanomaterials, as a paradigm shift for preparing material with novel properties, for niche innovative research and industrial applications. For instance, it has been shown that enzymatic reactions could be accelerated using a VFD, with/span> pressure waves effective in accelerating enzymatic reactions[26]. Despite chemical transformations being catalysed with outstanding regio- and stereo-specificities, extended reaction times limit numerous enzymes. However, Britton *et al.* found that the above pressure waves generated at specific rotational speeds allow an enzyme to respond, providing an acceleration landscape, Figure 2.8. Enzymatic efficiency (k_{cat}/K_m) and rate constants (k_{cat}) have been increased, with an average 15-fold enhancement for deoxyribose-5-phosphate aldolase, an a seven-fold average acceleration displayed by four other enzymes. The VFD increase the mass transfer such that the chattering events for the enzyme are more likely to be successful, with negative pressure collapsing the transition, i.e., mechanically changing the secondary structure of the enzyme. More recently, the fabrication of hybrid laccase-$Cu_3(PO_4)_2$ nanoflowers via an intermediate toroidal structure is dramatically accelerated in the VFD. This innovative approach leads to the formation of the composite material with enhanced catalytic activity (1.8-fold) compared to free laccase under diffusion control.[27] Following the fabrication process, the hybrid nanoflowers are subsequently integrated as a coating on the side wall of the reactor surface. The resulting coating exhibits exceptional stability and reusability. This remarkable durability enables a significant 16-fold enhancement in catalytic rates compared to the control conditions.

The VFD has also been utilized to procure a rapid protein refolding technique, with yields for proteins being increased for simple cell lines (Figure 2.8i), not to mention lowering costs, reducing streams of waste, and significantly reducing the time associated with protein expression for an extensive range of research and industrial applications, as reported by Yuan *et al.*[16] HEWL isolated from inclusion bodies without VFD processing exhibits a complete absence of lysozyme activity. In comparison, the application of VFD treatment to recombinant lysozyme results in the recovery of more than 82% of its activity, irrespective of whether it is conducted in confined or continuous flow modes. Particularly noteworthy is the potential scalability and parallelization of the continuous flow approach, making it an attractive choice for industrial applications demanding the treatment of exceptionally large volumes.

The shear stresses from fluid films micrometre wide have been observed in refolding lysozyme in hen egg-whites, Figure 2.8. Recombinant lysozyme in hen egg-whites and caveolin-1, and a protein much larger in size, cAMP-dependent protein kinase A, all of which require only minutes for processing, thereby being much faster than overnight dialysis by conventional means. In recent advancements, the ability to manipulate the unfolding and refolding of β-lactoglobulin has been established using the technology, aided by the monitoring of aggregation-induced emission luminogen (AIEgen), Tetraphenylethene maleimide (TPE-MI) which reacts with exposed cysteine thiol when the protein unfolds, as established with an increase in fluorescence intensity[53]. The AIEgen have been intensively explored in the biomedical field[54] and in this case they serve as a monitoring tool, enabling real-time observation of the folding behaviour of the protein during the processes. Furthermore, solutions with larger volumes (up to L) can be accommodated, with the VFD scaling up through multiple units for parallel processing or the continuous mode, consequently dramatically lowering financial costs and time for refolding inactive proteins on an industrial scale.

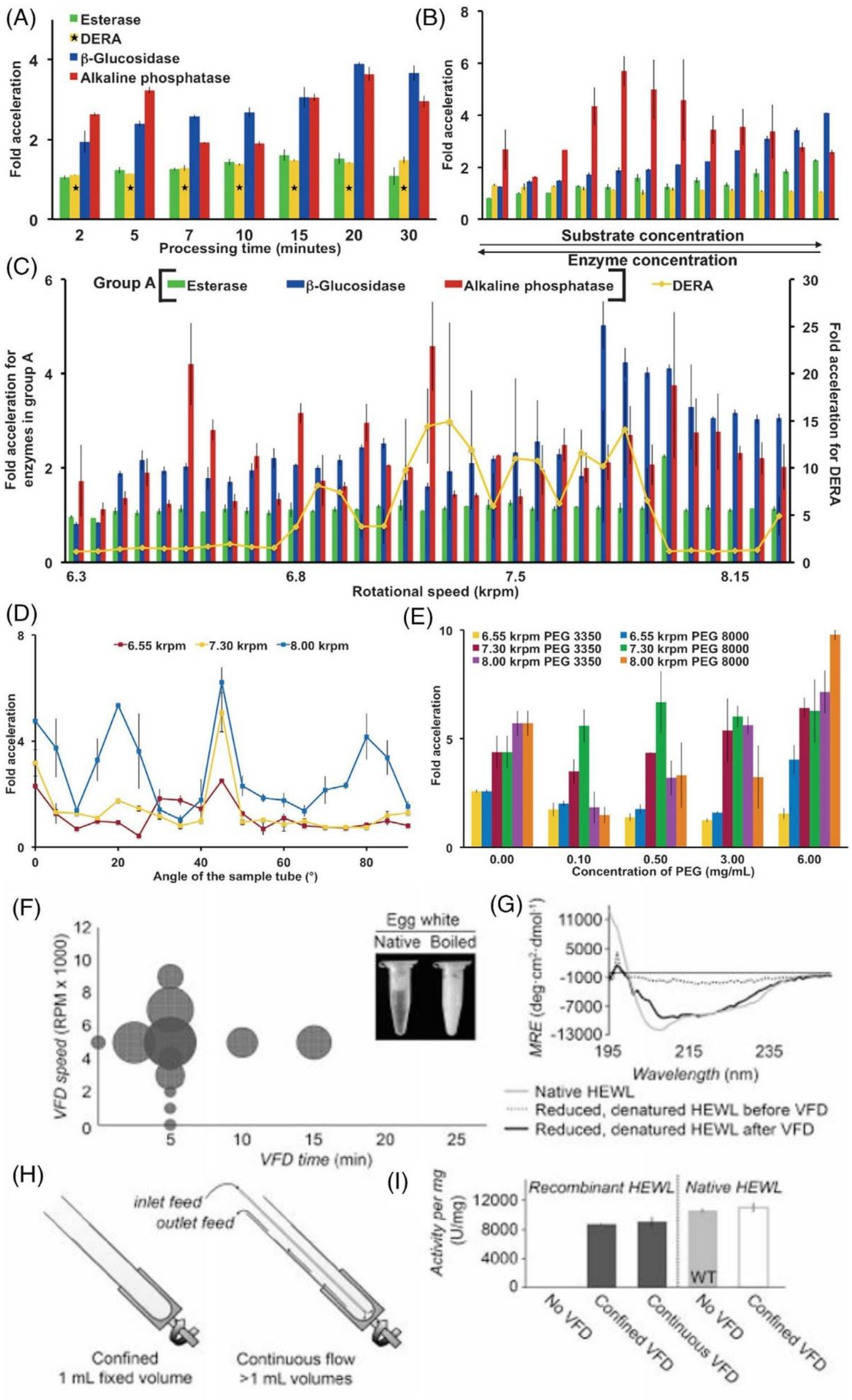

Figure 2.8 Innovative VFD transformations.

(a) Accelerated processing times for four enzymes as indicated, (b) reaction landscape for simultaneous changes in enzyme and substrate concentrations, (c) increments of 50 rpm for scans of rotational speeds, (d<="" span="" style="font-family: "Times New Roman"; colour: rgb(68, 84, 106);">alkaline phosphatase and substrate being processed with the tilt angle varied, (e) catalysis of alkaline phosphate affected by the addition of PEG, (f) lysozyme activity for boiled egg white after processing by the VFD per mg protein, with higher lysozyme, recovered activities represented by larger circles and lower activity represented by smaller circles, (g) CD spectra of denatured HEWL before and after being refolded by the VFD (h) solution of protein introduced at the bottom of the tube, and collection of folded proteins at the top of the VFD in continuous mode, (i) lysozyme activity of native and recombinantly expressed HEWL after refolding by the VFD per mg protein. (a-e) Reproduced with permission[26]. Copyright 2016, John Wiley and Sons (f-i) Reproduced with permission[16]. Copyright 2015, John Wiley and Sons.

Besides protein refolding, the VFD provides a novel processing methodology for phase demixing for the separation of proteins, as established for an aqueous two-phase system (ATPS) of aqueous potassium phosphate and polyethylene glycol, for a mixture of C-phycocyanin (C-PC) *Spirulina maxima*[29]. The process increased the efficacy of separation by 22% compared to conventional ATPS methods, with a 1.18-fold increase in C-PC purity in contrast to allophycocyanin, the primary contaminant protein, and a 9.3-fold increase in phase demixing efficiency, Figure 2.9. This VFD based methodology has potential for rapid phase demixing associated with purifying biologically active proteins. A mechanistic understanding of phase separation in VFD was established in 2022.[15] This is driven by micron to submicron size topological flow regimes in the thin films in VFD which induces high inter-phase mass transfer and facilitates the protein exchange. Briefly, this is achieved through a hemispherical base tube which creates a Coriolis force as a spinning top (ST) fluid flow in the less dense liquid which penetrates the denser layer of liquid, delivering liquid from the upper layer through the lower layer to the surface of the tube. In the same way, Faraday wave induced double helical flows penetrate both phases, also facilitating mass transfer across the phase boundary. Therefore, protein separation can be achieved instantaneously as a mixture with no evidence of damage to the proteins under the shearing.

Furthermore, Britton *et al.* reported utilizing thin film processing in a continuous mode as a versatile strategy for immobilizing enzymes, with glutaraldehyde and non-covalent bioconjugation immobilizing enzymes onto the surface of the tubes[55]. The stock protein solution was able to consecutively coat more than ten reactors even after being recycled, with the approach requiring only a nanogram of protein for each tube. This technique reduced the number of necessary proteins and a piranha-cleaning solution and other reagents by up to 96% by confining the reagents in thin films during immobilization, with no loss in catalytic activity after being processed for ten hours, Figure 2.9. Nature's machinery can generate complex molecules by incorporating biocatalysts into multistep processes, offering the potential for proteins with low expression to facilitate biocatalysts for complex substrate transformations in pharmaceutical manufacture. Another example of lysing/disrupting cells using VFD is for the biodiesel production.[56,57] The performance of the processing technology, both in confined and continuous flow mode, was evaluated by assessing the efficiencies of fatty acid extraction and the subsequent conversion of fatty acids to fatty acid methyl ester (FAME). Average extraction efficacies were 41% and conversion efficiencies >90% with the processing technology showing a broad tolerance to parameter settings.

The VFD is also capable of probing the structure of self-organized systems[58]. As reported by Mo *et al*., vesicles 107 ± 19 nm in diameter, shown in Figure 2.9, are found on the self-assembly of phenolic oxygen centres with tetra-para-phosphonomethyl calix[4]-arene bearing n-hexyl moiety attachments, were useful within a macrocycle cavity by binding to carboplatin under the shear stress induced by the dynamic thin films within the VFD[51]. Carboplatin was retained inside the calixarene's hierarchical cavity structure, and the diameters of the vesicles were maintained after shearing. The loading efficiency and release profile of the carboplatin were investigated, with the drugs loaded under shear. The vesicles are stable at a normal tissue pH with preferential release of the drug cargo at pH 6, which is the typical pH for cancerous tissues. Thus they have the potential for anticancer drug delivery applications. The hierarchical structured vesicles lower the concentration of IC50 10-fold, increasing carboplatin efficacy 4.5-fold for ovarian cancer cells and increasing cell percentage during DNA replication (S-phase) of the cell cycle. The vesicles mimic calixarene lipids and have potential application in drug delivery. This would only increase once a targeting agent was tagged alongside, such as fluorescent molecules with aggregation-induced emission characteristics.

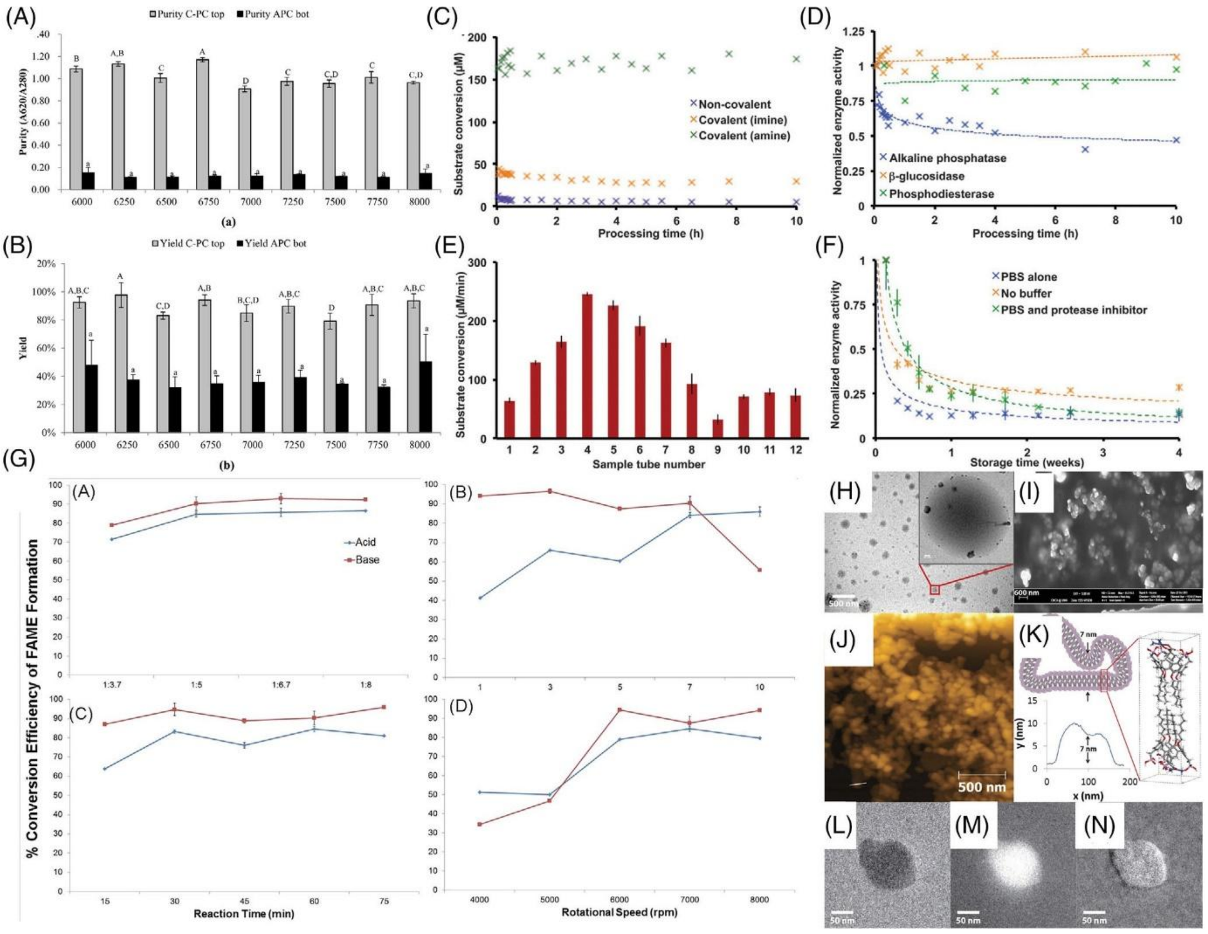

Figure 2.9 Other VFD transformations.

(a) Purity (A620/A280) and (b) APC and P-PC yield recovered after VFD-ATPS processing at various speeds of rotation[29], (c) conversion levels of substrates increase dramatically by swapping from non-covalent to covalent attachments, (d) optimized symmetrical amine-glutaraldehyde cross-linker for β-glucosidase applied for phosphodiesterase and alkaline phosphatase, with excellent stability after processing over ten hours, (e) β-glucosidase solution recycled, with the last sample tube having a similar substrate transformation to the first,

(f) >20% catalytic activity for enzyme-immobilized tubes without buffer after being stored for one month[55], (g) optimization of processing parameters (ratio of biomass to methanol, catalyst concentration, reaction time and rotational speed in rpm) for VFD-mediated dry biomass processing in confined mode. (h) TEM image (inset 10 nm scale bar), (i) SEM image, and (j) AFM image of P4C6-carboplatin host-guest vesicles after VFD processing, with (k) collapsed vesicle's sectional height profile and host-guest complex elemental mapping with energy-filtered transmission electron microscopy for (l) unfiltered, (m) carbon, and (n) platinum[51]. (a-b) Reproduced with permission[29]. Copyright 2016, American Chemical Society. (c-f) Reproduced under the terms of the CC BY 3.0 license[55]. Copyright 2016, Royal Society of Chemistry. (g) Reproduced with permission[56]. Copyright 2018, Elsevier. (h-n) Reproduced under the terms of the CC BY 4.0 International license[51]. Copyright 2015, Springer Nature.

Recently, aggregation induced-emission luminogens (AIEgens) with high emission efficiency in the aggregated state, excellent photo-stability, and increased sensitivity have become one of the most promising nanoprobes for both material and process characterizations due to their flexibility, versatility, and robustness when compared to other strategies[59]. The most frequently used approach to preparing AIEgen particles is precipitation. Without proper mixing under shear, AIE particles will be distributed in various sizes, affecting their ultimate brightness and applications. In the inaugural attempt for VFD-mediation of AIEgen size, controlling the size and shape of AIEgens was possible, impacting their fluorescence (FL) properties[59]. By increasing both water fraction (in tetrahydrofuran) and rotational speed (up to 5000 rpm) during the preparation of a particular AIEgen, tetraphenylethylene (TPE), the particle size was controlled and significantly reduced, with the smaller particles increasing the brightness. The ability of the VFD to produce AIEgens <10 nm in size with tunable FL intensities directly from a 90% solvent/antisolvent (SA) ratio at the VFD rotational speed of 5000 rpm is shown in Figure 2.10. In traditionally prepared TPE particles, a 40-times increase in the fluorescent maxima had been observed at the SA ratio of 95% compared to that of TPE particles prepared at the SA ratio of 80%. At SA ratios < 80%, the associated emissions had been zero. Surprisingly, it was found that VFD-derived solutions of TPE particles were fluorescent at the SA ratios < 80% (down to the SA ratio = 40%). At constant rotation speeds above 1000 rpm, the SA ratio increased to fluorescent maxima and maximum relative intensity. The highest maximum relative intensity for VFD-derived TPE particles was about 190 times greater for the SA ratio and rotation speed of 90% and 5000 rpm, respectively. Although other approaches, including multi-channel and microfluidic methods, had been unable to produce AIEgens <80 nm in size, use of the VFD provides a unique strategy to tune the size and control the FL property of AIEgens, which are important properties for different applications. As an advantage of size reduction, the direct diffusion of NPs (nano-sized) will occur which can cross a cellular membrane and enter a cell[60]. This opens new opportunities for biological and material studies.

In another study, TPE-2BA AIEgen, a derivative of tetraphenylethylene with two boronic acid groups, was physically coupled with a commercially available hyperbranched polymer (HBP; bis-MPA polyester-64-hydroxyl; generation 4) using VFD[61]. Significant differences in FL intensity were found for the AIE–HBP (HBP concentration = 1 mM) at different SA ratios, as shown in Figure 2.10. The FL intensity increased 32-fold with the SA ratio = 90% compared to te SA ratio of 40%. Negligible changes in particle size in the VFD-driven AIE-HBP particles were reported compared to those prepared without VFD. The formation of AIE-HBP under shear stress increased AIE molecules' penetration within the HBP structure, leading to significantly brighter AIE-HBP particles. It was reported that at the SA ratio = 90%, the average particle size for the traditionally prepared AIE-HBP was approximately 150 nm, with a relative FL intensity of 38 times greater than that of TPE-2BA alone. When the VFD was used, the particle size of the AIE-HBP was reduced to approximately 80 nm, and the relative FL intensity became 73 times greater. The formation of a smaller AIE-HBP complex containing more AIE molecules within the HBP molecule structure might be the reason for that observation. The authors concluded that, with the employment of a VFD, it was possible to form an AIE-HBP complex less than 100 nm in size under optimized conditions. This later resulted in the fabrication of fluorescent hydrogels with enhanced mechanical properties, and no sign of failure was observed in the hydrogel containing AIE-HBP (1 mM) over 800% strain.

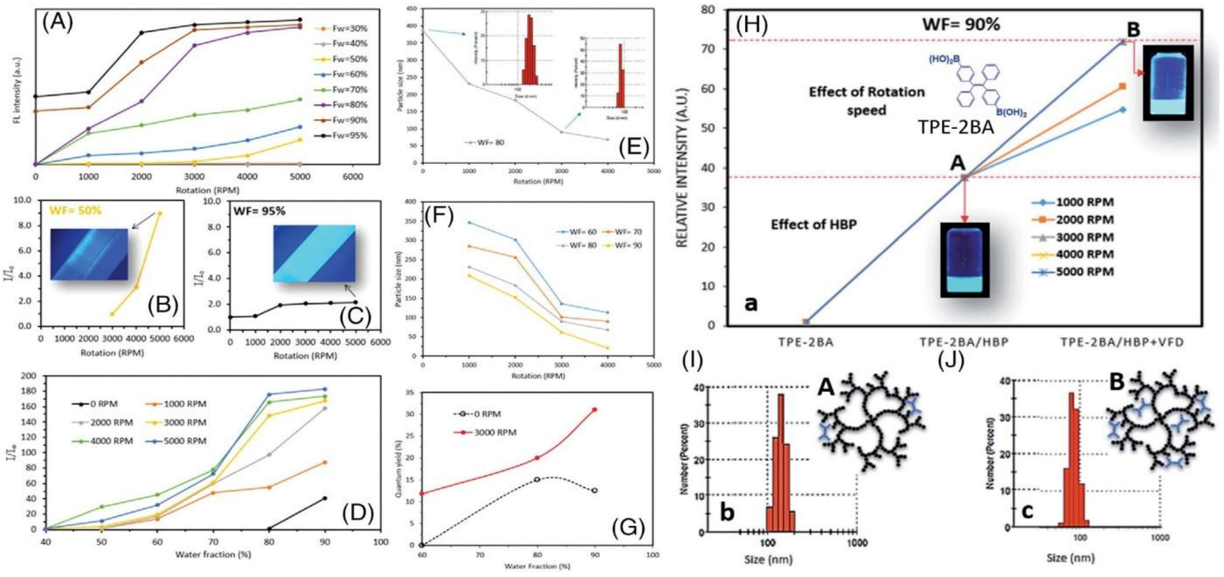

Figure 2.10 AIE-VFD transformations.

Effect of rotation speed and water fraction on the FL of solutions of TPE particles (a) change in the FL maxima at different rotation speeds and constant water fractions. Change in the relative FL maxima as a function of rotation speed at (b) 50% and (c) 95% water fraction. (d) Change in relative intensity of FL as a function of water fraction at constant rotation speeds. Effect of the rotation speed of the VFD tube on the size of the TPE particles. (e) Reduction of particle size by increasing rotational speed with the water fraction at 80%. (f) Relationship between TPE particle size and rotation speed at different water fractions (Inset: Distribution of TPE particles prepared at 0 and 3000 rpm rotation speeds). (g) The fluorescence quantum yield (%) was measured for VFD-mediated (red line) and conventional batch (dotted line) methods at different water fractions[59]. (h) The effect of rotation speed on the relative intensity of AIE-HBP (1 mM) and (i) and (j) size distribution and schematic drawing of AIE-HBP particles (1) before and (2) after VFD[61]. (a-g) Reproduced with pemission[59]. Copyright 2020, Royal Society of Chemistry. (h-j) Reproduced under the terms of the CC BY 3.0 license[61]. Copyright 2020, Royal Society of Chemistry.

2.7 Conclusion

Since the inception of the VFD in 2011, the thin film microfluidic platform has impacted on numerous diverse fields, thereby highlighting favourable support for vortex-based processing. These distinct applicable transformations suggest that the resulting Faraday waves (pressure waves) and the Coriolis from the base of the hemispherical tube of the VFD can impart on a wide variety of transformations with diminution of laborious handling. The Faraday waves generate eddies which are twisted by the Coriolis from the curved side wall of the tube into double helical flows, and these alone can be harnessed for certain applications. The Coriolis from the base of the tube takes on the shape of spinning top, typhoon like structure, which is effective for other applications, for example in the exfoliation of 2D material and exfoliation with scroll formation. Importantly with the knowledge base of the high shear topological fluid flows in the VFD there is now a heightened awareness of the predictability of processing parameters in tacking new applications of the VDF, which are seemingly endless. This review has highlighted the aptitudes of the VFD, including but not limited to the top-down transformation of graphene sheets being exfoliated, bottom-up fabrication of materials and accelerating enzymatic reactions through mechanical fluctuations in the secondary structure of the enzyme, and folding of proteins, and tuning properties of aggregation-induced emission nanoparticles. Through this novel device, we aim to reformulate how matter could be organized in precise ways using fluid flow mechanical induced effects, in striving towards accessing advanced materials, all the while circumventing any adverse effects of the engineered particles on the environment and human health. This includes adhering to the principles of green chemistry, from the inception of science to the product being in the marketplace, importantly reducing the use of toxic materials and the production of waste in the processing.

2.8 References

1. Mei, Ju, Yuning Hong, Jacky W. Y. Lam, Anjun Qin, Youhong Tang, and Ben Zhong Tang. “Aggregation-Induced Emission: The Whole Is More Brilliant than the Parts.” *Advanced Materials (Deerfield Beach, Fla.)* 26, no. 31 (August 20, 2014): 5429–79. https://doi.org/10.1002/adma.201401356.
2. Jeevanandam, Jaison, Ahmed Barhoum, Yen S. Chan, Alain Dufresne, and Michael K. Danquah. “Review on Nanoparticles and Nanostructured Materials: History, Sources, Toxicity and Regulations.” *Beilstein Journal of Nanotechnology* 9 (2018): 1050–74. https://doi.org/10.3762/bjnano.9.98.
3. Ward, Kevin, and Z Hugh Fan. “Mixing in Microfluidic Devices and Enhancement Methods.” *Journal of Micromechanics and Microengineering* 25, no. 9 (August 21, 2015): 094001. https://doi.org/10.1088/0960-1317/25/9/094001.
4. Cai, Gaozhe, Li Xue, Huilin Zhang, and Jianhan Lin. “A Review on Micromixers.” *Micromachines* 8, no. 9 (September 11, 2017). https://doi.org/10.3390/mi8090274.
5. Katircioglu-Bayel, Diler. “Effect of Combined Mechanical and Ultrasonic Milling on the Size Reduction of Talc.” *Mining, Metallurgy & Exploration* 37, no. 1 (February 1, 2020): 311–20. https://doi.org/10.1007/s42461-019-00105-8.
6. Eckelmann, Jens, and Ulrich Lüning. “Mixing Liquids—Mission Impossible? A Colorful Demonstration on Immiscible Systems.” *Journal of Chemical Education* 90, no. 2 (February 12, 2013): 224–27. https://doi.org/10.1021/ed2008262.
7. Jeong, Hyomin, Yonghun Lee, Myoungkuk Ji, Gyeonghwan Lee, and Hanshik Chung. “The Optimum Solidification and Crucible Rotation in Silicon Czochralski Crystal Growth.” *Journal of Mechanical Science and Technology* 24, no. 1 (January 1, 2010): 407–14. https://doi.org/10.1007/s12206-009-1113-x.
8. Delgado, Saraí M. Torres, David J. Kinahan, Fralett Suárez Sandoval, Lourdes Albina Nirupa Julius, Niamh A. Kilcawley, Jens Ducrée, and Dario Mager. “Fully Automated Chemiluminescence Detection Using an Electrified-Lab-on-a-Disc (eLoaD) Platform.” *Lab on a Chip* 16, no. 20 (2016): 4002–11. https://doi.org/10.1039/C6LC00973E.
9. Ribó, Josep M., Joaquim Crusats, Francesc Sagués, Josep Claret, and Raimon Rubires. “Chiral Sign Induction by Vortices During the Formation of Mesophases in Stirred Solutions.” *Science* 292, no. 5524 (June 15, 2001): 2063–66. https://doi.org/10.1126/science.1060835.
10. Grzybowski, Bartosz A., Yaroslav I. Sobolev, Olgierd Cybulski, and Barbara Mikulak-Klucznik. “Materials, Assemblies and Reaction Systems under Rotation.” *Nature Reviews Materials* 7, no. 5 (May 1, 2022): 338–54. https://doi.org/10.1038/s41578-021-00404-x.

11. Vimalanathan, Kasturi, and Colin L. Raston. “Dynamic Thin Films in Controlling the Fabrication of Nanocarbon and Its Composites.” *Advanced Materials Technologies* 2, no. 6 (June 1, 2017): 1600298. https://doi.org/10.1002/admt.201600298.
12. Strohmeier, O., M. Keller, F. Schwemmer, S. Zehnle, D. Mark, F. von Stetten, R. Zengerle, and N. Paust. “Centrifugal Microfluidic Platforms: Advanced Unit Operations and Applications.” *Chemical Society Reviews* 44, no. 17 (2015): 6187–6229. https://doi.org/10.1039/C4CS00371C.
13. Richards, R.G., D.M. MacHunter, P.J. Gates, and M.K. Palmer. “Gravity Separation of Ultra-Fine (−0.1mm) Minerals Using Spiral Separators.” *Minerals Engineering* 13, no. 1 (January 1, 2000): 65–77. https://doi.org/10.1016/S0892-6875(99)00150-8.
14. Jacobsen, Nikolas C., and Olaf Hinrichsen. “Micromixing Efficiency of a Spinning Disk Reactor.” *Industrial & Engineering Chemistry Research* 51, no. 36 (September 12, 2012): 11643–52. https://doi.org/10.1021/ie300411b.
15. Jellicoe, Matt, Aghil Igder, Clarence Chuah, Darryl B. Jones, Xuan Luo, Keith A. Stubbs, Emily M. Crawley, et al. “Vortex Fluidic Induced Mass Transfer across Immiscible Phases.” *Chemical Science* 13, no. 12 (2022): 3375–85. https://doi.org/10.1039/D1SC05829K.
16. Yuan, Tom Z., Callum F. G. Ormonde, Stephan T. Kudlacek, Sameeran Kunche, Joshua N. Smith, William A. Brown, Kaitlin M. Pugliese, et al. “Shear-Stress-Mediated Refolding of Proteins from Aggregates and Inclusion Bodies.” *ChemBioChem* 16, no. 3 (February 9, 2015): 393–96. https://doi.org/10.1002/cbic.201402427.
17. Britton, Joshua, Keith A. Stubbs, Gregory A. Weiss, and Colin L. Raston. “Vortex Fluidic Chemical Transformations.” *Chemistry – A European Journal* 23, no. 54 (September 27, 2017): 13270–78. https://doi.org/10.1002/chem.201700888.
18. Luo, Xuan, Peng Su, Wei Zhang, and Colin L. Raston. “Microfluidic Devices in Fabricating Nano or Micromaterials for Biomedical Applications.” *Advanced Materials Technologies* 4, no. 12 (December 1, 2019): 1900488. https://doi.org/10.1002/admt.201900488.
19. Al-Antaki, Ahmed Hussein Mohammed, Xuan Luo, Thaar M. D. Alharbi, David P. Harvey, Scott Pye, Jin Zou, Warren Lawrance, and Colin L. Raston. “Inverted Vortex Fluidic Exfoliation and Scrolling of Hexagonal-Boron Nitride.” *RSC Advances* 9, no. 38 (2019): 22074–79. https://doi.org/10.1039/C9RA03970H.
20. Britton, Joshua, Stuart B. Dalziel, and Colin L. Raston. “The Synthesis of Di-Carboxylate Esters Using Continuous Flow Vortex Fluidics.” *Green Chemistry* 18, no. 7 (2016): 2193–2200. https://doi.org/10.1039/C5GC02494C.
21. Yasmin, Lyzu, Xianjue Chen, Keith A. Stubbs, and Colin L. Raston. “Optimising a Vortex Fluidic Device for Controlling Chemical Reactivity and Selectivity.” *Scientific Reports* 3, no. 1 (July 25, 2013): 2282. https://doi.org/10.1038/srep02282.

22. He, Shan, Kasturi Vimalanathan, Peng Su, Matt Jellicoe, Xuan Luo, Wenjin Xing, Wanling Cai, et al. “Upsized Vortex Fluidic Device Enhancement of Mechanical Properties and the Microstructure of Biomass-Based Biodegradable Films.” *ACS Sustainable Chemistry & Engineering* 9, no. 43 (November 1, 2021): 14588–95. https://doi.org/10.1021/acssuschemeng.1c05534.
23. Vimalanathan, Kasturi, Jason R. Gascooke, Irene Suarez-Martinez, Nigel A. Marks, Harshita Kumari, Christopher J. Garvey, Jerry L. Atwood, Warren D. Lawrance, and Colin L. Raston. “Fluid Dynamic Lateral Slicing of High Tensile Strength Carbon Nanotubes.” *Scientific Reports* 6, no. 1 (March 11, 2016): 22865. https://doi.org/10.1038/srep22865.
24. Luo, Xuan, Ahmed Hussein Mohammed Al-Antaki, Kasturi Vimalanathan, Jillian Moffatt, Kun Zheng, Yichao Zou, Jin Zou, et al. “Laser Irradiated Vortex Fluidic Mediated Synthesis of Luminescent Carbon Nanodots under Continuous Flow.” *Reaction Chemistry & Engineering* 3, no. 2 (2018): 164–70. https://doi.org/10.1039/C7RE00197E.
25. Chen, Xianjue, John F. Dobson, and Colin L. Raston. “Vortex Fluidic Exfoliation of Graphite and Boron Nitride.” *Chemical Communications* 48, no. 31 (2012): 3703–5. https://doi.org/10.1039/C2CC17611D.
26. Britton, Joshua, Luz M. Meneghini, Colin L. Raston, and Gregory A. Weiss. “Accelerating Enzymatic Catalysis Using Vortex Fluidics.” *Angewandte Chemie International Edition* 55, no. 38 (September 12, 2016): 11387–91. https://doi.org/10.1002/anie.201604014.
27. Luo, Xuan, Ahmed Hussein Mohammed Al-Antaki, Aghil Igder, Keith A. Stubbs, Peng Su, Wei Zhang, Gregory A. Weiss, and Colin L. Raston. “Vortex Fluidic-Mediated Fabrication of Fast Gelated Silica Hydrogels with Embedded Laccase Nanoflowers for Real-Time Biosensing under Flow.” *ACS Applied Materials & Interfaces* 12, no. 46 (November 18, 2020): 51999–7. https://doi.org/10.1021/acsami.0c15669.
28. Luo, Xuan, Ahmed Hussein Mohammed Al-Antaki, Scott Pye, Robyn Meech, Wei Zhang, and Colin L. Raston. “High-Shear-Imparted Tunable Fluorescence in Polyethylenimines.” *ChemPhotoChem* 2, no. 4 (April 1, 2018): 343–48. https://doi.org/10.1002/cptc.201700206.
29. Luo, X., P. Smith, C. L. Raston, and W. Zhang. “Vortex Fluidic Device-Intensified Aqueous Two Phase Extraction of C-Phycocyanin from Spirulina Maxima.” *ACS Sustainable Chemistry & Engineering* 4, no. 7 (July 5, 2016): 3905–11. https://doi.org/10.1021/acssuschemeng.6b00756.
30. Alharbi, Thaar M. D., Matt Jellicoe, Xuan Luo, Kasturi Vimalanathan, Ibrahim K. Alsulami, Bediea S. AL Harbi, Aghil Igder, et al. “Sub-Micron Moulding Topological

Mass Transport Regimes in Angled Vortex Fluidic Flow.” *Nanoscale Advances* 3, no. 11 (2021): 3064–75. https://doi.org/10.1039/D1NA00195G.

31. Zhao, Weifeng, Ming Fang, Furong Wu, Hang Wu, Liwei Wang, and Guohua Chen. “Preparation of Graphene by Exfoliation of Graphite Using Wet Ball Milling.” *Journal of Materials Chemistry* 20, no. 28 (2010): 5817–19. https://doi.org/10.1039/C0JM01354D.
32. Hernandez, Yenny, Valeria Nicolosi, Mustafa Lotya, Fiona M. Blighe, Zhenyu Sun, Sukanta De, I. T. McGovern, et al. “High-Yield Production of Graphene by Liquid-Phase Exfoliation of Graphite.” *Nature Nanotechnology* 3, no. 9 (September 1, 2008): 563–68. https://doi.org/10.1038/nnano.2008.215.
33. Khan, Umar, Harshit Porwal, Arlene O’Neill, Khalid Nawaz, Peter May, and Jonathan N. Coleman. “Solvent-Exfoliated Graphene at Extremely High Concentration.” *Langmuir* 27, no. 15 (August 2, 2011): 9077–82. https://doi.org/10.1021/la201797h.
34. Vimalanathan, Kasturi, James Scott, Xun Pan, Xuan Luo, Soraya Rahpeima, Qiang Sun, Jin Zou, et al. “Continuous Flow Fabrication of Green Graphene Oxide in Aqueous Hydrogen Peroxide.” *Nanoscale Advances* 4, no. 15 (2022): 3121–30. https://doi.org/10.1039/D2NA00310D.
35. Alsulam, Ibrahim K., Thaar M. D. Alharbi, Mahmoud Moussa, and Colin L. Raston. “High-Yield Continuous-Flow Synthesis of Spheroidal C60@Graphene Composites as Supercapacitors.” *ACS Omega* 4, no. 21 (November 19, 2019): 19279–86. https://doi.org/10.1021/acsomega.9b02656.
36. Alharbi, Thaar M. D., Amjad E. H. Alotaibi, and Colin L. Raston. “Architected C70/Graphene Oxide Composites Prepared under Continuous Flow in a Vortex Fluidic Device: Implications for Supercapacitors.” *ACS Applied Nano Materials* 6, no. 13 (July 14, 2023): 12507–14. https://doi.org/10.1021/acsanm.3c02303.
37. Li, Lihua, Lingling Chen, Yao Lu, Binglin Li, Rong Hu, Ling Huang, Tao Zhang, Xiaoming Wei, Zhongmin Yang, and Chuanbin Mao. “Aggregated Carbon Dots-Loaded Macrophages Treat Sepsis by Eliminating Multidrug-Resistant Bacteria and Attenuating Inflammation.” *Aggregate* 4, no. 1 (February 1, 2023): e200. https://doi.org/10.1002/agt2.200.
38. Kang, Chunyuan, Songyuan Tao, Fan Yang, and Bai Yang. “Aggregation and Luminescence in Carbonized Polymer Dots.” *Aggregate* 3, no. 2 (April 1, 2022): e169. https://doi.org/10.1002/agt2.169.
39. Alharbi, Thaar M.D., Kasturi Vimalanathan, Warren D. Lawrance, and Colin L. Raston. “Controlled Slicing of Single Walled Carbon Nanotubes under Continuous Flow.” *Carbon* 140 (December 1, 2018): 428–32. https://doi.org/10.1016/j.carbon.2018.08.066.
40. Pierard, N, A Fonseca, Z Konya, I Willems, G Van Tendeloo, and J B.Nagy. “Production of Short Carbon Nanotubes with Open Tips by Ball Milling.” *Chemical Physics Letters* 335, no. 1 (February 16, 2001): 1–8. https://doi.org/10.1016/S0009-2614(01)00004-5.

41. Scott, Lawrence T., Edward A. Jackson, Qianyan Zhang, Brian D. Steinberg, Mihail Bancu, and Bo Li. “A Short, Rigid, Structurally Pure Carbon Nanotube by Stepwise Chemical Synthesis.” *Journal of the American Chemical Society* 134, no. 1 (January 11, 2012): 107–10. https://doi.org/10.1021/ja209461g.

42. Alharbi, Thaar M. D., Qin Li, and Colin L. Raston. “Thin Film Mechano-Energy Induced Slicing of Carbon Nanotubes under Flow.” *ACS Sustainable Chemistry & Engineering* 9, no. 48 (December 6, 2021): 16044–51. https://doi.org/10.1021/acssuschemeng.1c03109.

43. Alharbi, Thaar M. D., Yoshitaka Shingaya, Kasturi Vimalanathan, Tomonobu Nakayama, and Colin L. Raston. “High Yielding Fabrication of Magnetically Responsive Coiled Single-Walled Carbon Nanotube under Flow.” *ACS Applied Nano Materials* 2, no. 8 (August 23, 2019): 5282–89. https://doi.org/10.1021/acsanm.9b01135.

44. Jellicoe, Matt, Christopher T. Gibson, Jamie S. Quinton, and Colin L. Raston. “Coiling of Single-Walled Carbon Nanotubes via Selective Topological Fluid Flow: Implications for Sensors.” *ACS Applied Nano Materials* 5, no. 8 (August 26, 2022): 11586–94. https://doi.org/10.1021/acsanm.2c02579.

45. Alharbi, Thaar M. D., Ahmed H. M. Al-Antaki, Mahmoud Moussa, Wayne D. Hutchison, and Colin L. Raston. “Three-Step-in-One Synthesis of Supercapacitor MWCNT Superparamagnetic Magnetite Composite Material under Flow.” *Nanoscale Advances* 1, no. 9 (2019): 3761–70. https://doi.org/10.1039/C9NA00346K.

46. Tong, Chee Ling, Ramiz A. Boulos, Chengzhong Yu, K. Swaminathan Iyer, and Colin L. Raston. “Continuous Flow Tuning of Ordered Mesoporous Silica under Ambient Conditions.” *RSC Advances* 3, no. 41 (2013): 18767–70. https://doi.org/10.1039/C3RA42831A.

47. Kresge, C. T., M. E. Leonowicz, W. J. Roth, J. C. Vartuli, and J. S. Beck. “Ordered Mesoporous Molecular Sieves Synthesized by a Liquid-Crystal Template Mechanism.” *Nature* 359, no. 6397 (October 1, 1992): 710–12. https://doi.org/10.1038/359710a0.

48. Tong, Chee Ling, Ela Eroglu, Xiaofei Duan, Robert N. Lamb, Kevin Jarrett, Craig E. Buckley, and Colin L. Raston. “Nitrate Uptake Using Mesoporous Silica Embedded with Zero-Valent Palladium Nanoparticles.” *RSC Advances* 5, no. 26 (2015): 20557–61. https://doi.org/10.1039/C4RA16531D.

49. Tong, Chee Ling, Uwe H. Stroeher, Melissa H. Brown, and Colin L. Raston. “Continuous Flow Vortex Fluidic Synthesis of Silica Xerogel as a Delivery Vehicle for Curcumin.” *RSC Advances* 5, no. 11 (2015): 7953–58. https://doi.org/10.1039/C4RA15109G.

50. Alsulami, Ibrahim K., Thaar M. D. Alharbi, David P. Harvey, Christopher T. Gibson, and Colin L. Raston. “Controlling the Growth of Fullerene C60 Cones under Continuous

Flow." *Chemical Communications* 54, no. 57 (2018): 7896–99. https://doi.org/10.1039/C8CC03730B.

51. Mo, Jingxin, Paul K. Eggers, Xianjue Chen, Muhammad Rizwan Hussain Ahamed, Thomas Becker, Lee Yong Lim, and Colin L. Raston. "Shear Induced Carboplatin Binding within the Cavity of a Phospholipid Mimic for Increased Anticancer Efficacy." *Scientific Reports* 5, no. 1 (May 22, 2015): 10414. https://doi.org/10.1038/srep10414.

52. Kumari, Harshita, Steven R. Kline, Stuart R. Kennedy, Christopher Garvey, Colin L. Raston, Jerry L. Atwood, and Jonathan W. Steed. "Manipulating Three-Dimensional Gel Network Entanglement by Thin Film Shearing." *Chemical Communications* 52, no. 24 (2016): 4513–16. https://doi.org/10.1039/C6CC00171H.

53. Hu, Qi, Haozhen Hu, Xinyi Zhang, Kyle Fan, Yuning Hong, Colin L. Raston, and Youhong Tang. "In Situ Monitored Vortex Fluidic-Mediated Protein Refolding/Unfolding Using an Aggregation-Induced Emission Bioprobe." *Molecules (Basel, Switzerland)* 26, no. 14 (July 14, 2021). https://doi.org/10.3390/molecules26144273.

54. Kang, Miaomiao, Zhijun Zhang, Nan Song, Meng Li, Panpan Sun, Xiaohui Chen, Dong Wang, and Ben Zhong Tang. "Aggregation-Enhanced Theranostics: AIE Sparkles in Biomedical Field." *Aggregate* 1, no. 1 (December 1, 2020): 80–106. https://doi.org/10.1002/agt2.7.

55. Britton, Joshua, Colin L. Raston, and Gregory A. Weiss. "Rapid Protein Immobilization for Thin Film Continuous Flow Biocatalysis." *Chemical Communications* 52, no. 66 (2016): 10159–62. https://doi.org/10.1039/C6CC04210D.

56. Sitepu, Eko K., Kendall Corbin, Xuan Luo, Scott J. Pye, Youhong Tang, Sophie C. Leterme, Kirsten Heimann, Colin L. Raston, and Wei Zhang. "Vortex Fluidic Mediated Direct Transesterification of Wet Microalgae Biomass to Biodiesel." *Bioresource Technology* 266 (October 1, 2018): 488–97. https://doi.org/10.1016/j.biortech.2018.06.103.

57. Sitepu, Eko K., Darryl B. Jones, Youhong Tang, Sophie C. Leterme, Kirsten Heimann, Wei Zhang, and Colin L. Raston. "Continuous Flow Biodiesel Production from Wet Microalgae Using a Hybrid Thin Film Microfluidic Platform." *Chemical Communications* 54, no. 85 (2018): 12085–88. https://doi.org/10.1039/C8CC07610C.

58. Jiang, Yusheng, Tao He, Yuncong Chen, Yinlan Ruan, Yabin Zhou, Ben Zhong Tang, Jianguang Qin, and Youhong Tang. "Quantitative Evaluation and in Vivo Visualization of Mercury Ion Bioaccumulation in Rotifers by Novel Aggregation-Induced Emission Fluorogen Nanoparticles." *Environmental Science: Nano* 4, no. 11 (2017): 2186–92. https://doi.org/10.1039/C7EN00599G.

59. Tavakoli, Javad, Scott Pye, A. H. M. Mosinul Reza, Ni Xie, Jian Qin, Colin L. Raston, Ben Zhong Tang, and Youhong Tang. "Tuning Aggregation-Induced Emission

Nanoparticle Properties under Thin Film Formation." *Materials Chemistry Frontiers* 4, no. 2 (2020): 537–45. https://doi.org/10.1039/C9QM00585D.

60. Behzadi, Shahed, Vahid Serpooshan, Wei Tao, Majd A. Hamaly, Mahmoud Y. Alkawareek, Erik C. Dreaden, Dennis Brown, Alaaldin M. Alkilany, Omid C. Farokhzad, and Morteza Mahmoudi. "Cellular Uptake of Nanoparticles: Journey inside the Cell." *Chemical Society Reviews* 46, no. 14 (2017): 4218–44. https://doi.org/10.1039/C6CS00636A.

61. Tavakoli, Javad, Nikita Joseph, Colin L. Raston, and Youhong Tang. "A Hyper-Branched Polymer Tunes the Size and Enhances the Fluorescent Properties of Aggregation-Induced Emission Nanoparticles." *Nanoscale Advances* 2, no. 2 (2020): 633–41. https://doi.org/10.1039/D0NA00044B.

CHAPTER 3 : VORTEX FLUIDIC INDUCED MASS TRANSFER ACROSS IMMISCIBLE PHASES

Mixing immiscible liquids requires auxiliary substances, including phase transfer catalysts microgels, surfactants, complex polymers, nanoparticles, and micromixers. Centrifugally separated immiscible liquids of different densities in a 45° tilted rotating tube offer scope for avoiding their use. Micron to submicron size topological flow regimes in the thin films induce high inter-phase mass transfer depending on the nature of the two liquids. A hemispherical base tube creates a Coriolis force as a ‘spinning top’ (ST) topological fluid flow in the less dense liquid, which penetrates the denser layer of liquid, delivering liquid from the upper layer through the lower layer to the surface of the tube with the thickness of the layers determined using neutron imaging. Similarly, double helical (DH) topological flow in the less dense liquid, arising from Faraday wave eddy currents twisted by Coriolis forces, impacts the less dense liquid onto the surface of the tube. The lateral dimensions of these topological flows have been determined using ‘molecular drilling,’ impacting a thin layer of polysulfone on the surface of the tube and self-assembly of nanoparticles at the interface of the two liquids. At high rotation speeds, DH flow also occurs in the denser layer, with a critical rotational speed reached, resulting in rapid phase demixing of preformed emulsions of two immiscible liquids. ST flow is perturbed relative to double helical flow by changing the shape of the base of the tube while maintaining high mass transfer between phases, as demonstrated by circumventing the need for phase transfer catalysts. The findings presented here have implications for overcoming mass transfer limitations at liquids interfaces, providing new methods for extraction and separation science, and avoiding emulsions.

This chapter was modified from the publication of “Clarence Chuah et al. Vortex fluidic induced mass transfer across immiscible phases. Chemical Science, 2022, 13, 3375-3385”.

Author contributions: MJ, CC, and ZG carried out thermal imaging and mixing experiments; EMC, SJP, NJ, and FS carried out the neutron imaging experiments; DBJ analysed the neutron imaging experiments and interpreted the data; MJ and SH carried out the DLS experiments, XL carried out the nanomaterial synthesis at the interface between the liquids, KAS developed the organic synthesis, JMC, WZ, YT, JSQ, DM, XC, and KV contributed to the development of the experiments, DH carried out investigations of immiscible liquids of the same density, and CLR designed the VFD microfluidic platform, coordinated the research and developed the model for the fluid behaviour. All authors contributed to writing and editing the manuscript.

3.1 Abstract

Mixing immiscible liquids typically requires the use of auxiliary substances including phase transfer catalysts, microgels, surfactants, complex polymers and nanoparticles and/or micromixers. Centrifugally separated immiscible liquids of different densities in a 45° tilted rotating tube offer scope for avoiding their use. Micron to submicron size topological flow regimes in the thin films induce high inter-phase mass transfer depending on the nature of the two liquids. A hemispherical base tube creates a Coriolis force as a 'spinning top' (ST) topological fluid flow in the less dense liquid which penetrates the denser layer of liquid, delivering liquid from the upper layer through the lower layer to the surface of the tube with the thickness of the layers determined using neutron imaging. Similarly, double helical (DH) topological flow in the less dense liquid, arising from Faraday wave eddy currents twisted by Coriolis forces, impact through the less dense liquid onto the surface of the tube. The lateral dimensions of these topological flows have been determined using 'molecular drilling' impacting on a thin layer of polysulfone on the surface of the tube and self-assembly of nanoparticles at the interface of the two liquids. At high rotation speeds, DH flow also occurs in the denser layer, with a critical rotational speed reached resulting in rapid phase demixing of preformed emulsions of two immiscible liquids. ST flow is perturbed relative to double helical flow by changing the shape of the base of the tube while maintaining high mass transfer between phases as demonstrated by circumventing the need for phase transfer catalysts. The findings presented here have implications for overcoming mass transfer limitations at interfaces of liquids, and provide new methods for extractions and separation science, and avoiding the formation of emulsions.

3.2 Introduction

Mixing immiscible liquids is fundamentally important in process engineering for heat and mass transfer, in rendering mixtures of such liquids more homogeneous for promoting chemical and biochemical reactions, and in forming bi-continuous phases comprised of microstructures of immiscible liquids with high interfacial surface areas.[1] This typically requires the use of auxiliary substances including phase transfer catalysts,[2] microgels,[3–5] surfactants, complex polymers and nano-particles[6] and/or micromixers imparting hydrodynamic motion of two immiscible liquids, for example in the Archimedean screw effect,[7] electric field induced interfacial nano-mixing,[8] consecutive or cascade continuous stirred tank reactors (CSTRs)[9] and rotating surfaces.[10–12] The use of auxiliary substances can necessitate downstream purification processes though and can contribute to the generation of a waste stream. The use of immiscible liquids which are only sparingly soluble in each other can hinder reactions by maintaining physical separation of the reactants, and this needs to be addressed in designing synthetic methodology. However, there is potentially a drawback in avoiding the use of immiscible liquids, to overcome these limitations, in that it can lead to selecting liquids with reduced ability to dissolve the reactants. This is also applicable to contemporary developments in continuous flow synthesis where in addition to miscibility considerations, all reactants would usually be required to be dissolved in the liquid, leading to the use of non-traditional or non-optimal solvents. Device technologies capable of enhancing the miscibility of otherwise immiscible liquids offer exciting opportunities for chemical and biochemical processing, negating the need for the use of the aforementioned auxiliary substances and providing unique surface tension for materials processing.[9] Phase transfer catalysts bind reagents through non-covalent interactions and deliver them across phase boundaries[2] whereas microgels can compartmentalize immiscible liquids with enrichment of the corresponding phase or indeed homogenous phase formation[3–5] but require heating post-processing for phase separation and reaction work up[5].

Mechanoenergy that is generated centrifugally and diverted into dynamic thin films has been harnessed to mediate a diversity of chemical, biochemical and material processes. Such microfluidic platforms include spinning disc and rotating tube processes (reactors),[10] and the vortex fluidic device (VFD) which has a rapidly rotating tube tilted at 45° (θ) as the optimal processing angle for a myriad of applications, including in the chemical, biological and materials sciences, and it is the angle with unique fluid flow for processing homogeneous liquids in the device.[11] Moreover, the 45° tilt angle is optimal whether the VFD is used in the confined mode for a finite amount of liquid in the tube, or under continuous flow where jet feeds deliver reagents to the base of the tube and/or at positions along the tube Figure 3.1.[11] Unique high shear topological fluid flow regimes have been identified for monophasic liquids processed in the VFD along with the development of a general fluid flow model that accounts for all the processing in the device at $\theta = 45°$.[11] The impact on high heat and mass transfer in such liquids associated with these topological fluid flows has been established using moulding strategies, with the resulting structures taking on submicron to micron dimensions, depending on the nature of the liquid, and the dimensions and rotational speed, ω, of the tube, typically made of quartz with a hemispherical base, 20 mm in outside diameter (OD), 17.5 mm internal diameter (ID) and 18.5 cm in length.[11] Coriolis forces from the hemispherical base of the tube generates a ST (tornado type) topological fluid flow, with eddy currents from Faraday waves twisted by Coriolis forces generating DH topological flows, Figure 3.1. Faraday waves are pressure fluctuations that induce eddies on the inside of the curved VFD tube that are aligned vertically across the film.[11] Both topological fluid flows are present for increasing ω, with spicular or spherical flow arising from a combination of ST flow and DH flow of similar diameter and associated forces.[11,13] Importantly the shear stress in the VFD is not uniform, but rather it can be uniformly localised. The above moulding strategies included so called 'molecular drilling', and shear stress induced polymerisation, crystallisation and aggregation.[11] Related theoretical studies account for flow-mediated transport of molecules involved in shear stress induced aggregation of colloids,[14] colloidal breakup,[15] and nucleation and crystallisation of colloids.[16] The topological fluid flows are essentially vortex rings, which are prevalent in fluids and other states[17] with implications for biology studies.[18]

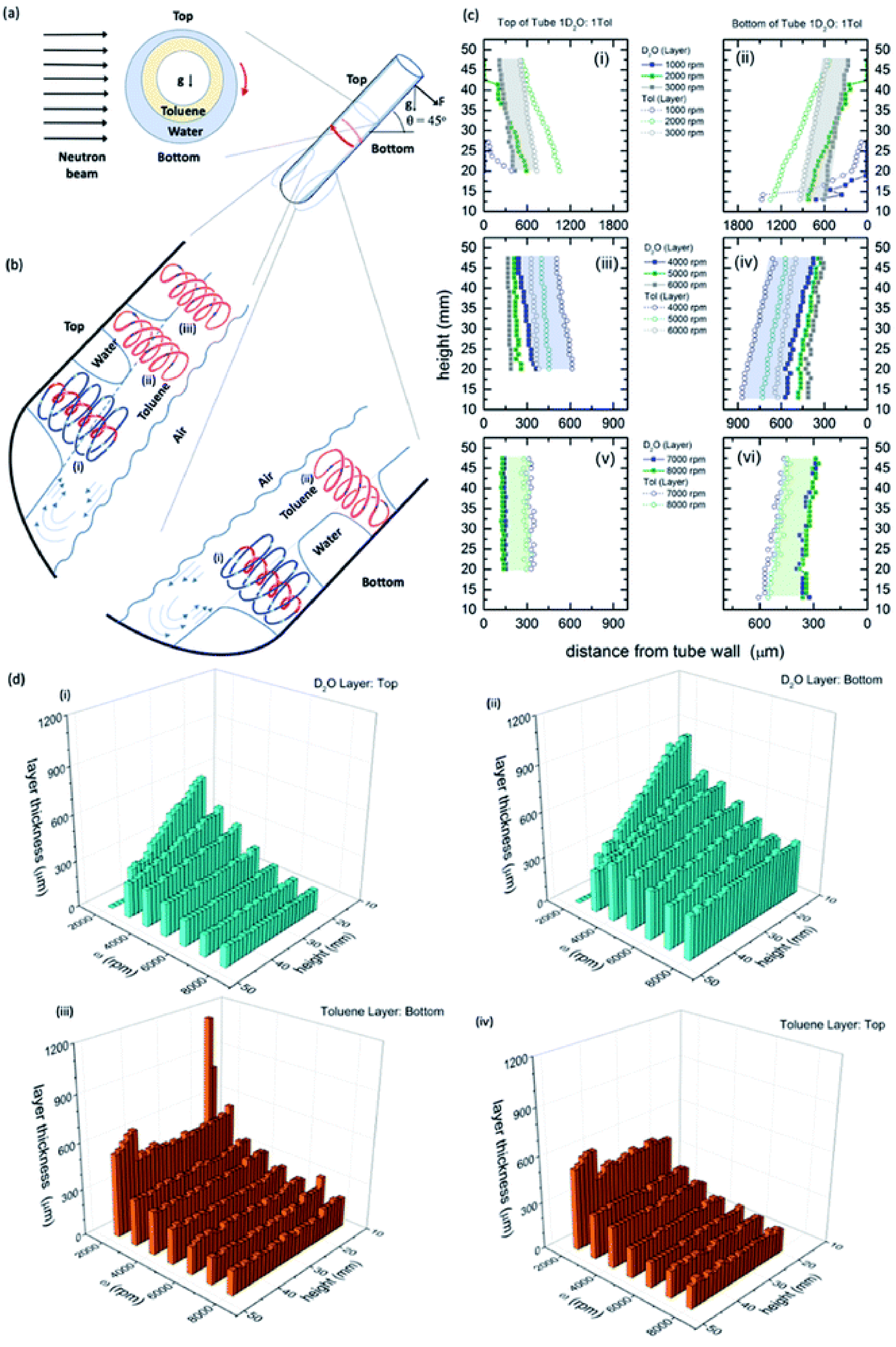

Figure 3.1 Neutron imaging derived film thicknesses and topological fluid flows.

(a) Cartoon of the relative film thickness on the upper and lower side of the rapidly rotating hemispherical base quartz tube (20 mm OD, 17.5 mm ID). Here g denotes the direction of gravity or its projection within the cross-sectional plane. (b) Fluid flows present in the films relative to the top and the bottom of the tube, as defined, with spinning top and double helical topological fluid flows, (i) and (ii) respectively, in the toluene layer impacting through the water layer onto the surface of the quartz tube titled at 45°, and where there is no distinction in the double helical flow for the two immiscible layers, (iii), where the thickness of the layers along the length of the top of the tube is constant. (c) Film thicknesses derived from neutron imaging with the direction of the neutron beam depicted in (a), for a 1 : 1 mixture of D_2O and toluene at the top (upper side) and bottom (lower side) of the VFD hemispherical base tube for (i and ii) 1000 to 3000 rpm, (iii and iv) 4000 to 6000 rpm, and (v and vi) 7000 to 8000 rpm, respectively; accuracy of relative film thickness ±50 μm, and accuracy of height of the film along the tube ±1 mm. The filled in areas highlight the uniformity of the thickness of the film of toluene over water for a specified speed. (d) Layer thickness as a function of height up the tube and rotational speed; (i) and (ii) the D_2O layer, top and bottom of tube respectively, and (iii) and (iv) the toluene layer, top and bottom of tube respectively.

3.2.1 Neutron Imaging Determined Film Thickness Methodology

An example ANSTO Neutron images is shown in Figure 3.2 (a). The image is calibrated by first obtaining the pixel-to-distance ratio. Here we take a cross-sectional profile of the test tube from the image [Figure 3.2 (c)], as the test tube has a known outer diameter of 20 mm. This also provides the internal dimension of the VFD tube, measured to be 16770 µm. Structural features are then identified from an alternative cross-sectional profile [Figure 3.2 (b)]. The height up the tube, with reference to the internal tube base, is then approximated based on the VFD design, schematically illustrated in Figure 3.2 (d). Film profiles of the liquid are then obtained at various heights up from the tube base by averaging the neutrons from regions illustrated in Figure 3.2 (a), with the film profiles observing a cross-sectional segment of the VFD tube, orthogonal to the rotational axis, at a specific height.

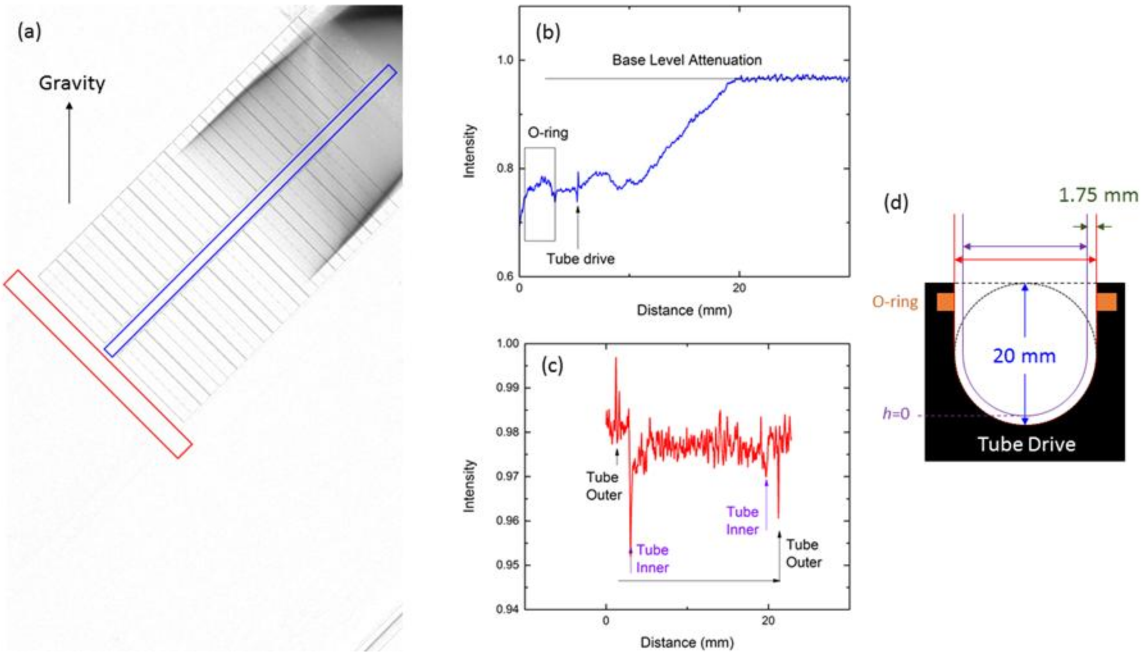

Figure 3.2 Neutron imaging.

(a) Neutron scattering image obtained at ANSTO. (b) The average Intensity profile is obtained from a blue highlighted section in part (a). (c) The average Intensity profile was obtained from a red highlighted section in part (a). (d) Schematic representation of the VFD tube highlighting key features used in calibrating neutron image.

In order to analyse the neutron imaging data, we have developed a neutron scattering attenuation model to describe the neutron beam passing through the fluid layers of the biphasic system. Looking at a cross-sectional segment of the VFD tube in the plane who's normal is parallel to the axis of rotation, we assume that we have 2 circular interfaces at the fluid-fluid and fluid-air boundaries. Based on a Beer-Lambert attenuation scattering description, that neglects refraction and reflections at the interfaces, the intensity of the neutron beam transmitted, I(x) through the tube can be described through

$$I(x) = I_0 \exp(-\sigma_1 l_1) \exp(-\sigma_2 l_2) \, .$$

Here, I_0 is the incident neutron beam intensity, σ_1 and σ_2 are the neutron scattering probabilities per unit length from layers 1 and 2, respectively. Lastly, l_1 and l_2 are the distances that the neutron beam traverses in layers 1 and 2, respectively.

In the model, the attenuating lengths for layers 1 and 2 at a cross-sectional position, x, referenced to the tube axis (positive values reflect the tube top with respect to gravity) can be obtained if the radius and centres of the circular interfaces are known (see Figure 3.3).

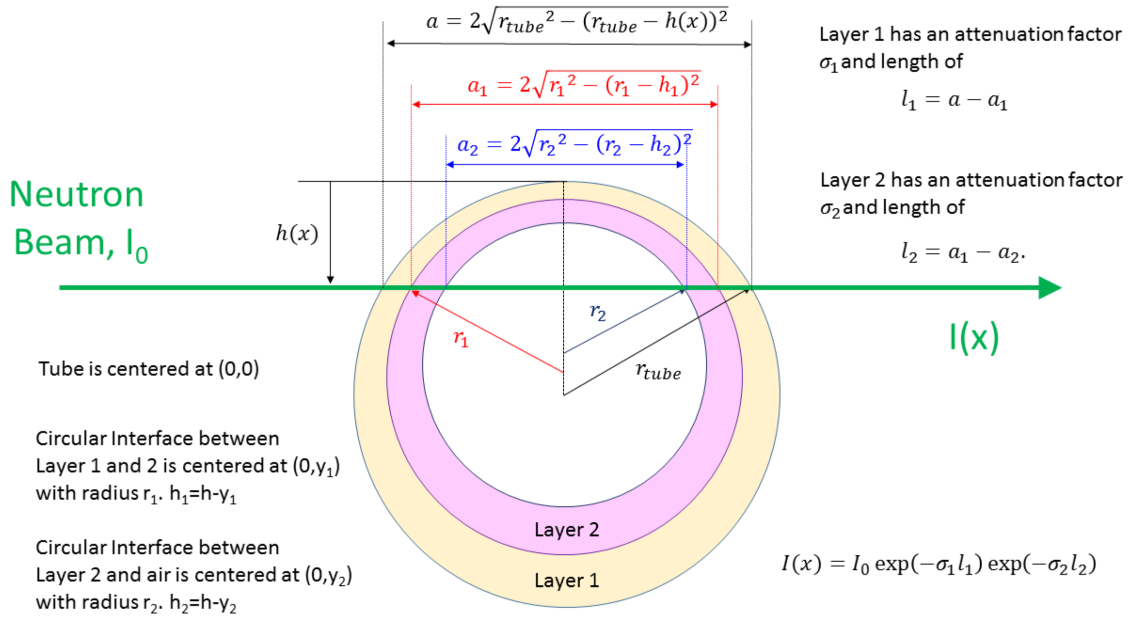

Figure 3.3 A schematic representation of the neutron beam attenuation is the experiment.

To test that this model is appropriate, we have synthesised the attenuation of a biphasic system, see Figure 3.4. This approach appears to describe all of the key features observed in the cross-section profiles observed in the neutron attenuation experiment. However, fitting the attenuation profile with this functional form to extract the properties of the film proved problematic. Specifically, convolving these attenuation properties with the instrumental response function is necessary, including additional processes such as neutron refraction and reflections at the interfaces. These refraction/reflective characteristics of the film change with variations in film thickness and are further complicated by the possibility of the neutron beam refracting through up to six different interfaces when transmitted through the biphasic system. This is complicated by the changing angle of incidence on the film across the diameter of the tube. We have found it impracticable to fit the vast amount of film attenuation profiles obtained at varying heights and rotational speeds, as the continually changing instrumental response function makes the non-linear fitting procedures unstable across the cross-sectional profiles extracted from a single image at a single rotational speed.

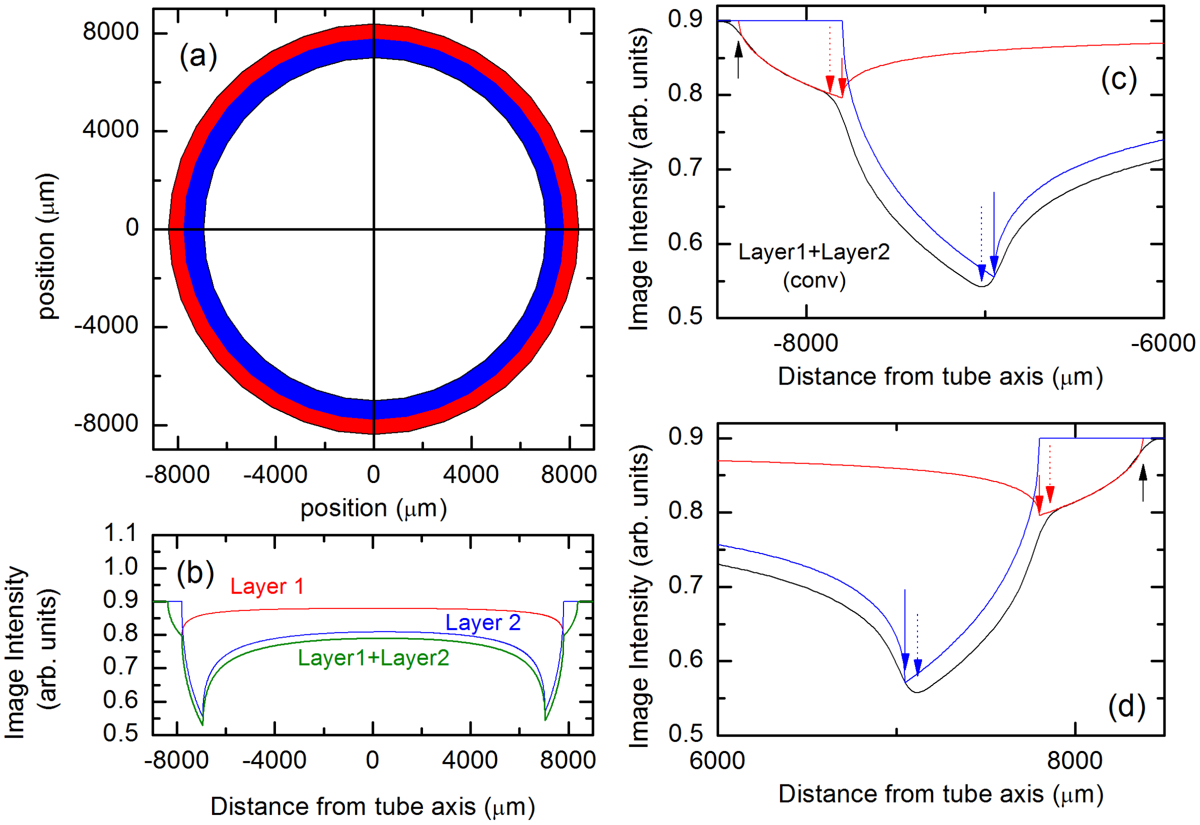

Figure 3.4 Attenuation of a biphasic system.

(a) A schematic of a hypothetical biphasic system is depicted, where the tube radius $\boldsymbol{r_T}$ = 8380 μm. Layer 1 (red) has an interface radius $\boldsymbol{r_1}$ = 7800 μm and is centred at (0,0), while Layer 2 (blue) has an interface radius $\boldsymbol{r_{L2}}$ = 7000 μm and is centred at (50,0). (b) The synthesized attenuation profile is shown for Layer 1 ($\boldsymbol{\sigma_1}$ =1.8x10^{-5} μm^{-1}), Layer 2 ($\boldsymbol{\sigma_2}$ =6.0x10^{-5} μm^{-1}), and the combined layers. The unattenuated intensity is set at 0.9 arbitrary units. (c, d) Gaussian-convoluted attenuation profiles are fitted at (c) the bottom and (d) the top of the tube. The unconvoluted attenuation profiles for the two layers are also displayed. Solid (dashed) arrows indicate the true (derived) parameters for the interface radii of Layers 1 and 2. The black arrow denotes the tube radius.

To extract data from the observed neutron images, we relate structural features in our cross-sectional profile to the physical parameters in the biphasic system. These features are indicated in Figure 3.5. Firstly, we locate the maximum attenuation (minima in profile), m, and use these values to determine the radius of the inner (layer 2) interface:

$$r_{L2} = \frac{m_+ - m_-}{2}$$

This circle describing this interface is positioned with centre:

$$c_{L2} = -\frac{m_+ + m_-}{2}.$$

Here, the subscript (+/-) references the fitting of either the top or bottom of the tube, respectively. We then obtain the difference between the attenuated curve, and a straight line running to the baseline intensity at the tube boundary. This difference curve (slope) approximates the derivative of the attenuation curve, with its maximum value (or local maximum) or inflection point reflecting the change in attenuation properties occurring from the change in neutron attenuation between different layers.

The maxima of the difference (slope), s are used to determine the radius of the outer (layer 1) interface,

$$r_{L1} = \frac{s_+ - s_-}{2}$$

This circular interface has its centre,

$$c_{L1} = -\frac{s_+ + s_-}{2}.$$

When a second layer is absent, the s value is set to either the tube radius or the outer interface. Here, the subscript (+/-) again refers to either the top or bottom of the tube, respectively.

This distance of the layer 1 interface from the top/bottom tube wall (Layer 1 thickness) is then

$$L_{1+} = r_T - (r_{L1} - c_{L1}),$$

or,

$$L_{1-} = r_T - (r_{L1} + c_{L1}),$$

respectively. This distance from the first to second interfaces (Layer 2 thickness) at the top/bottom of the tube is then

$$L_{2+} = r_{L1} - (r_{L2} - (c_{L2} - c_{L1})),$$

or,

$$L_{2-} = r_{L1} - (r_{L2} + (c_{L2} - c_{L1})),$$

respectively.

This distance between the second interface at the top/bottom of the tube from the tube wall is then

$$L_{+} = L_{1+} + L_{2+}$$

or

$$L_{-} = L_{1-} + L_{2-}$$

Note that these quantities must satisfy the conservation relationship,

$$2r_{Tube} = L_{1+} + L_{2+} + 2r_{L2} + L_{2-} + L_{1-}.$$

We verify the correlation of these parameters with the film properties by analysing our synthetic attenuation profile, which has been convoluted with a Gaussian instrumental function (standard deviation = 100 µm), as shown in Figure 3.4(c,d). We found that all derived parameters were consistent with the synthetic parameters within the standard deviation used for the convolution. Consequently, these parameters are deemed reliable for extracting film thickness information from the neutron beam attenuation profiles, despite the inability to fit the attenuation curve directly.

Additionally, for very thin films (less than 200 microns), refraction and reflections can cause the inflection point to appear outside the tube boundary. In such cases, we adjust the film thickness measurement to half the distance between the inflection point and the distance required for the attenuation intensity to return to its baseline level. We estimate the relative accuracy of the film thickness to be ±50 microns. However, systematic uncertainties from the neutron instrumental response may lead to greater absolute film thickness measurement discrepancies. Finally, we estimate the height accuracy to be within ±1 mm.

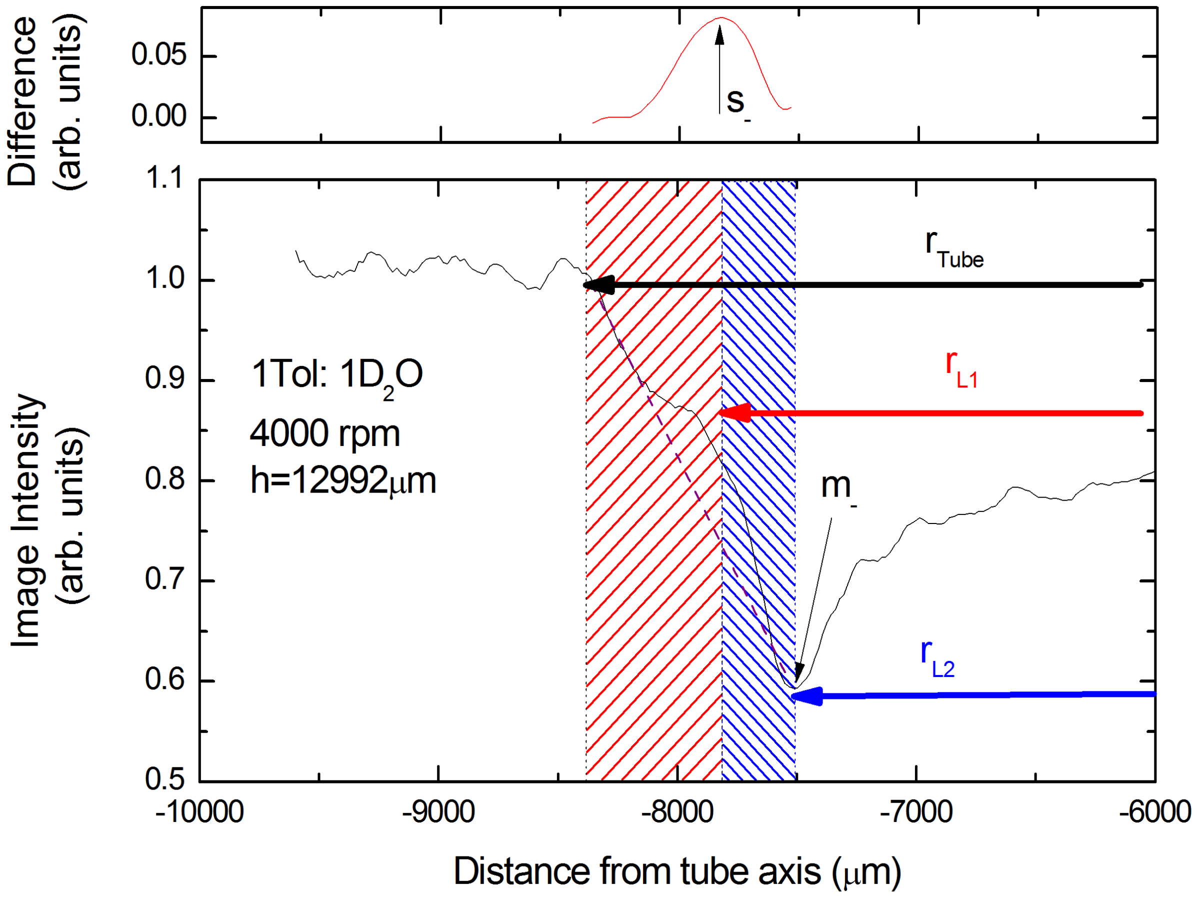

Figure 3.5 An illustration of how parameters of the film cross-sectional profile at the bottom of the tube are interpreted in terms of the film characteristics.

The analysis procedure works well and has been used to extract data regarding the film thickness. We did experience some issues with the fitting procedure in the transition regime when Layer 1 disappeared. Here the microfluidic fluid volume may become unstable to support a single phase with stable thickness. Here the space occupied by the fluid may be shared between the layers, or two phases may mix. In the time-averaged image, this manifests as the higher attenuating toluene layer having a blurred boundary, and a seeping of the attenuating intensity across the interface. This is shown in Figure 3.6.

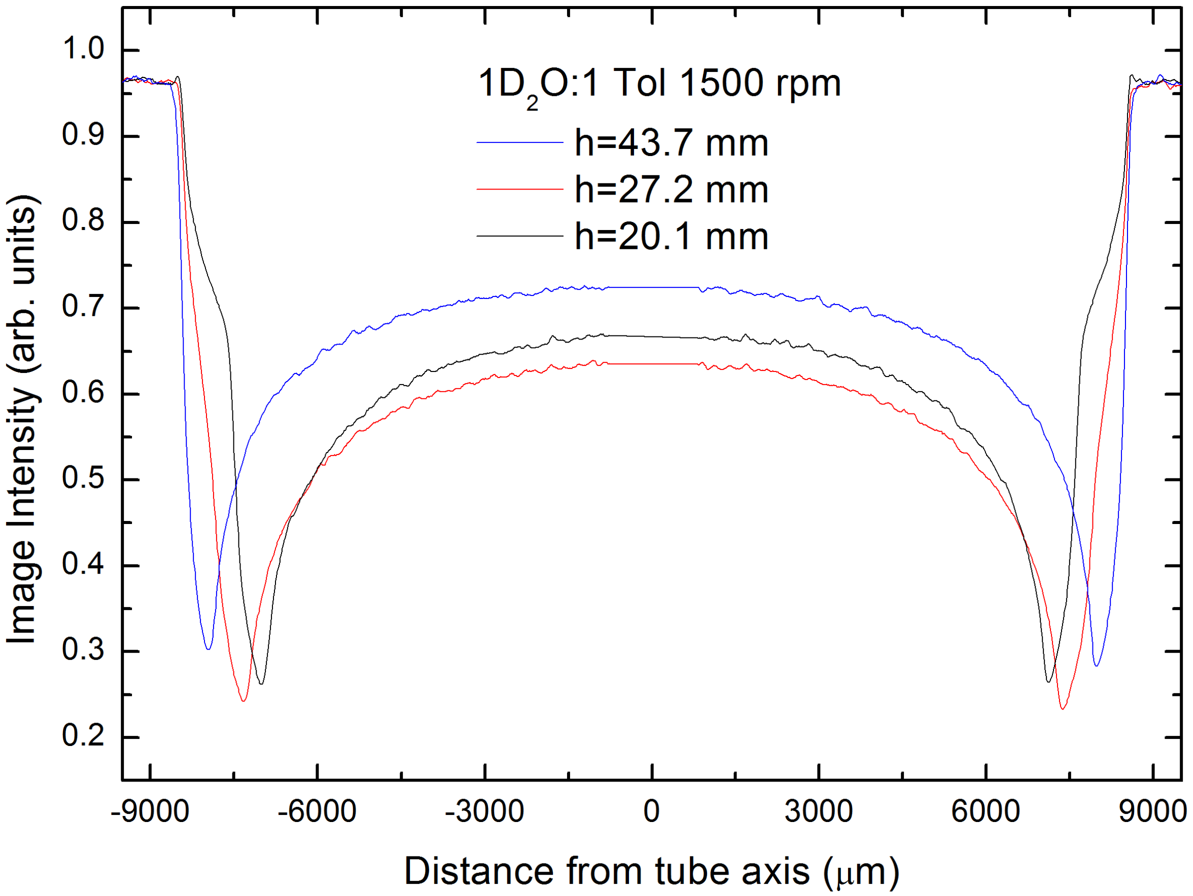

Figure 3.6 Film profiles at varying heights observe phase changes.

At different heights within the tube, we observe variations in the phasic structure of the film. Two distinct phases are present in the lower section of the tube (h = 20.1 mm, black). Only the toluene phase is observed in the upper section (h = 43.7 mm, blue). The distinction between the two phases becomes less defined in the transition region (h = 27.2 mm). It is important to note that the attenuation at the tube edge in this mixing region is weaker compared to that observed for a pure toluene phase, suggesting that the toluene phase at the tube edge does not exhibit the same density (concentration) as in the pure toluene phase.

VFD processing of immiscible liquids can result in well-defined separated phases rather than emulsions,[19] as in (i) biodiesel synthesis (three separate phases),[20,21] (ii) protein separation in a mixture of PEG and aqueous potassium phosphate[22] with no evidence of damage to the proteins under periodic high shear in the topological fluid flows which is in accord with the ability to use the VFD to refold proteins into their native states and to accelerate enzymatic reactions,[20] (iii) where water seemingly acts as an 'anti-solvent' for a toluene solution of fullerene C_{60} in forming self-assembled C_{60} nano-tubules,[23] (iv) surface tension induced slicing of single and multiwalled carbon nano-tubes[24] and (v) scrolling of graphene directly from graphite.[25] Spatially controlled energy delivery in the topological fluid flows creates conditions for controlling chemistry, which relates to fundamental insights into enhancing catalytic activity in general.[26]

We hypothesised that eddies associated with Faraday waves on the surface of a liquid centrifugally forced over a more-dense immiscible liquid in the VFD tube tilted at 45° can lead to DH flow which intersect both thin films of the liquid when the rotational speed is above that required for DH flow for the individual liquids in separate tubes also tilted at 45°. At the interface of the two liquids, molecules in the liquid held against the surface of the glass tube would be streaming into the other liquid and *vice versa*, beyond diffusion control limits.[11] The resulting *in situ* generated localised high surface area under such non-equilibrium conditions can then promote high mass transfer between the immiscible liquids. In testing this hypothesis, the nature of the topological fluid flow including its dimensionality for two immiscible liquids with different densities in the VFD has been investigated using (i) direct *in situ* neutron imaging of immiscible liquids with derivable relative film thickness, (ii) time dependent mixing experiments and temperature profiling for the hemispherical base tube, and for comparison a flat base tube, (iii) 'molecular drilling' across a uniform layer of polysulfone inside the tube (tube-liquid interface), (iv) the structure and dimensionality of self-assembled material at the interface of the two liquids (liquid–liquid interface), and (v) the ability to promote two phase organic reactions in the absence of phase transfer catalysts. A challenge with the rotating reference frame for the spinning tube in the VFD is that the dimensions of the topological fluid flows, as established for a monophasic systems,[11] cannot be measured directly, with distortions in the tube ∼100 times greater than the dimensions of the topological fluid flows.[11] Related to this is the use of immiscible liquids of different densities in a vertical aligned spinning disc with the ability for mass transfer across liquids to promote chemical reactions by changes in the rotational speeds.[12] In the VFD, the thickness of the film can be ≥150 mm with centrifugal force dominating over surface tension, in a way similar to vertically concentric rings of liquids of different density on the aforementioned spinning disc,[12] with a topological fluid flow understanding of the behaviour of the two liquids.

3.3 Results and Discussion

3.3.1 Neutron Imaging Determined Film Thickness

The relative thicknesses of two immiscible liquids as a function of rotational speed for the unique tilt angle θ at 45° were determined using neutron imaging for a 1 : 1 mixture of deuterated water (D_2O) and toluene, as presented in Figure 3.1. Water and toluene represent an archetypal immiscible solvent system (solubility of toluene in water is 0.52 g L^{-1} at 20 °C).[27] Also presented in Figure 3.1 is the model of the interpenetrating topological fluid flows in the immiscible liquid layers. Processing the data from the neutron imaging required taking into account the different attenuating lengths of the layers of liquid across the width of the tube. The resultant cross-sectional thickness determined in the tube is strikingly different for both liquids with the less dense toluene forming a thin film of uniform thickness along the tube, of the same thickness for both the upper (top) and lower surfaces (bottom) of the tube, Figure 3.1(c), (d) and (i), (ii). This uniformity of thickness is expected in the presence of Faraday waves, with the earlier modelling of the liquid in the VFD based on a wedge shape film along the tube.[28] The thickness of the film decreases for increasing ω, ∼350 mm at 3000 rpm (the lower limit for maintaining such a uniform film) to ∼160 mm at 9000 rpm (the upper limit for the VFD). In contrast, the water layer is significantly thinner at the upper surface (top) relative to the lower surface (bottom), with the film wedge shaped, becoming thinner towards the open end of the tube, except at high rotational speeds ω, 8000 and 9000 rpm, where the upper surface is of uniform thickness along the tube (∼150 mm thick), but not so for the lower surface (ranging from ∼280 to 400 mm), Figure 3.1(c), (d) and (iii), (iv). At these high rotational speeds, the uniformity on the upper surface is indicative of a Faraday wave in this section of the water film.

Neutron imaging established that the toluene layer is behaving as if there was no water present in forming uniform films along the tube, which is further born out from mixing time experiments (see below). Moreover, the thickness of the toluene layer is close to the average film thickness previously determined for toluene by itself in the VFD (∼220 mm at 5000 rpm),[11] which was determined from the weight of liquid in the tube for a film of liquid extending to the open end of the tube. This approach is not applicable in the present study for complex immiscible liquids. The average film thickness of water by itself in the VFD is ∼320 mm at 5000 rpm where the film is uniform in thickness along the tube, with the thickness decreasing periodically for increasing rotational speed while preserving $\omega \cdot P$, where P is the pitch of the DH, Figure 3.1(a).[11] For the mixture of water and toluene, the wedge-shaped thinning of the film for rotational speeds between ∼3000 and 7000 rpm is consistent with the absence of Faraday wave driven DH flows in the water phase for the upper (top) and lower (bottom) sections of the liquid. Interestingly, the layer of water centrifugally pinned on the surface of the tube by the toluene layer, is effectively removing the effects of any distortions in the glass tube itself.[11] For $\omega <\sim 2000$ rpm, the vortex in the tube is not maintained to the base of the tube, and indeed when this occurs the fluid flow behaves distinctly different, with unique optimal processing for aggregation induced emission/graphene oxide system.[29]

Similar findings were also found for a 1 : 3, 3 : 1 and 9 : 1 ratio of water to toluene with respect to the uniform toluene layer, and wedged shaped water layer. However, only in the 1 : 3 ratio does the uniform thin film of water form in the upper (top) part of the tube, as for the 1 : 1 mixture; toluene rich mixtures have insufficient water to form such a uniform layer of water with the findings establishing the importance of the choice of ratio of the two immiscible liquids. The very similar thicknesses of the toluene and water layers in the upper (top) part of the tube is consistent with the presence of Faraday waves with their eddy currents in unison, and having a common DH flow, *i.e.*, the DH flows intersect both layers and deliver mass transfer across the interface of the two liquids. With an understanding of the effect of rotational speed on film thickness for immiscible liquids along and across the tube, we then turned to physical methods involving mixing and demixing in the liquids, and phenomena at the liquid–liquid and liquid-VFD tube surface interfaces.

3.3.2 Mixing and Demixing of Immiscible Liquids

3.3.2.1 Signatures of monophasic and biphasic systems

A FLIR (T62101) camera was used to record temperature variation of different liquids at rotational speeds between 3000 to 9000 rpm, 20 mm O.D for mimicking the continuous flow mode of operation at an inclination angle q = 45^{o} in hemispherical and flat base tubes (where stated). The settings of the FTIR camera included emissivity 0.95, object distance 30.48 cm, relative humidity 50%, and the use of the rainbow colour pallet. All experiments were conducted in triplicate using the same quartz tube for each liquid for consistency of measurements within a temperature-controlled environment (average temperature 19 ^{o}C). In mimicking continuous flow processing sufficient liquid was added to the tube such that for any rotational speed, the generated thin film of liquid extends to the lip at the top of the tube. Mixing experiments were conducted in Figures 3.7, 3.8, and 3.9 below, whereby the time in the aqueous phase corresponds to the time taken for a drop of water containing a small amount of dye (blue) added at the bottom of the tube rotating at a specific speed to visibly uniformly mix in halfway up the preformed film generated from 1 mL of water (measured in triplicates)1. Mixing time in the organic phase corresponds to the time taken for a drop of organic solvent containing a small amount of beta-carotene added at the bottom of the tube rotating at a specific speed to visibly uniformly mix in halfway up the preformed film generated from 1 mL of organic solvent (measured in triplicates). De-mixing times are when an emulsion is formed of an organic solvent and water after 10 minutes of sonication. Placing 2 mL of the interface in a 20 mm O.D hemispherical or flat base tube (where stated), the VFD is rotated between 3000 to 9000 rpm. The time is recorded (120 seconds max) for the liquid to de-mix and becomes clear in the tube. The solution is kept under sonication and all experiments were conducted in triplicate using the same quartz tube for each liquid for consistency of measurements.

The selection of toluene, dichloromethane (DCM), chlorobenzene, and cyclohexene for mixing studies with water is based on their diverse physical and chemical properties. DCM and chlorobenzene are denser than water while toluene and cyclohexene are less dense. In addition, DCM is polar and highly soluble in water, while toluene and cyclohexene are nonpolar with low solubility in water, and chlorobenzene has intermediate solubility. These solvents provide a broad range of profiles and behaviours, making them ideal for studying phase separation, emulsion formation, and solvent-water interactions. Of note is that the temperature response for DCM in Figure 3.9 differs significantly from other solvents, with a decrease followed by an increase. This is hypothesised to be due to DCM’s higher vapour pressure, which leads to rapid evaporation and initial cooling, an endothermic process. DCM also has a high latent heat of vaporisation, which further absorbs heat, causing a temperature drop. As evaporation slows and stabilises, the temperature rises similarly to the other solvents. Another standout is toluene in Figure 3.10 and its sudden increase in mixing time. This is hypothesised to be due to toluene’s higher viscosity, density, and surface tension compared to the other solvents. These properties make toluene more resistant to mixing at higher speeds, requiring more time to achieve uniformity as it resists flow and takes longer to disperse under high shear forces.

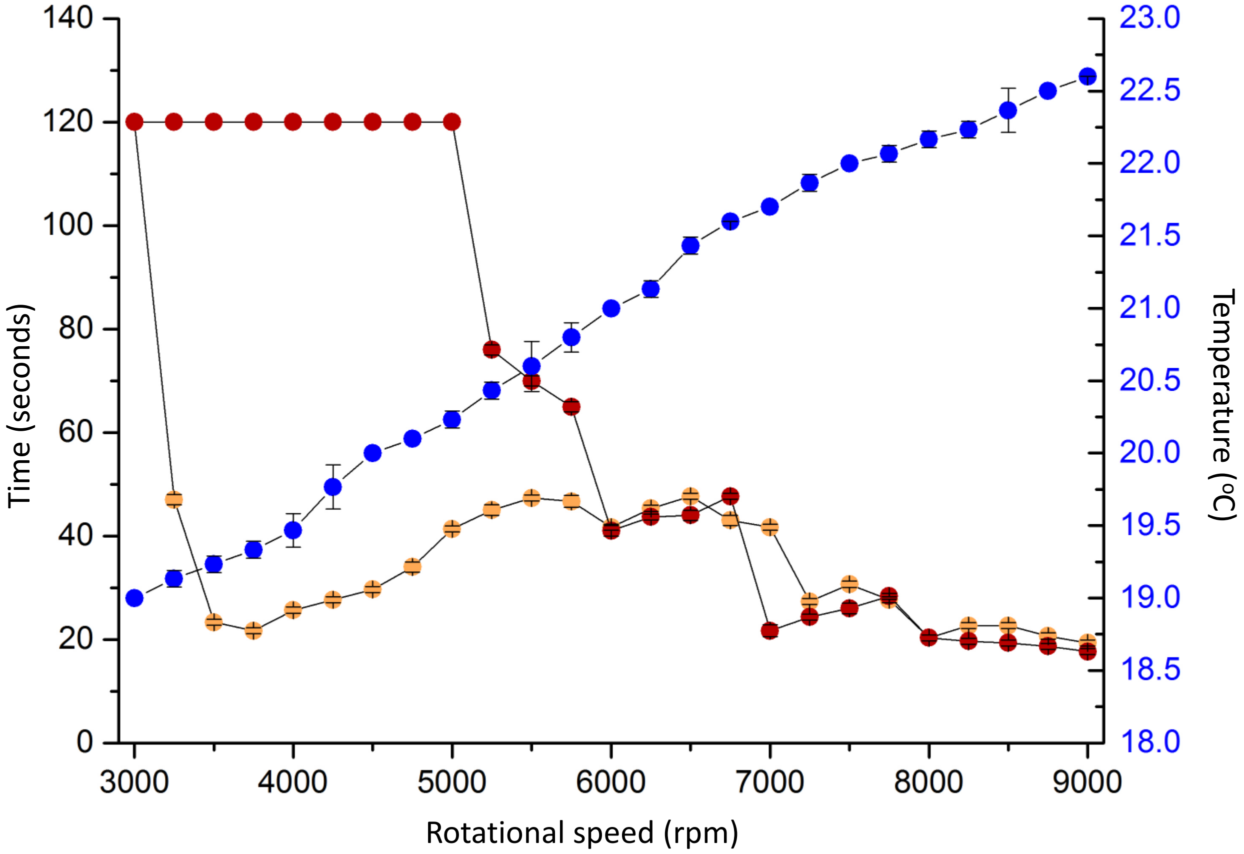

Figure 3.7 Signature of chlorobenzene and water.

Showing the mixing times of the aqueous phase (red), organic phase (orange), and the thermal response (blue) of a 1:1 mixture in a hemispherical base quartz tube (20 mm OD, 17.5 mm ID, 18.5 cm in length) as a function of ω at θ = 45°.

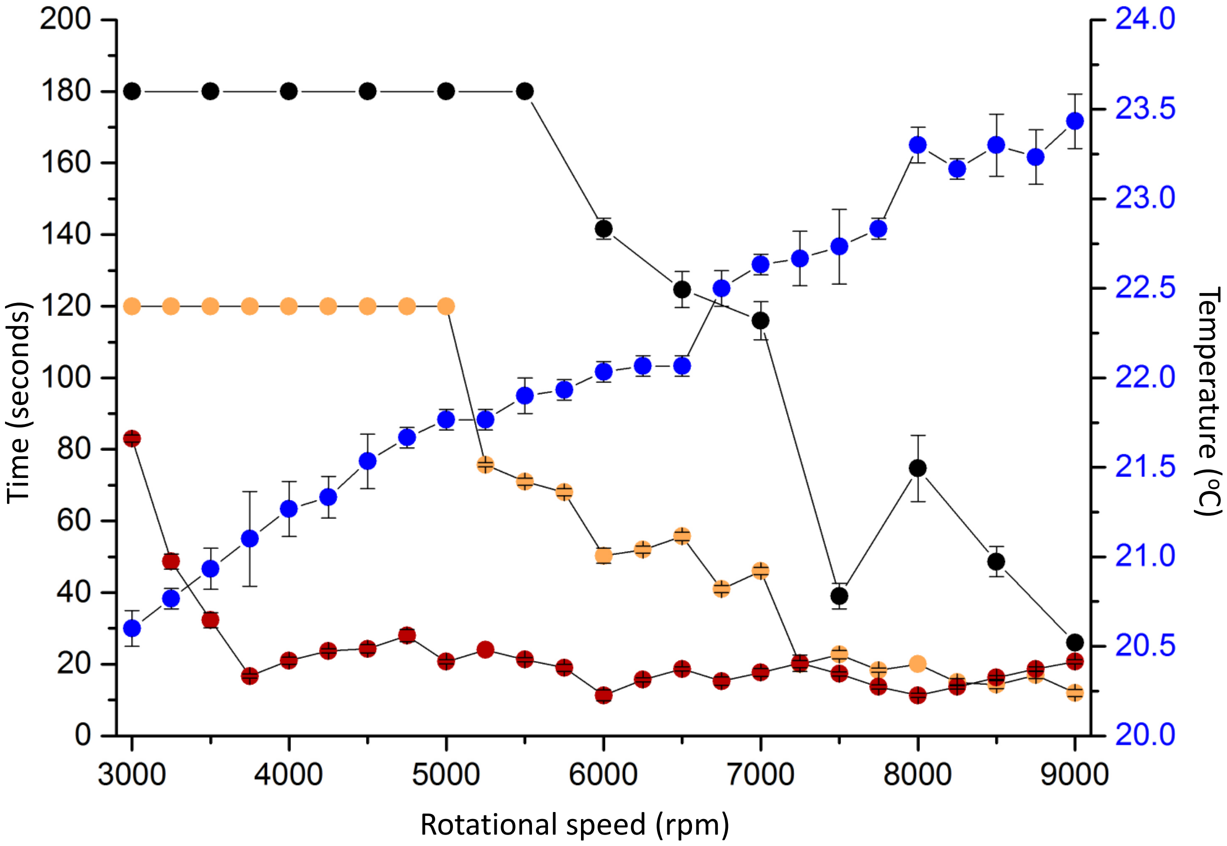

Figure 3.8 Signature of cyclohexene and water.

Showing the mixing times of the aqueous phase (red), organic phase (orange) and the thermal response (blue) of a 1:1 mixture in a hemispherical base quartz tube (20 mm OD, 17.5 mm ID, 18.5 cm in length) as a function of ω at $\theta = 45°$. The black line corresponds to the demixing time, which is the time taken for 2 mL of a preformed emulsion of cyclohexene and water placed in the VFD to phase separate.

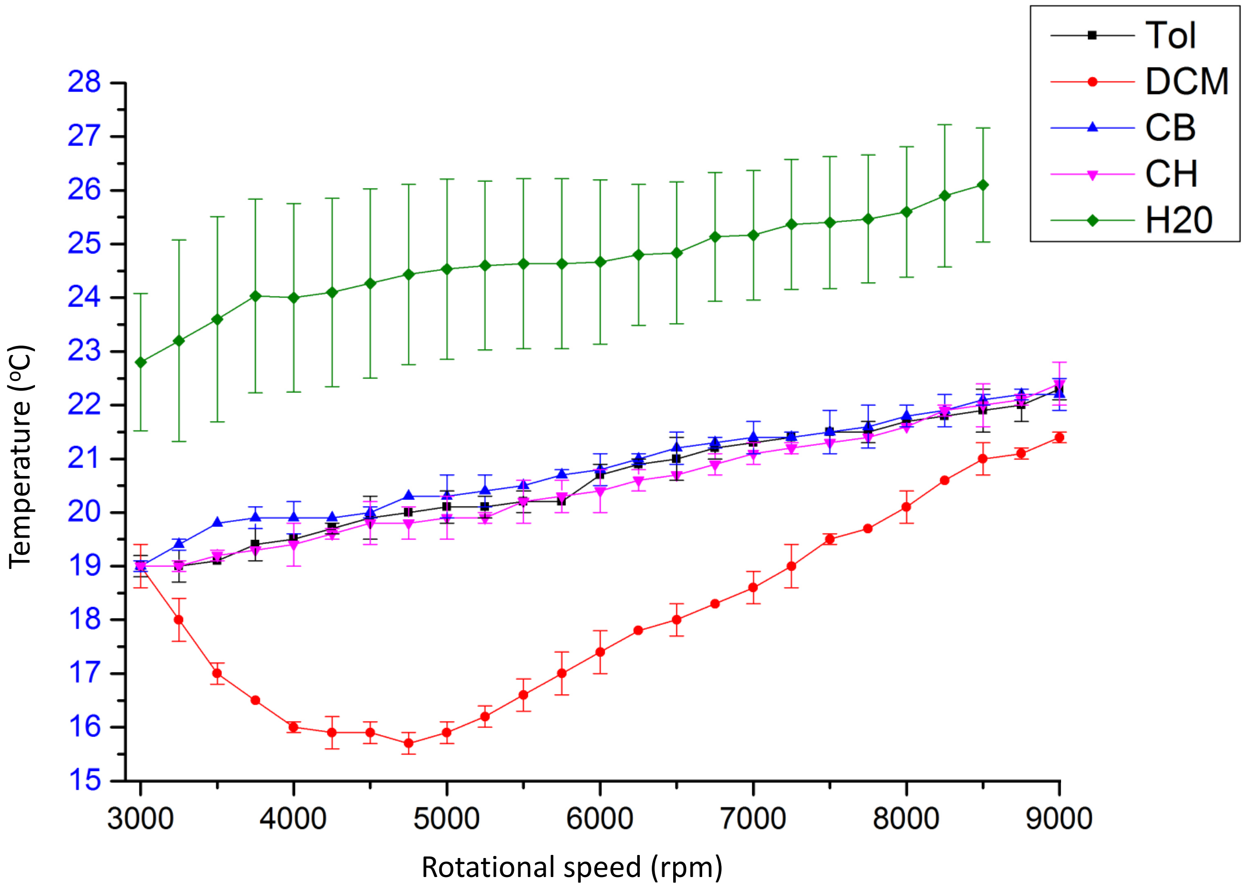

Figure 3.9 Thermal responses for various solvents.

(Tol: toluene, DCM; dichloromethane, CB: chlorobenzene, CH: cyclohexene) in a monophasic system in a flat base quartz tube (20 mm OD, 17.5 mm ID, 18.5 cm in length) as a function of ω at θ = 45°.

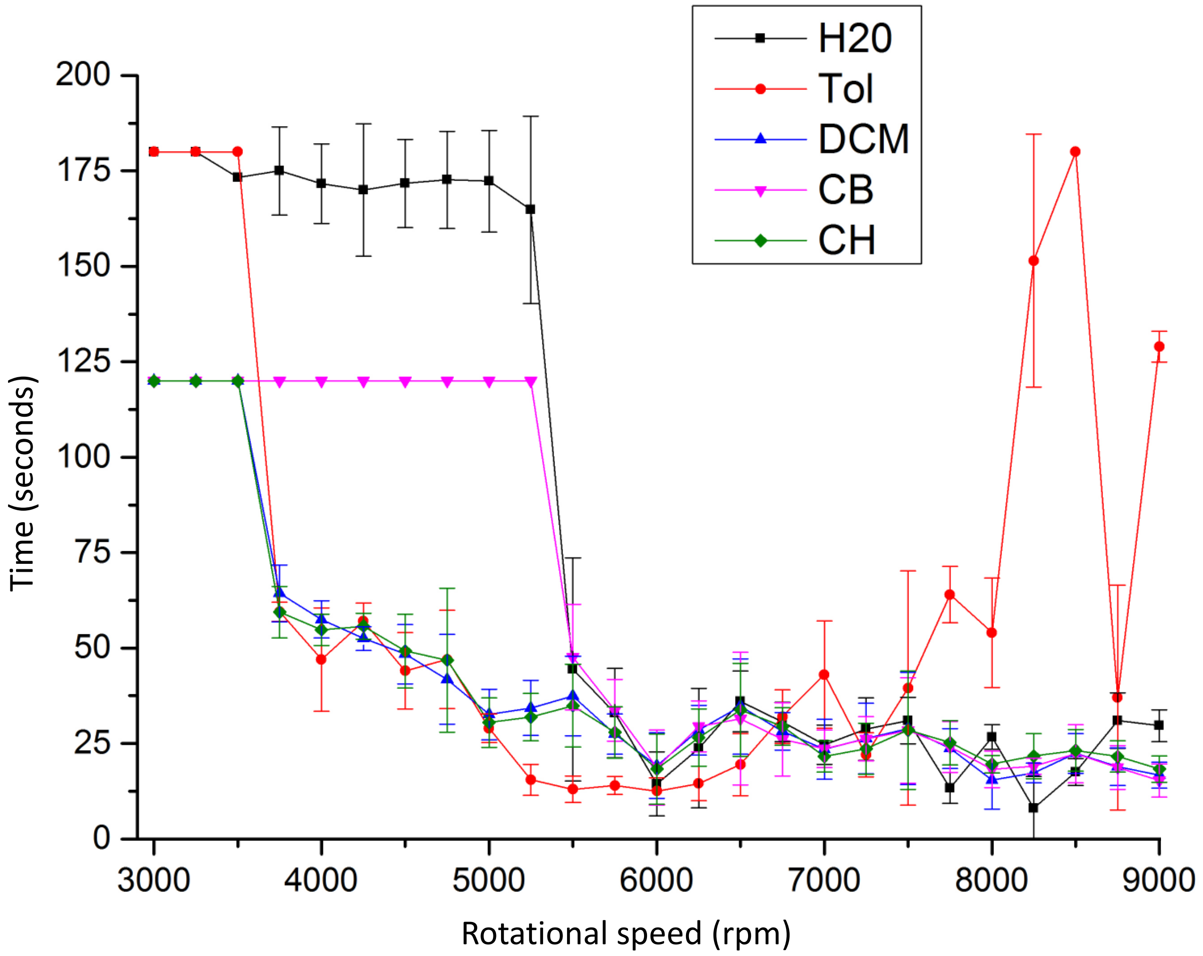

Figure 3.10 Mixing times for various solvents.

(Tol: toluene, DCM; dichloromethane, CB: chlorobenzene, CH: cyclohexene) in a monophasic system in a flat base quartz tube (20 mm OD, 17.5 mm ID, 18.5 cm in length) as a function of ω at θ = 45°.

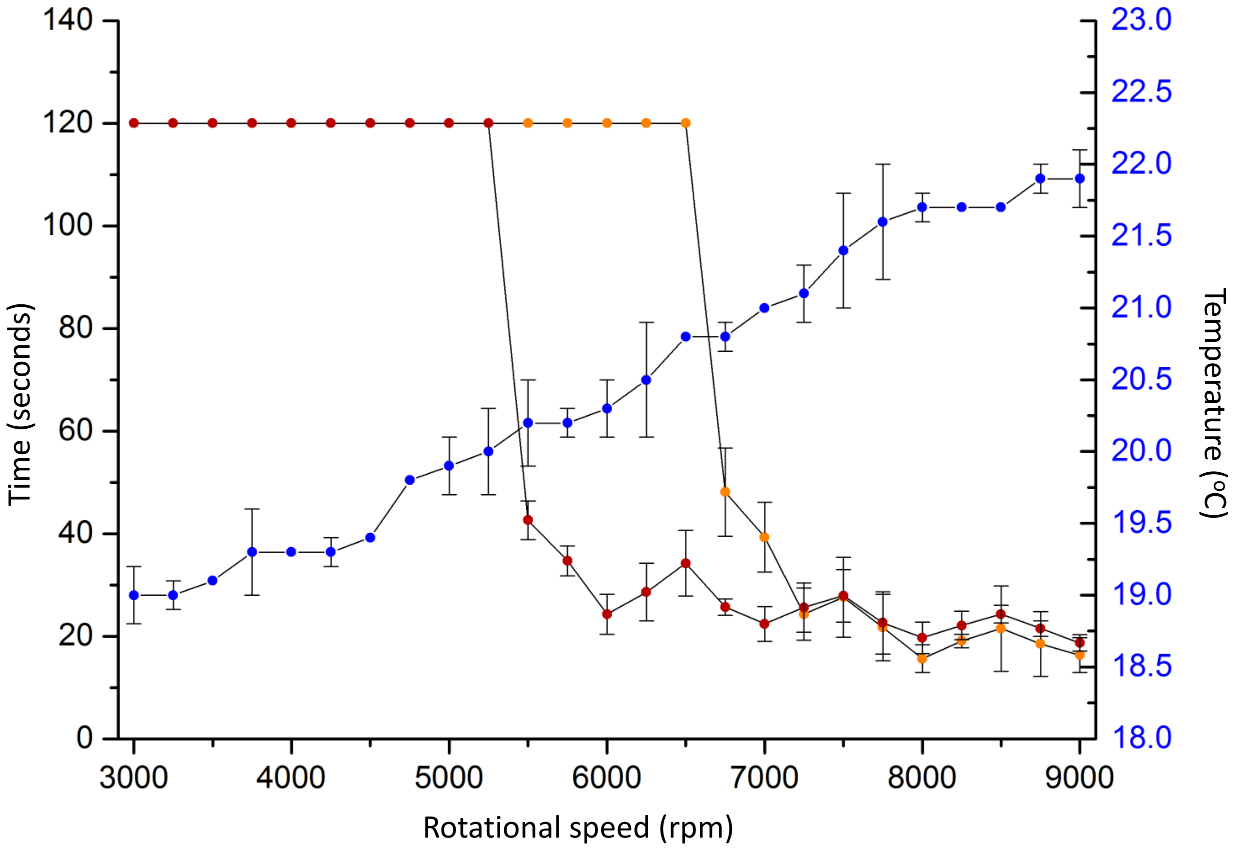

Figure 3.11 Signature of chlorobenzene and water.

Showing the mixing times of the aqueous phase (red), organic phase (orange) and the thermal response (blue) of a 1:1 mixture in a flat base quartz tube (20 mm OD, 17.5 mm ID, 18.5 cm in length) as a function of ω at θ = 45°.

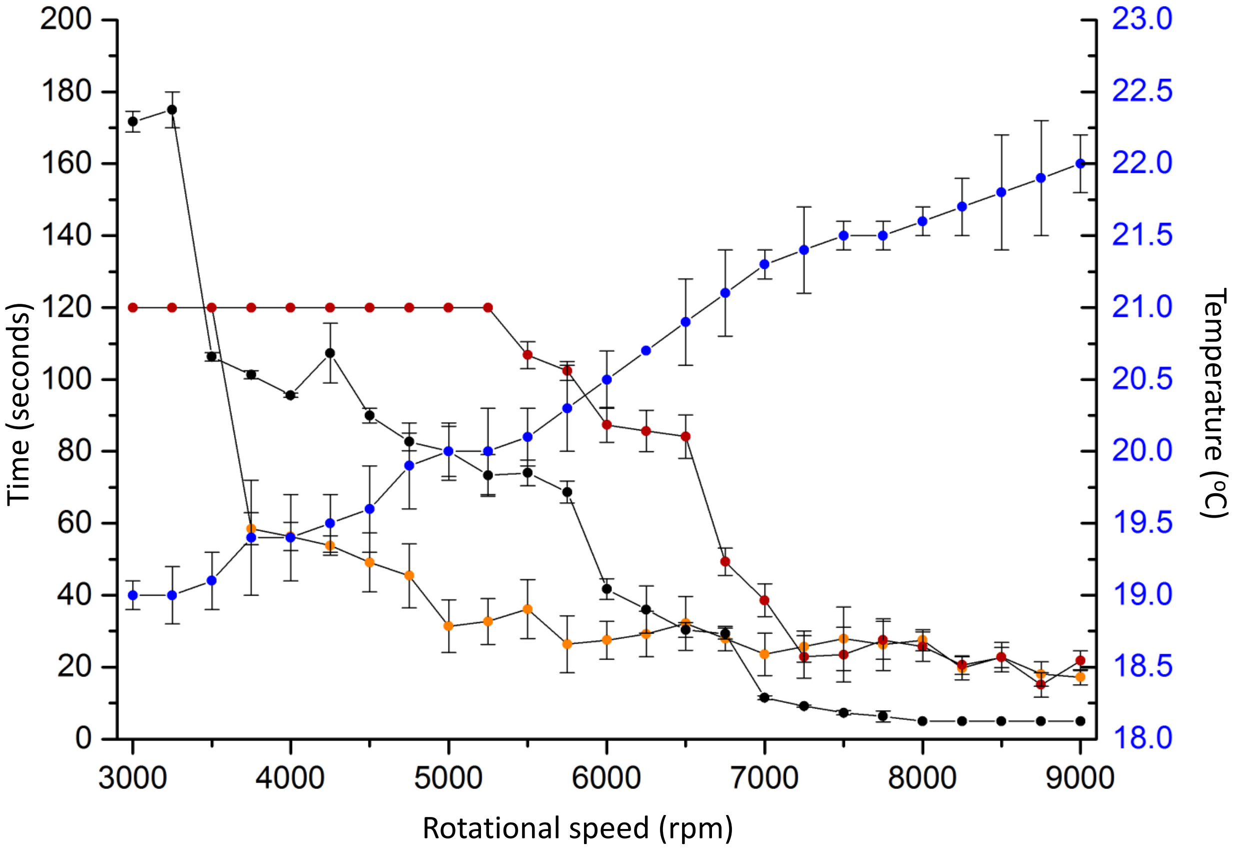

Figure 3.12 Signature of cyclohexene and water.

showing the mixing times of the aqueous phase (red), organic phase (orange) and the thermal response (blue) of a 1:1 mixture in a flat base quartz tube (20 mm OD, 17.5 mm ID, 18.5 cm in length) as a function of *ω* at *θ* = 45°.

Sonication of a mixture of water and toluene affords an emulsion, and in treating this emulsion in the VFD, rapid demixing occurs for rotational speeds ≥ 7000 rpm at *θ* 45°, Figure 3.13(a)–(c). Determining mixing times for a 1 : 1 mixture of phase separated toluene and water for the same mixture, using the same procedure as for individual phases in the VFD[11] in the standard hemispherical base tube, provided insight into the nature of the topological fluid flow, as did comparing the results for the two phases in a flat base tube, and where water is mixed with an immiscible liquid now of greater density, namely dichloromethane (DCM), Figure 3.13(g) and (h). For toluene and water the temperature change for increasing rotational speeds *ω* is uninformative, unlike for individual liquids themselves where sudden changes in temperature occur for changes in dominant topological fluid flows.[11] However, mixing behaviour provide topological fluid insights. This is highlighted by a drop of toluene added to the base of the tube containing some dye having similar mixing times in the toluene layer to that in the absence of a water layer below it.

But on close inspection, there is now a periodic step change in the mixing time for increasing rotational speeds, in intervals of 1000 rpm, between 4000 and 8000 rpm. These periodic changes are more pronounced than for toluene by itself and corelate with the thinning of the uniform film of toluene suddenly changing as the pitch (*P*) of the DH flow diminishes to a threshold whereby the film thickness cannot be maintained by the Faraday wave. Our previous study hypothesises that this periodic step change, observed with increasing rotational speed, is consistent with the sustained presence of DH flow.[11] However, as rotational speed increases, the *P* of the DH decreases, presumably to maintain the characteristic rotational *P* of the fluid flow. As the *P* continues to decrease, a threshold is eventually reached where the opposing upward and downward flow along the helix can no longer be sustained. At this point, the length scales of the Faraday wave and ST Coriolis flows become comparable, leading to a dynamic equilibrium that arises from the interplay of these two flow patterns. Beyond this threshold, further increases in rotational speed result in a thinner liquid, with the DH flow re-emerging with a larger *P*, ultimately dominating over the ST flow.[11]

The diameter of the DH flow then diminishes in forming a thinner film, initially with a larger *P*, with ω. *P* then the same across a 1000 rpm range, before the film thins again and so on. In addition, for toluene, the onset of ST flow is ~3000 rpm, with its presence persisting across the rotational landscape but with its diameter increasing for increasing ω, Figure 3.13(c). In contrast, mixing a drop of water with a dye into the water layer is distinctly different to that of water by itself, with mixing times dramatically decreasing at 5000 rpm (*cf.* 3000 rpm for water by itself)[11] with some changes closely matching Faraday wave driven reduction in film thickness, Figure 3.13(e). When considered collectively, the data is consistent with the onset of DH and ST topological fluid flows in water >5000 rpm, which is further supported by determining of the diameters of DH and ST. We note that the demixing time for an emulsion of toluene and water, discussed above, at 7000 rpm, coincides with where water and toluene have the same mixing times. This suggests that the DH flow is driving the demixing, where the distinction between DH flow in water and toluene is lost and where there is consequential high mass transfer, and this also coincides when the thickness of the film of water and toluene on the upper surface, becomes uniform along the tube. The change in demixing time with tilt angle, Figure 3.13(b), is also informative. Tilt angles ≤45° have low mixing times where DH flows are expected, whereas for θ >45° the mixing times dramatically increase as expected for diminishing Faraday wave effects in approaching θ = 90°.

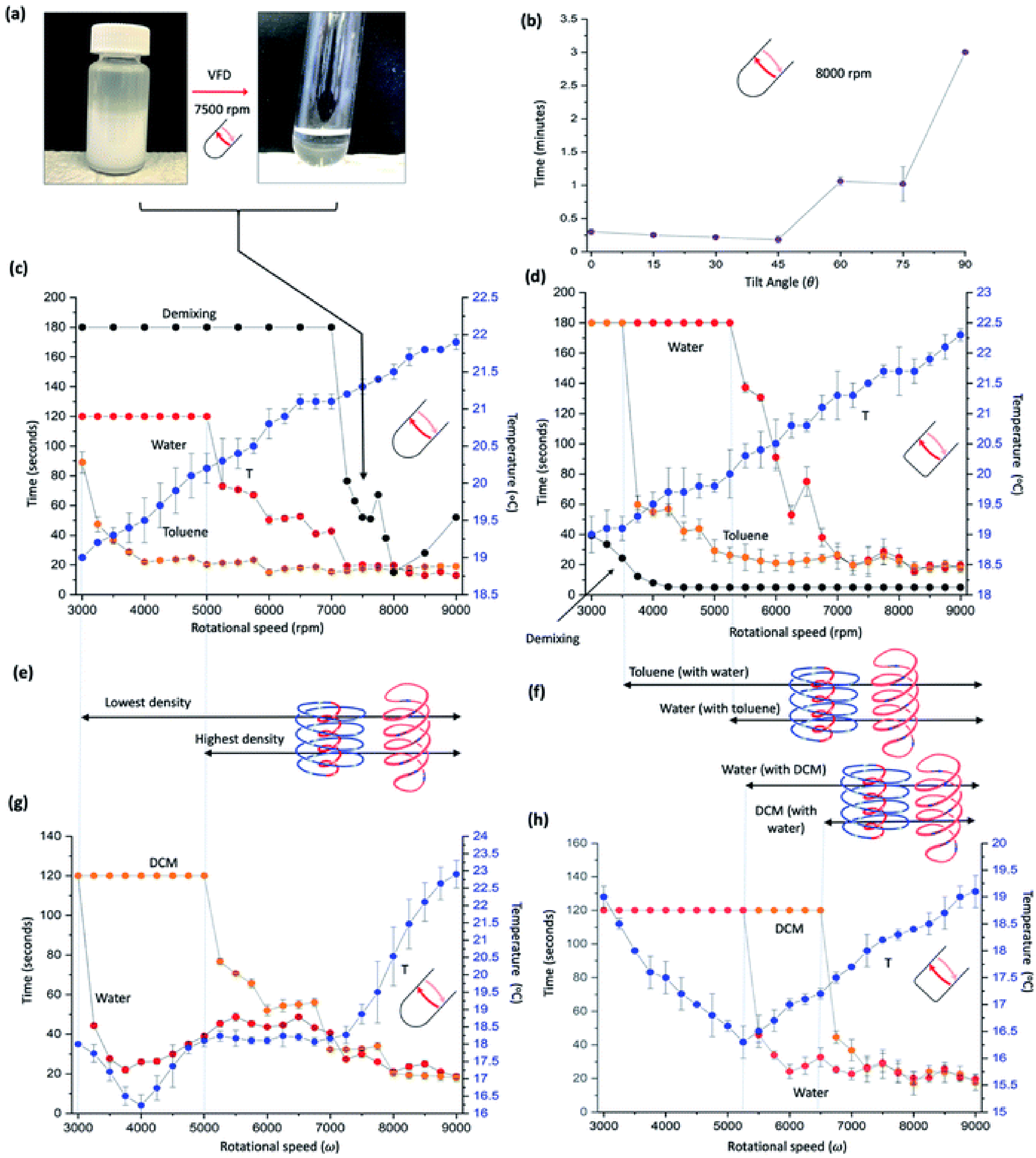

Figure 3.13 Mixing different immiscible systems.

(a) Photographs of emulsified toluene and water, and the demixed liquids post VFD processing at *ω* 7500 rpm, tilt angle 45°, in a quartz tube 20 mm OD, 17.5 mm ID, 18.5 cm in length. (b) Effect of tilt angle on demixing times of toluene and water (1 : 1) in a hemispherical base at *ω* 8000 rpm. (c) Thermal response and mixing times, *versus* *ω* for a 1 : 1 mixture of water and toluene in a hemispherical base tube. Mixing times (red and orange for water and toluene respectively) correspond to the time taken for a drop of water containing a small amount of dye added at the bottom of the tube rotating at a specific speed to uniformly mix in halfway up the preformed film, and similarly for toluene for a drop of toluene containing a small amount of dye. The temperature (blue) was measured midway along the tube using an IR camera, for residual water and toluene present in the tube, being equivalent to the continuous flow mode of operation of the VFD (water and toluene along the complete length of the tube). The demixing time (black) is the time taken for 2 mL of a preformed emulsion of toluene and water placed in the VFD to phase separate. (d) As for (c) for a 1 : 1 mixture of toluene and water using a ‘flat’ base VFD tube (20 mm OD, 17.5 mm ID, 18.5 cm in length) with a 2 mm radius of curvature where the base is fused to the side wall (*cf.* 8.75 mm radius of curvature for the hemispherical bas tube). (e) and (f) Designated dominant topological fluid flows in the two thin films in (c) and (d) respectively, for increasing *ω*, and linked to the thermal response and mixing times, *versus* *ω* for a 1 : 1 mixture of water and dichloromethane (DCM) in a hemispherical base tube (g) and a flat base tube (h), respectively. All data points in (b) and (c) and (g) and (h) measured in triplicates.

3.3.2.2 Equal Density Immiscible Liquids.

To investigate the effect of density on the processing of immiscible liquids in the VFD, H_2O, and chlorobenzene were spun at speeds between 3000-9000 rpm; the mass of the tube post-processing was recorded, and the volume of fluid remaining in the tube was calculated from this. calcium chloride was added to H2O, increasing its density to 1.11 g/mL, the density of chlorobenzene. To confirm the densities of H2O.CaCl2 and chlorobenzene were approximately equal when mixed solutions (Figure 3.14). Visual confirmation of density was repeated before each experimental run to ensure the densities were equal within experimental limits. To ensure the native film volume, in the absence of a second liquid, was known, the experiments were repeated for H2O alone, H2O.CaCl2 and chlorobenzene. All experiments were performed in triplicate and repeated with a second tube to determine the effect of the tube on the final volume. The experiments were repeated on a separate VFD to account for the effect of intermachine variability.

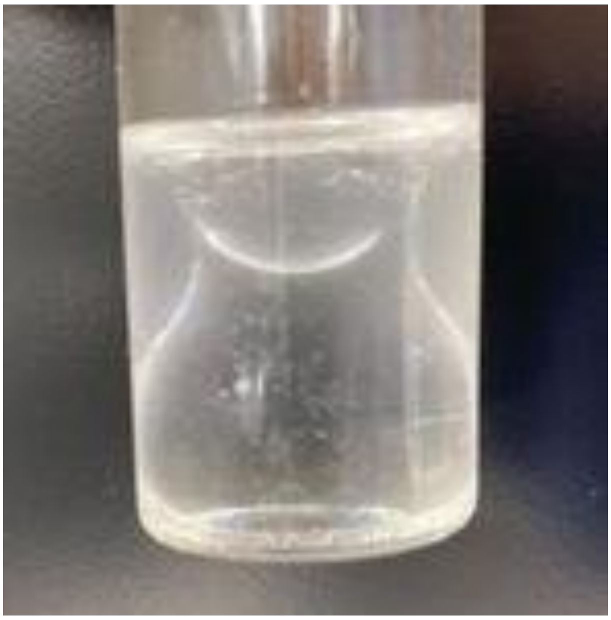

Figure 3.14 Layers of chlorobenzene and $H_2O.CaCl_2$ separated vertically.

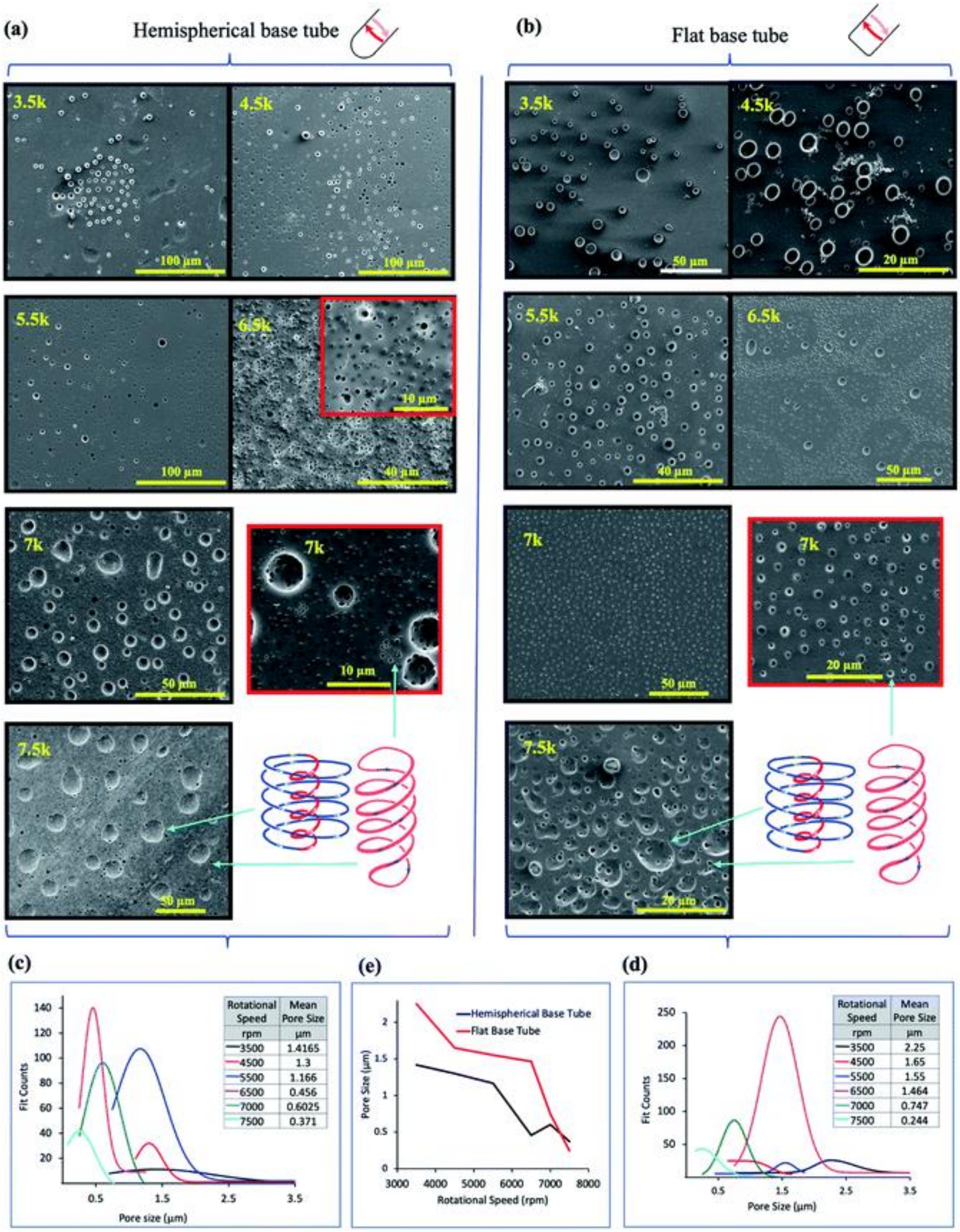

Rotational Speed rpm	Mean Pore Size µm
3500	1.4165
4500	1.3
5500	1.166
6500	0.456
7000	0.6025
7500	0.371

Rotational Speed rpm	Mean Pore Size µm
3500	2.25
4500	1.65
5500	1.55
6500	1.464
7000	0.747
7500	0.244

Figure 3.15 *In situ* moulding of topological fluid flow impacting on the surface of the tube.

(a) and (b) SEM images of the inner surface of polysulfone films (glass–polymer interface) peeled away from the surface of the tube after processing in the VFD in a 1 : 1 mixture of toluene and water, at 20 °C, $\theta = 45°$, at the rotational speeds specified, using the confined mode processing for 30 minutes, for the hemispherical and flat base tubes, respectively. For each experiment, a film of polysulfone was generated in the VFD *ca* 20 µm thick (as established using SEM of the liquid nitrogen fractured polysulfone thin films) *via* evaporation of a methylene chloride solution of the polymer (100 mg mL^{-1}) in the VFD tube rotating at 6000 rpm and tilted at θ 5°.[11] For the subsequent biphasic processing at θ 45°, the volume of the liquid in the tube was adjusted to ensure the thin film of liquid extended to the top of the tube, and after processing the liquid was removed and the film washed with hexane prior to peeling way form the surface of the tube. (c) and (d) Pore size distribution of the holes formed on the underneath surface of the film at the different rotational speeds in the hemispherical and flat base tubes respectively. (e) Plot of the mean pore size (excluding the large craters) *versus* rotational speed for both types of tube (20 mm OD, 17.5 mm ID, 18.5 cm in length).

For a mixture of DCM and water, mixing of water with a drop of water containing a dye into the water layer behaves as if the denser DCM liquid was absent,[11] and the DCM behaves like water when pinned centrifugally against the surface of the tube by the toluene, Figure 3.13(g). These findings are consistent with the onset of the different topological flows in the same way, Figure 3.13(e), as for a mixture of toluene and water. Water and DCM do not form a stable emulsion, unlike water and toluene, and thus demixing experiments for this immiscible mixture was not possible. However, a mixture of chlorobenzene and water form an emulsion where the density of the organic phase is also greater than that of water, with demixing behaviour and mixing times similar to that of toluene and water. A mixture of cyclohexene and water also underwent rapid demixing, where water is now denser than that of the organic phase. Temperature changes for a DCM and water mixture show a drop in temperature at 4000 rpm which is close to where the ST flow in water dominates the shear stress fluid flow (~3750 rpm), with onset of DH, as evidenced by a slight increase in mixing time in water beyond this speed, *i.e.*, where the ST flow clashes with DH flow and *vice versa*, in slowing the mixing along the tube.

We have also changed the base of the quartz tube to a flat base, albeit with a 2 mm radius of curvature necessary to fuse the side walls of the tube to the base, with the results presented in Figure 3.13(d), (f), (h). This base perturbs the mixing time for both toluene and water, with a dramatic reduction in the demixing rotational speed, from ~7000 rpm for the hemispherical base tube to ~3500 rpm. This is consistent with DH flow being common for both phases, where the distinction between the two phases is lost, and where there is high mass transfer between the two phases, in accelerating the demixing. As for the two immiscible systems in the hemispherical base tube, temperature changes are uninformative for water and toluene. However, for a mixture of DCM and water there is a dramatic reduction in temperature at ~5250 rpm which coincides with the onset of ST and DH topological flows from the Coriolis force for the now 2 mm radius curvature of the base of the tube, *cf.* 8.75 mm radius of curvature for the hemispherical base tube. The significant reduction in temperature arises from latent heat of evaporation of highly volatile DCM (b.p. 39.6 °C), where the topological fluid flows in the water phase are breaking through the DCM phase, with the DCM evaporating at the air–liquid interface. The onset of the different topological fluid flows can be deduced from the changes in mixing times for the water/toluene and DCM/water mixtures in the VFD, Figure 3.13(f). For water with DCM, the water behaves as if it was the sole liquid in the tube,[11] whereas the behaviour of toluene by itself is distinctly different >6000 rpm relative to a mixture of toluene with water, with the mixing time fluctuating, and increasing dramatically above 8000 rpm. An increase in mixing time can arise from a reduction in the effect of the ST flow as the liquid is pushed up tube. Essentially removing this in the presence of water, Figure 3.13(d), can arise by the water cushioning the effect of distortions in the glass tube.

The rapid demixing of an emulsion of toluene and water at much lower speed in the flat base tube, 3000 rpm (*versus* 7000 rpm in the hemispherical base tube), is noteworthy and for this a different process occurs whereby the small radius of curvature, ~2 mm, creates a different type of high shear topological fluid flow. We also studied the effect of having two immiscible liquids that are close in density, utilising a mixture of chlorobenzene with water containing calcium chloride to increase the density near that of the organic solvent. As the density of water approached that of chlorobenzene there was no significant change to the final volume in the tube, *i.e.*, the two liquids are volume additive in the tube. However, this system is difficult to control due to the high vapour pressure and rapid evaporation changing the density of the phases in localised regions.

3.3.3 *In situ* Moulding of Topological Fluid Flow Impacting on the Surface of the Tube

The dimensionality and spatial arrangement of the topological fluid flows in a biphasic mixture of water and toluene as a 1 : 1 mixture has been established by 'molecular drilling' on a thin layer of polysulfone ~20 mm thick fabricated on the inner surface of the quartz tube by evaporation of a DCM solution of the polymer for the tube rotating at 6000 rpm and tilted at 5° to ensure uniformity of the layer along the length of the tube, where the VFD is effectively operating as a rotary evaporator. Holes and craters are evident only on the inner surface of the polymer layer (sitting over the quartz tube), after carefully peeling it away for scanning electron microscopy (SEM) studies, Figure 3.15. In comparing the mixed solution with the outcome of treating polysulfone film solely with toluene, we note that for toluene by itself in the VFD, the holes drilled into the film are also on the inner surface of the film, with some solubility of the polymer in toluene effectively smoothing out the polymer film at the interface with toluene.[11] In addition, for water only in the VFD, no molecular drilling is evident with a smooth upper and lower surface of the polymer layer unperturbed, establishing the importance of some solubility of the polymer being required to mould (*via* drilling) the shape of the topological fluid flow. For a mixture of water and toluene, where the water is centrifugally held on the surface of the tube, with water being denser than toluene, holes and craters are also formed on the inner surface of the film, Figure 3.15, for both the hemispherical and flat base tubes. Their presence indicates that mass transport of toluene occurs and is thought to occur *via* Faraday wave vertical motion toward the surface. Toluene molecules are forced onto the surface of the polymer, such that both the DH and ST topological flows in toluene strike the quartz surface. Unlike for toluene alone in the VFD, holes (but not the craters) are often evident on the surface of the polymer in contact with the liquids, which establishes that the water primarily covering this surface is protecting the polymer from being dissolved and recycled under the influence of the high shear topological fluid flows. The much smaller diameter of the holes *versus* the craters, effectively protects them from being smoothed over in the presence of toluene contacting the surface. Also noteworthy is that the dissolution of the polymer associated with ‘drilling’ is reflected in crystallisation of small particles of the polymer, indeed with some of them having holes drilled through them.

SEM images for the polysulfone films following processing in a 1 : 1 mixture of toluene and water show a clear trend of increasing diameter of the ST flow for increasing ω, whereas the diameters become smaller for the DH flows, Figure 3.15(a) and (b), in the hemispherical and flat base tubes, respectively. Unlike for toluene by itself in the VFD,[11] there are no ordered arrays of the holes running parallel to the rotational axis of the tube; the ordered arrays correspond to the time domain arrangement of DH flows. The absence of such arrays in the biphasic mixture is consistent with the layer of toluene moving relative to the layer of water, as for vertically aligned layers of immiscible liquids of different densities in a spinning disc.[12] This also supports the water layer effectively eliminating effects of defects in the quartz tube (see above). Analysis of the size of the holes drilled (pores) into the polymer films is shown in Figure 3.15(c) and (d) for hemispherical and flat base tubes, respectively, with a comparison of the average pore size in Figure 3.15(e). For the hemispherical base tube, the distinction between the diameter of the holes arising from ST and DH flows is clearly defined at high rotational speeds, 7000 and 7500 rpm, at ~0.6 mm, and ~0.37 mm, respectively, with the diameters of ST and DH similar at lowers speeds, where there is the formation of spherical or spicular flow.[11] For the flat base tube, the distinction between the ST and DH occurs at a lower speed, 6500 rpm, where they are ~1.46 mm in mean diameter, but this is lost at 7000 rpm, then re-emerging at 7500 rpm where they are ~0.75 to 0.35 mm in mean diameter. At this rotational speed the diameter of the holes is on average smaller than that for the hemispherical base tube. As to the DH generated holes, the mean diameters for both the hemispherical and flat base tubes become progressively smaller for increasing ω, but with those for the latter being significantly higher until 7000 rpm where they become similar, ~0.6 and 0.75 mm for the hemispherical and flat based tubes respectively. The similarity is consistent with the DH flow being the dominant focused high shear in the VFD, *i.e.*, where the Faraday waves dominate the shear stress. The reason for the lack of clearly defined holes for ST flow in the flat base tube at 7000 rpm, is likely due to the diameter of the ST and DH being the same, *i.e.*, where spicular flow prevails.[11] This is at much higher ω than that for the hemispherical base tube, which appears to be at ~4500 rpm, and the difference between them of ~2500 rpm reflects the difference in curvature at the base of the tube generating the ST. This aside, the diameters of the DH flows which incorporate the same Coriolis forces associated with curvature along the tube are not overly different. Overall, the drilling experiments provide insight into the ω dependent dominance of ST *versus* DH flows with the drilling into the polymer film arising from the mechanical energy which is reflected in high temperature heating zones presented on the surface of the tube.[11]

3.3.3.1 Molecular Drilling in Polysulfone (PSF)

To generate a uniform thin film adhering to the inner surface of the VFD tube, 1.4 mL of 100 mg/mL of PSF dissolved in dichloromethane (DCM), which involved adding a solution of the polymer to a

VFD tube (20 mm OD, 17.5 mm ID) with the operational condition mentioned in earlier research, tube tilted at 5° which was then spun at 6000 rpm for ~15 min. The thin film formed due to the facilitated evaporation caused by high mass and heat transfer in the open-end tube, followed by washing with hexane and drying under a flow of dry nitrogen. Three different samples were taken from the peeled-off polymeric thin film from the tube. Sections of the film were then peeled from the surface of the tube at three different locations. The thin film created in the VFD was relatively uniform, smooth, and without any structure variation.

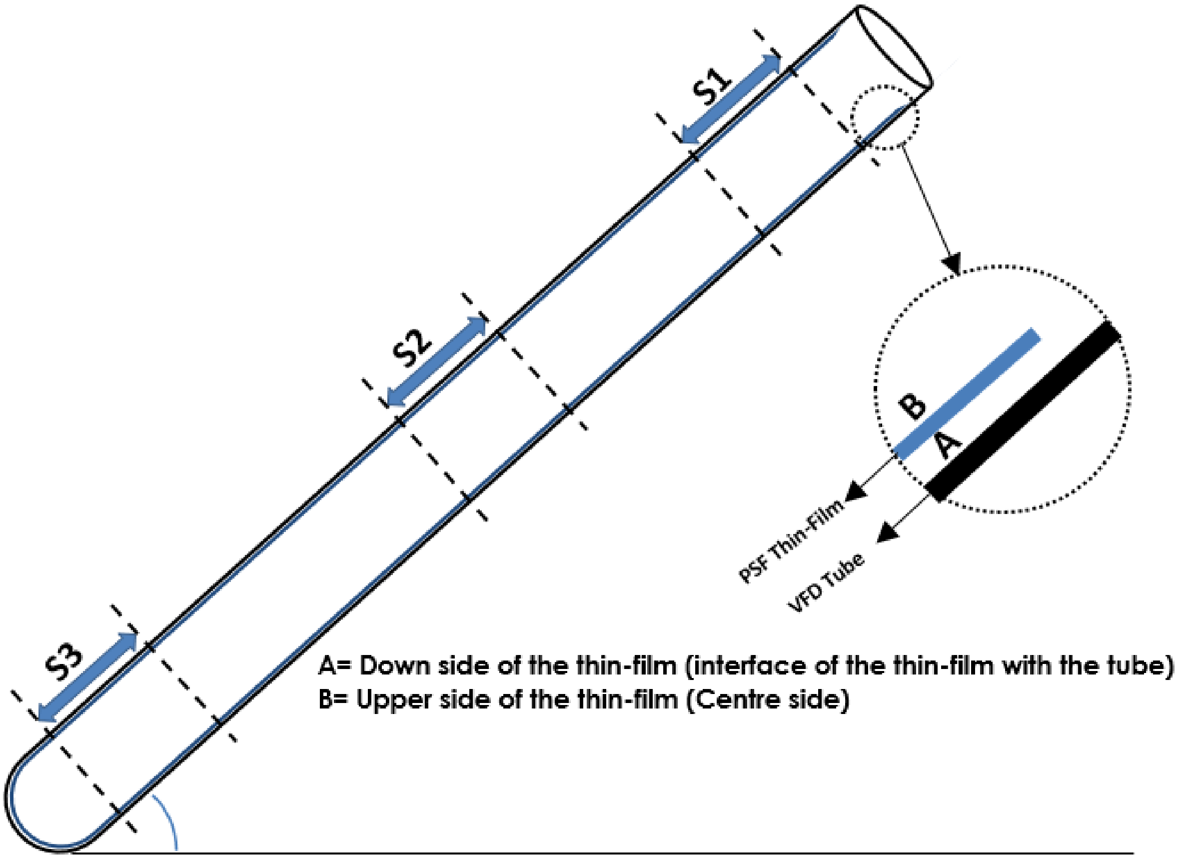

Figure 3.16 PSF thin film formation.

Locations of samples S1, S2, and S3 taken from the PSF thin film formed in the VFD; samples S1A and S1B refer to the interface of the film with the tube and air from the bottom of the tube respectively, and similarly S2A and S2B, and S3A and S3B, from the middle and top of the tube1.

Previously, we investigated the fluid flow in the monophasic system (mainly toluene) in a hemispherical base tube, with the fluid flow investigated herein in a biphasic system (1:1 toluene and water) in both hemispherical and flat base tubes. To do this, two sets of experiments were conducted in the VFD using toluene and water (1:1), which were added to the polymeric-coated VFD. VFD processing of the thin film was conducted in the tube at operational conditions mentioned in Table 3.17. The polymer is only sparingly soluble in toluene, and in each experiment, the tube was rotated at different rotational speeds, rpm at θ = 45°, at room temperature, for 30 minutes. After processing, the liquid was drained, and the film was washed with hexane several times and purged with nitrogen gas for drying purposes for 2h.

Three samples of every processed thin film were removed from each tube and studied using SEM, Figure 3.15. The results revealed arrays of indentations and some holes on the polymer – tube interfaces which have been introduced in our earlier research as molecular drilling occurred due to the double helical flow in the VFD1. SEM imaging the other side of the PSF film (side B) post-VFD processing using the same conditions also showed some molecular drilled holes which was absent in earlier research in monophasic. This could be related to the effect of water which is a non-solvent for the drilled polymer and would prevent smoothing the holes which were drilled by toluene. The experiments were conducted in different rotational speeds (ω 3.5k, 4.5k, 5.5k, 6.5k, 7k, 7.5k rpm) in both hemispherical and flat base tubes. Given the structures revealed on surface SA for biphasic (toluene and water), all subsequent processing was done in toluene and water followed by washing with hexane.

3.3.4 Liquid-Liquid Interfacial High Mass Transport

Dynamic light scattering (DLS) for processing at 3000, 5250 and 7500 rpm in a 1 : 1 mixture of toluene and water in the hemispherical base tube established the presence of nano-particulates in both phases immediately post VFD processing (~5 min) and 24 hours later the particles present are smaller, Figure 3.17(a) and (b), respectively. These nanoparticles are comprised exclusively of just water and/or toluene. For the water phase, the change in diameter of the particles observed is from ~70 to 30 nm, ~125 to 30 nm, and ~1 μm to 20 nm, at 3000, 5250 and 75 000 rpm, respectively, with the corresponding changes in the toluene phase at ~120 to 12 nm, ~125 to 8 nm and ~80 to 2 nm respectively. High mass transfer between the two phases is therefore prevalent in the VFD at 45° tilt angle, with the biggest particles formed in water at 7500 rpm, which corresponds to the rotational speed where emulsions of the two phases rapidly demix, and where the evidence supports that the DH flow is common to both phases, as detailed above. In contrast, DLS data for the water phase processed in the flat base tube reveal that they all have particles close to 80 nm in diameter immediately following VFD processing. They change to ~300 nm after 24 hours processing at 3000 rpm, and for the other two speeds, the particles are essentially unchanged over the same period. This is consistent with the uniqueness of the fluid flow at *ω* 7500 rpm in the hemispherical base tube. For the toluene phase in the flat base tube, the initially formed particles formed at *ω* 3000 and 5250 rpm are ~8 and 1 μm respectively, changing now to larger particles after 24 hours, to ~50 and 9 μm, whereas for *ω* 7500 rpm the particles are unchanged at ~150 nm. The size of the nanoparticles comprised of one or two phases in one phase and *vice versa* depends on the shape of the base of the tube, and thus where different topological fluid flows with different shear stress are generated.

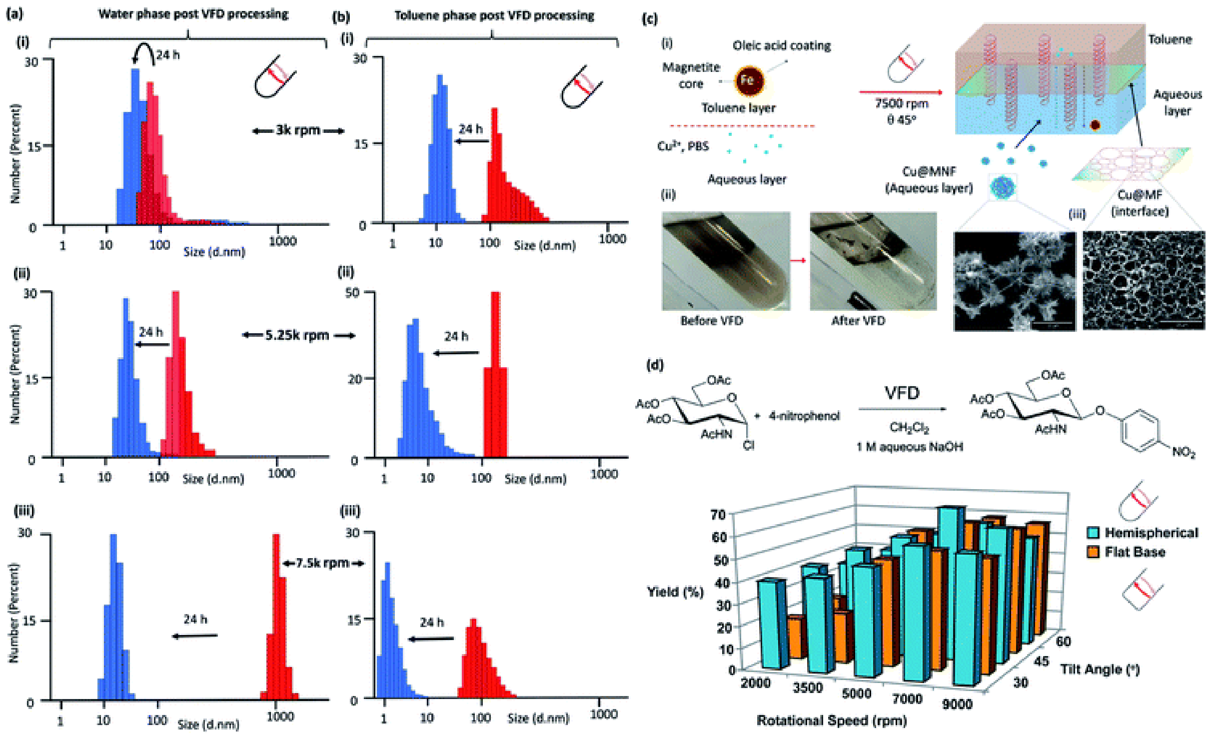

Figure 3.17 Liquid-liquid interfacial high mass transport.

Dynamic light scattering (DLS) of the water phase immediately (red) after processing in confined mode in the vortex fluidic device with a 1 : 1 mixture of toluene for 15 minutes at rotational speeds, ω, (i) 3000 rpm, (ii) 5250 rpm and (iii) 7500 rpm, tilt inclination of θ +45° and 24 hours later (blue). (b) DLS of the toluene phase immediately (red) after processing in confined mode in the vortex fluidic device with a 1 : 1 mixture of water for 15 minutes at rotational speeds, ω, (i) 3000 rpm, (ii) 5250 rpm and (iii) 7500 rpm, tilt inclination of θ, +45° and 24 hours later (blue). (c) Fabrication of $Cu_3(PO_4)_2$@Magnetite thin film (Cu@MF) and $Cu_3(PO_4)_2$@Magnetite nanoflower (Cu@MNF) in a biphasic system of toluene and phosphate buffer saline (PBS) in a 20 mm OD, 17.5 mm ID quartz tube, 39 cm long with a hemispherical base. (i) Schematic of the formation of Cu@M composites in a VFD; oleic acid coated magnetite nanoparticles were dispersed in the toluene phase at 0.2 mg mL^{-1} with all experiments conducted using 5 mL toluene and 5 mL PBS (10 mM). The biphasic system was briefly sonicated followed by quick addition of 536 µL $CuSO_4$ with then immediate VFD processing at 7500 rpm for 30 min. Cu@MF was observed at the toluene/interface whereas Cu@MNF was observed in the PBS phase, (ii), as shown in the SEM, (c). (d) Reaction of 2-acetamido-3,4,6-tri-*O*-acetyl-α-D-glucopyranosyl chloride with 4-nitrophenol in the presence of aqueous sodium hydroxide solution and dichloromethane, in the absence of a phase transfer catalyst, with the yield of the product plotted as a function of tilt angle θ and rotational speed of a quartz tube (20 mm OD, 17.5 mm ID quartz tube, 18.5 cm long) with either a hemispherical or flat base.

3.3.4.1 Interfacial Self-Assembly of Nanoparticles

Oleic acid coated magnetite nanoparticles were prepared by chemical co-precipitation. Briefly, 2.7 g FeCl3·6H2O and 1 g FeCl2·4H2O were dissolved in 100 mL MilliQ under a flow of N2. The solution was stirred and heated to 80°C. A total of 43 mL NaOH (1 M) was added with a final pH of 12.1. 6.3 mL of oleic acid was then added, and the mixture was maintained at 80°C for another 60 min. The mixture was cooled to room temperature naturally and the black product was collected using a magnet and thoroughly washed with ethanol and MilliQ water to remove excess non-reactants and freeze-dried. The biphasic experiments were conducted in either VFD with hemisperical based tube (20 mm OD, 17.5 mm ID, length 19.3 cm), flat based tube (20 mm OD, 17 mm ID length 19 cm) or long hemispherical based tube (20 mm OD, 17.1 mm ID, length 39 cm). The control experiment without using VFD was carried out in a benchtop vortex. Optimal condition for interface Cu3(PO4)2@Magnetite film generation is by adding 5 mL toluene (with oleic acid coated magnetite nanoparticles at 0.2 mg/mL) to 5 mL PBS (10 mM) followed by brief bath sonication, quick addition of 536 µL CuSO4 and immediate VFD processing at 7500 rpm for 30 min or benchtop vortexing for 30 min.

Post-VFD processing, toluene and PBS were spontaneously demixed where a thin film named Cu3(PO4)2@Magnetite film or Cu@MF was observed in the interface and Cu3(PO4)2@Magnetite nanoflower or Cu@MNF in the PBS phase (Figure 3.17). In comparison, flat-based VFD tube or benchtop vortex was unable to generate Cu@MF from the interface (Figure 3.18b, d). The morphology of the Cu@MF could be varied by changing the volume of starting material. When increasing the volume mixture from 3 to 10 mL, the Cu@MF became less dense and ended up being spider-web-like (Figure 3.18a,c). Magnetite dispersed in the toluene phase was trapped through the van der Waals interaction-induced physisorption into the Cu3(PO4)2 petal sites and finally became stabilised in the PBS phase. To prove this, elemental EDX maps on O, Fe and Cu overlap over both structures which was further confirmed by FTIR and XRD. FT-IR analysis on Cu@MNF reveals peaks at 1044 and 990 cm-1 corresponding to phosphate P-O vibrations1 and 2977 and 2894 cm-1 corresponding to C-H vibrations and the peak at 1254 cm-1 to the C-O vibration.2 XRD patterns show that the Cu@MNF fit well with magnetite and Cu3(PO4)2 from the database (Figure 3.19c).

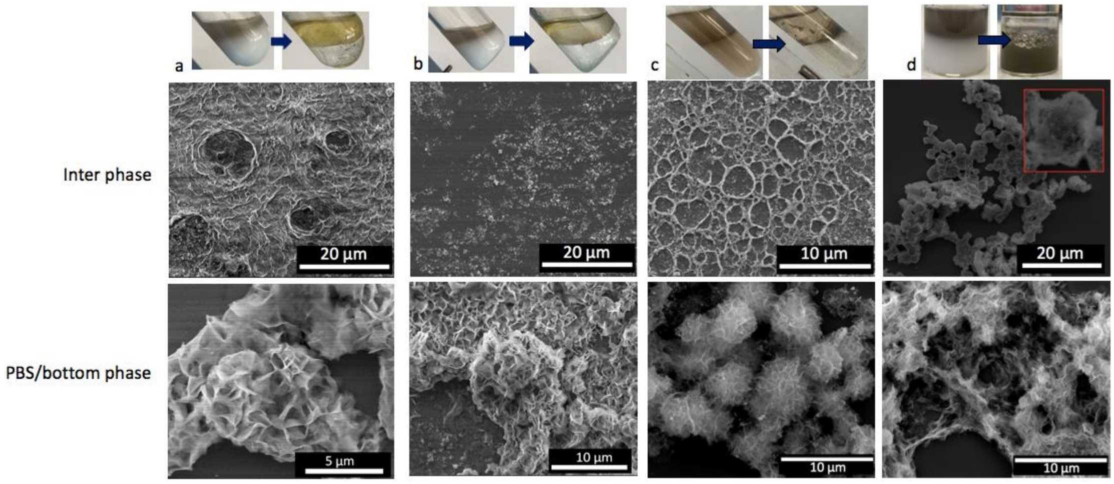

Figure 3.18 Fabrication of Cu@MF and Cu@MNF.

Fabrication of Cu3(PO4)2@Magnetite thin film (Cu@MF) and Cu3(PO4)2@Magnetite nanoflower (Cu@MNF) in a biphasic system of toluene and phosphate buffer saline (PBS) using different VFD tubes (a) hemispherical-based VFD tube (20 mm o.d., 17.5mm i.d., length 19.3 cm) with 3 mL biphasic mixture and 160.8 µL CuSO4 processed at 7500 rpm for 30 min (b) flat-based VFD tube with 3 mL (20 mm o.d., 17 mm i.d., length 19 cm) biphasic mixture and 160.8 µL CuSO4 processed at 7500 rpm for 30 min (c) long hemispherical-based VFD tube (20 mm o.d. 17.1 mm i.d., length 39 cm) with 10 mL biphasic mixture and 536 µL CuSO4 processed at 7500 rpm for 30 min (d) benchtop vortexing with 10 mL biphasic mixture and 536 µL CuSO4 for 30 min. The biphasic system was briefly sonicated followed by quick addition of CuSO4 and immediate processing as described. SEM showed a typical structure obtained from the interface or the PBS/bottom phase. Photos indicated pre and post-processing of the biphasic system using each method.

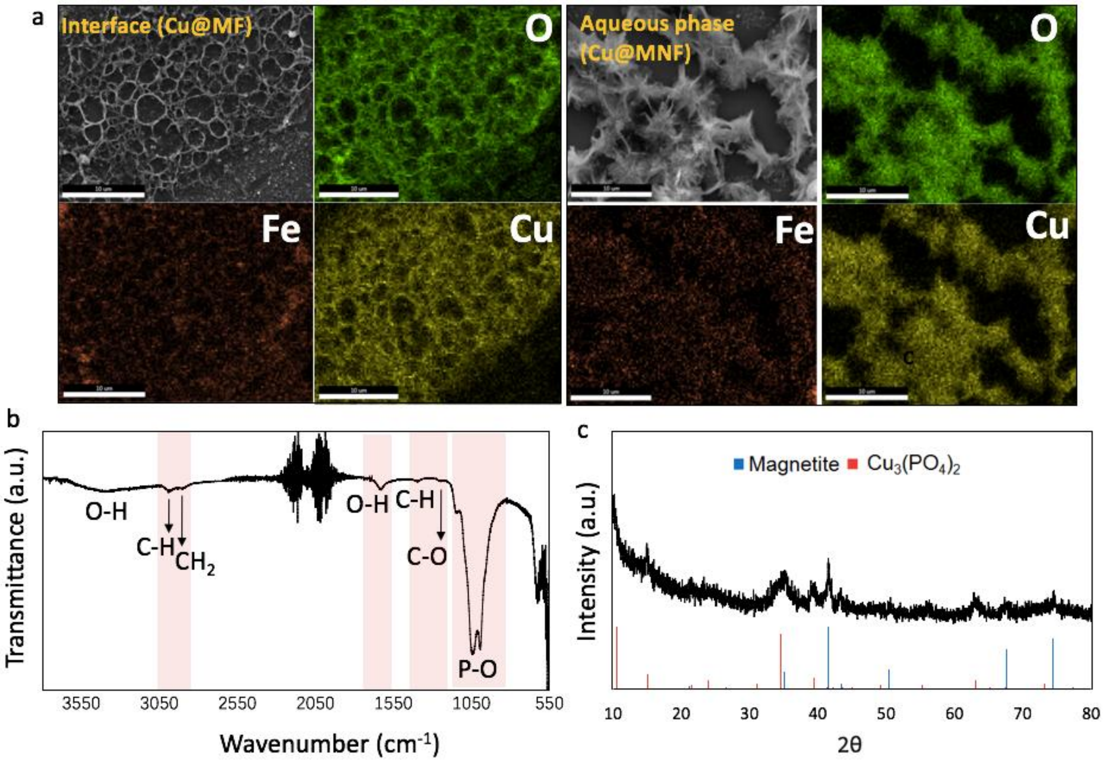

Figure 3.19 SEM/EDX of the Cu@MF and Cu@MNF.

SEM/EDX of the Cu@MF and Cu@MNF by using long hemispherical-based VFD tube with elemental mapping images for O, Fe and Cu, respectively. (b) FT-IR spectra of the Cu@MNF. (c) XRD patterns of Cu@MNF.

The impact of DH flow generated at 7500 rpm at the interface of a 1 : 1 mixture of an aqueous phase and toluene was explored using the self-assembly of inorganic nanoparticles. Here the aqueous phase was phosphate buffer saline or PBS with Cu^{2+} and toluene phase was a colloidal suspension of oleic acid coated magnetite nanoparticles, processed at ω 7500 rpm (θ 45°), Figure 3.17(c) and (i). VFD processing resulted in phase demixing, Figure 3.17(c) and (ii), with a film of $Cu_3(PO_4)_2$@Magnetite (Cu@MF) formed at the interface of the two liquids showing a pattern of holes ~2 to 4 μm in diameter which is the dimensionality for DH flow, *i.e.*, the holes represent a region where the DH was common to both phases at the liquid–liquid interface, with the assembled material representing a mould of the outer peripheral as such in the plane parallel to the surface of the tube, with nanoflowers of $Cu_3(PO_4)_2$@Magnetite (Cu@MNF) formed in the PBS phase, Figure 3.17(c) and (iii). In comparison, benchtop vortexing of the same mixture did not generate a layer of $Cu_3(PO_4)_2$@Magnetite, and the flat base tube did not form a structured interface. The latter is understood by the smaller dimensionality of the ST being similar to that of the DH flow, disrupting the self-assembly for the DH flow at the interface. Both Cu@MF and Cu@MNF formed as a result of induced mass transfer of oleic acid coated magnetite striking the phase boundary driven by the DH flow in the VFD. Magnetite particles dispersed in the toluene phase were trapped through the van der Waals interaction-induced physisorption into the $Cu_3(PO_4)_2$ petal sites[30] and finally became stabilised in the PBS phase. To prove this, elemental EDX maps on O, Fe, and Cu overlap over both structures, which was further confirmed by FTIR and XRD. FTIR analysis on Cu@MF revealed peaks at 1044 and 990 cm^{-1} corresponding to phosphate P–O vibrations[31] and 2977 and 2894 cm^{-1} corresponding to C–H vibrations, and the peak at 1254 cm^{-1} to the C–O vibration.[32] XRD patterns show that the Cu@MNF fits well with well-known magnetite and $Cu_3(PO_4)_2$ crystallinities from the crystallography database (00-001-0054) and magnetite (00-001-1111). This displays the distinctive properties and characteristics that the copper complexes synthesized using the VFD exhibit beyond morphological changes.

The effect of the choice of *w* and shape of the base of the tube on reactions that would otherwise require a phase transfer catalyst were also studied, along with the effect of changing the tilt angle of the tubes, 15° either side of that optimal 45° for applications in the hemispherical base tube was studied, Figure 3.17(d). This was for the reaction of 2-acetamido-3,4,6-tri-*O*-acetyl-α-D-glucopyranosyl chloride in dichloromethane with sodium 4-nitrophenoxide generated *in situ* in water from 4-nitrophenol and sodium hydroxide solution, as an immiscible two-phase system in a 1 : 1 ratio with the denser DCM centrifugally held on the surface of the quartz tube with water above extending to the air–liquid interface. This reaction was studied in the absence of a phase transfer catalyst in the hemispherical base tube, and for comparison the flat base tube, Figure 3.17(d). The hemispherical base tube has the highest yield at ω 7000 rpm for a 45° tilt angle, with yields for the flat base tube being significantly less although it is nevertheless optimal at θ 45°. We note that ω 7000 rpm for the hemispherical base tube corresponds to the speed where the mixing times for water and DCM become the same for increasing ω, such that the signature of the mixture, matches the expected optimal rotational speed. The finding is also consistent with ω 7000 rpm corresponding to the commonality of the expected DH flow at the interface of the two liquids, *i.e.*, where there is the highest mass transfer, thereby circumventing the need for a phase transfer catalyst. The control experiment of mixing the same solutions together using batch processing yielded only traces of the product. Also noteworthy is that the yield using the flat base tube is significantly higher at lower rotational speeds. In this context, phase demixing of an emulsion of toluene and water occurs at much lower speeds in the flat base tube (water and DCM do not form a stable emulsion for comparative studies). Translating this finding to the water/DCM mixture in the flat base tube would predict higher mass transfer between the two phases at lower speeds relative to the hemispherical base tube, and this is indeed the case. Thus, we have a model for interpreting the signature of a mixture of immiscible liquids (mixing times, demixing times if available, and change in temperature for increasing ω), for predicting the ability to accelerate reactions without the need for a phase transfer catalyst. This is understood by a dominance of DH high mass transfer topological fluid flow, with the process adhering to the tenets of green chemistry in avoiding the use of an auxiliary substance. We also note that reactions occurring without the need for a phase transfer catalyst relate to a possible explanation of ‘on water’ effects,[33–35] for now where there is mixing occurring between immiscible liquids at the submicron dimension scales.

3.4 Conclusions

Unique insights into understanding the nature of the high shear topological flow in thin films of two immiscible liquids in the VFD at the optimal beneficial tilt angle of 45° have been achieved in this work. These have occurred through integrating a number of different investigative strategies for overcoming the challenges associated with having a rotating reference frame and the small dimensionality of the high shear topological flows in liquid films ≥~150 mm thick. The rotational speed dependent strategies have included the combination of (i) neutron imaging film thickness studies, (ii) mixing experiments within each of the immiscible liquids along with temperature changes, and (iii) structural perturbation of polymer films on the surface of the tube and nanomaterials assembled at the interface of immiscible liquids. This understanding provides a level of predictability for the optimal rotational speed ω within the VFD for a tilt angle θ of 45°, as highlighted for carbohydrate transformations in an immiscible mixture of water and dichloromethane, Figure 3.17(d). The interfacial tension between the two liquids, and immiscible liquids in general, is transitioned in the VFD which provides the energy cost for high mass transfer of two liquids into each other, with DLS revealing the particulates of each phase within the other. Remarkably the use of the VFD in this way does not result in the formation of emulsions, despite high mass transfer being maintained between the two liquids. The formation of nanoparticles within each phase for a biphasic mixture during VFD processing is consistent with high surface area of the two liquids relative to each other. Interestingly, combining toluene and water is a well-studied archetypal immiscible biphasic system with toluene having almost no effect on the hydrate phase equilibrium boundary of the methane–water system.[36] At the air–liquid interface in the VFD, there is the expected increase in mass transfer of gases into the water phase, and indeed for both phases of immiscible liquids in the VFD. In this context, for the water layer, dissolved gases can limit the solubility of oil[37] (*cf.* toluene in the present study) and how this is manifested under shear is yet to be realised. Also noteworthy is the Faraday wave driven uniformity of the toluene and other less dense liquids in biphasic mixtures in the VFD. This relates to levitating a liquid, where excitation resonance of the supporting air layer prevails.[38]

Pre-formed emulsions of water and toluene in the VFD can be rapidly demixed at an increasing rotational speed threshold, being consistent with the general model of topological fluid flow, notably (i) high shear ST topological fluid arising from Coriolis forces from the base of the tube, in a way depending on its shape, either for a hemispherical base or a flat base with a small radius of curvature of the tube where the base is fused to its side walls, and (ii) DH flow arising from a combination of Faraday wave eddy currents and Coriolis forces. The different dimensionalities and *w* dependent onset of different topological fluid flows bodes well for changing the shape of the base beyond those studied herein for added control in certain applications, and how the topological fluid flow changes with change in diameter of the tube. The formation of nanoparticles in the phase separated layers, as unstable nano-emulsions (decomposing over 24 hours), is from the high mass transfer associated with the micron/sub-micron sized topological fluid flows at the interface between the immiscible layers. The use of the VFD in this regard simplifies processing with immiscible liquids, in avoiding the need for phase transfer catalysts to drive chemical reactions where there is preferential take up in the different layers for different reacting substrates. The combined understanding of fluid flow with changing the shape of the base of the tube opens new opportunities for VFD processing, for harnessing mechanical energy generated with topological fluid flow of differently focused energy, and in dealing with challenges associated with using highly viscous liquids. Interestingly the non-equilibrium spatially arranged DH fluid flow regimes in the toluene layer in the VFD impacting on the water layer though to the surface of the tube are laterally moving relative to the surface of the tube such that the molecular drilling results in a random array of holes, unlike for a mono-phasic system of toluene alone on the VFD.[11] This effectively creates a more uniform non-equilibrium conditions at the interface of the tube for a binary mixture of liquids. In addition, perforating the layer of polysulfone with holes has potential for fabricating material for used as a size-exclusion filter or dialysis-like membrane to separate varying diameter particulates.

Chapter 3 primarily investigates the mixing behaviour of organic solvent-water mixtures in the VFD. The degree of mixing is assessed by observing phase separation and how long it takes for the liquids to separate. In the case of immiscible liquids, mixing is evaluated visually by observing the clarity of the mixture and the time required for phase separation. The VFD can facilitate the mixing of organic solvents and water, as well as serve purposes related to demixing. This can be controlled through regulating the rotational speed.

3.5 References

1. Demurtas, Davide, Paul Guichard, Isabelle Martiel, Raffaele Mezzenga, Cécile Hébert, and Laurent Sagalowicz. “Direct Visualization of Dispersed Lipid Bicontinuous Cubic Phases by Cryo-Electron Tomography.” *Nature Communications* 6, no. 1 (November 17, 2015): 8915. https://doi.org/10.1038/ncomms9915.
2. Paria, Suva, Qi-Kai Kang, Miho Hatanaka, and Keiji Maruoka. “Design of Efficient Chiral Bifunctional Phase-Transfer Catalysts Possessing an Amino Functionality for Asymmetric Aminations.” *ACS Catalysis* 9, no. 1 (January 4, 2019): 78–82. https://doi.org/10.1021/acscatal.8b03292.
3. Gumerov, Rustam A., Artem M. Rumyantsev, Andrey A. Rudov, Andrij Pich, Walter Richtering, Martin Möller, and Igor I. Potemkin. “Mixing of Two Immiscible Liquids within the Polymer Microgel Adsorbed at Their Interface.” *ACS Macro Letters* 5, no. 5 (May 17, 2016): 612–16. https://doi.org/10.1021/acsmacrolett.6b00149.
4. Rumyantsev, Artem M., Rustam A. Gumerov, and Igor I. Potemkin. “A Polymer Microgel at a Liquid–Liquid Interface: Theory vs. Computer Simulations.” *Soft Matter* 12, no. 32 (2016): 6799–6811. https://doi.org/10.1039/C6SM01231K.

5. Wiese, Susanne, Antje C. Spiess, and Walter Richtering. “Microgel-Stabilized Smart Emulsions for Biocatalysis.” *Angewandte Chemie International Edition* 52, no. 2 (January 7, 2013): 576–79. https://doi.org/10.1002/anie.201206931.

6. Sheth, Tanvi, Serena Seshadri, Tamás Prileszky, and Matthew E. Helgeson. “Multiple Nanoemulsions.” *Nature Reviews Materials* 5, no. 3 (March 1, 2020): 214–28. https://doi.org/10.1038/s41578-019-0161-9.

7. Ito, Yoichiro. “Golden Rules and Pitfalls in Selecting Optimum Conditions for High-Speed Counter-Current Chromatography.” *Journal of Chromatography A* 1065, no. 2 (February 18, 2005): 145–68. https://doi.org/10.1016/j.chroma.2004.12.044.

8. Wuethrich, Alain, Abu Ali Ibn Sina, Mostak Ahmed, Ting-Yun Lin, Laura G. Carrascosa, and Matt Trau. “Interfacial Nano-Mixing in a Miniaturised Platform Enables Signal Enhancement and in Situ Detection of Cancer Biomarkers.” *Nanoscale* 10, no. 23 (2018): 10884–90. https://doi.org/10.1039/C7NR09496E.

9. Chapman, Michael R., Maria H. T. Kwan, Georgina King, Katherine E. Jolley, Mariam Hussain, Shahed Hussain, Ibrahim E. Salama, et al. “Simple and Versatile Laboratory Scale CSTR for Multiphasic Continuous-Flow Chemistry and Long Residence Times.” *Organic Process Research & Development* 21, no. 9 (September 15, 2017): 1294–1301. https://doi.org/10.1021/acs.oprd.7b00173.

10. Chen, Xianjue, Nicole M. Smith, K. Swaminathan Iyer, and Colin L. Raston. “Controlling Nanomaterial Synthesis, Chemical Reactions and Self Assembly in Dynamic Thin Films.” *Chemical Society Reviews* 43, no. 5 (2014): 1387–99. https://doi.org/10.1039/C3CS60247H.

11. Alharbi, Thaar M. D., Matt Jellicoe, Xuan Luo, Kasturi Vimalanathan, Ibrahim K. Alsulami, Bediea S. AL Harbi, Aghil Igder, et al. “Sub-Micron Moulding Topological Mass Transport Regimes in Angled Vortex Fluidic Flow.” *Nanoscale Advances* 3, no. 11 (2021): 3064–75. https://doi.org/10.1039/D1NA00195G.

12. Cybulski, Olgierd, Miroslaw Dygas, Barbara Mikulak-Klucznik, Marta Siek, Tomasz Klucznik, Seong Yeol Choi, Robert J. Mitchell, Yaroslav I. Sobolev, and Bartosz A. Grzybowski. “Concentric Liquid Reactors for Chemical Synthesis and Separation.” *Nature* 586, no. 7827 (October 1, 2020): 57–63. https://doi.org/10.1038/s41586-020-2768-9.

13. Jellicoe, Matt, Kasturi Vimalanathan, Jason R. Gascooke, Xuan Luo, and Colin L. Raston. “High Shear Spheroidal Topological Fluid Flow Induced Coating of Polystyrene Beads with C60 Spicules.” *Chemical Communications* 57, no. 46 (2021): 5638–41. https://doi.org/10.1039/D0CC07165J.

14. Zaccone, Alessio, Hua Wu, Daniele Gentili, and Massimo Morbidelli. “Theory of Activated-Rate Processes under Shear with Application to Shear-Induced Aggregation

of Colloids." *Physical Review E* 80, no. 5 (November 16, 2009): 051404. https://doi.org/10.1103/PhysRevE.80.051404.

15. Conchúir, Breanndán Ó, and Alessio Zaccone. "Mechanism of Flow-Induced Biomolecular and Colloidal Aggregate Breakup." *Physical Review E* 87, no. 3 (March 29, 2013): 032310. https://doi.org/10.1103/PhysRevE.87.032310.
16. Mura, Federica, and Alessio Zaccone. "Effects of Shear Flow on Phase Nucleation and Crystallization." *Physical Review E* 93, no. 4 (April 11, 2016): 042803. https://doi.org/10.1103/PhysRevE.93.042803.
17. Donnelly, Claire, Konstantin L. Metlov, Valerio Scagnoli, Manuel Guizar-Sicairos, Mirko Holler, Nicholas S. Bingham, Jörg Raabe, Laura J. Heyderman, Nigel R. Cooper, and Sebastian Gliga. "Experimental Observation of Vortex Rings in a Bulk Magnet." *Nature Physics* 17, no. 3 (March 1, 2021): 316–21. https://doi.org/10.1038/s41567-020-01057-3.
18. Kilner, Philip J., Guang-Zhong Yang, A. John Wilkes, Raad H. Mohiaddin, David N. Firmin, and Magdi H. Yacoub. "Asymmetric Redirection of Flow through the Heart." *Nature* 404, no. 6779 (April 1, 2000): 759–61. https://doi.org/10.1038/35008075.
19. Pye, Scott J., Scott J. Dalgarno, Justin M. Chalker, and Colin L. Raston. "Organic Oxidations Promoted in Vortex Driven Thin Films under Continuous Flow." *Green Chemistry* 20, no. 1 (2018): 118–24. https://doi.org/10.1039/C7GC03352D.
20. Britton, Joshua, Keith A. Stubbs, Gregory A. Weiss, and Colin L. Raston. "Vortex Fluidic Chemical Transformations." *Chemistry – A European Journal* 23, no. 54 (September 27, 2017): 13270–78. https://doi.org/10.1002/chem.201700888.
21. Britton, Joshua, and Colin L. Raston. "Continuous Flow Vortex Fluidic Production of Biodiesel." *RSC Advances* 4, no. 91 (2014): 49850–54. https://doi.org/10.1039/C4RA10317C.
22. Luo, X., P. Smith, C. L. Raston, and W. Zhang. "Vortex Fluidic Device-Intensified Aqueous Two Phase Extraction of C-Phycocyanin from Spirulina Maxima." *ACS Sustainable Chemistry & Engineering* 4, no. 7 (July 5, 2016): 3905–11. https://doi.org/10.1021/acssuschemeng.6b00756.
23. Vimalanathan, Kasturi, Rekha Goswami Shrestha, Zhi Zhang, Jin Zou, Tomonobu Nakayama, and Colin L. Raston. "Surfactant-Free Fabrication of Fullerene C60 Nanotubules Under Shear." *Angewandte Chemie International Edition* 56, no. 29 (July 10, 2017): 8398–8401. https://doi.org/10.1002/anie.201608673.
24. Alharbi, Thaar M. D., Qin Li, and Colin L. Raston. "Thin Film Mechano-Energy Induced Slicing of Carbon Nanotubes under Flow." *ACS Sustainable Chemistry & Engineering* 9, no. 48 (December 6, 2021): 16044–51. https://doi.org/10.1021/acssuschemeng.1c03109.

25. Vimalanathan, Kasturi, Irene Suarez-Martinez, M. Chandramalika R. Peiris, Joshua Antonio, Carla de Tomas, Yichao Zou, Jin Zou, et al. “Vortex Fluidic Mediated Transformation of Graphite into Highly Conducting Graphene Scrolls.” *Nanoscale Advances* 1, no. 7 (2019): 2495–2501. https://doi.org/10.1039/C9NA00184K.

26. Chen, Rui, Simona Neri, and Leonard J. Prins. “Enhanced Catalytic Activity under Non-Equilibrium Conditions.” *Nature Nanotechnology* 15, no. 10 (October 1, 2020): 868–74. https://doi.org/10.1038/s41565-020-0734-1.

27. Neely, Brian J., Jan Wagner, Robert L. Jr. Robinson, and Khaled A. M. Gasem. “Mutual Solubility Measurements of Hydrocarbon–Water Systems Containing Benzene, Toluene, and 3-Methylpentane.” *Journal of Chemical & Engineering Data* 53, no. 1 (January 1, 2008): 165–74. https://doi.org/10.1021/je700449z.

28. Solheim, Timothy E., Filomena Salvemini, Stuart B. Dalziel, and Colin L. Raston. “Neutron Imaging and Modelling Inclined Vortex Driven Thin Films.” *Scientific Reports* 9, no. 1 (February 26, 2019): 2817. https://doi.org/10.1038/s41598-019-39307-x.

29. Tavakoli, Javad, Nikita Joseph, Clarence Chuah, Colin L. Raston, and Youhong Tang. “Vortex Fluidic Enabling and Significantly Boosting Light Intensity of Graphene Oxide with Aggregation Induced Emission Luminogen.” *Materials Chemistry Frontiers* 4, no. 7 (2020): 2126–30. https://doi.org/10.1039/D0QM00270D.

30. Luo, Xuan, Ahmed Hussein Mohammed Al-Antaki, David P. Harvey, Yinlan Ruan, Shan He, Wei Zhang, and Colin L. Raston. “Vortex Fluidic Mediated Synthesis of Macroporous Bovine Serum Albumin-Based Microspheres.” *ACS Applied Materials & Interfaces* 10, no. 32 (August 15, 2018): 27224–32. https://doi.org/10.1021/acsami.8b09316.

31. Yu, Yi, Xu Fei, Jing Tian, Longquan Xu, Xiuying Wang, and Yi Wang. “Self-Assembled Enzyme–Inorganic Hybrid Nanoflowers and Their Application to Enzyme Purification.” *Colloids and Surfaces B: Biointerfaces* 130 (June 1, 2015): 299–304. https://doi.org/10.1016/j.colsurfb.2015.04.033.

32. Liang, Jiling, Haiping Li, Jingen Yan, and Wanguo Hou. “Demulsification of Oleic-Acid-Coated Magnetite Nanoparticles for Cyclohexane-in-Water Nanoemulsions.” *Energy & Fuels* 28, no. 9 (September 18, 2014): 6172–78. https://doi.org/10.1021/ef501169m.

33. Mellouli, Sonia, Lise Bousekkine, Ashleigh B. Theberge, and Wilhelm T. S. Huck. “Investigation of ‘On Water’ Conditions Using a Biphasic Fluidic Platform.” *Angewandte Chemie International Edition* 51, no. 32 (August 6, 2012): 7981–84. https://doi.org/10.1002/anie.201200575.

34. Song, Choong Eui, Si Joon Park, In-Soo Hwang, Min Jung Jung, So Young Shim, Han Yong Bae, and Ji Yoon Jung. “Hydrophobic Chirality Amplification in Confined Water Cages.” *Nature Communications* 10, no. 1 (February 20, 2019): 851. https://doi.org/10.1038/s41467-019-08792-z.

35. Oksdath-Mansilla, Gabriela, Renata L. Kucera, Justin M. Chalker, and Colin L. Raston. “Azide–Alkyne Cycloadditions in a Vortex Fluidic Device: Enhanced ‘on Water’ Effects and Catalysis in Flow.” *Chemical Communications* 57, no. 5 (2021): 659–62. https://doi.org/10.1039/D0CC04401F.

36. Mohammadi, Amir H., Veronica Belandria, and Dominique Richon. “Can Toluene or Xylene Form Clathrate Hydrates?” *Industrial & Engineering Chemistry Research* 48, no. 12 (June 17, 2009): 5916–18. https://doi.org/10.1021/ie900362v.

37. Pashley, R. M., M. Rzechowicz, L. R. Pashley, and M. J. Francis. “De-Gassed Water Is a Better Cleaning Agent.” *The Journal of Physical Chemistry B* 109, no. 3 (January 1, 2005): 1231–38. https://doi.org/10.1021/jp045975a.

38. Apffel, Benjamin, Filip Novkoski, Antonin Eddi, and Emmanuel Fort. “Floating under a Levitating Liquid.” *Nature* 585, no. 7823 (September 1, 2020): 48–52. https://doi.org/10.1038/s41586-020-2643-8.

CHAPTER 4 : VORTEX FLUIDICS EXTRACTION OF PERFLUOROOCTANOIC ACID

4.1 Abstract

Perfluorooctanoic acid (PFOA) is a member of the expanding class of emerging contaminants known as per- and polyfluoroalkyl substances (PFAS), which have recently garnered heightened concern due to their potentially hazardous effects. These compounds are classified as toxic and are prevalent in various aquatic environments. The extensive use of PFAS across multiple industries has led to significant environmental and biological accumulation, raising critical concerns about their persistence and carcinogenic potential. The identification and removal of these substances from the environment are therefore of paramount importance. The introduction of the VFD offers a remarkable solution, distinguished by its cost-effectiveness, simplicity, and innovative design. Utilising dynamic thin-film microfluidic technology, the VFD facilitates the efficient extraction of the anionic surfactant PFOA. This liquid-phase extraction (LPE) method operates similarly to the methylene blue active substances (MBAS) approach, wherein the hydrophobic ion-pair of dye (ethyl violet) and PFOA is extracted into an organic phase (ethyl acetate). The advantages of this LPE methodology are further highlighted by its rapid processing time; within just 10 minutes, PFOA is effectively extracted from water, as confirmed by liquid chromatography-mass spectrometry (LCMS). The VFD's potential for large-scale application is evident, underscoring its scalability and operational efficiency.

4.2 Introduction

One prominent component of the broad class of recognised pollutants known as per- and polyfluoroalkyl substances (PFAS) is perfluorooctanoic acid (PFOA). PFAS is an extraordinary class of synthetic chemicals with exceptional properties, most notably outstanding chemical and thermal stability. Their inherent resilience makes them highly resistant to oxidation and degradation processes.[1] PFAS have been around since the 1940s and are widely used in various consumer products and industrial settings, and aqueous film-forming foams are essential to aerial firefighting operations.[2, 3]

The robustness of the carbon–fluorine (C-F) link, which gives these perfluorinated compounds their persistence, inertness, and steadfastness, is essential to the long-term stability of PFAS molecules.[4] As such, PFAS are not readily biodegradable, a characteristic further supported by estimates indicating that PFOA has a half–year hydrolysis–life extrapolated to be greater than 41 years at 25 °C (USEPA 505-F-14-001).

PFAS, notable for their exceptional persistence, exhibit an enduring presence within diverse environmental matrices, encompassing but not limited to surface water bodies, sewage networks, sedimentary deposits, and biological organisms.[5] These substances can enter the water cycle through various routes, including but not restricted to isolated point sources like municipal and industrial wastewater treatment plants, industrial complexes, and locations used for firefighting training exercises. Furthermore, PFAS dispersal is aided by air deposition and nonpoint sources such as groundwater and drainage penetration.[6, 7] Figure 4.1 is a schematic delineating the intricate pathways PFAS traverse, ultimately culminating in human exposure.

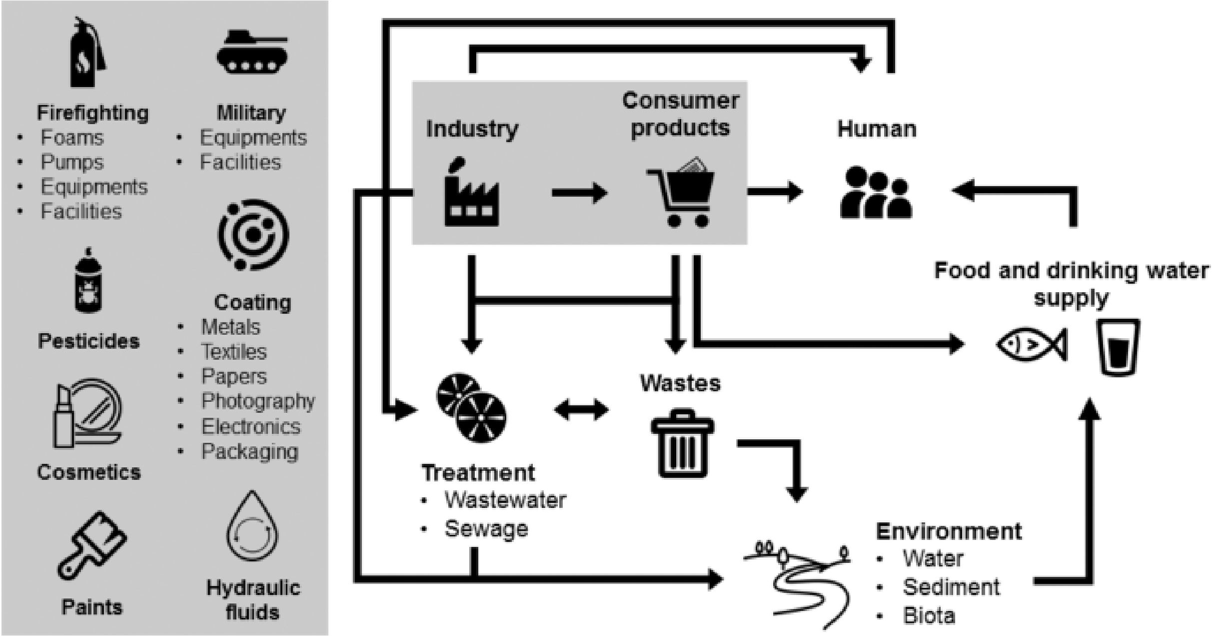

Figure 4.1 PFAS extensive use.

Due to extensive use, PFAS contamination is ubiquitous and moves through ecosystems and food chains, bioaccumulating in humans as the final consumers.[8]

One of the main ways humans are exposed to PFAS is through ingesting contaminated food and water, which can lead to various harmful health effects. These consequences range over a wide range of illnesses, such as thyroid disease, liver damage, and cancer.[9] The discovery of PFOA in groundwater reservoirs is especially problematic, as it has raised concerns about the possible effects on susceptible groups, including impaired development during pregnancy and lactation, hepatic disruptions, carcinogenic susceptibilities, thyroid issues, and immune system impairments.[10]

Due to their well-established harmful effects and persistent existence, PFAS must be eliminated from water and wastewater systems.[11] Many review articles have meticulously investigated the occurrence, fate, dynamics of transport, and treatment strategies related to PFAS contamination, both in situ and ex-situ. [6, 7, 12-18]

Research on the removal of PFAS has employed a wide range of techniques, such as adsorption, nanofiltration, reverse osmosis, biological degradation, thermal degradation, photolysis, electrolysis, and chemical oxidation and reduction processes.[16, 17] Reverse osmosis and nanofiltration, two notable membrane-based separation methods, have proven to be highly effective in reducing a wide range of PFAS pollutants. However, membrane fouling and high energy requirements stand in the way of these techniques' widespread application. [17]

The C-F bond's strong stability and the fluoride ions' strong electronegativity present intrinsic difficulties for biological degradation mechanisms.[20] Chemical oxidation and reduction techniques, as examples of technologically advanced oxidation procedures, have demonstrated remarkable efficacy in achieving complete mineralisation of PFAS.[20] However, technological limitations and operational demands still limit their large-scale practical implementation, such as slow reaction kinetics.

Sample preparation, filtration, and concentrating samples for PFAS detection are only a few of the challenging problems that come with the analytical procedures required. The extraction processes for PFAS from solid and liquid matrices are illustrated in Figure 4.2. This process uses well-established techniques, such as alkaline digestion, liquid-liquid extraction (LLE), dispersive liquid-liquid microextraction, and ion-pair extraction.[21] These methodologies occasionally suffer from inefficiencies and protracted procedures, sometimes mandating the simultaneous extraction of lipids, exacerbating the complexity of chromatographic analysis. Additionally, their execution frequently requires further external analysis to be performed.

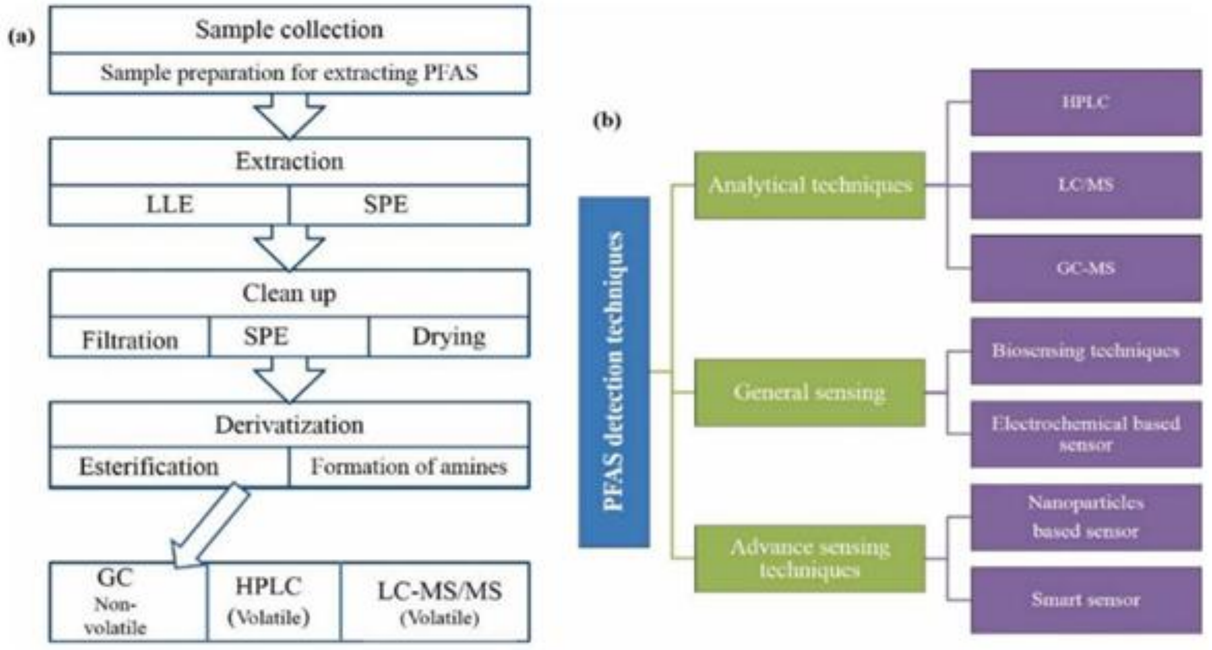

Figure 4.2 PFAS extraction process and detection techniques.

a) An overview of the PFAS extraction process from solid or liquid samples. b) A range of detection techniques for finding PFAS in environmental samples. [22, 23] Notes: LLE = Liquid-liquid extraction, SPE =

Solid phase extraction, GC = Gas chromatography, HPLC = High-performance liquid chromatography, LC-MS/MS = Liquid chromatography with tandem mass spectrometry.

This chapter highlights the concurrent endeavours in surfactant extraction, explicitly emphasising the anionic surfactant (AS) PFOA. astkCARE^{TM}, a refined iteration of methylene blue active substrates (MBAS), is a colour-based assay previously developed by CRC CARE.[24] Within this framework, AS PFOA engages in a reactive interplay with the cationic dye (such as methylene blue or ethyl violet) in the test to form an ion pair. Notably, this ion pair assumes a hydrophobic disposition because their hydrophilic terminates are blocked by each other due to electrostatic interaction. Consequently, this hydrophobic ion pair is immiscible in the aqueous phase, thereby facilitating its extraction into a non-aqueous organic phase (ethyl acetate).

Recently, CRC CARE has explored astkCARE^{TM} for colour justification to analyse substances for the presence of PFOA as an onsite prescreening tool preceding quantitative measurement.[24] However, this method relies significantly on visual detection aided by a provided colour chart as a reference, rendering it a semi-quantitative assay characterised by notable variability. Moreover, challenges such as visual fatigue and the potential interference from background illumination pose additional complexities to this visual detection process.

To ensure the precision of colour interpretation, it’s advisable to employ a colorimetric scanning device or a reading kit, thereby mitigating the inherent limitations associated with manual colour assessment. Alternatively, implementing background correction strategies facilitated by specialised software could offer a viable solution to enhance the accuracy of colour readings in this context.

Thus, CRC CARE has advanced the capabilities of astkCARE^{TM} by integrating a smartphone app tailored to discern PFOA concentrations.[24] The devised app employs a reading kit to maintain a consistent background illumination, as demonstrated in Figure 4.3. This ensures the establishment of a robust correlation between colourimetric changes and PFOA concentrations. The output concentration variation is successfully restricted to less than 10% in a 10-1000 ppb range.

Moreover, CRC CARE advocates the implementation of solid-phase extraction techniques to enhance the assay's sensitivity.[24] Additionally, flourous solid-phase extraction minimises interference stemming from nonfluorinated anionic surfactants, thereby refining the specificity of PFOA detection. Given these advancements, CRC CARE posits the smartphone app as a viable prescreening tool for onsite testing, underscoring its potential significance in environmental monitoring endeavours.

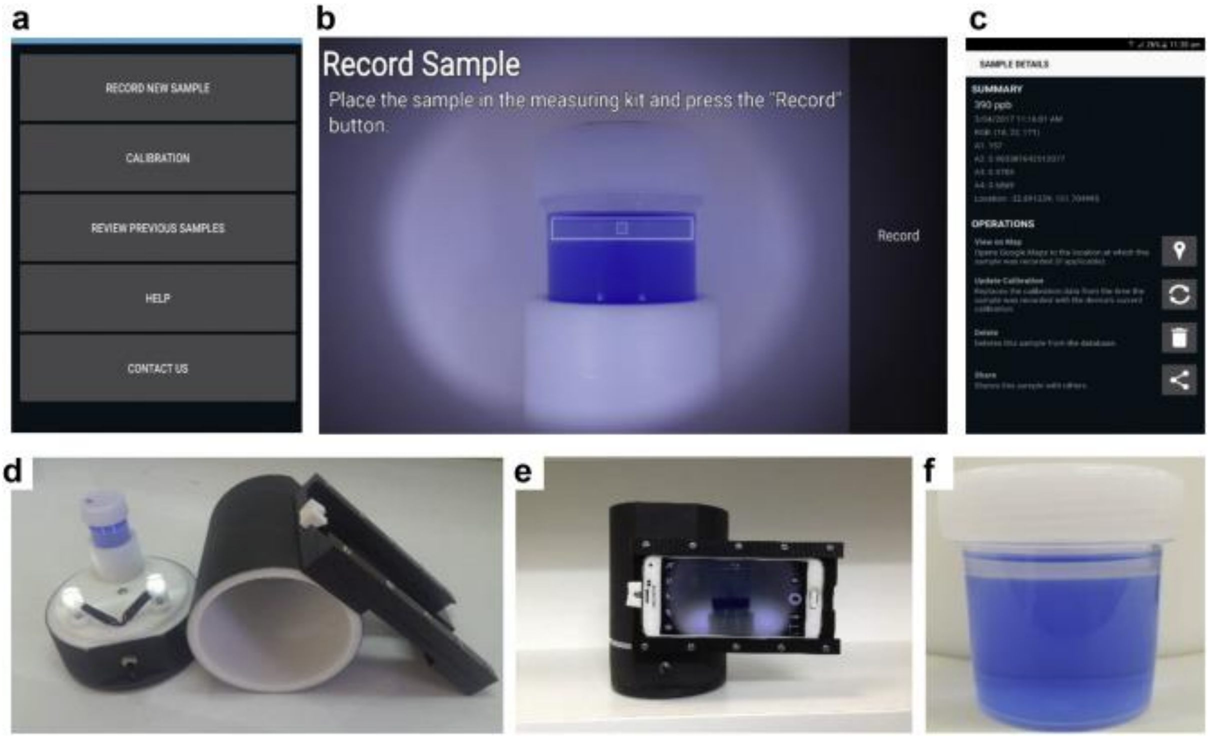

Record Sample

Place the sample in the measuring kit and press the "Record" button.

Figure 4.3 CRC CARE process.

Snapshots (a-c) of the app, photos of the reading kit (d, e), and samples (b, f). In (b), the delineated rectangle denoting the reading screen is precisely aligned over the non-aqueous phase layer, emphasising the central region, constituting the designated colour reading area within the inner square. In (d), two white LEDs are on, and a container containing the sample is securely positioned in a sample holder. In (e), the smartphone holder is shown holding a smartphone in the reading position.[24]

This chapter takes things one step further, with liquid-phase extraction (LPE) employed using the vortex fluidic device (VFD) to extract the AS PFOA. Figure 4.4 below depicts the VFD, a marvel of cost-effectiveness, simplicity, and ingenuity. It stands out for its dynamic thin film microfluidic technology leveraging intense mass transfer and micro-mixing across immiscible phases. The efficiency advantages provided by this LPE methodology are notably enhanced by its rapidity; after only 10 minutes of processing, PFOA is extracted from the water, as confirmed through liquid chromatography-mass spectrometry (LCMS). This efficiency bodes well for the process's feasibility and scalability, especially when considering its implementation in large-scale production environments.

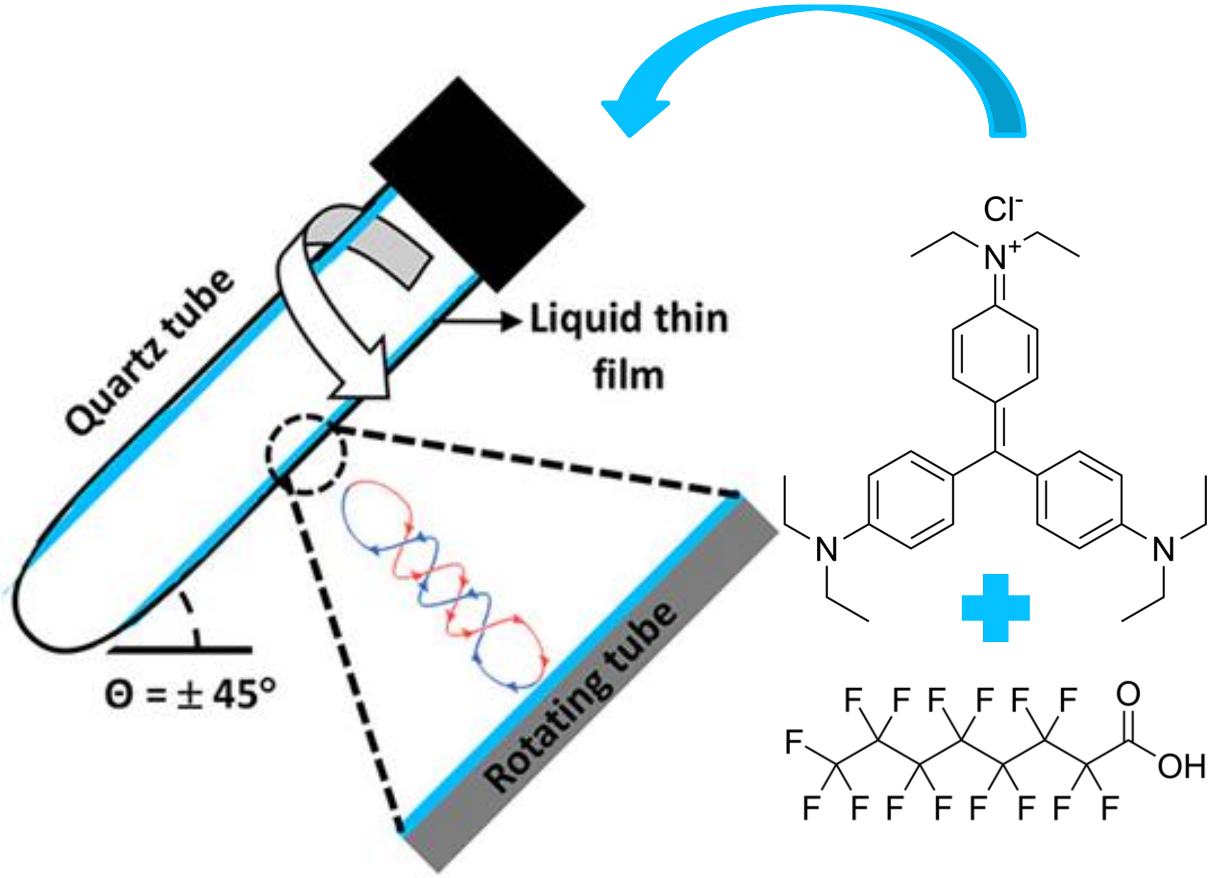

Figure 4.4 VFD PFOA processing.

Schematic of a vortex fluidic device (VFD) alongside a representation of the chemical structures of ethyl violet and PFOA.

4.3 Materials and Reagents

All chemicals, including anionic surfactants (AS) of PFOA, solvents including acetone, methanol, ethyl acetate, ammonium acetate (NH_4Ac), and ethyl violet dye, were purchased from Sigma-Aldrich.

4.4 Methods

4.4.1 Sample Preparation

PFOA was spiked in milli-Q water (MQ water). AstkCARE^{TM} reagent (ethyl acetate: acetone: ethyl violet, 3: 3: 1 in volume) was provided by CRC CARE (Australia).

4.4.2 Sample Analysis: LCMS

5 µL sample solution was injected into Waters Acquity UHPLC (LCMS) fitted with a Phenomenex kinetex XB-C18 100A column kept at 30 °C with the following dimensions: 2.1 mm internal diameter, 50 mm length, and 2.6 µm particle size. The flow rate was 0.5 mL/min for the gradient mobile phase of methanol. The Waters Synapt HDMS detector was maintained in negative mode for scanning. We expect to see a lot of in-source fragmentation of PFOA, so two lots of data were generated. One set

displays the chromatogram for the ion at m/z = 369 (fragment of PFOA, likely due to the loss of CO_2) and the other for m/z = 413 (intact PFOA) for the extraction of the molecular ions. Quantification was done by producing a calibration curve using standard solutions (external) of PFOA, with correlation coefficients higher than 0.99 and a detection limit of ~2 ppb. Blank samples of MQ water and methanol were run before each set of tests to minimise the background contamination. The drying gas flow rate was 500 L/hr, the temperature was set to 350 °C, and the capillary voltage was +3000 V.

For quality assurance and quality control, at least three samples are run in parallel for each test. One blank sample and one standard sample are for control, while one sample (or one batch of samples with different concentrations) is for the test.

4.5 Results and Discussions

4.5.1 Non-VFD PFOA

Aqueous samples fortified with PFOA are subjected to treatment with the astkCARE^{TM} reagent. Following a brief agitation period of approximately 10 seconds, the mixture is allowed to stand undisturbed for 1 to 2 minutes. During this interval, the desired ion-pair complex of the cationic dye and the AS preferentially migrate to the ethyl acetate organic phase. Analogous to the methodology employed by MBAS, the luminosity exhibited by the organic phase is indicative of the concentration of the ion-pair complex therein.

In the illustrated Figure 4.5, photographic representations portray various concentrations of PFOA dissolved in MQ water. Intriguingly, within the lower concentration spectrum from 0 to 100 ppb, no perceptible distinctions are discernible to the naked eye.

Figure 4.5 Spiked MQ PFOA samples.

Photo images of spiked MQ samples containing different concentrations of PFOA (indicated) with AstkCARE^{TM} reagent.

A demonstrative representation of the results obtained from LCMS analysis is shown in Figure 4.6. This figure illustrates the variation in PFOA concentrations at different ppb values. The identifiable peaks that appear at specific time points are clear markers that indicate the presence and concentration of PFOA in the sample under investigation in the LCMS.

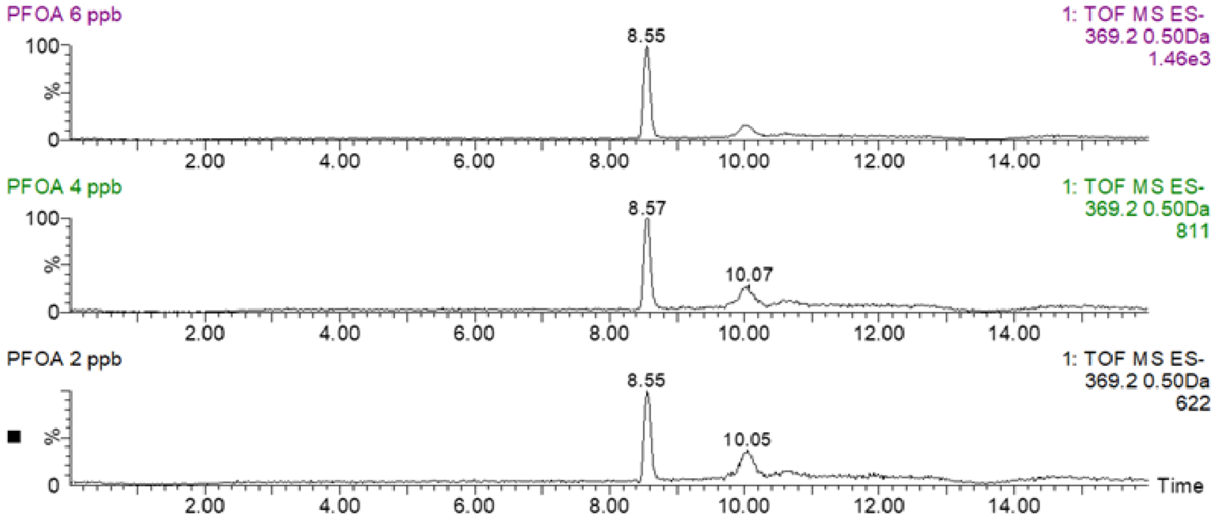

Figure 4.6 LCMS of Spiked MQ PFOA samples.

LCMS graphs of MQ samples containing different concentrations of PFOA (indicated).

spiked in milli-Q water (MQ water). AstkCARE^{TM} reagent (ethyl acetate: acetone: ethyl violet, 3: 3: 1 in volume) was provided by CRC CARE (Australia).

4.5.2 VFD Signature of Ethyl Acetate and AstkCARE^{TM} Reagent Processing

Mixing experiments, whereby the time is taken for a drop of dye added to a finite volume of liquid in the tube to form a uniformly mixed solution halfway up the film visibly, were performed across a range of rotational speeds at θ = 45° to understand the fluid flow better. This data provides a signature for each liquid, as depicted for AstkCARE^{TM} reagent and AstkCARE^{TM} reagent with samples for testing at ~20 °C in a 20 mm OD tube (17.5 mm ID) in Figure 4.7 a and b, respectively, for use in predicting rotational speed processing outcomes.

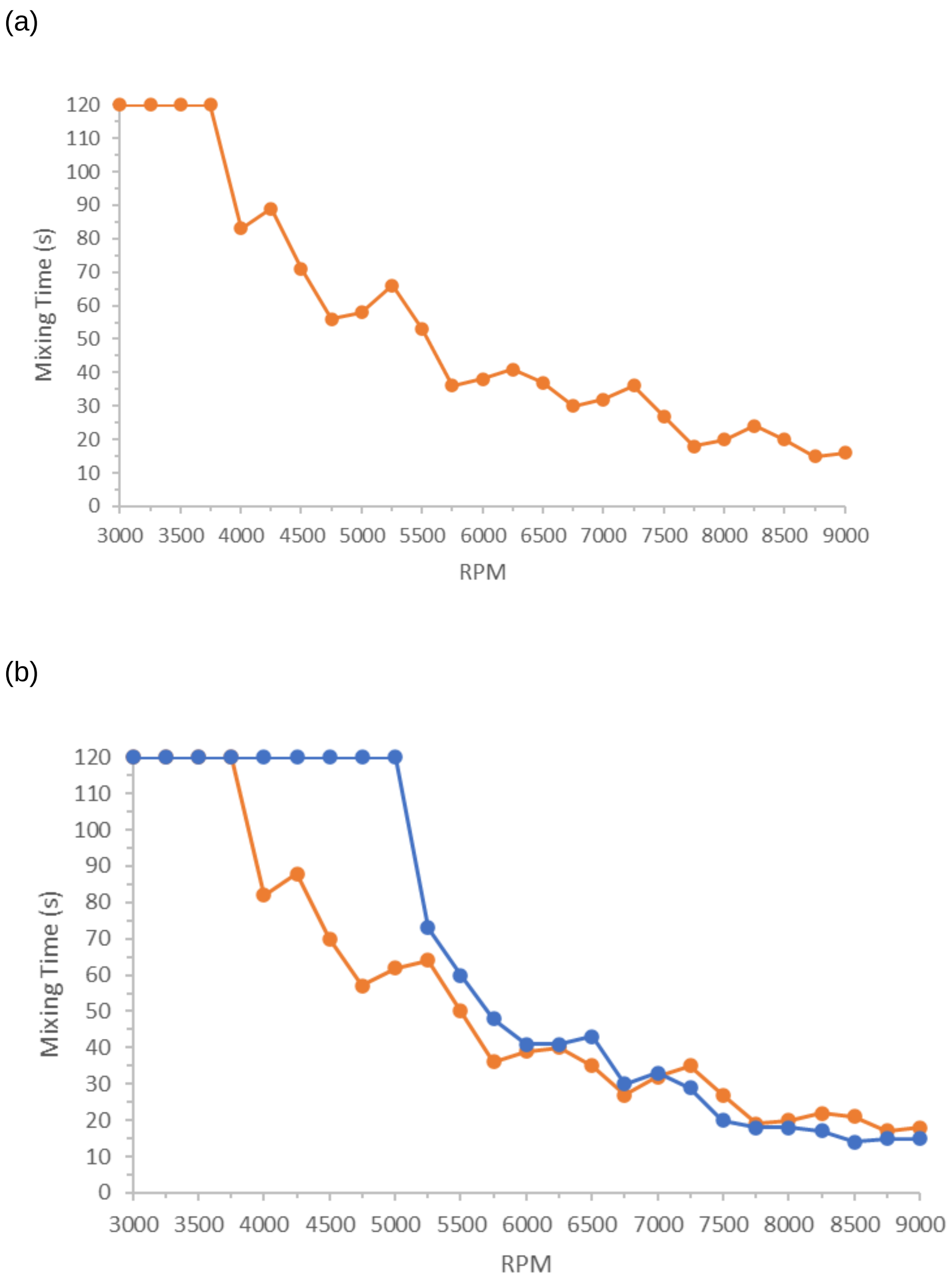

Figure 4.7 Signature of fluid flow in the VFD.

(a) VFD Signature of Ethyl Acetate and (b) VFD Signature of Ethyl Acetate and AstkCARE^{TM} reagent processing, with orange and blue depicting Ethyl Acetate and AstkCARE^{TM} reagent, respectively.

This was conducted to elucidate how the physical properties of a liquid, such as viscosity, density, and surface tension, influence and define the characteristic flow dynamics within the VFD's environment. By determining the mixing times for a 1:1 mixture of phase-separated liquids—ethyl acetate and an acetone/water solution—using the same procedure as for individual phases in the VFD's standard hemispherical base tube, we gained valuable insights into the nature of topological fluid flow. This behaviour is particularly evident when a drop of ethyl acetate containing a dye is added to the base of the tube; the mixing times in the ethyl acetate layer remain consistent whether or not a water layer is present below it.

The periodic step changes in mixing time observed with increasing rotational speeds are correlated with the dynamic thinning of the ethyl acetate film. This phenomenon occurs as the pitch of the double-helical flow diminishes to a critical point, at which the Faraday wave can no longer sustain the film's thickness. Consequently, the diameter of the double-helical flow reduces, forming a thinner film that initially has a larger pitch before undergoing further thinning.

In contrast, the mixing behaviour of a drop of water with dye into the water layer differs markedly from that of water alone. Where ethyl acetate and water exhibit similar mixing times, it is hypothesised that the double-helical flow facilitates mixing between the two phases. This interaction likely blurs the distinction between the double-helical flow patterns in ethyl acetate and water, leading to significantly enhanced mass transfer, especially beyond the 7500-rpm threshold.

4.5.3 VFD Tuned PFOA Extraction

A series of procedures were meticulously carried out on spiked solutions standardised to a concentration of 250 ppb PFOA. Once the AstkCARE^{TM} reagent was added to the aqueous solution, one solution was sonicated for 10 minutes as a standard for comparison. Five other solutions were run through different iterations in the VFD. Processing time was evaluated as a variable in the experiment. However, no significant change was observed in the results until after 10 minutes of VFD processing. This suggests that any effects of processing in the VFD did not become apparent within the initial 10-minute period.

Within the VFD, the solutions were subjected to a range of rotational speeds commencing at 1500 rpm, with subsequent solutions in increments of 1500 rpm till a maximum of 7500 rpm, as shown in Figure 4.8. The VFD tube was positioned at a tilt angle of 45°, ensuring optimal fluid dynamics at an ambient temperature of 20 °C throughout the experiment.

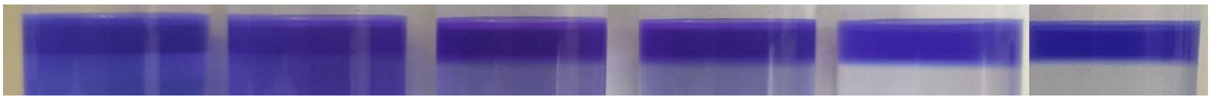

Figure 4.8 Post VFD processing.

Photo images of previously spiked MQ samples containing 250 ppb PFOA after 10 minutes of processing with AstkCARE^{TM} reagent through, from left to right, sonication, 1500 rpm, 3000 rpm, 4500 rpm, 6000 rpm, and 7500 rpm employed by the VFD, respectively.

The outcome of this investigation yielded solutions that were conspicuously disparate in their visual characteristics, as depicted in Table 4.1. The observation of ethyl violet exhibiting a discernible migration pattern towards the ethyl acetate layer was particularly noteworthy. This migration phenomenon correlates positively with increased mass transfer and micro-mixing, an effect attributed to the increased rotational speeds employed by the VFD.

Table 4.1 LCMS PFOA concentrations post processing.

LCMS	PFOA ppb	PFOA Fragment ppb
Sonication	250 ± 2	250 ± 2
1500 rpm	250 ± 2	250 ± 2
3000 rpm	250 ± 2	250 ± 2
4500 rpm	250 ± 2	250 ± 2
6000 rpm	20 ± 5	20 ± 4
7500 rpm	10 ± 2	10 ± 3

LCMS was employed as the analytical tool to elucidate the potential correlation between the migration of ethyl violet from the aqueous phase into the ethyl acetate layer and the simultaneous extraction of PFOA. VFD processing at 7500 rpm corresponds to an extraction efficiency of approximately 95%, down from the initially spiked 250 ppb to only 10 ppb remaining, highlighting the effectiveness of the removal process of PFOA from water. This investigative endeavour supports the hypothesis above, indicating a discernible relationship between the phenomena mentioned earlier. This outcome underscores the efficacy of high-speed solvent extraction techniques in facilitating the selective transference of analytes, thereby accentuating the utility of the VFD as an LPE methodology due to its intense mass transfer and micro-mixing across immiscible phases.

4.6 Conclusion

The VFD leveraged its dynamic thin film microfluidic technology and intense micro-mixing to extract PFOA from water using the AstkCARE^{TM} reagent. Akin to the MBAS, this LPE removes the hydrophobic ion-pair of dye (ethyl violet)-AS to an organic phase (ethyl acetate). The efficiency advantages provided by this LPE methodology are notably enhanced by its rapidity; after only 10 minutes of processing, as much as 95% of PFOA is extracted from the water, from the initially spiked 250 ppb to only 10 ppb remaining, as confirmed through LCMS. This efficiency bodes well for the process's feasibility and scalability, especially when considering its implementation in large-scale production environments.

4.7 References

1. Li, Yasong, Danielle P. Oliver, and Rai S. Kookana. “A Critical Analysis of Published Data to Discern the Role of Soil and Sediment Properties in Determining Sorption of per and Polyfluoroalkyl Substances (PFASs).” *The Science of the Total Environment* 628–629 (July 1, 2018): 110–20. https://doi.org/10.1016/j.scitotenv.2018.01.167.
2. Gao, Ke, Jianjie Fu, Qiao Xue, Yili Li, Yong Liang, Yuanyuan Pan, Aiqian Zhang, and Guibin Jiang. “An Integrated Method for Simultaneously Determining 10 Classes of Per- and Polyfluoroalkyl Substances in One Drop of Human Serum.” *Analytica Chimica Acta* 999 (January 25, 2018): 76–86. https://doi.org/10.1016/j.aca.2017.10.038.
3. Liu, Yang, WeiJian Liu, YunSong Xu, YongZhi Zhao, Pei Wang, ShuangYu Yu, JiaoDi Zhang, et al. “Characteristics and Human Inhalation Exposure of Ionic Per- and Polyfluoroalkyl Substances (PFASs) in PM(10) of Cities around the Bohai Sea: Diurnal Variation and Effects of Heating Activity.” *The Science of the Total Environment* 687 (October 15, 2019): 177–87. https://doi.org/10.1016/j.scitotenv.2019.06.103.
4. Bentel, Michael J., Yaochun Yu, Lihua Xu, Zhong Li, Bryan M. Wong, Yujie Men, and Jinyong Liu. “Defluorination of Per- and Polyfluoroalkyl Substances (PFASs) with Hydrated Electrons: Structural Dependence and Implications to PFAS Remediation and Management.” *Environmental Science & Technology* 53, no. 7 (April 2, 2019): 3718–28. https://doi.org/10.1021/acs.est.8b06648.
5. Sunderland, Elsie M., Xindi C. Hu, Clifton Dassuncao, Andrea K. Tokranov, Charlotte C. Wagner, and Joseph G. Allen. “A Review of the Pathways of Human Exposure to Poly- and Perfluoroalkyl Substances (PFASs) and Present Understanding of Health Effects.” *Journal of Exposure Science & Environmental Epidemiology* 29, no. 2 (March 2019): 131–47. https://doi.org/10.1038/s41370-018-0094-1.
6. Merino, Nancy, Yan Qu, Rula A. Deeb, Elisabeth L. Hawley, Michael R. Hoffmann, and Shaily Mahendra. “Degradation and Removal Methods for Perfluoroalkyl and Polyfluoroalkyl Substances in Water.” *Environmental Engineering Science* 33, no. 9 (September 1, 2016): 615–49. https://doi.org/10.1089/ees.2016.0233.
7. Ahrens, Lutz, and Mirco Bundschuh. “Fate and Effects of Poly- and Perfluoroalkyl Substances in the Aquatic Environment: A Review.” *Environmental Toxicology and Chemistry* 33, no. 9 (September 1, 2014): 1921–29. https://doi.org/10.1002/etc.2663.
8. Wee, Sze Yee, and Ahmad Zaharin Aris. “Revisiting the ‘Forever Chemicals’, PFOA and PFOS Exposure in Drinking Water.” *Npj Clean Water* 6, no. 1 (August 21, 2023): 57. https://doi.org/10.1038/s41545-023-00274-6.
9. Braun, Joseph M., Aimin Chen, Megan E. Romano, Antonia M. Calafat, Glenys M. Webster, Kimberly Yolton, and Bruce P. Lanphear. “Prenatal Perfluoroalkyl Substance Exposure and Child Adiposity at 8 Years of Age: The HOME Study.” *Obesity (Silver Spring, Md.)* 24, no. 1 (January 2016): 231–37. https://doi.org/10.1002/oby.21258.

10. Verduzco, Rafael, and Michael S. Wong. “Fighting PFAS with PFAS.” *ACS Central Science* 6, no. 4 (April 22, 2020): 453–55. https://doi.org/10.1021/acscentsci.0c00164.
11. Flynn, R. Wesley, Michael F. Chislock, Megan E. Gannon, Stephanie J. Bauer, Brian J. Tornabene, Jason T. Hoverman, and Maria S. Sepúlveda. “Acute and Chronic Effects of Perfluoroalkyl Substance Mixtures on Larval American Bullfrogs (Rana Catesbeiana).” *Chemosphere* 236 (December 2019): 124350. https://doi.org/10.1016/j.chemosphere.2019.124350.
12. Kucharzyk, Katarzyna H., Ramona Darlington, Mark Benotti, Rula Deeb, and Elisabeth Hawley. “Novel Treatment Technologies for PFAS Compounds: A Critical Review.” *Journal of Environmental Management* 204, no. Pt 2 (December 15, 2017): 757–64. https://doi.org/10.1016/j.jenvman.2017.08.016.
13. Ahmed, Mohammad Boshir, Md. Masruck Alam, John L. Zhou, Bentuo Xu, Md Abu Hasan Johir, Aneek Krishna Karmakar, Md. Saifur Rahman, Jewel Hossen, A.T.M. Kamrul Hasan, and Mohammad Ali Moni. “Advanced Treatment Technologies Efficacies and Mechanism of Per- and Poly-Fluoroalkyl Substances Removal from Water.” *Process Safety and Environmental Protection* 136 (April 1, 2020): 1–14. https://doi.org/10.1016/j.psep.2020.01.005.
14. Crone, Brian C., Thomas F. Speth, David G. Wahman, Samantha J. Smith, Gulizhaer Abulikemu, Eric J. Kleiner, and Jonathan G. Pressman. “Occurrence of Per- and Polyfluoroalkyl Substances (PFAS) in Source Water and Their Treatment in Drinking Water.” *Critical Reviews in Environmental Science and Technology* 49, no. 24 (June 2019): 2359–96. https://doi.org/10.1080/10643389.2019.1614848.
15. Arias Espana, Victor Andres, Megharaj Mallavarapu, and Ravi Naidu. “Treatment Technologies for Aqueous Perfluorooctanesulfonate (PFOS) and Perfluorooctanoate (PFOA): A Critical Review with an Emphasis on Field Testing.” *Environmental Technology & Innovation* 4 (October 1, 2015): 168–81. https://doi.org/10.1016/j.eti.2015.06.001.
16. Sznajder-Katarzyńska, Katarzyna, Magdalena Surma, and Iwona Cieślik. “A Review of Perfluoroalkyl Acids (PFAAs) in Terms of Sources, Applications, Human Exposure, Dietary Intake, Toxicity, Legal Regulation, and Methods of Determination.” *Journal of Chemistry* 2019, no. 1 (January 1, 2019): 2717528. https://doi.org/10.1155/2019/2717528.
17. Ross, Ian, Jeffrey McDonough, Jonathan Miles, Peter Storch, Parvathy Thelakkat Kochunarayanan, Erica Kalve, Jake Hurst, Soumitri S. Dasgupta, and Jeff Burdick. “A Review of Emerging Technologies for Remediation of PFASs.” *Remediation Journal* 28, no. 2 (March 1, 2018): 101–26. https://doi.org/10.1002/rem.21553.
18. Nzeribe, Blossom Nwedo, Michelle Crimi, Selma Mededovic Thagard, and Thomas M. Holsen. “Physico-Chemical Processes for the Treatment of Per- And Polyfluoroalkyl

Substances (PFAS): A Review." *Critical Reviews in Environmental Science and Technology* 49, no. 10 (May 19, 2019): 866–915. https://doi.org/10.1080/10643389.2018.1542916.

19. Higgins, Christopher P. "Treatment Mitigation Strategies for Poly-and Perfluoroalkyl Substances [Project # 4322]," 2016. https://api.semanticscholar.org/CorpusID:43630594.

20. Wanninayake, Dushanthi M. "Comparison of Currently Available PFAS Remediation Technologies in Water: A Review." *Journal of Environmental Management* 283 (April 1, 2021): 111977. https://doi.org/10.1016/j.jenvman.2021.111977.

21. Miaz, Luc T., Merle M. Plassmann, Irina Gyllenhammar, Anders Bignert, Oskar Sandblom, Sanna Lignell, Anders Glynn, and Jonathan P. Benskin. "Temporal Trends of Suspect- and Target-per/Polyfluoroalkyl Substances (PFAS), Extractable Organic Fluorine (EOF) and Total Fluorine (TF) in Pooled Serum from First-Time Mothers in Uppsala, Sweden, 1996–2017." *Environmental Science: Processes & Impacts* 22, no. 4 (2020): 1071–83. https://doi.org/10.1039/C9EM00502A.

22. Ganesan, Sunantha, Chamorn Chawengkijwanich, Mohan Gopalakrishnan, and Dao Janjaroen. "Detection Methods for Sub-Nanogram Level of Emerging Pollutants - Per and Polyfluoroalkyl Substances." *Food and Chemical Toxicology : An International Journal Published for the British Industrial Biological Research Association* 168 (October 2022): 113377. https://doi.org/10.1016/j.fct.2022.113377.

23. Tabassum, Sumaya, Asif Ahmed, Shoeb Rahman, Mayida Rubya Tithi, Maliha Mehjabin, and Jinat Tasnim Dristy. "Recent Advancements in Per- and Polyfluoroalkyl Substances (PFAS) Detection by Sensors and Surface-Enhanced Raman Scattering (SERS) Method: A Review." *Preprints*, January 22, 2024. https://doi.org/10.20944/preprints202401.1557.v1.

24. Fang, Cheng, Xian Zhang, Zhaomin Dong, Liang Wang, Mallavarapu Megharaj, and Ravi Naidu. "Smartphone App-Based/Portable Sensor for the Detection of Fluoro-Surfactant PFOA." *Chemosphere* 191 (January 2018): 381–88. https://doi.org/10.1016/j.chemosphere.2017.10.057.

CHAPTER 5 : GRAPHENE OXIDE ENHANCEMENT OF AGGREGATION-INDUCED EMISSION NANOPARTICLES IN VORTEX FLUIDICS

The pursuit of sensors with exceptional signal sensitivity, especially at trace concentrations, is crucial in the field of fluorescent biosensing. The VFD employs dynamic thin film microfluidic technology, utilising intense micromixing to amplify the emission of a graphene oxide (GO)/fluorophore complex. Operating within a concave-based tube at a low rotational speed of 1500 rpm, the VFD demonstrates its capabilities remarkably. In merely 5 minutes of processing, the resulting emission is five times brighter than that achieved through conventional batch production methods. The VFD's potential for large-scale production highlights its scalability and efficiency. The crux of this technology lies in elucidating the mechanism that governs the adherence of fluorophores to the structural matrix of GO sheets. This understanding is essential for optimising the production process, paving the way for integrating this technology into advanced biosensing methodologies.

Only Figures 5.2 and 5.3 were adapted from the publication of “Tavakoli, Javad, Nikita Joseph, Clarence Chuah, Colin L. Raston, and Youhong Tang. “Vortex Fluidic Enabling and Significantly Boosting Light Intensity of Graphene Oxide with Aggregation Induced Emission Luminogen.” Materials Chemistry Frontiers 4, no. 7 (2020): 2126–30.”

Author contributions: CC and JT performed the literature research, carried out experiments, summarised data, and analysed the contents. NJ carried out AFM experiments. CR and YT provided advice on how to improve the quality of the manuscript. All authors assisted with revising the manuscript before journal submission.

5.1 Introduction

Over the past two decades, the revelation of the aggregation–induced emission (AIE) phenomenon has expanded the fluorescence landscape, particularly with the emergence of non–emissive fluorogenic particles such as tetraphenylethylene (TPE). This phenomenon involves inducing these particles to fluoresce remarkably by forming aggregates. The impact of AIE fluorophores has been felt across diverse fields, including imaging and bio-/chemo-sensing, owing to an awareness of their unique properties.[1]

At the heart of AIE lies the well-accepted concept of the restriction of intramolecular motion. In this paradigm, the fluorescence of AIE fluorophores experiences a significant boost, effectively being ‘turned on’ when placed in a confined space. This intriguing behaviour results from restricting rotor rich AIE’s intramolecular motions, a phenomenon that occurs specifically under these conditions. This understanding of the AIE mechanism expands the realms of fluorescence applications and opens avenues for tailored applications in imaging and sensing technologies.

With its distinct electrical, thermal, mechanical, and optical properties, graphene oxide (GO), a two-dimensional carbon sheet with hydroxyl and epoxy groups on either side of the basal plane and peripheral carboxyl groups, provides a new platform for a wide range of possible applications in chemistry, material science, and medicine.[2, 3, 4, 5] GO is a fluorescence (FL) quenching agent that lowers fluorophore brightness. Energy transfer via non-radiative pathways is stimulated when GO and fluorophores form a strong pi–pi interaction.

AIE/GO has been widely used as a probe for diverse applications.[6-8] A myriad of biomolecules, such as single-strand DNA, has been successfully detected by developing ultrasensitive optical sensors utilising the properties of AIE/GO materials.[9] However, the widespread commercialisation of AIE/GO materials has been impeded by a couple of inherent flaws. Primarily, the intricate nature of chemical reactions involved in the synthesis of AIE/GO materials renders bulk manufacturing economically prohibitive. Despite this challenge, the allure lies in the fact that when biomolecules interact with AIE/GO materials, there is a remarkable enhancement in fluorescence intensity, often reaching up to threefold. Despite this promising feature, the quest for highly responsive and selectively tuned AIE/GO-based sensors persists. Overcoming these challenges is pivotal for unlocking the full potential of AIE/GO in optical sensing, promising innovations in detection methodologies, and paving the way for their widespread adoption in a myriad of applications.[10, 11]

According to one study, GO improved the AIE's FL property; at a given GO concentration, there was a 4-fold increase in relative FL intensity. The work presented here presents a novel dynamic thin-film microfluidic platform called a vortex fluidic device (VFD) for producing GO/AIE material with an unprecedented high FL property. The VFD platform's dynamic thin film is created on a surface that rotates quickly, resulting in substantial shear stress and micro-mixing. [12, 13] By delivering mechanical energy to regulate chemical transformations and adjust the complex's size and characteristics, VFD technology enables processing that goes beyond batch manufacturing and has the potential to be commercialised at a reasonable cost.[14, 15]

In investigating the impacts of shear stress on material formation, we employed three reactor tube types: hemispherical, flat, and concave-based (Figure 5.1). This choice aimed to explore the influence of tube base geometry on fluid flow phenomena, including Coriolis-driven spinning top flow, Faraday waves, and spicular flow. This study then delves into the nuanced interplay of these fluid dynamics, revealing how the base structure affects the Coriolis-driven spinning top flow at different rotational speeds and the coupling with Faraday waves. The exploration sheds light on the complex interactions leading to spicular flow and contributes to a deeper understanding of shear stress effects on material formation in diverse tube configurations.

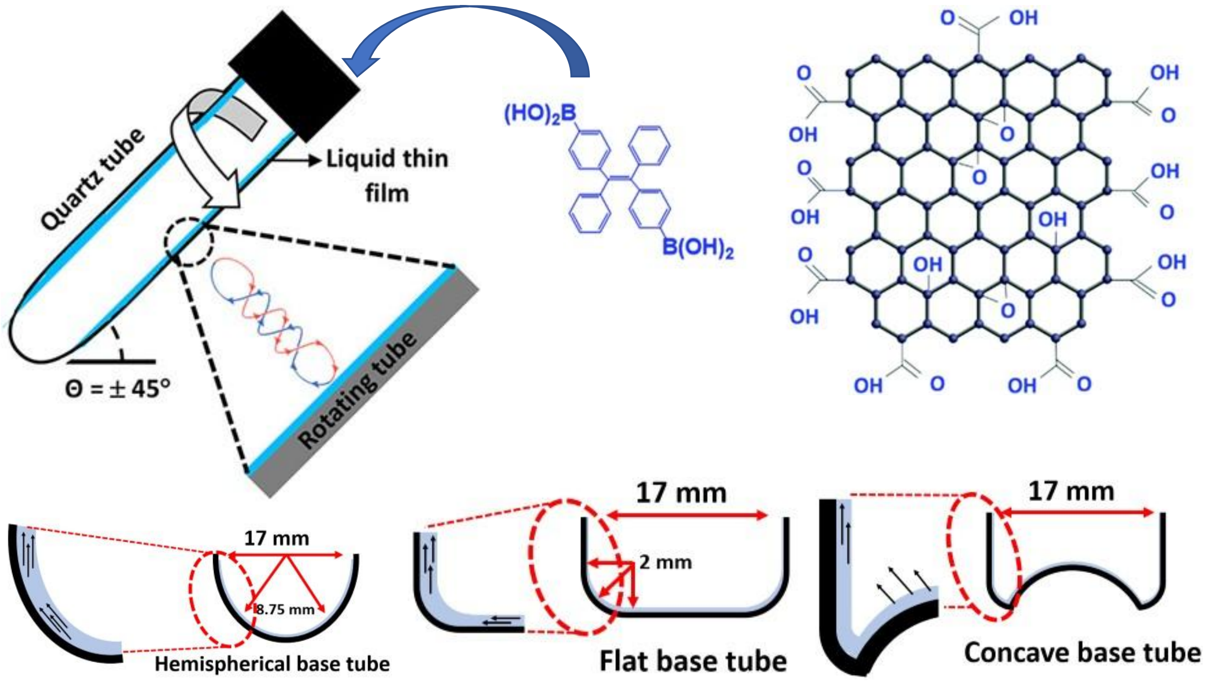

Figure 5.1 Schematic of VFD with TPE-2BA AIE and GO.

Schematic of a vortex fluidic device (VFD) alongside a representation of the chemical structures of TPE-2BA (AIE fluorogen) and GO, three VFD tube geometries including hemispherical, flat, and concaved.

5.2 Materials and Reagents

A single-layer graphene oxide dispersion, water-soluble (CAS No.: 7782-42-5), was procured from ACS Materials. Dimethyl sulfoxide (DMSO) was obtained from Sigma-Aldrich, and TPE-2BA was sourced from AIEgen Biotech Co., Ltd.

5.3 Methods

5.3.1 Sample Preparation

A DMSO stock solution of TPE-2BA with a concentration of 10 mM was prepared. This solution was stored in a refrigerator at 4 °C for subsequent use. Meanwhile, GO solutions in water were prepared at a concentration of 0.0025 mg/mL.

5.3.2 Preparation of TPE-2BA (AIE) and AIE/GO

The TPE-2BA stock solution was transferred to 5 mL volumetric flasks. DMSO was introduced, and the resultant aliquot solutions, under stirring, were mixed with water to yield 100 µM solutions. As for preparing the AIE/GO complex, a solution of TPE-2BA in DMSO (100 µM) was added to the GO solution. The ratio of TPE-2BA in DMSO to GO in water was adjusted to achieve the desired water fraction at 80%.

5.3.3 Experimentation

Fluorescence measurements were conducted on samples prepared at 80% water fraction. The spectrophotometer employed for this purpose was the Cary Eclipse by Agilent Technologies. TPE-2BA particle sizes were measured through a dynamic light scattering method employing a Zetasizer from Malvern. Samples were analysed using an Inspect FEI F50 SEM instrument after drop cast on a silicon wafer and airdried overnight. Images for AFM were acquired using the Bruker Dimension FastScan AFM, with a Nanoscope V controller and Nanoscope control software. Images were recorded using a fluorescent microscope under 365 nm excitation wavelength.

5.4 Results and Discussions

5.4.1 Non-VFD TPE-2BA and GO

In the absence of GO solution, the fluorescence (FL) intensity of TPE-2BA particles at a concentration of 100 µM was strongly influenced by the water-to-DMSO ratio. Specifically, the FL intensity was negligible for water fractions (WF) below 70%, but it increased as WF approached 80% (Figure 5.2). Upon introducing GO at a concentration of 0.0025 mg/mL to the TPE-2BA solution, the particles exhibited significantly enhanced brightness for WF values greater than 70%, with a 13-fold increase in FL relative intensity at WF = 80% compared to that at WF = 50%. When comparing this with TPE-2BA alone, the AIE/GO composite produced at WF = 80% demonstrated a 110% enhancement in FL relative intensity. As indicated by the AIE curve for TPE-2BA aggregates in Figure 5.2, WF = 80% corresponds to the peak FL intensity for TPE-2BA aggregates, a condition that was maintained consistently in subsequent experiments. Processing time was evaluated as a variable in the experiment. However, no significant change was observed in the results until after 5 mins of VFD processing. This suggests that any effects of processing via the VFD did not become apparent within the initial 5-minute period.

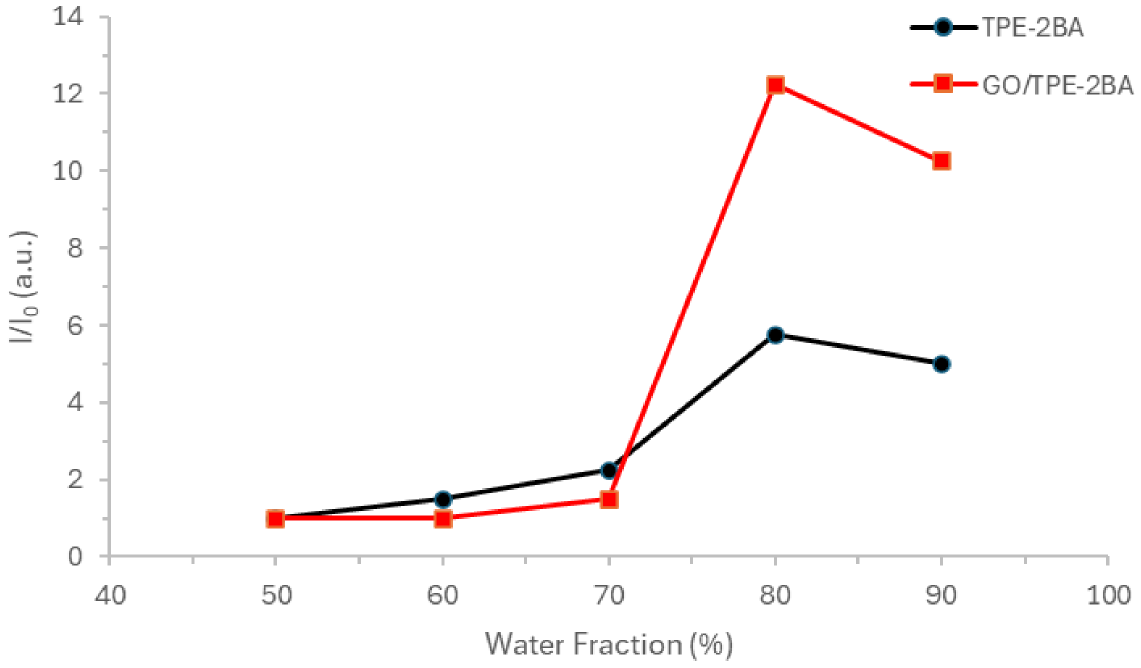

Figure 5.2 Relative FL intensity as a function of WF for TPE-2BA (AIE) and GO at 310 nm excitation. The GO and TPE-2BA concentrations were maintained at 0.0025 mg/mL and 100 µM, respectively. Insets include camera images of AIEgen and AIE/GO solutions at various WFs, captured under UV light at an excitation wavelength of 365 nm.

Further investigation demonstrated that the concentration of GO significantly influences the FL properties of TPE-2BA. The optimal FL intensity was observed at a GO concentration of 0.0025 mg/mL, with the WF held constant at 80% (Figure 5.3). Increasing the GO concentration from 0 to 0.0025 mg/mL enhanced the relative FL intensity of TPE-2BA, rising from 5.9 to 12.3, after which the intensity declined as the GO concentration approached 0.007 mg/mL.

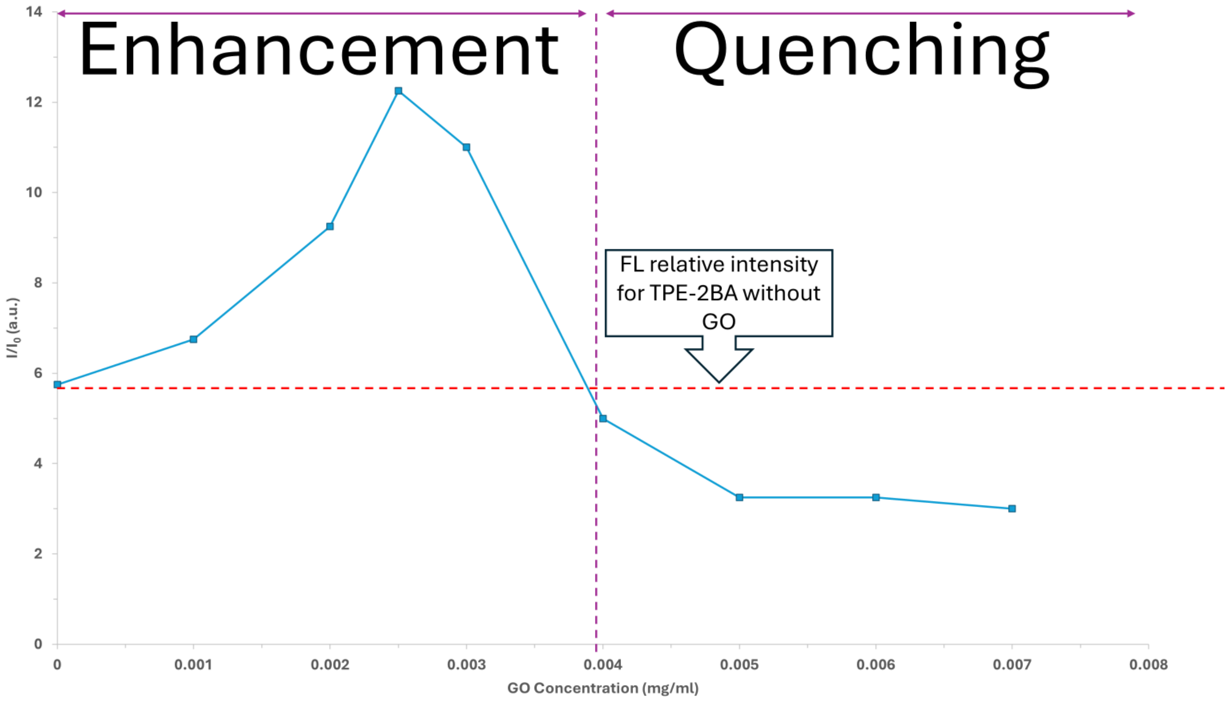

Figure 5.3 Effect of GO on the relative FL intensity of TPE-2BA (AIE) at 310 nm excitation wavelength. Insets display camera images of AIEgen and AIE/GO solutions at varying GO concentrations, captured under UV light with an excitation wavelength of 365 nm. The concentration of TPE-2BA was consistently maintained at 100 µM. Additional insets show camera images of AIEgen and AIE/GO solutions at different water fractions (WF), also captured under UV light at 365 nm.

At low GO concentrations (ranging from 0 to 0.025 mg/mL), the FL intensity of AIE/GO was predominantly governed by the interaction between TPE-2BA aggregates and individual GO sheets. The formation of hydrogen bonds in this context enhanced FL intensity. However, as the GO concentration increased beyond 0.0025 mg/mL, it is likely that TPE-2BA aggregates became encapsulated by multiple GO sheets, leading to FL quenching. This observation aligns with findings from another study, which also noted the influence of GO concentration on the FL intensity of 2,5-diethynylsilole.[6]

5.4.2 VFD-Tuned TPE-2BA

With a TPE-2BA solution at 100 µM, the processing unfolded within the confines of the VFD tube, allowing for the exploration of diverse base geometries under controlled mixing conditions. This apparatus rotated from 1000 to 5000 rpm while tilting at an angle of 45°. The 45° tilt angle was deliberate, grounded in its proven efficacy as the optimal angle for many VFD studies.[16, 17, 18, 19] The resultant effect on the FL is depicted in Figure 5.4. At a WF of 80%, it’s observed that the particle size of TPE-2BA was reduced as the rotational speed increased. This phenomenon aligns seamlessly with earlier research that underscored the VFD’s capability to alter the sizes of AIE nanoparticles, concurrently enhancing FL intensities. A significant reduction in particle size appeared after processing in the concave tube, more than its hemispherical and flat-based equivalent. This was similar for all cases when the rotating speed was gradually increased. This observed behaviour raises the possibility of increased shear stress inside the concave tube, which is thought to result from increased turbulent mixing dynamics.

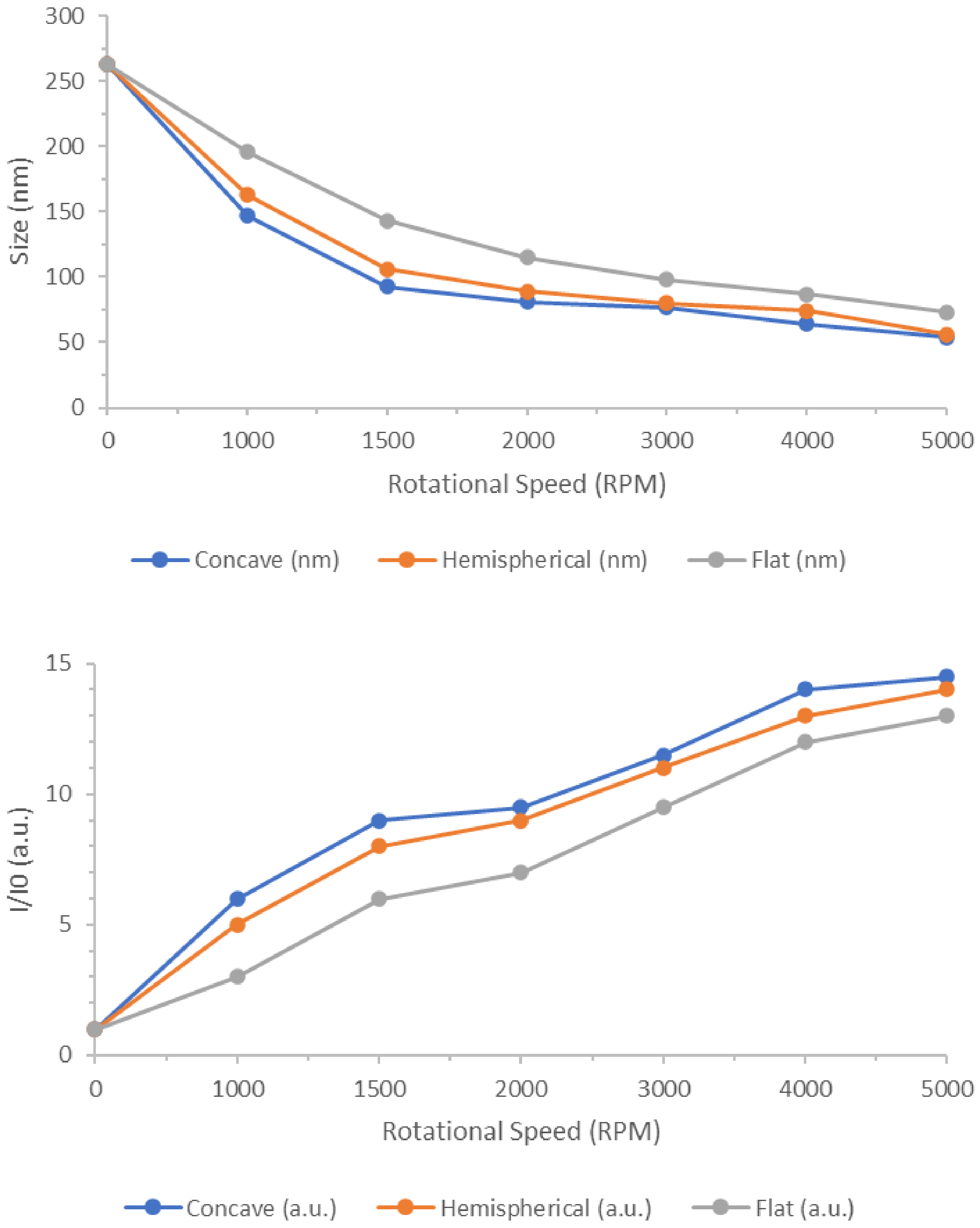

Figure 5.4 Correlation between VFD processing speed against TPE-2BA size and relative intensity. The correlation between TPE-2BA particle size and increase in fluorescence (ex. 310 nm) by increasing the rotational speed at WF = 80% in various base geometries, θ = 45°. Concentration of TPE-2BA is 100 µM.

5.4.3 VFD-Tuned AIE/GO

Interestingly, the FL intensity followed a similar trend to its particle size, with concave-based processing producing brighter probes than both the hemispherical and flat-based processing. Additionally, it was most pronounced at higher rotational speeds, especially those beyond the 3000 rpm. At this juncture, the heightened shear stress was also thought to have played a pivotal role in diminishing the size of the AIE particles. However, Figure 5.5 displayed that the combination of AIE/GO was significantly brighter at a low rotational speed of 1500 rpm.

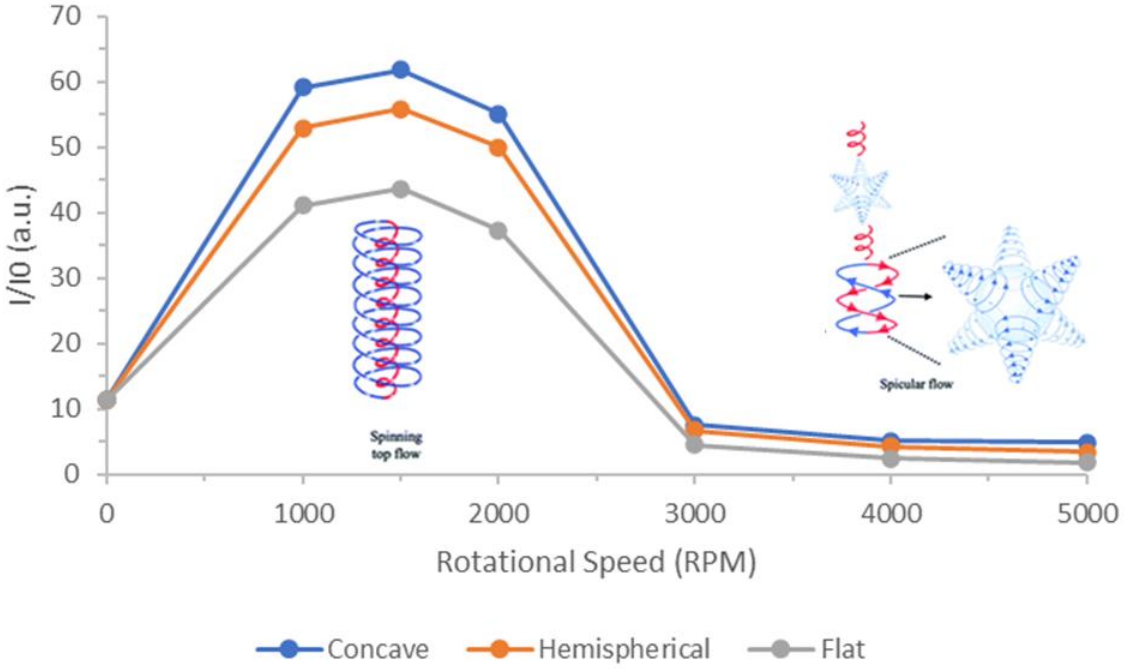

Figure 5.5 Correlation between VFD processing speed and AIE/GO material's relative intensity.

Change in relative FL intensity of AIE/GO material as a function of VFD tube rotational speed in different base geometries at WF = 80%, θ = 45°. The concentrations of TPE-2BA and GO were 100 µM and 0.0025 mg mL^{-1}, respectively.

The FL intensity underwent a notable enhancement as the rotational speed increased from 0 to 3000 rpm. Intriguingly, this amplification was met with an unexpected quenching effect as the speed increased from 3000 to 5000 rpm. The optimal FL intensity was discerned at the sweet spot of 1500 rpm, unveiling a 500% surge in the FL intensity of the AIE/GO compared to its non-VFD counterpart.

Beyond the 3000-rpm threshold, an inverse relationship unfolded, with the GO exerting a suppressive influence on the FL property. Delving deeper into this, scanning electron microscopy (SEM), as depicted in Figure 5.6, uncovered an alteration in the physical morphology of the GO. This structural transformation provides crucial insights into the dynamic interplay between rotational speed and the intermolecular dynamics governing the fluorescence behaviour of the AIE/GO complex.

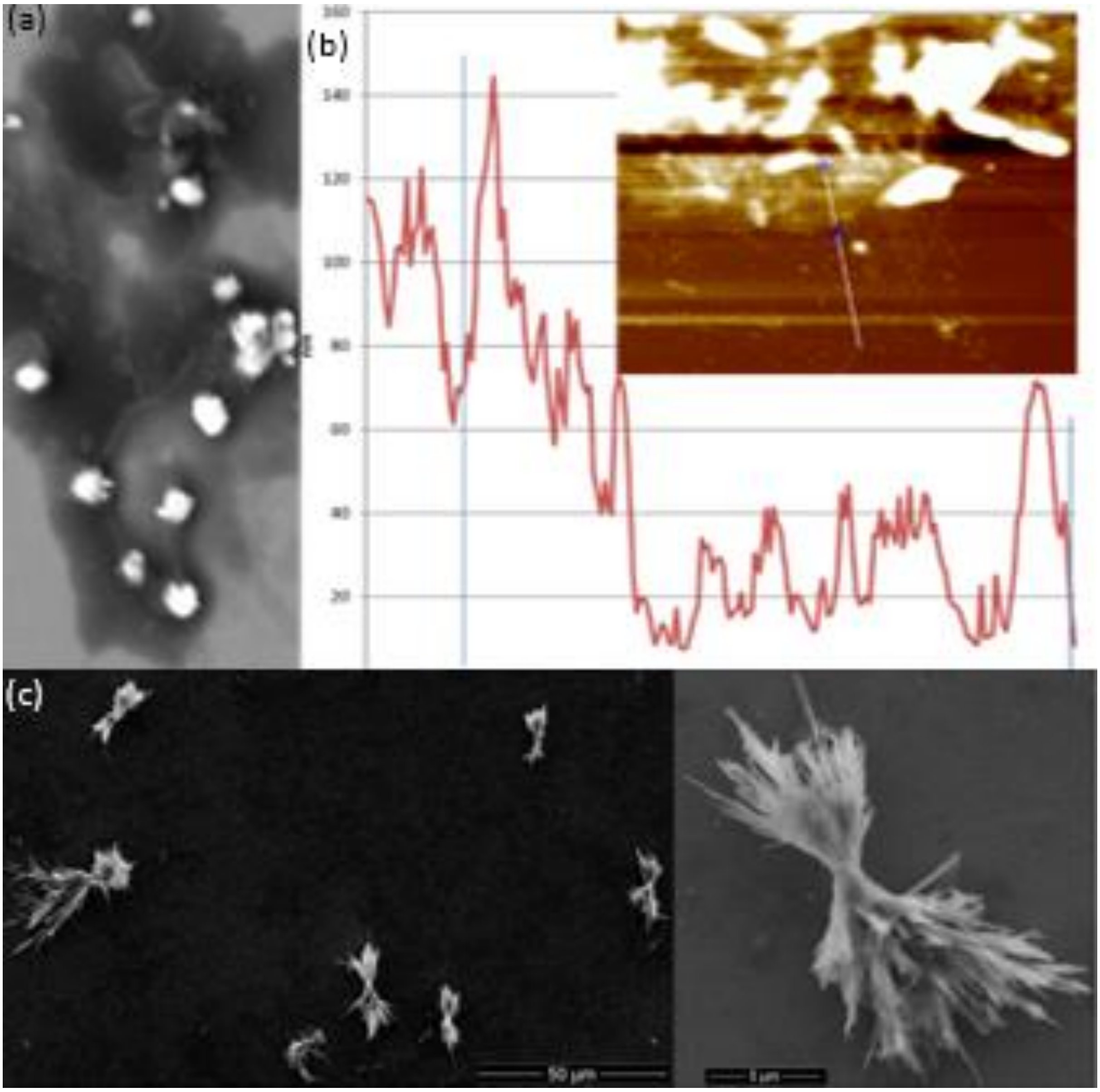

Figure 5.6 SEM and AFM of AIE/GO.

(a) SEM of AIE/GO after processing in the VFD with a concave-based tube at 1500 rpm, WF = 80%. (b) AFM of AIE/GO. (c) SEM of the GO sheets after processing in the VFD with a concave-based tube at 5000 rpm, WF = 80%.

Following VFD processing at 5000 rpm, the GO sheets transformed into a bowtie-like configuration, as depicted in the SEM image presented in Figure 5.6(c). This distinct structural alteration sets it apart from the AIE/GO sheets, which, in contrast, maintained a flat conformation when subjected to processing at 1500 rpm, as evidenced in Figure 5.6(a). The VFD was vital in this transformative process, exhibiting a unique capability to induce a spicular topological fluid flow that imparts a distinctive bowtie twist onto the GO sheets. This phenomenon is achieved through an interplay of factors, including the Coriolis-driven spinning top flow, originating from the curved surface along the tube, and the double helical topological fluid flow, intricately connected with the onset of Faraday waves coupling with the Coriolis-driven spinning top.

Building upon previous investigations into the impact of GO on the fluorescent properties of AIE nanoparticles, two pivotal findings have emerged. Firstly, GO's effective fluorescence quenching distance has been pinpointed at approximately 30 nm, aligning closely with the predicted value for pristine graphene.[21] This revelation provides crucial insight into the spatial limitations of GO’s quenching influence.

Secondly, when the size of AIE nanoparticles is larger than the quenching distance, the adsorption of AIE nanoparticles on both the surface and sides of GO sheets increases the AIE nanoparticle’s fluorescence intensity. The interplay becomes particularly intriguing at higher concentrations of AIE nanoparticles, where the likelihood of encapsulation by GO sheets or proximity to multiple GO sheets is heightened, giving rise to the formation of layered structures.

The structural arrangement of the AIE probes between these bowtie-like GO sheets could lead to the suppression of fluorescence. This suppression is facilitated through the stimulation of energy transfer between the AIE probes and GO sheets via non-radiative pathways.

Moreover, investigations have unveiled the exploitation of shear stress as an energy source for exfoliation.[20, 22] At a low rotational speed within the VFD tube, the induced shear stress functions as a stabilising surfactant, strategically thwarting the tendency of graphene sheets to reassemble or restack. This unique characteristic ensures the production of flat GO sheets, which serve as an ideal canvas for interaction with numerous AIE nanoparticles, thus enhancing their fluorescence properties.

This heightened fluorescence is not uniform across the composite but instead showcases quenching effects precisely where the GO sheets tend to stack together, as illustrated in Figure 5.7. The quenching phenomenon serves as a nuanced visual representation of the interplay between the AIE nanoparticles and the GO sheets, offering valuable insights into the intricacies of this dynamic interaction. This revelation enhances our understanding of the underlying processes and opens avenues for fine-tuning and optimising this technology for diverse applications in material science and beyond.

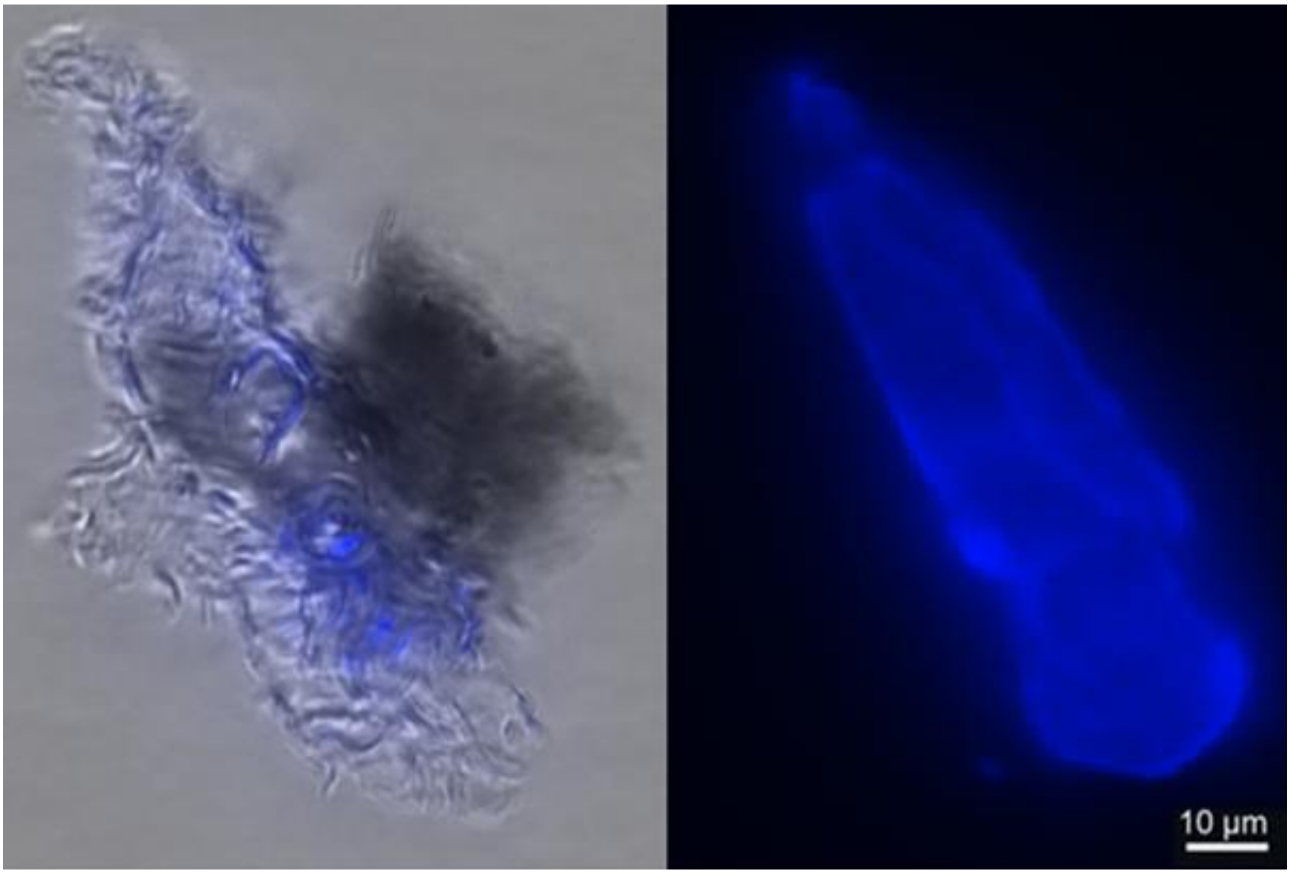

Figure 5.7 FL microscopy of AIE/GO.

AIE/GO material was obtained from light and FL microscope under 365 nm excitation wavelength after processing in the VFD with a concave–based tube at 1500 rpm rotation, WF = 80%.

5.5 Conclusion

Following VFD processing within a concave-based tube at a low rotational speed of 1500 rpm, the formulation of AIE/GO material had a remarkable increase in relative fluorescence intensity. Compared to AIE nanoparticles alone, this process procures brightly fluorescent AIE/GO material. Numerous chemical processes that require the interplay between solid and liquid phases could benefit from the technique presented. One such example is diagnostics, whereby molecular recognition frequently necessitates binding molecules in the liquid phase to bind to a target attached to a solid substrate. This VFD processing, which operates at a low 1500 rpm, may help to speed up the equilibration of sluggish binding events. Furthermore, the strategy detailed here could be adapted for industrial and clinical spaces due to its cost-effectiveness.

5.6 References

1. Han, Ting, Xinnan Wang, Dong Wang, and Ben Zhong Tang. “Functional Polymer Systems with Aggregation-Induced Emission and Stimuli Responses.” *Topics in Current Chemistry* 379, no. 1 (January 11, 2021): 7. https://doi.org/10.1007/s41061-020-00321-7.
2. Zhang, Minwei, Chengyi Hou, Arnab Halder, Hongzhi Wang, and Qijin Chi. “Graphene Papers: Smart Architecture and Specific Functionalization for Biomimetics, Electrocatalytic Sensing and Energy Storage.” *Materials Chemistry Frontiers* 1, no. 1 (2017): 37–60. https://doi.org/10.1039/C6QM00145A.
3. Cao, Xianyi, Arnab Halder, Yingying Tang, Chengyi Hou, Hongzhi Wang, Jens Øllgaard Duus, and Qijin Chi. “Engineering Two-Dimensional Layered Nanomaterials for Wearable Biomedical Sensors and Power Devices.” *Materials Chemistry Frontiers* 2, no. 11 (2018): 1944–86. https://doi.org/10.1039/C8QM00356D.
4. Chen, Ying, Yue Cao, Cheng Ma, and Jun-Jie Zhu. “Carbon-Based Dots for Electrochemiluminescence Sensing.” *Materials Chemistry Frontiers* 4, no. 2 (2020): 369–85. https://doi.org/10.1039/C9QM00572B.
5. Zhang, Guofeng, Yuyang Han, Changxiang Shao, Nan Chen, Guoqiang Sun, Xuting Jin, Jian Gao, Bingxue Ji, Hongsheng Yang, and Liangti Qu. “Processing and Manufacturing of Graphene-Based Microsupercapacitors.” *Materials Chemistry Frontiers* 2, no. 10 (2018): 1750–64. https://doi.org/10.1039/C8QM00270C.
6. Qi, Xiaoying, Hai Li, Jacky Wing Yip Lam, Xintong Yuan, Jun Wei, Ben Zhong Tang, and Hua Zhang. “Graphene Oxide as a Novel Nanoplatform for Enhancement of Aggregation-Induced Emission of Silole Fluorophores.” *Advanced Materials* 24, no. 30 (August 8, 2012): 4191–95. https://doi.org/10.1002/adma.201200026.
7. Zhu, Huangtianzhi, Liqing Shangguan, Bingbing Shi, Guocan Yu, and Feihe Huang. “Recent Progress in Macrocyclic Amphiphiles and Macrocyclic Host-Based Supra-Amphiphiles.” *Materials Chemistry Frontiers* 2, no. 12 (2018): 2152–74. https://doi.org/10.1039/C8QM00314A.
8. Su, Wen, Hao Wu, Huimin Xu, Yang Zhang, Yunchao Li, Xiaohong Li, and Louzhen Fan. “Carbon Dots: A Booming Material for Biomedical Applications.” *Materials Chemistry Frontiers* 4, no. 3 (2020): 821–36. https://doi.org/10.1039/C9QM00658C.
9. Tyagi, Abhishek, Kin Leung Chu, Irfan Haider Abidi, Aldrine Abenoja Cagang, Qicheng Zhang, Nelson L. C. Leung, Engui Zhao, Ben Zhong Tang, and Zhengtang Luo. “Single-Probe Multistate Detection of DNA via Aggregation-Induced Emission on a Graphene Oxide Platform.” *Acta Biomaterialia* 50 (March 1, 2017): 334–43. https://doi.org/10.1016/j.actbio.2016.12.003.
10. Mei, Ju, Yuning Hong, Jacky W. Y. Lam, Anjun Qin, Youhong Tang, and Ben Zhong Tang. “Aggregation-Induced Emission: The Whole Is More Brilliant than the Parts.”

Advanced Materials (Deerfield Beach, Fla.) 26, no. 31 (August 20, 2014): 5429–79. https://doi.org/10.1002/adma.201401356.

11. Li, Xing, Ke Ma, Shoujun Zhu, Shiyu Yao, Zhaoyang Liu, Bin Xu, Bai Yang, and Wenjing Tian. “Fluorescent Aptasensor Based on Aggregation-Induced Emission Probe and Graphene Oxide.” *Analytical Chemistry* 86, no. 1 (January 7, 2014): 298–303. https://doi.org/10.1021/ac403629t.
12. Britton, Joshua, Justin M. Chalker, and Colin L. Raston. “Rapid Vortex Fluidics: Continuous Flow Synthesis of Amides and Local Anesthetic Lidocaine.” *Chemistry – A European Journal* 21, no. 30 (July 20, 2015): 10660–65. https://doi.org/10.1002/chem.201501785.
13. Tavakoli, Javad, Colin L. Raston, Yong Ma, and Youhong Tang. “Vortex Fluidic Mediated One-Step Fabrication of Polyvinyl Alcohol Hydrogel Films with Tunable Surface Morphologies and Enhanced Self-Healing Properties.” *Science China Materials* 63, no. 7 (July 1, 2020): 1310–17. https://doi.org/10.1007/s40843-020-1301-y.
14. Britton, Joshua, Keith A. Stubbs, Gregory A. Weiss, and Colin L. Raston. “Vortex Fluidic Chemical Transformations.” *Chemistry (Weinheim an Der Bergstrasse, Germany)* 23, no. 54 (September 27, 2017): 13270–78. https://doi.org/10.1002/chem.201700888.
15. Sitepu, Eko K., Kendall Corbin, Xuan Luo, Scott J. Pye, Youhong Tang, Sophie C. Leterme, Kirsten Heimann, Colin L. Raston, and Wei Zhang. “Vortex Fluidic Mediated Direct Transesterification of Wet Microalgae Biomass to Biodiesel.” *Bioresource Technology* 266 (October 2018): 488–97. https://doi.org/10.1016/j.biortech.2018.06.103.
16. Tavakoli, Javad, Nikita Joseph, Clarence Chuah, Colin L. Raston, and Youhong Tang. “Vortex Fluidic Enabling and Significantly Boosting Light Intensity of Graphene Oxide with Aggregation Induced Emission Luminogen.” *Materials Chemistry Frontiers* 4, no. 7 (2020): 2126–30. https://doi.org/10.1039/D0QM00270D.
17. Britton, Joshua, Stuart B. Dalziel, and Colin L. Raston. “Continuous Flow Fischer Esterifications Harnessing Vibrational-Coupled Thin Film Fluidics.” *RSC Advances* 5, no. 3 (2015): 1655–60. https://doi.org/10.1039/C4RA11777H.
18. Alharbi, Thaar M. D., Matt Jellicoe, Xuan Luo, Kasturi Vimalanathan, Ibrahim K. Alsulami, Bediea S. AL Harbi, Aghil Igder, et al. “Sub-Micron Moulding Topological Mass Transport Regimes in Angled Vortex Fluidic Flow.” *Nanoscale Advances* 3, no. 11 (2021): 3064–75. https://doi.org/10.1039/D1NA00195G.
19. Tavakoli, Javad, Scott Pye, A. H. M. Mosinul Reza, Ni Xie, Jian Qin, Colin L. Raston, Ben Zhong Tang, and Youhong Tang. “Tuning Aggregation-Induced Emission Nanoparticle Properties under Thin Film Formation.” *Materials Chemistry Frontiers* 4, no. 2 (2020): 537–45. https://doi.org/10.1039/C9QM00585D.

20. Alharbi, Thaar M.D., David Harvey, Ibrahim K. Alsulami, Nazila Dehbari, Xiaofei Duan, Robert N. Lamb, Warren D. Lawrance, and Colin L. Raston. “Shear Stress Mediated Scrolling of Graphene Oxide.” *Carbon* 137 (October 1, 2018): 419–24. https://doi.org/10.1016/j.carbon.2018.05.040.
21. Swathi, R. S., and K. L. Sebastian. “Long Range Resonance Energy Transfer from a Dye Molecule to Graphene Has (Distance)(-4) Dependence.” *The Journal of Chemical Physics* 130, no. 8 (February 28, 2009): 086101. https://doi.org/10.1063/1.3077292.
22. Chen, Xianjue, John F. Dobson, and Colin L. Raston. “Vortex Fluidic Exfoliation of Graphite and Boron Nitride.” *Chemical Communications* 48, no. 31 (2012): 3703–5. https://doi.org/10.1039/C2CC17611D.

CHAPTER 6 : PRELIMINARY INVESTIGATIONS INTO WATER AND TOLUENE RODS

6.1 Abstract

Although theoretically possible, a clathrate containing water and toluene is not common. These compounds are examples of inclusion complexes, in which host molecules form complex structures resembling cages that can trap guest molecules inside them. In this situation, the water molecules function as the builders, creating a cage for the toluene molecules inside. The formation of clathrate structures depends on the coordination of molecular sizes and shapes, which guarantees the harmonious coexistence of host and guest species. The difficulty lies in the fact that cages of water molecules are only capable of holding molecules of particular sizes and forms. Toluene molecules' larger size poses a challenge that might prevent them from integrating well into the water-derived cages. As such, it seems unlikely that clathrates would spontaneously develop between water and toluene in normal conditions. However, it becomes possible to induce the development of such a clathrate in high-pressure settings, such as those created by the vortex fluidic device (VFD). In these circumstances, the shear stress provided by the VFD might overcome the natural steric obstacles and promote the formation of water cages that can hold toluene. Therefore, while being unorthodox, the realisation of a water-toluene clathrate beckons upon further testing beyond this preliminary investigation.

6.2 Introduction

A class of substances known as clathrate hydrates is distinguished by a lattice structure in which guest molecules, usually gases or liquids, are encapsulated by water molecules. The integrity of this complex molecular structure depends on these guest molecules. Without their stabilising effect, the lattice would give way to the fluidity of liquid water. Remarkably, a wide range of gases, including low molecular weight species like O_2, H_2, N_2, CO_2, CH_4, and H_2S, as well as heavier ones such as Ar, Kr, and Xe, and some higher hydrocarbons and freons, show a tendency to form hydrates when the proper pressure is met.

Although mistakenly thought of as chemical compounds, clathrate hydrates do not fit the conventional description since the guest molecules and host lattice do not establish covalent bonds. Rather than chemical reactions, their formation and breakdown appear as first-order phase transitions, a distinction essential to comprehend their behaviour. Even though they have been known about since Sir Humphry Davy's groundbreaking discovery in 1810, who found that water was a primary component of what was earlier thought to be solidified chlorine [1], the complex molecular processes that control their synthesis and breakdown are still poorly understood [2, 3, 4], underscoring the continuous search for deeper comprehension.

Clathrates are molecular architecture widely found in nature, with an example of their natural occurrence being seen in the ocean's depths, where methane clathrate deposits contain 6.4 trillion (6.4 x 10^{12}) tonnes of methane.[5] This natural gas hydrate reservoir presents an enticing opportunity for energy extraction, leading many countries to launch focused programs to realise this enormous potential.[6]

Clathrate hydrates are helpful not only as an energy source but also as essential enablers in many other fields of technology. Their diverse uses include gas storage, saltwater desalination, and even carbon dioxide capture and storage projects.[7] Additionally, their usefulness goes beyond traditional energy paradigms, as, among other new uses, they are employed as cooling mediums for data centres and district cooling systems.

As hydrocarbon clathrates tend to build inside gas pipes and create obstructions, they present significant issues to the petroleum sector. Using deep-sea carbon dioxide clathrate deposition as a tactical countermeasure has become a workable way to reduce the amount of this greenhouse gas in the atmosphere and lessen the effects of climate change. Furthermore, clathrates are found in several celestial entities, including moons, trans-Neptunian objects, and outer planets. In these worlds, they are capable of retaining gases at elevated temperatures.[8]

There isn't widespread consensus over the existence of clathrates made of water and toluene. Furthermore, it is still unclear if water-toluene clathrate synthesis is theoretically feasible. This uncertainty arises from the different molecular sizes of toluene and water. Water molecules have an affinity to form well-defined cage structures with exact dimensions that can easily accommodate smaller guest molecules. Still, toluene's weight could hinder its smooth integration into these aqueous cages, preventing clathrate production. As a result, academic studies of clathrate phenomena often focus on studies of small guest species like methane, which blend well with the natural architecture of water cages.

This idea came about as fullerene C_{60} nanotubules were synthesised without surfactants in the vortex fluidic device (VFD), with shear acting as a driving force.[9] Figure 6.1 illustrates the VFD's capacity to control the dynamics of self-assembly and radial growth of nanotubular structures originating from the *fcc* phase of C_{60}. This accomplishment is noteworthy for being free of stabilising chemicals, eliminating the problem of solvent molecules becoming trapped during crystallisation.

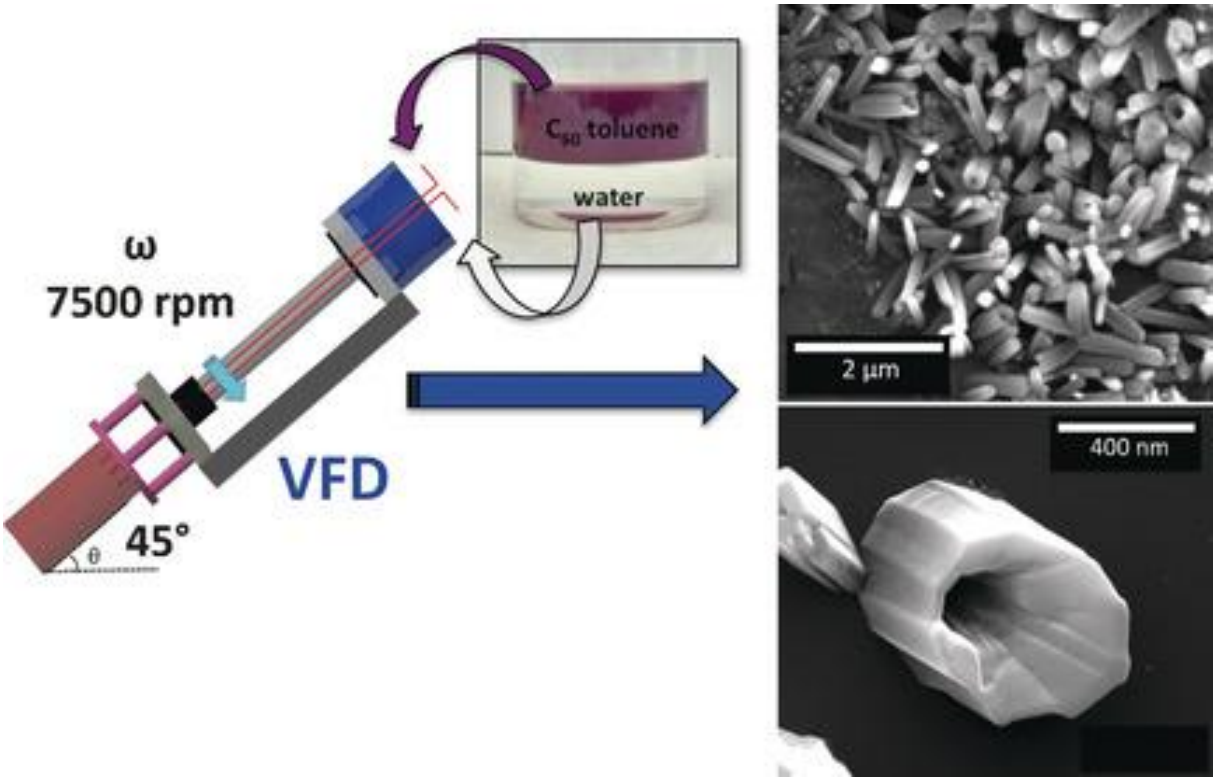

Figure 6.1 Self-Assembly of C_{60} through VFD's shear stress.

Without stabilising chemicals, shear stress in a VFD efficiently regulates the self-assembly of C_{60} molecules into nanotubules. Uniform pores were developed on the surface of nanotubules produced in the *fcc* phase of C_{60}. [9]

The resulting spontaneous C_{60} nanotubules form quickly in an insoluble solvent medium of toluene and water, forming micron-sized tubular structures with a hollow core that ranges in diameter from 100 to 400 nm. These nano-porous microcrystals are inclined to selectively adsorb various solvent molecules, highlighting their usefulness in sensitive molecular species discrimination.

After 30 minutes of processing, nanotubules appeared on their own and were easily collected without the need for further processing. This procedure produced pure *fcc* C_{60} with no trapped solvents, which is noteworthy. Unlike previous findings that require using surfactants and solvent evaporation by heating, this approach provides a direct and solvent-free pathway to creating these nanotubules.

This was further investigated in a later paper that used toluene as the solvent medium rather than the immiscible solvent combination of water and toluene used in the earlier work. Shear tension caused fullerene C_{60} to crystallise, forming characteristic rods and spicules as a consequence, as seen in Figure 6.2.[10] These rods and spicules only appeared at rotational speeds higher than 6000 rpm, indicating that they are dependent on conditions that promote significant mass transfer in the liquid phase. Under thermodynamic equilibrium, they would dissolve if these circumstances weren't maintained. As a result, the formation of spicules can be understood as an expression of fluid dynamics, showing an interaction between double helical flow and spinning top flow, as seen in Figure 6.3.[10]

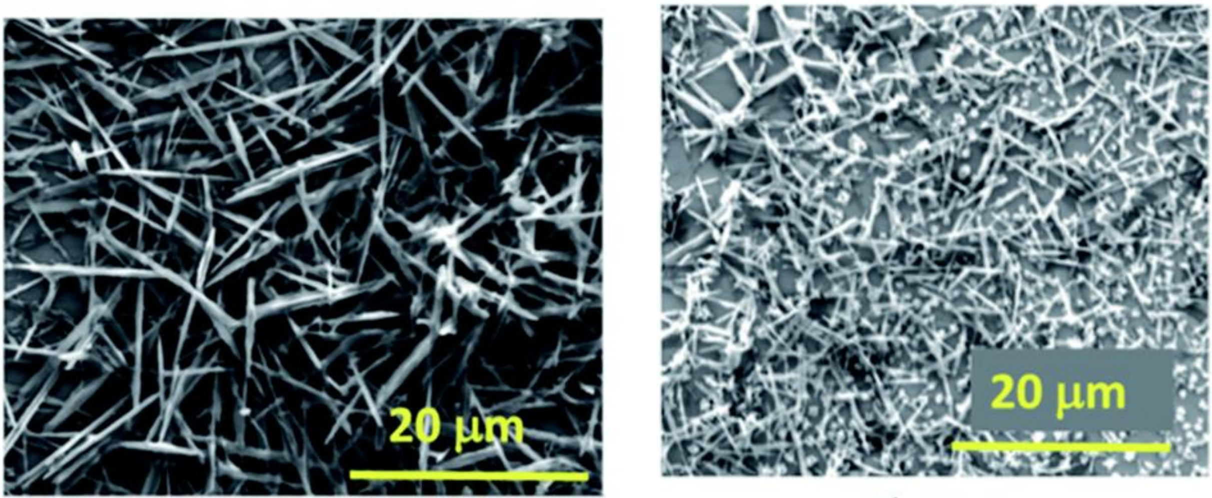

7k rpm

6k rpm

Figure 6.2 Moulding nano-carbon material.

Shear stress-induced crystallisation and self-assembly of C60 in toluene (0.1 mg mL-1, θ 45°), affording rods and mixtures of spicules and rods at 7000 and 6000 rpm, corresponding to the transition from specular to double-helical flow and helical flow, respectively. [10]

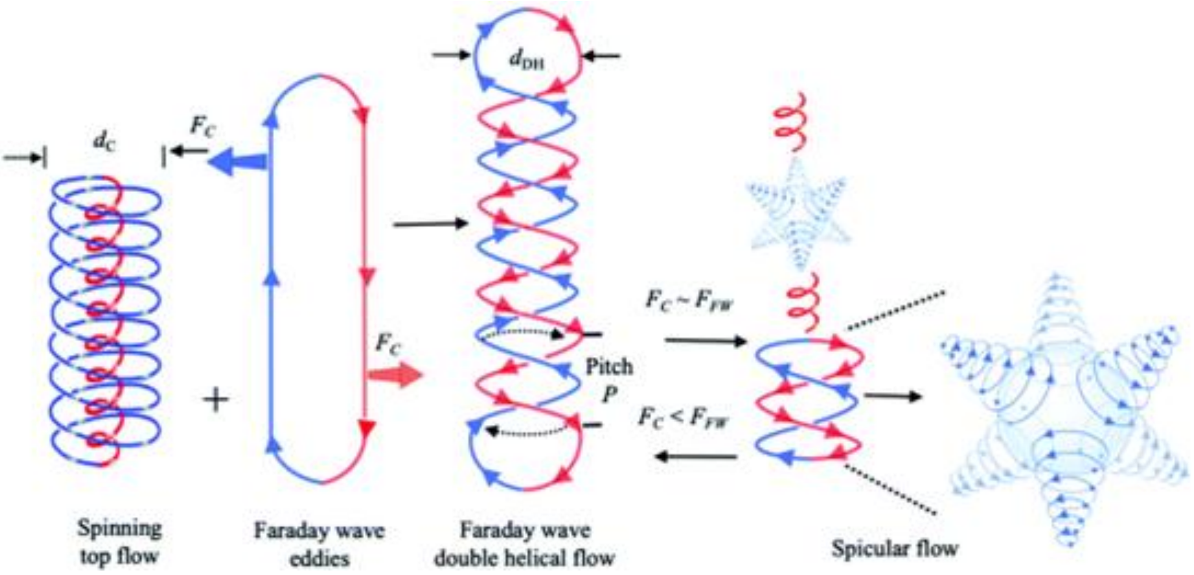

Figure 6.3 VFD fluid flow behaviours.

A representation of the fluid flow behaviour for the spinning top and double-helical flow from Faraday waves into the spicular flow. [10]

After close inspection, the rods have curved surfaces, as seen in Figure 6.2 above. This finding is consistent with the theory that they originate in the shearing dynamics seen in the double-helical liquid flow. This contrasts the traditional crystallisation method, guided by clearly defined crystallographic facets. Notably, these rods tend to dissolve again when they are not in the previously described conditions. This effect is especially noticeable when the rotational speed is above a threshold of 6000 rpm, which reduces the spinning top flow's dominating influence caused by Coriolis forces. This decrease in flow dominance is increasingly noticeable as the film gets thinner. Furthermore, these rods' diameter, about 0.5 μm, resembles the double-helix structure's overall diameter, supporting their close relationship.

This chapter will use this relationship to investigate the formation of water and toluene rod structures, explore the complexities of biphasic liposomes and liposomes down to monomeric phospholipids, conclude whether clathrate hydrates of water and toluene were formed, and discuss directions for further studies.

6.3 Materials and Reagents

1-Palmitoyl-2-oleoyl-sn-glycerol-3-phosphocholine (POPC) was purchased from Sapphire Bioscience (NSW, Australia). Toluene was purchased from Sigma-Aldrich and Milli-Q water was utilised for all the experiments.

6.4 Methods

6.4.1 Sample Preparation for Water and Toluene Rod Structures

A 1:1 mL ratio of water and toluene was processed in a VFD at an optimised speed of 7500 rpm for 30 mins at a 45° tilt angle. One drop from the interface of toluene and water was then drop-cast onto a silicon wafer for SEM.

6.4.2 Sample Preparation for Biphasic Liposomes

A phospholipid suspension of 1 mg mL^{-1} in Milli-Q water and toluene at a 1:1 mL ratio was processed in a VFD at an optimised speed of 7500 rpm for 30 mins at a 45° tilt angle. One drop from the toluene and water layer was then drop-cast onto a silicon wafer for SEM.

6.4.3 Sample Preparation of Liposomes for Small-Angle Neutron Scattering (SANS)

Solutions of 0.1 wt.% POPC phospholipid in D_2O was prepared. 2 mL of solution was added into a quartz VFD tube OD 20 mm in confined mode at lower speeds of 3800, 4000, 4500, and 5000 rpm, while 1 mL of solution was added for higher speeds such as 7000, 8000, and 9000 rpm. Then, every sample gathered from the VFD tests was characterised using traditional SANS methods. A raw sample was also subjected to SANS characterisation as a benchmark for comparison analysis.

6.4.4 Sample Analysis: Scanning Electron Microscopy (SEM)

Samples were characterised using an Inspect FEI F50 SEM instrument. Sample preparation for SEM was as follows: as-prepared sample was drop-cast onto a silicon wafer and air dried.

6.4.5 Sample Analysis: SANS Data Acquisition

All Small-Angle Neutron Scattering (SANS) experiments were conducted on the Bilby instrument at ANSTO, Lucas Heights, Australia. The VFD was mounted on an XYZ goniometer stage, which was equipped with an aluminium shield containing a silicon window to allow the neutron beam to pass through. The stage was precisely aligned with the neutron beam, ensuring that the beam centre was positioned 3 cm above the base of the VFD tube.

Data collection on the Bilby instrument[11] utilised the VFD tube in a time-of-flight configuration, employing neutron wavelengths in the range of $\lambda = 2–20$ Å with a wavelength resolution of $\frac{\Delta\lambda}{\lambda} - 0.12$. Sample-detector distances were set at 3.5 m, 4.5 m, and 7.0 m, allowing for coverage of the full q-range from 0.00216 $Å^{-1}$ to 0.36309 $Å^{-1}$, where the scattering vector q is defined as $q = (4\pi/\lambda)\sin(\theta/2)$, with λ representing the neutron wavelength and θ the scattering angle. Measurements were conducted at room temperature (~20 °C) without active temperature control.

All datasets were corrected for solvent scattering using D_2O blanks measured at the same speed, empty quartz tube scattering, and detector sensitivity. The data were normalized to an absolute scale using attenuated direct beam transmission measurements. The reduced 2D data were radially averaged to produce the 1D scattering curve. For data reduction, Mantid software[12] was employed, while data fitting was performed using the NIST macros for Igor Pro (Wavemetrics, Portland, OR, USA).[13]

6.5 Results and Discussions

6.5.1 Water and Toluene Rod Structures

Rods of water and toluene were fabricated in the VFD by utilising the Faraday wave double-helical flow found at high rotational speeds. The resulting structures illustrated in Figure 6.4 were produced by VFD processing at 7500 rpm for 30 mins at a tilt angle θ of 45°.

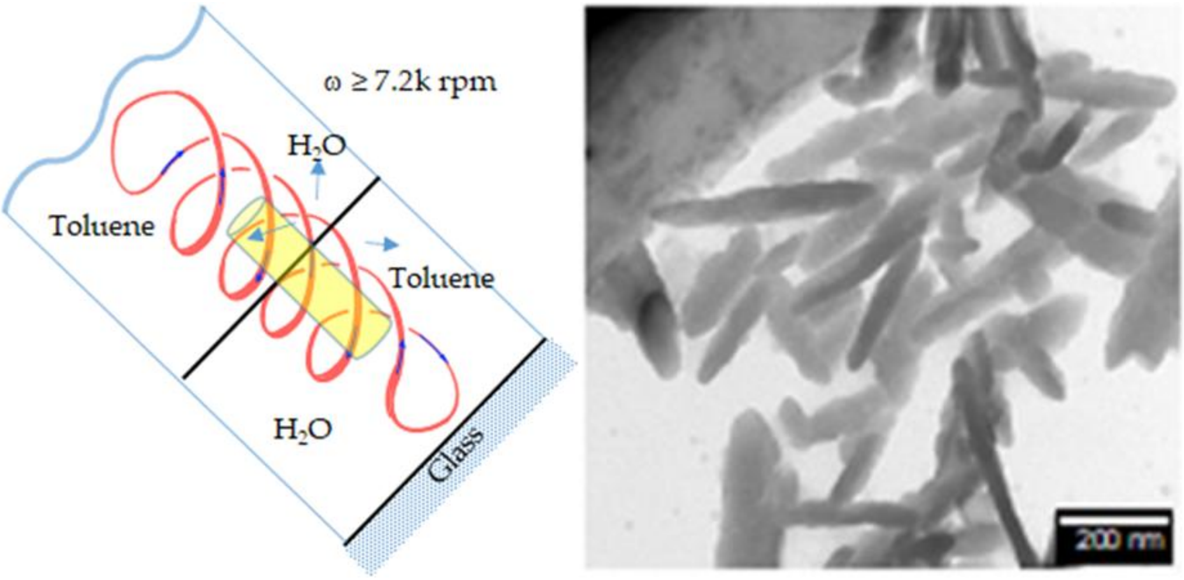

Figure 6.4 Schematic and SEM of water and toluene rod structures post VFD processing.

These rod-like formations are only obtainable at high rotational speeds, indicating that they depend on circumstances that allow for significant mass transfer between the insoluble liquid phases of toluene and water. It is important to emphasise that these rod formations would dissolve under thermodynamic equilibrium if these specific conditions were not maintained. The signature of water and toluene can further explain these dynamics, as seen in Figure 6.5 below.[14]

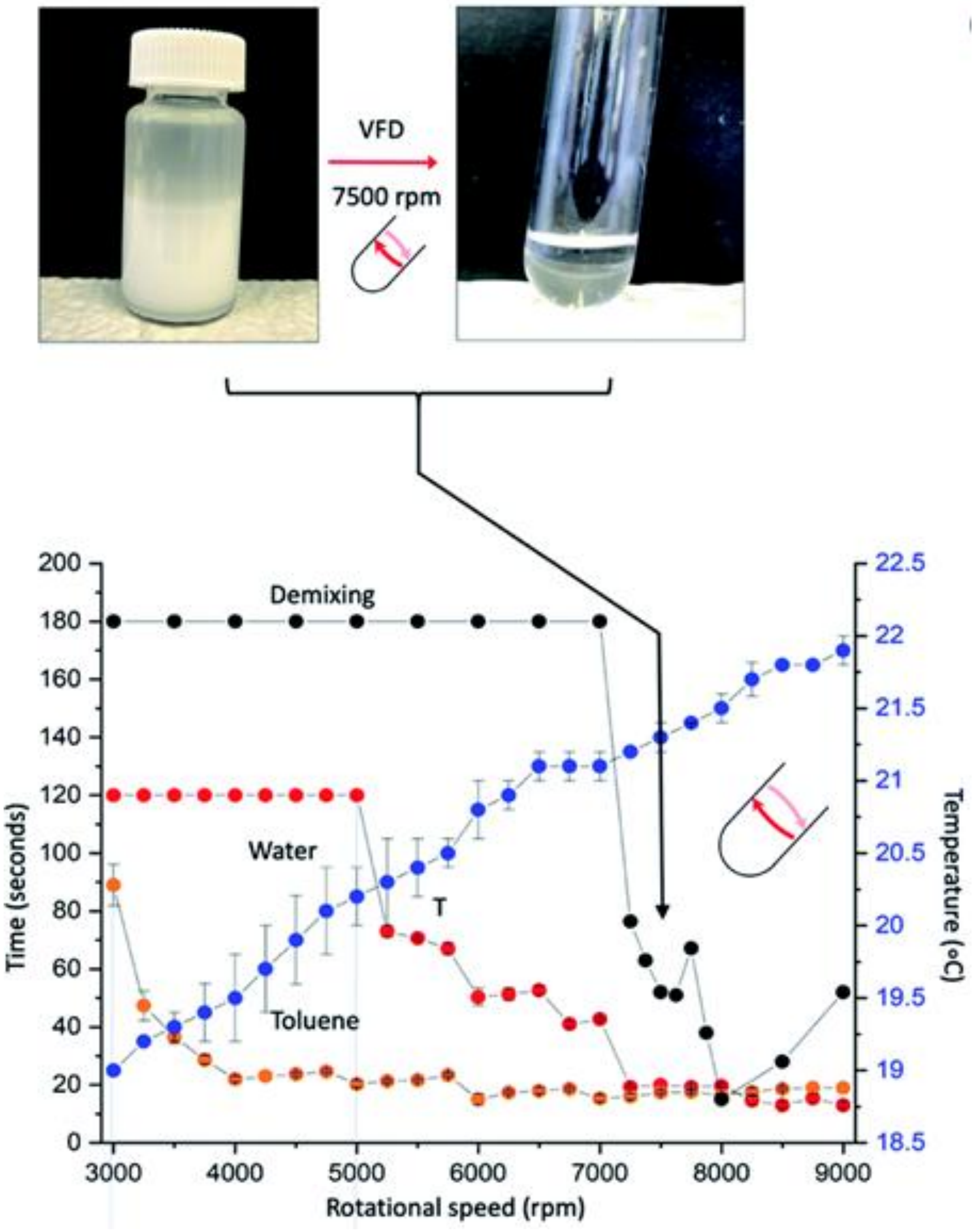

Figure 6.5 Mixing an immiscible system of water and toluene.[14]

Photographs depict the emulsified mixture of water and toluene, as well as the separated liquids following VFD processing at 7500 rpm with a 45° tilt angle, using a quartz tube with an outer diameter of 20 mm, an inner diameter of 17.5 mm, and a length of 18.5 cm. The thermal response and mixing times were recorded for a 1:1 mixture of water and toluene in a hemispherical base tube. The mixing times, indicated in red for water and orange for toluene, correspond to the duration required for a drop of water or toluene, each containing a small amount of dye, to uniformly mix halfway up the preformed film as the tube rotates at a specified speed. The temperature, represented in blue, was monitored at the midpoint of the tube using an infrared camera. The demixing time, shown in black, refers to the time needed for 2 mL of a preformed emulsion of toluene and water placed in the VFD to completely separate into distinct phases.

Examining the mixing dynamics of a 1:1 mixture of phase-separated water and toluene contributes significantly to understanding the complex nature of topological fluid processes.[14] The temperature differences in the combined system are uninformative compared to their individual counterparts. The sharp temperature changes usually seen in single liquid systems suggest substantial changes in topological fluid dynamics.[10]

However, a detailed analysis of the mixing behaviour provides valuable insights into the underlying topological fluid dynamics. The entry of a droplet of toluene with dye into the bottom of the tube serves as an example, demonstrating similar mixing periods in the toluene layer regardless of the existence of an underlying water layer. Notably, the synchronisation of demixing durations between water-toluene emulsions at 7500 rpm mimics the mixing timings seen when a separate water phase is absent. This convergence points to the crucial role of double helical flow mechanisms in demixing processes, where the differentiation between these flows in water and toluene coincides and results in high mass transfer occurrences.

However, it’s essential to recognise that water-toluene rods are inherently unstable, which makes them vulnerable to dissipation. Liposomes will be used as a strategic intervention to address this issue and to improve stability for further investigations.

6.5.2 Biphasic Liposome Rod Structures

Biphasic liposome rods were fabricated in the VFD utilising the Faraday wave double-helical flow present at a high rotational speed. Figure 6.6 illustrates the resultant biphasic liposome rods after VFD processing at 7500 rpm for 30 mins at a tilt angle θ of 45°.

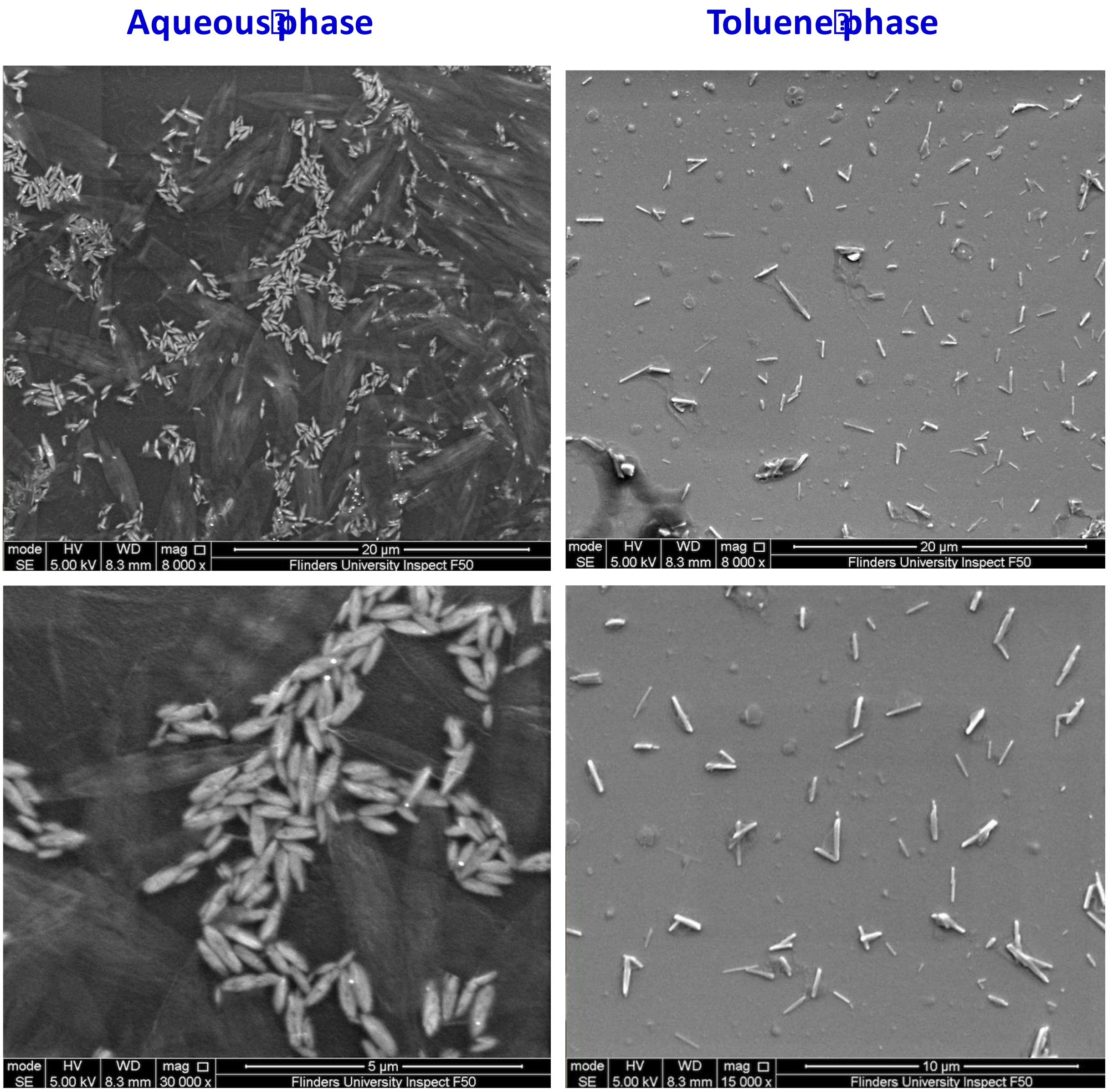

Figure 6.6 SEM of biphasic liposome rods obtained post VFD processing.

Notably, the formation of biphasic liposome rod-like structures in the system was only obtained at high rotational speeds. This observation emphasises how critically their production depends on conditions that allow significant mass exchange between the immiscible water and toluene liquid phases.

6.5.3 SANS Analysis of Liposomes

The self-assembly of these rods in dynamic thin films under high shear in the VFD is inherently complex. Utilising in situ techniques is then necessary to understand the mechanism behind rod creation and provide significant insights. Thus, in situ SANS technology is employed to investigate the shapes and sizes of phospholipid structures created in shear conditions on length scales ranging from a few nanometres to several hundred nanometres.[15] This in situ VFD technique offers a dynamic view of the process as it is specifically designed for real-time nano-encapsulation.[16] Data was collected at ANSTO using a VFD tube with solutions containing 0.1 wt.% POPC in D_2O, as illustrated in Figure 6.7.

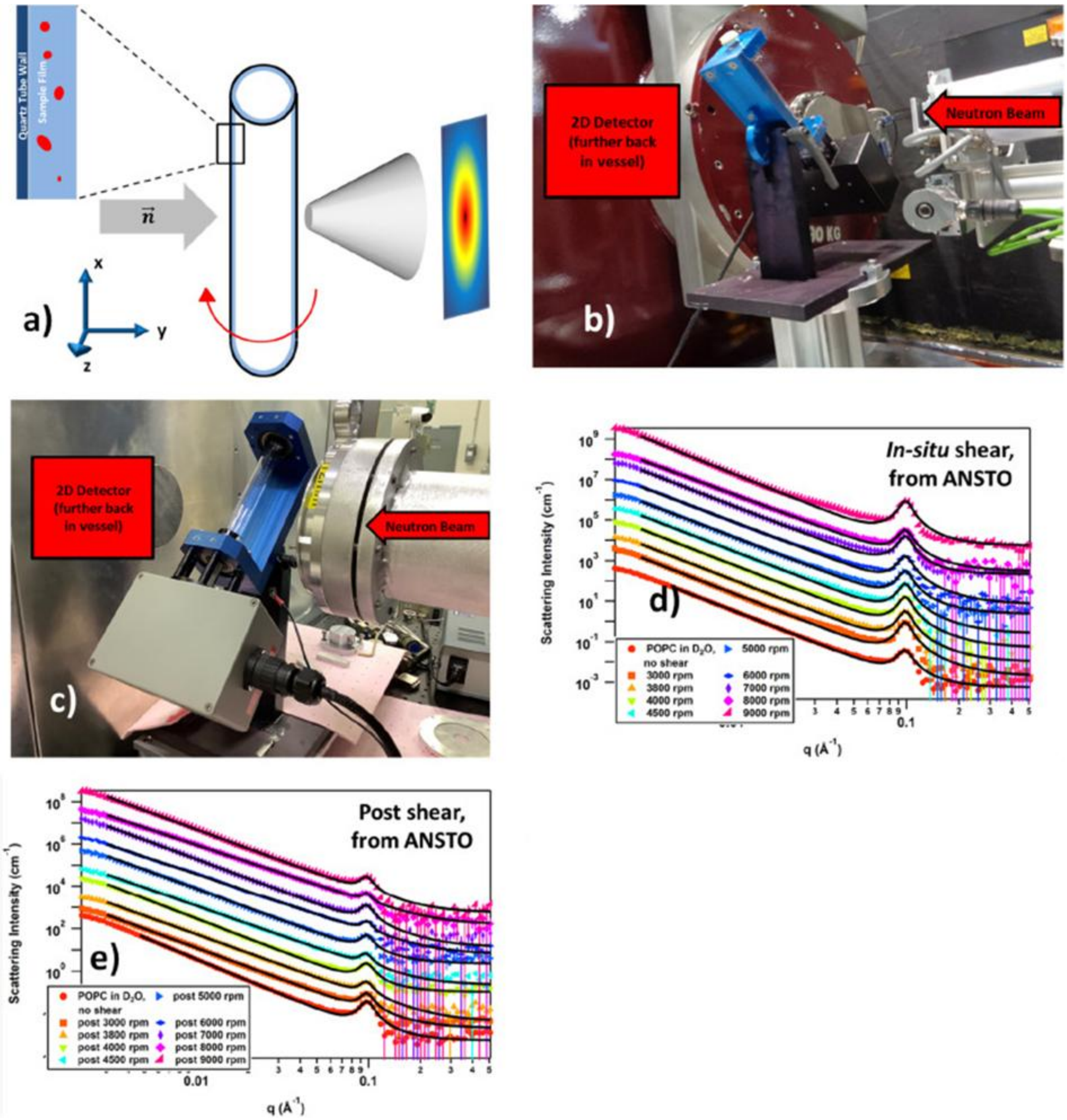

Figure 6.7 SANS data overlays of POPC liposomes in D_2O generated at the specified rotation speeds.

(a) An overhead-view schematic illustrating the VFD tube, the sample film, and the neutron beam, which passes through and is scattered by the tube and sample film before reaching the 2D detector; (b) the BILBY sample area at ANSTO, showcasing the VFD setup; (c) the Bio-SANS sample area at ORNL, also featuring the VFD setup; (d) real-time VFD-SANS data collected from ANSTO, presented as a function of increasing rotational speeds; (e) static SANS measurements from ANSTO taken after each real-time VFD study. The data sets in (d) and (e) were offset by powers of 5 for clarity, with black lines representing model fits the data using a power law combined with a Lorentzian peak summed model.[15]

The SANS data and their fits using a summed, unsmeared power law + Lorentzian peak model is shown in Figure 6.7 above.[15] Across all cases, whether the analysis is done post-shear or in real-time, exhibited strong low-q scattering and a well-defined peak at $q \approx 0.1$ Å^{-1}. This low-q scattering is due to structures whose dimensions $\gg q_{min}^{-1}$, where q_{min} is the minimum accessible q value. This dispersion comes from large-scale entities, such as liposomes, vesicles, or similar macroscopic structures. The slope of the low-q scattering reflects the smoothness of the surface of these structures.

On the other hand, the peak originates from intraparticle repeats, primarily characteristic of multilamellar liposomes. These observed patterns remain consistent regardless of changes in shearing speed, suggesting that the component structures remain remarkably stable when subjected to shear. In real-time shear data, a noteworthy observation is the marginal excess scattering at $q = 0.04$ Å^{-1}, between the pronounced peak and the low-q scattering region. This suggests the presence of some small amount of POPC rods or vesicles. Nonetheless, further focused research is necessary to understand the production processes behind the POPC rods formed in the VFD fully.

6.6 Conclusion

Water and toluene rod structures were formed alongside biphasic liposome rod structures. This was possible due to the high-pressure settings found in the VFD. In this circumstance, the shear stress provided by the VFD holds promise for overcoming the natural steric obstacles by promoting the formation of water cages that can hold toluene and other similar compounds. However, further investigations are required to understand the clathrate further.

6.7 References

1. Faraday M. On Hydrate of Chlorine. Quarterly J of Sci. 1859.
2. Gao, Shuqiang, Waylon House, and Walter G. Chapman. “NMR/MRI Study of Clathrate Hydrate Mechanisms.” *The Journal of Physical Chemistry. B* 109, no. 41 (October 20, 2005): 19090–93. https://doi.org/10.1021/jp052071w.
3. Gao, Shuqiang, Walter G. Chapman, and Waylon House. “NMR and Viscosity Investigation of Clathrate Hydrate Formation and Dissociation.” *Industrial & Engineering Chemistry Research* 44, no. 19 (September 1, 2005): 7373–79. https://doi.org/10.1021/ie050464b.
4. Choudhary, Nilesh, Suman Chakrabarty, Sudip Roy, and Rajnish Kumar. “A Comparison of Different Water Models for Melting Point Calculation of Methane Hydrate Using Molecular Dynamics Simulations.” *Chemical Physics* 516 (January 4, 2019): 6–14. https://doi.org/10.1016/j.chemphys.2018.08.036.
5. Buffett, Bruce, and David Archer. “Global Inventory of Methane Clathrate: Sensitivity to Changes in the Deep Ocean.” *Earth and Planetary Science Letters* 227, no. 3 (November 15, 2004): 185–99. https://doi.org/10.1016/j.epsl.2004.09.005.
6. Chong, Zheng Rong, She Hern Bryan Yang, Ponnivalavan Babu, Praveen Linga, and Xiao-Sen Li. “Review of Natural Gas Hydrates as an Energy Resource: Prospects and Challenges.” *Applied Energy* 162 (January 15, 2016): 1633–52. https://doi.org/10.1016/j.apenergy.2014.12.061.
7. Babu, Ponnivalavan, Praveen Linga, Rajnish Kumar, and Peter Englezos. “A Review of the Hydrate Based Gas Separation (HBGS) Process for Carbon Dioxide Pre-Combustion Capture.” *Energy* 85 (June 1, 2015): 261–79. https://doi.org/10.1016/j.energy.2015.03.103.
8. Ghosh, Jyotirmoy, Rabin Rajan J. Methikkalam, Radha Gobinda Bhuin, Gopi Ragupathy, Nilesh Choudhary, Rajnish Kumar, and Thalappil Pradeep. “Clathrate Hydrates in Interstellar Environment.” *Proceedings of the National Academy of Sciences of the United States of America* 116, no. 5 (January 29, 2019): 1526–31. https://doi.org/10.1073/pnas.1814293116.
9. Vimalanathan, Kasturi, Rekha Goswami Shrestha, Zhi Zhang, Jin Zou, Tomonobu Nakayama, and Colin L. Raston. “Surfactant-Free Fabrication of Fullerene C(60) Nanotubules Under Shear.” *Angewandte Chemie (International Ed. in English)* 56, no. 29 (July 10, 2017): 8398–8401. https://doi.org/10.1002/anie.201608673.
10. Alharbi, Thaar M. D., Matt Jellicoe, Xuan Luo, Kasturi Vimalanathan, Ibrahim K. Alsulami, Bediea S. AL Harbi, Aghil Igder, et al. “Sub-Micron Moulding Topological Mass Transport Regimes in Angled Vortex Fluidic Flow.” *Nanoscale Advances* 3, no. 11 (2021): 3064–75. https://doi.org/10.1039/D1NA00195G.

11. Sokolova, Anna, Andrew E. Whitten, Liliana de Campo, Jason Christoforidis, Andrew Eltobaji, John Barnes, Frank Darmann, and Andrew Berry. “Performance and Characteristics of the BILBY Time-of-Flight Small-Angle Neutron Scattering Instrument.” *Journal of Applied Crystallography* 52, no. 1 (February 2019): 1–12. https://doi.org/10.1107/S1600576718018009.
12. Arnold, O., J.C. Bilheux, J.M. Borreguero, A. Buts, S.I. Campbell, L. Chapon, M. Doucet, et al. “Mantid—Data Analysis and Visualization Package for Neutron Scattering and μ SR Experiments.” *Nuclear Instruments and Methods in Physics Research Section A: Accelerators, Spectrometers, Detectors and Associated Equipment* 764 (November 11, 2014): 156–66. https://doi.org/10.1016/j.nima.2014.07.029.
13. Kline, Steven R. “Reduction and Analysis of SANS and USANS Data Using IGOR Pro.” *Journal of Applied Crystallography* 39, no. 6 (December 2006): 895–900. https://doi.org/10.1107/S0021889806035059.
14. Jellicoe, Matt, Aghil Igder, Clarence Chuah, Darryl B. Jones, Xuan Luo, Keith A. Stubbs, Emily M. Crawley, et al. “Vortex Fluidic Induced Mass Transfer across Immiscible Phases.” *Chemical Science* 13, no. 12 (2022): 3375–85. https://doi.org/10.1039/D1SC05829K.
15. Joseph, Nikita, Marzieh Mirzamani, Tarfah Abudiyah, Ahmed Hussein Mohammed Al-Antaki, Matt Jellicoe, David P. Harvey, Emily Crawley, et al. “Vortex Fluidic Regulated Phospholipid Equilibria Involving Liposomes down to Sub-Micelle Size Assemblies.” *Nanoscale Advances* 6, no. 4 (2024): 1202–12. https://doi.org/10.1039/D3NA01080E.
16. He, Shan, Nikita Joseph, Marzieh Mirzamani, Scott J. Pye, Ahmed Hussein Mohammed Al-Anataki, Andrew E. Whitten, Yaonan Chen, Harshita Kumari, and Colin L. Raston. “Vortex Fluidic Mediated Encapsulation of Functional Fish Oil Featuring in Situ Probed Small Angle Neutron Scattering.” *NPJ Science of Food* 4 (2020): 12. https://doi.org/10.1038/s41538-020-00072-1.

CHAPTER 7 : CONCLUSIONS

7.1 Overall Discussion

Since its inception in 2011, the VFD has revolutionised multiple fields, demonstrating the unparalleled versatility of vortex-based processing within this innovative thin-film microfluidic platform. The unique transformations enabled by the VFD, propelled by Faraday waves and Coriolis forces, open up a vast array of possibilities while reducing labour-intensive handling. These Faraday waves create eddies, which are then twisted by the Coriolis forces from the tube's curved sidewall into double-helical flows, enabling precise manipulation for many applications. The Coriolis forces at the tube's base generate a spinning, typhoon-like structure, particularly effective for processes such as the exfoliation of 2D materials and scroll formation.

This thesis underscores the vast potential of the VFD, demonstrating its utility in a wide range of applications. The VFD's applications are diverse and exciting, from the top-down exfoliation of graphene sheets to the bottom-up fabrication of new materials and the acceleration of enzymatic reactions through mechanical modulation of the enzyme’s secondary structure and protein folding. Furthermore, the VFD can fine-tune the properties of aggregation-induced emission (AIE) nanoparticles. Through this cutting-edge device, we seek to redefine the precise organization of matter by leveraging fluid flow-induced mechanical effects, all while ensuring environmental and human safety. The VFD's strong alignment with the principles of green chemistry, emphasizing the reduction of toxic material use and waste production from the initial stages of research to the final product, provides reassurance about its environmental impact, instilling a sense of responsibility and care in our approach to scientific research.

Chapter 3 explores the intricate nature of high-shear topological flow in thin films of immiscible liquids within a VFD at an optimal tilt angle of 45°. The investigation integrates multiple strategies to address the complexities of a rotating reference frame and the small scale of the liquid films. These strategies include neutron imaging for film thickness, mixing experiments with temperature variations, and structural perturbations at fluid interfaces. This enables precise predictions of optimal rotational speed for specific chemical transformations, such as carbohydrate reactions in immiscible water-dichloromethane mixtures. The chapter also explores how different base shapes of the VFD tube influence fluid flow, opening new possibilities for controlling fluid dynamics in various applications. Notably, the study highlights the formation of nanoparticles in phase-separated layers and the potential for fabricating materials like size-exclusion filters through molecular drilling, driven by unique topological fluid flow patterns.

Chapter 4 leveraged the VFD's dynamic thin film microfluidic technology and intense micro-mixing. The VFD has been successfully utilised to extract perfluorooctanoic acid (PFOA) from water using the AstkCARE™ reagent. Similar to the MBAS method, this liquid-phase extraction (LPE) removes the hydrophobic ion-pair of dye (ethyl violet)-AS to an organic phase (ethyl acetate). The efficiency advantages provided by this LPE methodology are notably enhanced by its rapidity; after only 10 minutes of processing, PFOA is extracted from the water, as confirmed through liquid chromatography-mass spectrometry (LCMS). This efficiency bodes well for the process's feasibility and scalability, particularly when considering its implementation in large-scale production environments, instilling confidence in the VFD's potential.

Chapter 5's VFD processing within a concave-based tube at a low rotational speed of 1500 rpm, the AIE/graphene oxide (GO) material formulation exhibited a remarkable increase in relative fluorescence intensity. Compared to AIE nanoparticles alone, this process produces brightly fluorescent AIE/GO material. Numerous chemical processes that require the interplay between solid and liquid phases could benefit from the technique presented. For example, in diagnostics, molecular recognition often requires molecules in the liquid phase to bind to a target attached to a solid substrate. This VFD processing, operating at a low 1500 rpm, may help speed up the equilibration of sluggish binding events. Furthermore, the strategy detailed here could be adapted for industrial and clinical applications due to its cost-effectiveness.

In Chapter 6, water and toluene rod structures were formed alongside biphasic liposome rod structures under the high-pressure settings found in the VFD. The shear stress provided by the VFD holds promise for overcoming natural steric obstacles by promoting the formation of water cages that can encapsulate toluene and similar compounds. However, further investigations are required to understand these clathrate structures better.

The VFD's dynamic capabilities and the growing understanding of its high-shear topological fluid flows have significantly broadened the horizons for its applications. The predictability of processing parameters has opened the door to endless possibilities, from advanced material fabrication to environmental remediation. As we continue to explore and refine this technology, the potential for innovative and sustainable solutions in various fields becomes increasingly optimistic. The VFD is not just a tool but a platform for future innovations and applications, instilling a sense of optimism and excitement about its potential.

7.2 Future Research Directions for the VFD

The results of each project presented in this thesis are detailed in separate chapters, collectively establishing a foundation for utilising vortex-induced fluidic mixing in multi-solvent systems. These findings offer valuable insights for further applications and pave the way for addressing related processes. The conclusions underscore the exceptional utility of the VFD in the synthesis and transformation of various nanomaterials. The distinctive fluid dynamics within the VFD position it as a transformative advancement in microfluidic devices. Once the fluid flow within the VFD is characterised, it allows for a level of predictability in processing outcomes, unlocking new possibilities for future device applications.

7.2.1 Post Chapter 3: Immiscible Liquids in the VFD

The interfacial tension between two immiscible liquids is modified in the VFD, facilitating high mass transfer between the phases. DLS reveals the presence of particulates from each phase dispersed within the other. This process in the VFD does not lead to emulsion formation, despite the sustained high mass transfer between the liquids. The observed nanoparticle formation within each phase during VFD processing is attributed to the increased surface area interaction between the liquids. The combination of toluene and water, a well-established immiscible biphasic system, exemplifies this behaviour, with toluene having minimal impact on the hydrate phase equilibrium boundary in the methane-water system.[1] Additionally, at the air-liquid interface in the VFD, there is a significant increase in gas mass transfer into the water phase and, similarly, into both phases of immiscible liquids. For the water layer, dissolved gases can potentially limit oil solubility,[2] though the effects of shear on this phenomenon remain to be fully understood.

7.2.1.1 De-Gassed Water in the VFD

Research has shown that the near-total removal of dissolved gases from water significantly enhances its ability to disperse and eliminate hydrophobic dirt, as seen in Figure 7.1.[2] When the contaminant is a hydrophobic liquid, the cleaning effect is significantly enhanced by de-gassing both the liquid and the water. This observation indicates the possibility of detergent-free cleaning by utilising a sequence of de-gassed hydrophobic solvents, followed by rinsing with de-gassed water. By employing a range of de-gassed hydrophobic solvents, the versatility of this cleaning method could be expanded to accommodate various systems. A preliminary investigation into the electrical conductivity of single-distilled water revealed that while nitrogen-purged distilled water closely matches literature values, fully de-gassed water exhibits notably higher conductivity. These findings indicate that even small amounts of dissolved nonpolar gases can disrupt the structure of water, thereby reducing its electrical conductivity.

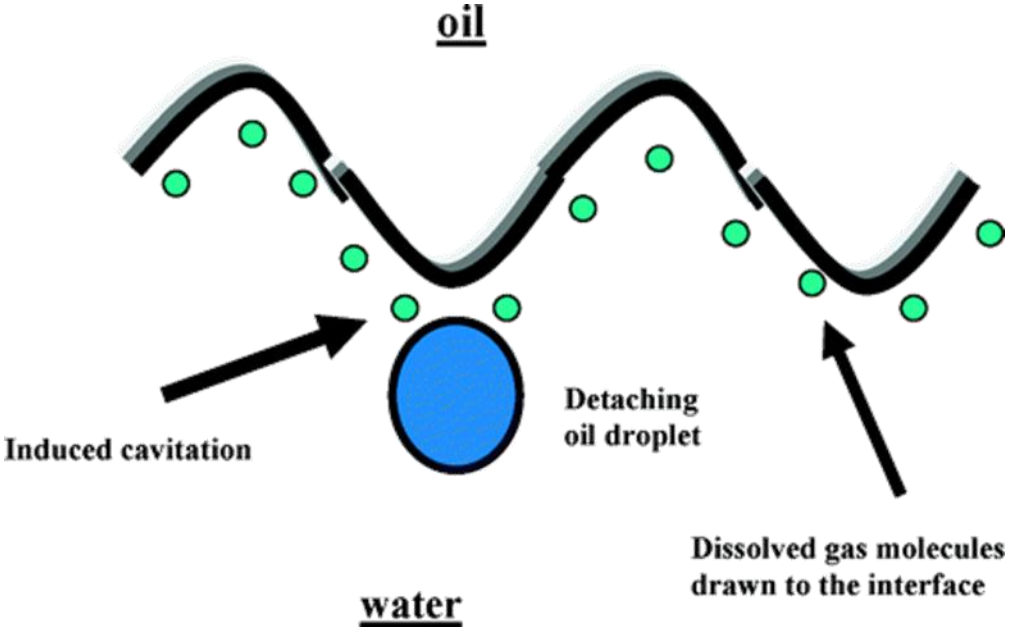

Figure 7.1 A schematic diagram illustrates the detachment of an oil droplet from an oil/water interface. Dissolved atmospheric gas molecules are attracted to the interface, facilitating the cavitation that typically occurs as two hydrophobic surfaces separate in water. Reprinted with permission from REF.[2] Copyright 2005, American Chemical Society.

7.2.1.2 Nano-emulsions in the VFD

Nano-emulsions represent a cutting-edge drug delivery system with broad applications in medicine. Their distinct features—small droplet size, improved stability, and the capacity to encapsulate hydrophilic and lipophilic drugs—make them highly effective carriers for delivering active pharmaceutical compounds to targeted sites. Nano-emulsions have demonstrated significant potential in enhancing drug solubility, bioavailability, and precision in delivery, addressing many limitations of traditional drug delivery methods. Their adaptability is evident across various administration routes, including oral, parenteral, ocular, and intranasal. Additionally, their ability to encapsulate multiple drugs, from small molecules to biomacromolecules like proteins and genetic material, underscores their value in therapeutic applications. Ongoing innovation in this field is highlighted by developing specialised formulations, such as cationic nano-emulsions for gene delivery and targeted therapies.

However, nano-emulsions can be unstable under certain conditions, leading to alterations in physical properties, including droplet size changes, aggregation, or phase separation.[3] Physical stress from agitation or high shear forces during handling, transportation, or processing can disrupt the nano-emulsion, causing droplet coalescence or phase separation,[4] as illustrated in Figure 7.2.[5] Nevertheless, as demonstrated in this thesis, the VFD offers a promising solution to mitigate these instability issues.

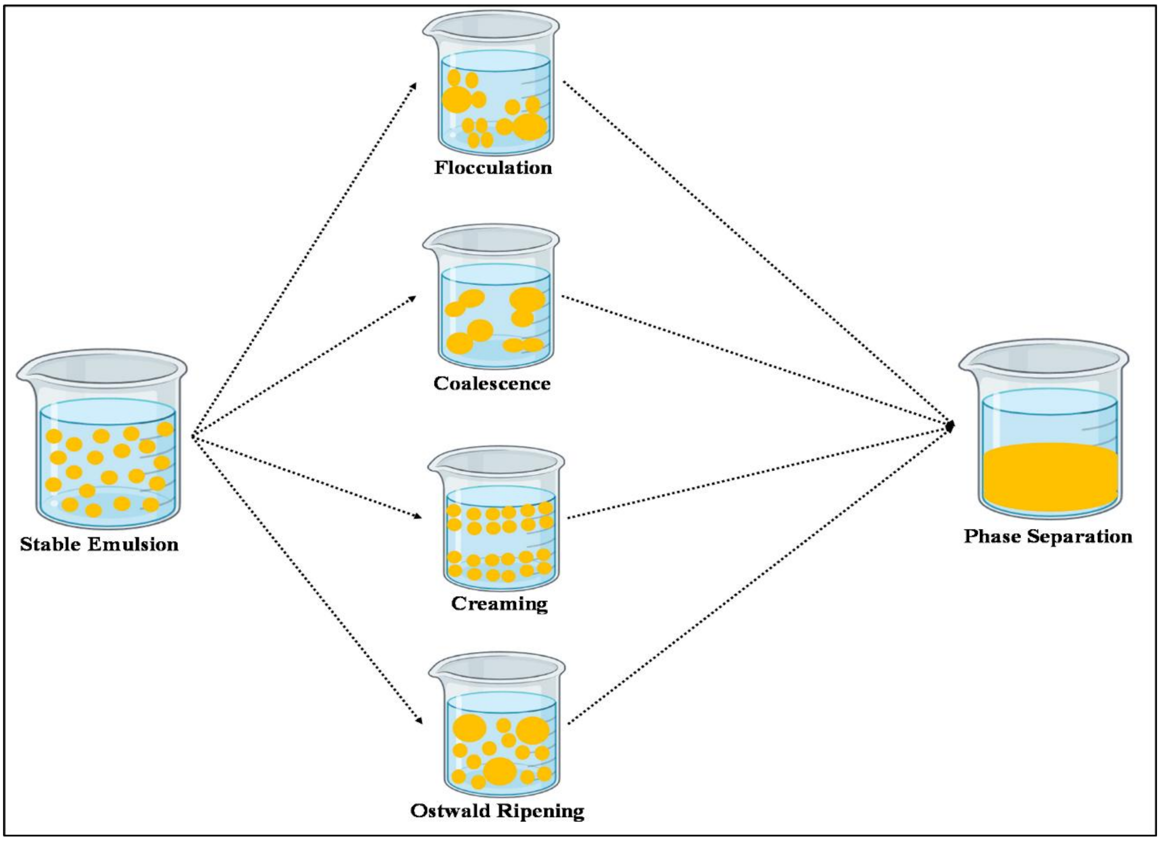

Figure 7.2 Schematic illustration of nano-emulsion instability.

7.2.2 Post Chapter 4: Per- and Polyfluoroalkyl Substances (PFAS) Degradation in the VFD

In this thesis, liquid-phase extraction (LPE), similar to the methylene blue active substances (MBAS) method, is utilised to extract the hydrophobic ion-pair formed between the dye ethyl violet and anionic surfactants like perfluorooctanoic acid (PFOA) into an organic phase (ethyl acetate). This approach can also be extended to perfluorooctane sulfonate (PFOS) and other PFAS compounds. Anionic surfactants, including PFOA and PFOS, interact with cationic dyes such as methylene blue or ethyl violet to form ion pairs. Due to their hydrophilic ends being neutralised through electrostatic interaction, these ion pairs exhibit hydrophobic behaviour, rendering them immiscible in water and extractable into a non-aqueous phase.

The recent global focus on remediating PFAS-contaminated water has driven efforts to develop advanced removal strategies that address the limitations of conventional treatment methods. Photocatalysis has gained traction as an effective, chemical-free method for mineralising PFAS. At the same time, adsorption remains the most widely used technique despite its inability to destroy PFAS and waste sludge generation. Innovative strategies, such as ‘concentrate and destroy’ techniques, have emerged as promising solutions, combining adsorption with photocatalysis for PFAS removal. Although some of these methods have been successfully implemented at pilot or commercial scales, many degradation technologies are still confined to the laboratory. Ongoing efforts aim to establish cost-effective and environmentally friendly processes for large-scale PFAS water treatment.

To enhance the adsorption and photocatalytic treatment of PFAS, research is focused on carbon-based materials better to understand their mechanisms and practical effectiveness in PFAS remediation. Carbon-based materials are essential in removing organic pollutants from water due to their cost-effectiveness, high adsorption capacity, and ease of modification, making them promising candidates for adsorptive photocatalysts. The adsorption performance of biochar and activated carbon (AC) varies depending on their raw material sources and synthesis methods. The separation of PFAS using carbon-based sorbents relies primarily on electrostatic and hydrophobic interactions. Moreover, synergistic interactions between PFAS and carbon-based composites can result in diverse adsorption modes, promoting photocatalytic degradation through decarboxylation and defluorination reactions. Enhancements in photocatalytic degradation have been achieved by doping with metals or non-metals, forming heterojunctions, creating oxygen vacancies, and incorporating metal oxides or perovskite-type mixed oxides. Experimental evidence suggests that holes, $^{\bullet}OH$ and $^{\bullet}O_2^-$ radicals, play a significant role in the photocatalytic degradation of PFAS on carbon-based materials. The potential application of carbon-based materials in photocatalytic ozonation for the degradation of PFOA has garnered considerable attention. However, the efficacy of degradation varies among different PFAS classes, with some compounds breaking down into shorter-chain intermediates that are more persistent and potentially toxic. Direct removal through adsorption may be a more effective approach in these instances. Integrating photocatalysis with complementary treatment methods—such as ozonation, Fenton-like reactions, electrochemical oxidation, sonochemical degradation, and membrane filtration—could be crucial for comprehensively eliminating reaction intermediates.

Future research should aim to fine-tune the surface chemistry of carbon materials to enhance selective adsorption and targeted degradation of PFAS in the VFD. Carbon-based hydrogels, aerogels, and engineered nano-functionalised materials offer promising opportunities for nano-enhanced PFAS remediation in the VFD. It's also crucial to extend PFAS degradation studies to natural wastewater, groundwater, and surface water to assess the effectiveness of photocatalytic processes under varied environmental conditions with interfering species. Finally, while most studies have focused on PFOA and PFOS, future research should address the degradation of shorter-chain PFAS to gain a more comprehensive understanding of PFAS remediation technologies.

7.2.3 Post Chapter 5: AIE Transformation Through the VFD

In Chapter 5, a straightforward, innovative, and cost-effective method for preparing AIE/GO materials with enhanced fluorescence properties using a VFD platform was developed. This technique produces highly fluorescent AIE/GO material, achieving over a 1400% increase in relative fluorescence intensity compared to AIE fluorogen alone. The results introduce a novel application of the VFD in achieving exceptionally high fluorescence intensity and reveal a new optimal rotational speed regime. Unlike the typical optimal speeds ranging from 4000 to 9000 rpm, this process operates effectively at 1500 rpm. This lower rotational speed suggests significantly different fluid dynamics, presenting a key challenge for future research.

Additionally, exploring other AIE transformations using the VFD could provide valuable insights. Previous approaches have focused on adjusting the size and fluorescence properties of AIEgens, which is crucial for creating fluorescent hydrogels with enhanced mechanical and fluorescence characteristics. Controlling the size of AIEgens is critical for applications in material characterization at the micro- and nanoscale. The VFD offers a means of delivering mechanical energy to mediate and control chemical and biochemical transformations, including tuning size and properties and regulating the physical characteristics of hydrogels. This capability extends beyond traditional batch production, enabling the one-step fabrication of fluorescent hydrogels with significant potential for future biomedical applications, particularly in cell adhesion, growth, and proliferation.

These studies lead to several important conclusions that could significantly shape future application strategies. Firstly, AIEgens hold great promise in life sciences and biomedical engineering, particularly for in vitro and in vivo imaging of biomolecules, cells, tissues, and organisms, as well as in fabricating fluorescent hydrogels. AIEgens offer distinct advantages over traditional fluorescent dyes, including bright emission, high efficiency, excellent photostability, strong biocompatibility, and substantial optical nonlinearity. However, a significant challenge remains in precisely controlling the particle size and fluorescence properties of AIEgens to advance their use in biological and medical applications.

Secondly, the VFD-mediated approach can revolutionise AIEgen-hydrogel assembly and research by enabling precise control over the size, morphology, and surface properties of AIEgens and the bulk properties of hydrogels. The benefits of VFD-mediated transformations of AIEgens are becoming increasingly apparent. The critical challenge now is to systematically understand the transformation mechanisms, which could lead to developing a universal toolkit for practical applications. Given the unique fluid dynamics of the VFD, gaining insight into these mechanisms and establishing a clear signature for the photophysical properties of VFD-mediated AIEgens and fluorescent hydrogels could enable more precise control over molecular transformations and inspire new synthetic protocols.

Thirdly, a new pathway for creating fluorescent hydrogels can be explored by developing platforms for synthesizing and functionalising various AIEgens through copolymerisation with hydrophilic monomers using the VFD. This approach could lead to the construction of fluorescent hydrogels with shorter reaction times, reduced catalyst requirements, enhanced reaction efficiency, and a streamlined purification process.

7.2.4 Post Chapter 6: Biphasic Liposomes in the VFD

In Chapter 6, a straightforward method has been developed for fabricating biphasic liposomes using continuous flow processing in the VFD. The optimal processing conditions have been established, including the phospholipid concentration and the rotational speed of the tube inclined at +45° in the thin film microfluidic platform. In situ SANS was employed to analyse the morphology of species present under shear within the VFD, utilising both a hydrophobically coated quartz tube and an uncoated quartz tube. The study revealed that large liposomes and multilamellar structures coexisted in the system regardless of the tube type, although the shear speed-dependent trends differed between the two tubes. In the hydrophobically coated tube, no clear trends emerged with shear speed. Still, a significant reduction in overall POPC concentration was observed at each shear level due to sludge formation on the tube surface, with shear predominantly impacting multilamellar structures and, to a lesser extent, large liposomes. Fluorophore tags can be incorporated into liposomes without altering their final structure (without VFD processing). When two types of liposomes containing 1% fluorophores are mixed in the VFD, the resulting liposomes contain equal proportions of the two fluorophores, as indicated by SANS. This approach marks a paradigm shift in liposome fabrication, allowing control over their disassembly and reorganisation without needing downstream processing. The mechanical energy induced by the VFD promotes the in-situ assembly of sub-micelle species into ~110 nm diameter liposomes, which are thermodynamically stable and similar in size to exosomes, suggesting that similar factors may also govern their diameter. However, membrane proteins may also play a role.

Beyond incorporating fluorophore tags into liposomes, future research could explore the remote loading of drugs into liposomes, an essential step toward successfully translating liposomal products. Enhanced drug-loading strategies in nanocarriers could salvage drugs with high efficacy that might otherwise fail in development due to high toxicity or low solubility. Remote loading enables the administration of higher doses per unit volume while maintaining stability in vivo and during storage.

The properties of liposomes can be tailored for specific applications through various drug delivery routes.[6, 7] A critical quality attribute of liposomal formulations is the ratio of free to encapsulated drugs, as a higher proportion of free drugs is associated with increased side effects, particularly in cancer therapies.[8] This is especially pertinent for highly toxic anticancer drugs with a narrow therapeutic index, which balances efficacy against toxicity. The co-encapsulation of multiple liposome drugs at precise stoichiometric ratios, resulting in synergistic cytotoxic effects in cancer tissues, has recently gained significant attention in nanomedicine. The approval of Vyxeos, a liposomal co-encapsulated product for acute myeloid leukemia, highlights the potential of this approach. Another innovative method is used in Lipoplatin, a proprietary cisplatin-liposomal formulation. Unlike conventional liposomes, Lipoplatin achieves drug loading through the formation of a reverse micelle of cisplatin within the anionic lipid dipalmitoyl phosphatidyl glycerol under optimal conditions,[9] which is then converted into liposomes using neutral lipids and repeatedly extruded to obtain ~110 nm nanoparticles.[10]

Remote loading is crucial for co-loading multiple drugs in precise molar ratios, a challenge for other encapsulation methods. However, this process has limitations. One significant issue is the potential for acid-catalysed lipid hydrolysis during storage, leading to instability,[11, 12] particularly when stored outside the optimal pH range of 6-7.[11] Moreover, there is no single, standardised method for encapsulating all drugs, necessitating extensive optimisation to achieve the optimal balance between drug loading and retention while preventing leakage. The drug release rate can also vary, exhibiting either biphasic or zero-order kinetics, depending on whether the dissolution of drug nanocrystals or membrane transport is the rate-limiting step. Liposomes that lack well-formed doxorubicin sulphate nanocrystals or possess poorly crystalline structures often show biphasic release, while those containing stable nanocrystals tend to follow zero-order kinetics. Overcoming these challenges and improving the predictability of drug loading through the development of mathematical models could significantly streamline the creation of stable and effective liposomal formulations.

7.3 References

1. Mohammadi, Amir H., Veronica Belandria, and Dominique Richon. “Can Toluene or Xylene Form Clathrate Hydrates?” *Industrial & Engineering Chemistry Research* 48, no. 12 (June 17, 2009): 5916–18. https://doi.org/10.1021/ie900362v.
2. Pashley, R. M., M. Rzechowicz, L. R. Pashley, and M. J. Francis. “De-Gassed Water Is a Better Cleaning Agent.” *The Journal of Physical Chemistry B* 109, no. 3 (January 1, 2005): 1231–38. https://doi.org/10.1021/jp045975a.
3. Manish Kumar, Ram Singh Bishnoi, Ajay Kumar Shukla, and Chandra Prakash Jain. “Techniques for Formulation of Nanoemulsion Drug Delivery System: A Review.” *Preventive Nutrition and Food Science* 24, no. 3 (2019): 225–34. https://doi.org/10.3746/pnf.2019.24.3.225.
4. Barradas, Thaís Nogueira, and Kattya Gyselle de Holanda e Silva. “Nanoemulsions of Essential Oils to Improve Solubility, Stability, and Permeability: A Review.” *Environmental Chemistry Letters* 19, no. 2 (April 1, 2021): 1153–71. https://doi.org/10.1007/s10311-020-01142-2.
5. Kumar, Mohit, Nitasha Chauhan, Devesh Kumar, Syed Mahmood, Shruti Chopra, and Amit Bhatia. “Revolutionizing Nanomedicine: Expanding Horizons of Nanoemulsions in Drug Delivery and Beyond.” *Journal of Dispersion Science and Technology*, n.d., 1–26. https://doi.org/10.1080/01932691.2024.2369835.
6. Farooqui, Raziya Khatoon, Monika Kaurav, Manoj Kumar, M. S. Sudheesh, and Ravi Shankar Pandey. “Permeation Enhancer Nanovesicles Mediated Topical Delivery of Curcumin for the Treatment of Hyperpigmentation.” *Journal of Liposome Research* 32, no. 4 (October 2, 2022): 332–39. https://doi.org/10.1080/08982104.2021.2024567.
7. Krishna, S. Swathi, M. S. Sudheesh, and Vidya Viswanad. “Liposomal Drug Delivery to the Lungs: A Post Covid-19 Scenario.” *Journal of Liposome Research* 33, no. 4 (October 2, 2023): 410–24. https://doi.org/10.1080/08982104.2023.2199068.
8. Kapoor, Mamta, Sau L. Lee, and Katherine M. Tyner. “Liposomal Drug Product Development and Quality: Current US Experience and Perspective.” *The AAPS Journal* 19, no. 3 (May 1, 2017): 632–41. https://doi.org/10.1208/s12248-017-0049-9.
9. Boulikas, Teni. “Clinical Overview on Lipoplatin^{TM}: A Successful Liposomal Formulation of Cisplatin.” *Expert Opinion on Investigational Drugs* 18, no. 8 (August 1, 2009): 1197–1218. https://doi.org/10.1517/13543780903114168.
10. Stathopoulos, G. P., and T. Boulikas. “Lipoplatin Formulation Review Article.” *Journal of Drug Delivery* 2012, no. 1 (January 1, 2012): 581363. https://doi.org/10.1155/2012/581363.
11. Barenholz, Yechezkel, Shimon Amselem, Dorit Goren, Rivka Cohen, Dan Gelvan, Amram Samuni, Elisabeth B. Golden, and Alberto Gabizon. “Stability of Liposomal

Doxorubicin Formulations: Problems and Prospects.” *Medicinal Research Reviews* 13, no. 4 (July 1, 1993): 449–91. https://doi.org/10.1002/med.2610130404.

12. Grit, Mustafa, and Daan J.A. Crommelin. “Chemical Stability of Liposomes: Implications for Their Physical Stability.” *Chemistry and Physics of Lipids* 64, no. 1 (September 1, 1993): 3–18. https://doi.org/10.1016/0009-3084(93)90053-6.

SUPPLEMENTARY INFORMATION AND APPENDICES

These supplementary pieces of information and appendices were extracted from the publication of "Matt Jellicoe, Aghil Igder, Clarence Chuah, Darryl B. Jones, Xuan Luo, Keith A. Stubbs, Emily M. Crawley, Scott J. Pye, Nikita Joseph, Kasturi Vimalananthan, Zoe Gardner, David P. Harvey, Xianjue Chen, Filomena Salvemini, Shan He, Wei Zhang, Justin M. Chalker, Jamie S. Quinton, Youhong Tang, Colin L. Raston. Vortex fluidic induced mass transfer across immiscible phases. Chemical Science, 2022, 13, 3375-3385".

1 Neutron Imaging Determined Film Thickness

An example of neutron scattering images from ANSTO is presented in Figure S0.1(a). Calibration of the image was achieved by first determining the pixel-to-distance ratio. A cross-sectional profile of the test tube, depicted in Figure S0.1(c), was used for this calibration, given that the test tube has a known outer diameter of 20 mm. This measurement provides the internal dimension of the VFD tube, which was found to be 16,770 microns. Structural features were then identified from an alternative cross-sectional profile, shown in Figure S0.1(b). The height within the tube, relative to the internal base, was approximated according to the VFD's design, as illustrated schematically in Figure S0.1(d). Film profiles of the liquid were subsequently obtained at various heights above the tube base by averaging neutron scattering images from the regions indicated in Figure S0.1(a). These profiles reflect a cross-sectional segment of the VFD tube, orthogonal to the rotational axis, at specific heights.

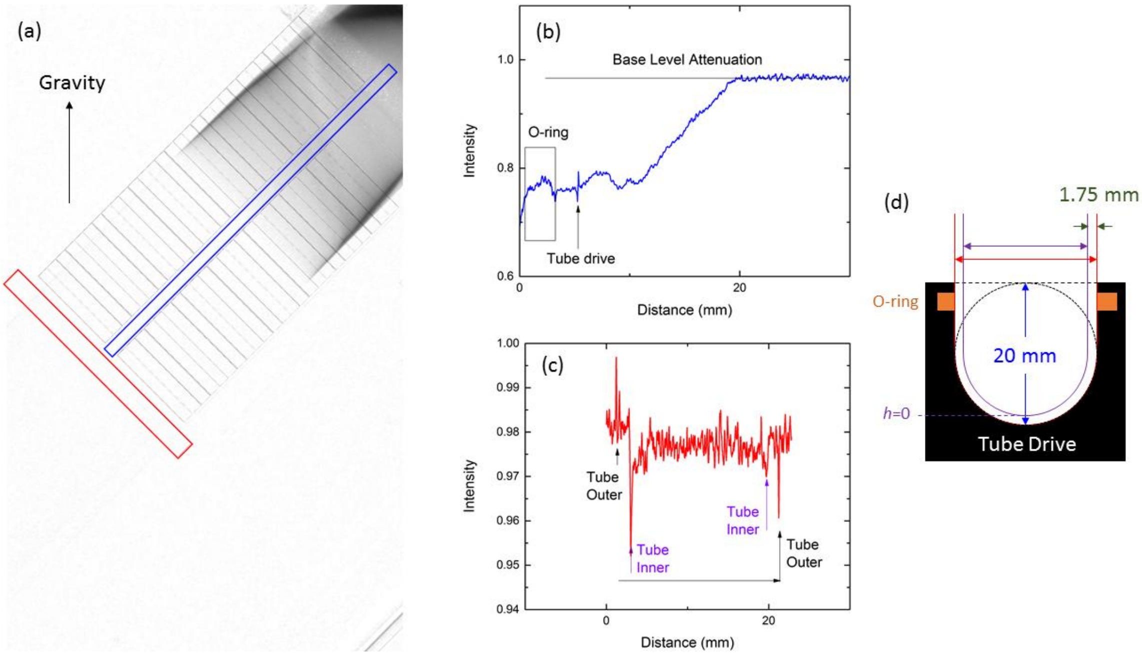

Figure S0.1 Neutron imaging.

(a) Neutron scattering image captured at ANSTO. (b) Average intensity profile derived from the blue-highlighted region in panel (a). (c) Average intensity profile derived from the red-highlighted region in panel (a). (d) Schematic of the VFD tube, emphasizing critical features used for calibrating the neutron image.

To analyse the neutron imaging data, we have developed a neutron scattering attenuation model to describe the behaviour of the neutron beam as it traverses the fluid layers within the biphasic system. Considering a cross-sectional view of the VFD tube in a plane parallel to the axis of rotation, we assume the presence of two circular interfaces: one between the fluid phases and another between the fluid and air. Using a Beer-Lambert attenuation model that disregards refraction and reflections at these interfaces, the intensity of the neutron beam transmitted through the tube, $I(x)$, can be expressed as follows:

$$I(x) = I_0 \exp(-\sigma_1 l_1) \exp(-\sigma_2 l_2) \, .$$

Here, I_0 represents the intensity of the incident neutron beam while σ_1 and σ_2 denote the neutron scattering cross-sections per unit length for layers 1 and 2. Additionally, l_1 and l_2 are the distances that the neutron beam travels through layers 1 and 2, respectively.

In the model, the attenuating lengths for layers 1 and 2 at a given cross-sectional position x, where \(x\) is measured from the tube axis (with positive values indicating positions towards the top of the tube relative to gravity), can be determined if the radii and centres of the circular interfaces are known, as illustrated in Figure S0.2.

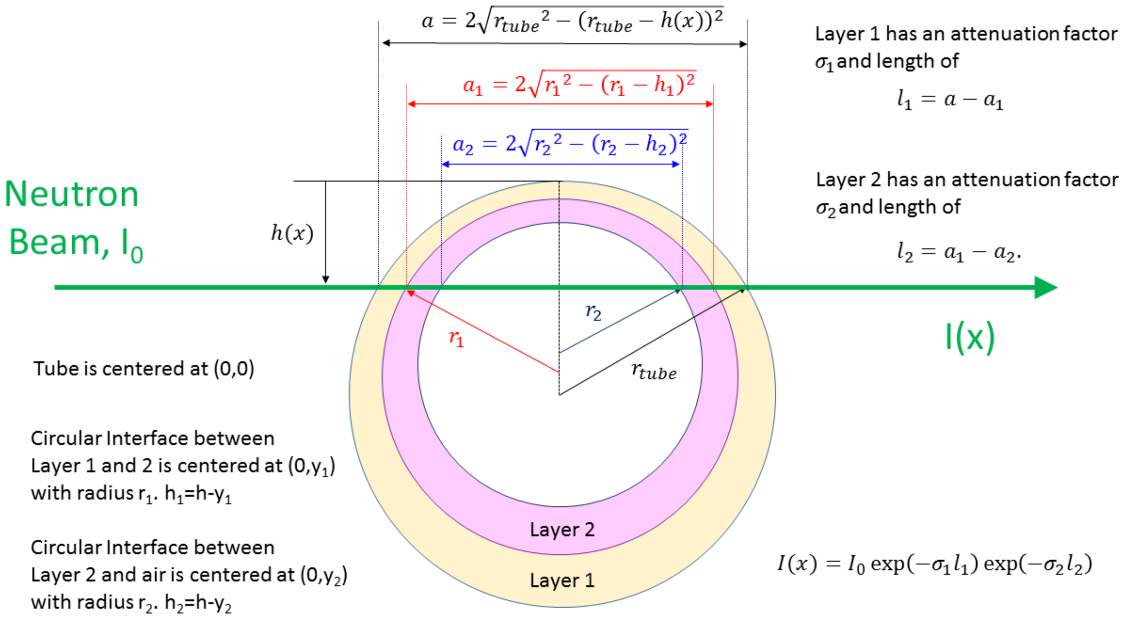

Figure S0.2 A schematic representation of neutron beam attenuation.

To validate the suitability of this model, we synthesized attenuation data for a biphasic system, as illustrated in Figure S0.3. The model effectively captures the primary features observed in the cross-sectional profiles from the neutron attenuation experiment. However, fitting this attenuation profile to extract film properties proved challenging. Specifically, convolving the attenuation data with the instrumental response function is essential, and it must account for additional factors such as neutron refraction and reflections at the interfaces. These refraction and reflection characteristics vary with film thickness. They are further complicated by the neutron beam interacting with up to six different interfaces as it passes through the biphasic system. The varying angle of incidence across the tube's diameter adds another layer of complexity. Consequently, fitting the extensive array of film attenuation profiles obtained at different heights and rotational speeds became impractical. The continually changing instrumental response function rendered non-linear fitting procedures unstable across the cross-sectional profiles derived from a single image at a single rotational speed.

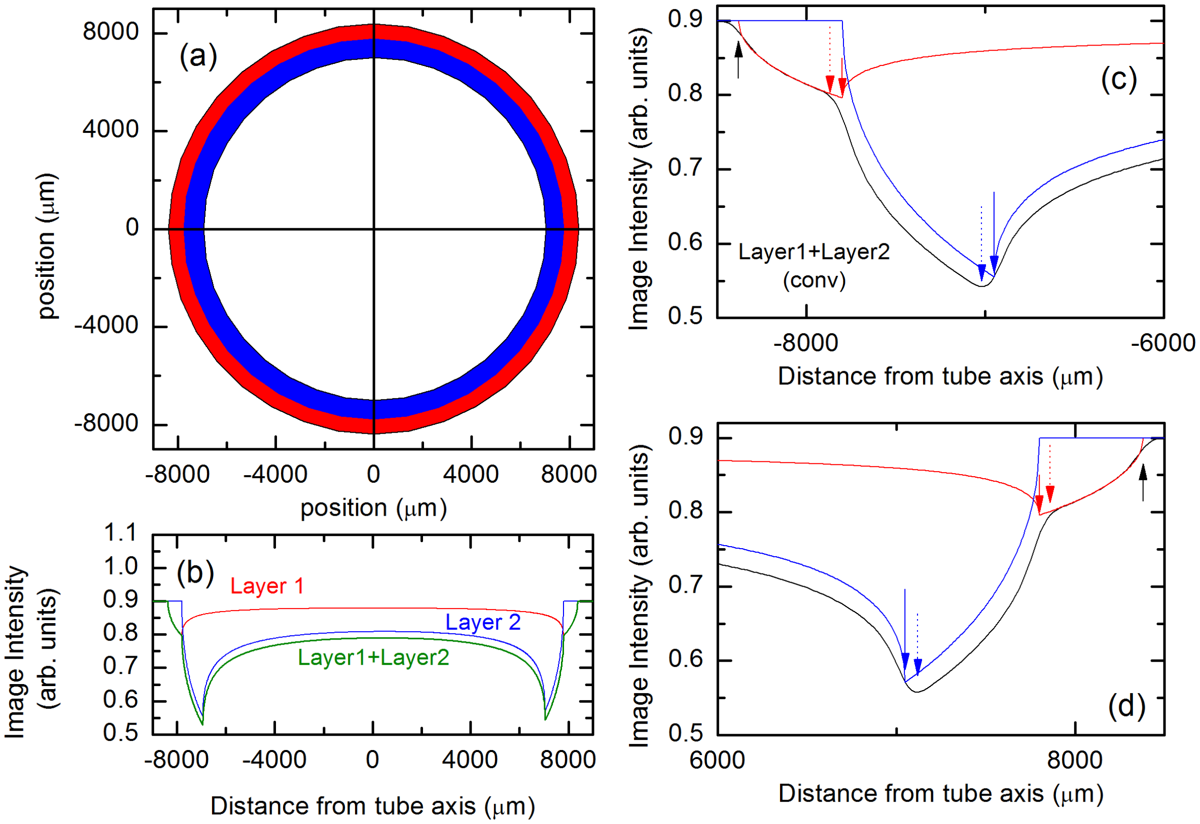

Figure S0.3 Attenuation of a biphasic system.

(a) A schematic of a hypothetical biphasic system is depicted, where the tube radius $\boldsymbol{r_T}$ = 8380 µm. Layer 1 (red) has an interface radius. $\boldsymbol{r_1}$ = 7800 µm and is centred at (0,0), while Layer 2 (blue) has an interface radius $\boldsymbol{r_{L2}}$ = 7000 µm and is centred at (50,0). (b) The synthesized attenuation profile is shown for Layer 1 ($\boldsymbol{\sigma_1}$ =1.8x10^{-5} µm^{-1}), Layer 2 ($\boldsymbol{\sigma_2}$ =6.0x10^{-5} µm^{-1}), and the combined layers. The unattenuated intensity is set at 0.9 arbitrary units. (c, d) Gaussian-convoluted attenuation profiles are fitted at (c) the bottom and (d) the top of the tube. The unconvoluted attenuation profiles for the two layers are also displayed. Solid (dashed) arrows indicate the true (derived) parameters for the interface radii of Layers 1 and 2. The black arrow denotes the tube radius.

To extract data from the observed neutron images, we correlate the structural features in our cross-sectional profiles with the physical parameters of the biphasic system, as illustrated in Figure S0.4. Specifically, we identify the maximum attenuation (minima in the profile) and use these values to determine the radius of the inner (Layer 2) interface. To extract data from the observed neutron images, we relate structural features in our cross-sectional profile to the physical parameters in the biphasic system. These features are indicated in Figure S0.4. Firstly, we locate the maximum attenuation (minima in profile), m and use these values to determine the radius of the inner (layer 2) interface:

$$r_{L2} = \frac{m_+ - m_-}{2}$$

The circle describing the interface is centred at:

$$c_{L2} = -\frac{m_+ + m_-}{2}.$$

Here, the subscripts (+/-) refer to measurements taken at the top or bottom of the tube, respectively. We then calculate the difference between the attenuated curve and a straight line extending to the baseline intensity at the tube boundary. This difference curve, or slope, approximates the derivative of the attenuation curve, with its maximum value (or local maximum) indicating changes in attenuation properties due to variations in neutron attenuation between different layers.

The maxima of the difference curve (slope), denoted as s, are utilized to determine the radius of the outer (Layer 1) interface.

$$r_{L1} = \frac{s_+ - s_-}{2}$$

The centre of this circular interface is given by:

$$c_{L1} = -\frac{s_+ + s_-}{2}.$$

Without a second layer, the s value corresponds to either the tube radius or the outer interface. Again, the subscripts (+/-) denote the top or bottom of the tube, respectively.

The distance from the layer 1 interface to the top/bottom wall of the tube (Layer 1 thickness) is then:

$$L_{1+} = r_T - (r_{L1} - c_{L1}),$$

or,

$$L_{1-} = r_T - (r_{L1} + c_{L1}),$$

respectively. The distance between the first and second interfaces (Layer 2 thickness) at the top/bottom of the tube is:

$$L_{2+} = r_{L1} - (r_{L2} - (c_{L2} - c_{L1})),$$

or,

$$L_{2-} = r_{L1} - (r_{L2} + (c_{L2} - c_{L1})),$$

respectively.

the distance from the second interface to the tube wall at the top/bottom of the tube is:

$$L_+ = L_{1+} + L_{2+}$$

or

$$L_- = L_{1-} + L_{2-}$$

It is essential to ensure that these measurements adhere to the conservation relationship.

$$2r_{Tube} = L_{1+} + L_{2+} + 2r_{L2} + L_{2-} + L_{1-}.$$

We verify the correlation of these parameters with the film properties by analysing our synthetic attenuation profile, which has been convoluted with a Gaussian instrumental function (standard deviation = 100 µm), as shown in Figure S0.3(c,d). We found that all derived parameters were consistent with the synthetic parameters within the standard deviation used for the convolution. Consequently, these parameters are deemed reliable for extracting film thickness information from the neutron beam attenuation profiles despite the inability to fit the attenuation curve directly.

Additionally, for very thin films (less than 200 microns), refraction and reflections can cause the inflection point to appear outside the tube boundary. In such cases, we adjust the film thickness measurement to half the distance between the inflection point and the distance required for the attenuation intensity to return to its baseline level. We estimate the relative accuracy of the film thickness to be ±50 microns. However, systematic uncertainties from the neutron instrumental response may lead to more significant absolute film thickness measurement discrepancies. Finally, we estimate the height accuracy to be within ±1 mm.

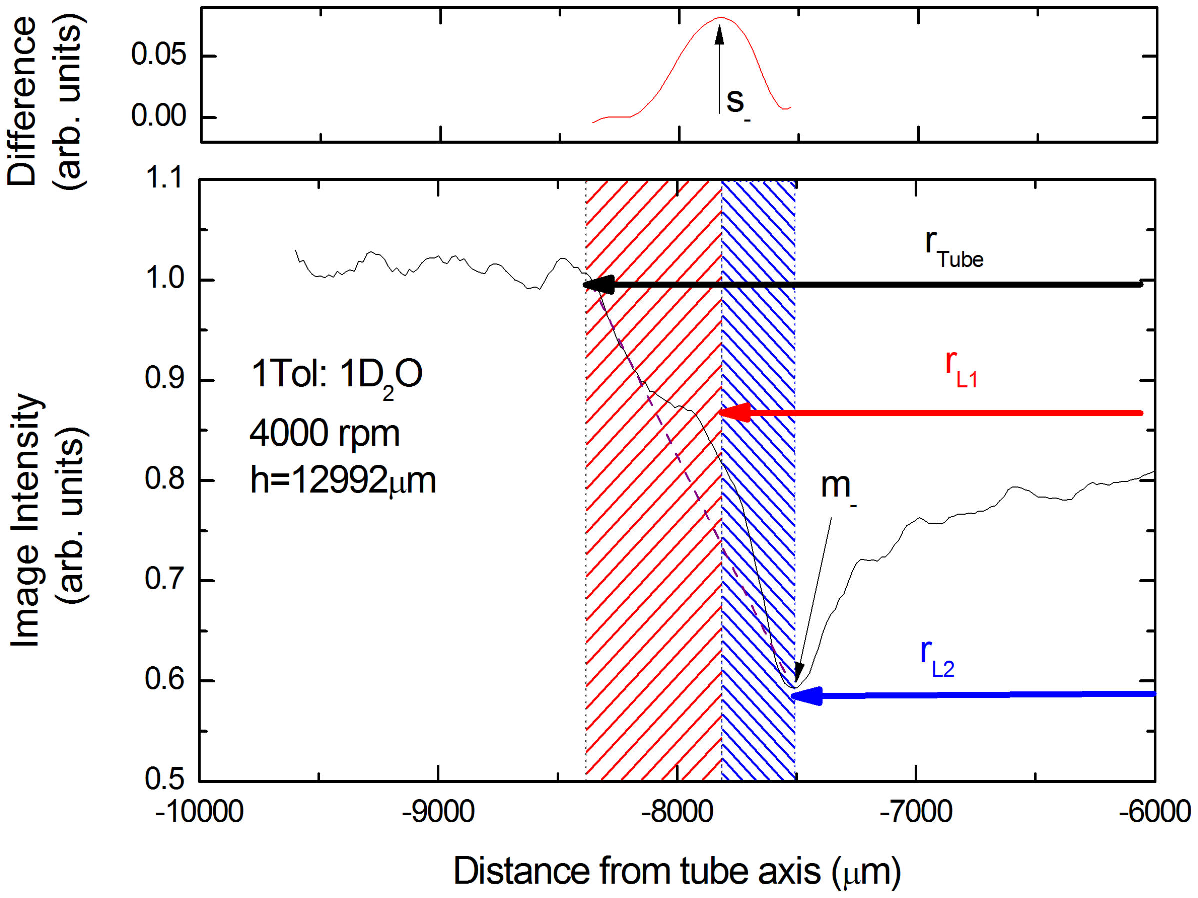

Figure S0.4 Data extracted from observed neutron images.

An illustration of how the parameters from the film's cross-sectional profile at the bottom of the tube are interpreted to determine film characteristics.

The analysis method employed is effective for extracting data on film thickness. However, challenges arose during the fitting procedure, particularly in the transitional regime when Layer 1 disappears. In this regime, the microfluidic fluid volume may become unstable, leading to difficulty in maintaining a single phase with a consistent thickness. Consequently, the fluid space may be divided between layers, or the two phases may begin to mix. In the time-averaged image, this instability is evident as a blurred boundary for the higher-attenuating toluene layer, along with the diffusion of attenuation intensity across the interface. This issue is illustrated in Figure S0.5.

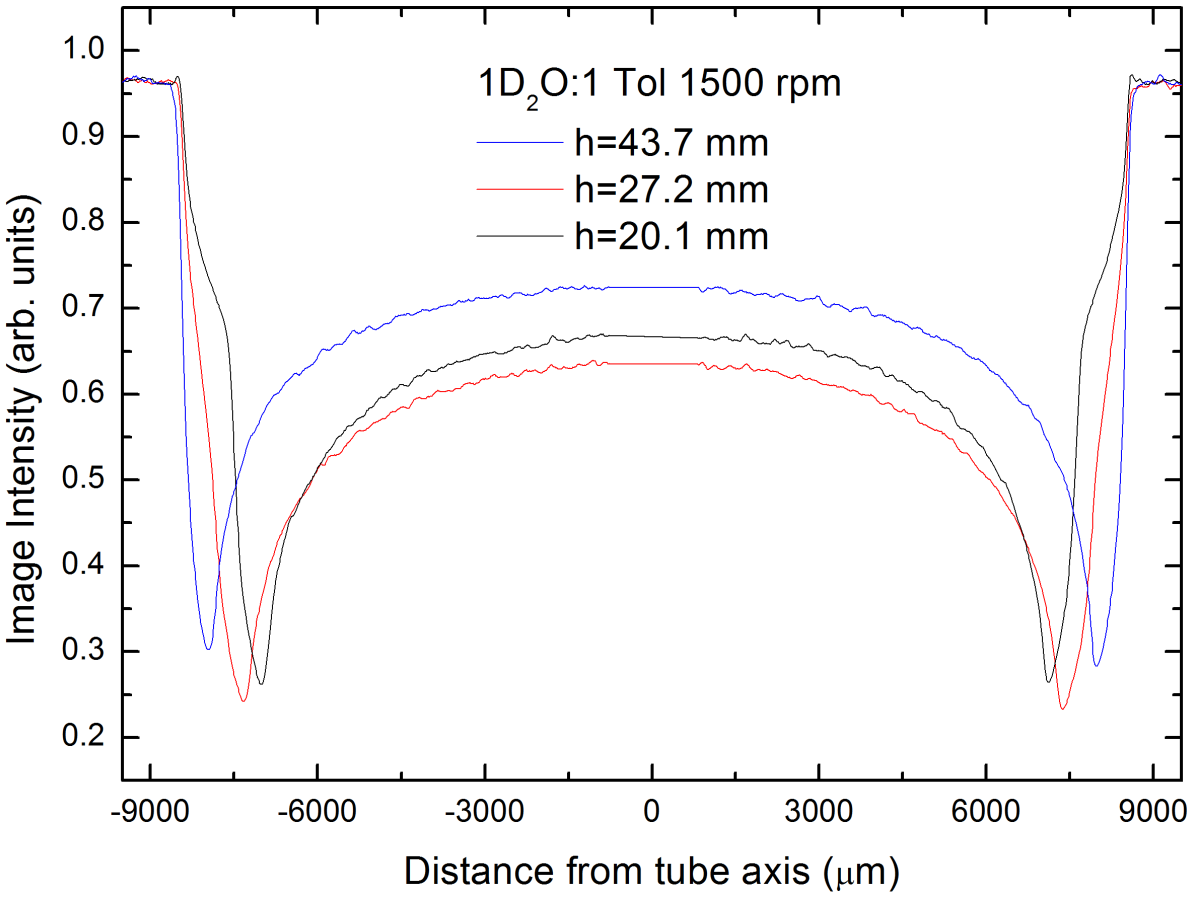

Figure S0.5 Film profiles at varying heights observe phase changes.

At different heights within the tube, we observe variations in the phasic structure of the film. Two distinct phases are present in the lower section of the tube (h = 20.1 mm, black). Only the toluene phase is observed in the upper section (h = 43.7 mm, blue). The distinction between the two phases becomes less defined in the transition region (h = 27.2 mm). It is important to note that the attenuation at the tube edge in this mixing region is weaker compared to that observed for a pure toluene phase, suggesting that the toluene phase at the tube edge does not exhibit the same density (concentration) as in the pure toluene phase.

2 Mixing and Demixing of Immiscible Liquids: Signatures of Monophasic and Biphasic Systems

Temperature variations of different liquids were recorded using a FLIR (T62101) camera at rotational speeds ranging from 3000 to 9000 rpm. The experiments were conducted in tubes with a 20 mm outer diameter to simulate continuous flow conditions at an inclination angle of 45° in both hemispherical and flat base tubes, as specified. The camera settings included an emissivity of 0.95, an object distance of 30.48 cm, a relative humidity of 50%, and a rainbow colour palette. All experiments were performed in triplicate using the same quartz tube for each liquid to ensure consistency within a temperature-controlled environment, with an average temperature of 19°C.

For continuous flow simulation, sufficient liquid was added to the tube so that, at any rotational speed, the thin liquid film extended to the tube's lip. Mixing time in the aqueous phase was measured as the time required for a drop of water containing a small amount of blue dye, added at the bottom of the rotating tube, to visibly mix uniformly halfway up the preformed film made from 1 mL of water (measured in triplicates). Similarly, mixing time in the organic phase was determined by the time needed for a drop of organic solvent containing beta-carotene, added at the bottom of the rotating tube, to mix uniformly halfway up the preformed film from 1 mL of organic solvent (measured in triplicates).

Demixing times were assessed by forming an emulsion of organic solvent and water after 10 minutes of sonication. A 2 mL interface sample was placed in a 20 mm outer diameter hemispherical or flat base tube, and the VFD was rotated between 3000 to 9000 rpm. The time required for the liquid to demix and become clear in the tube was recorded, with a maximum duration of 120 seconds (Figure S0.2a). The solution was maintained under sonication throughout, and all experiments were conducted in triplicate using the same quartz tube for consistency.

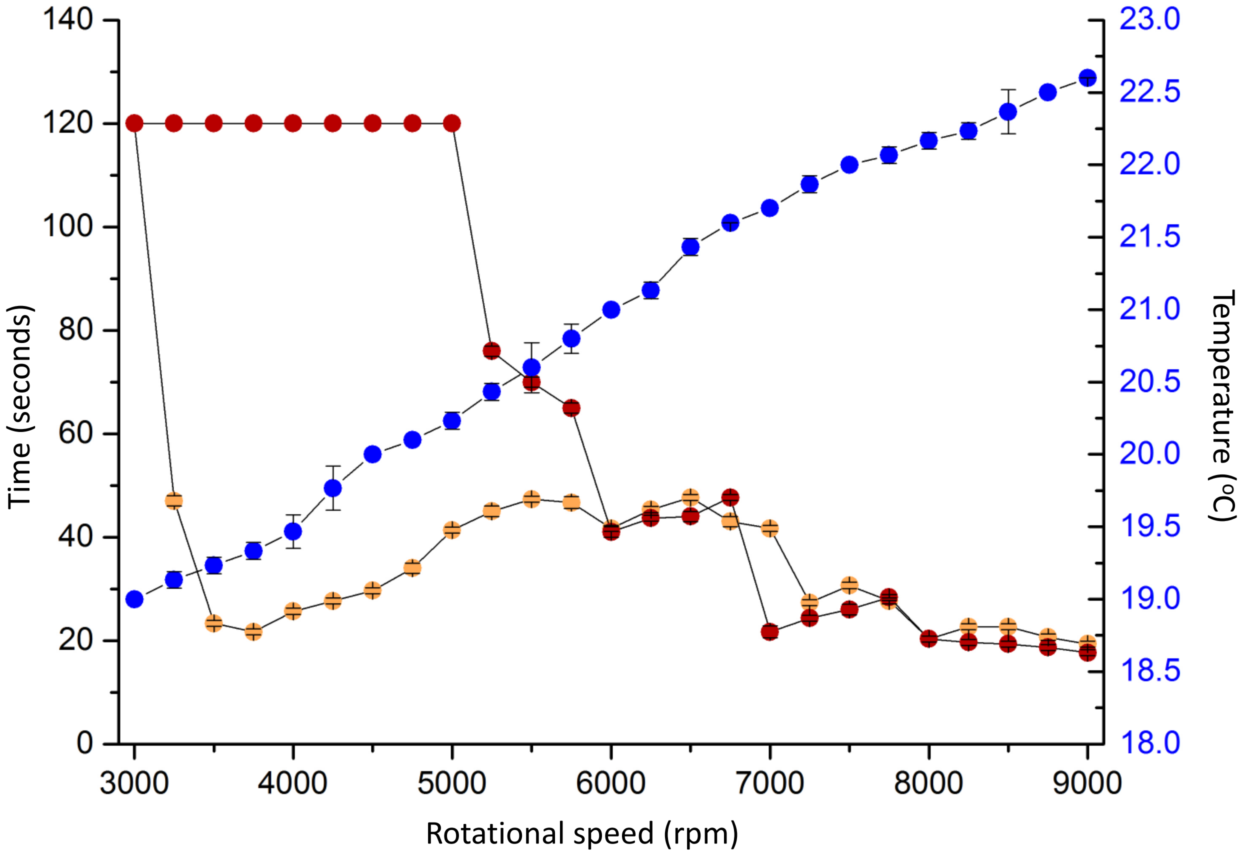

Figure S0.6 Signature of chlorobenzene and water.

This analysis presents the mixing times for the aqueous phase (red) and organic phase (orange), along with the thermal response (blue) of a 1:1 mixture in a hemispherical base quartz tube (20 mm OD, 17.5 mm ID, 18.5 cm in length). These parameters are depicted as functions of rotational speed (ω) at an inclination angle of 45°.

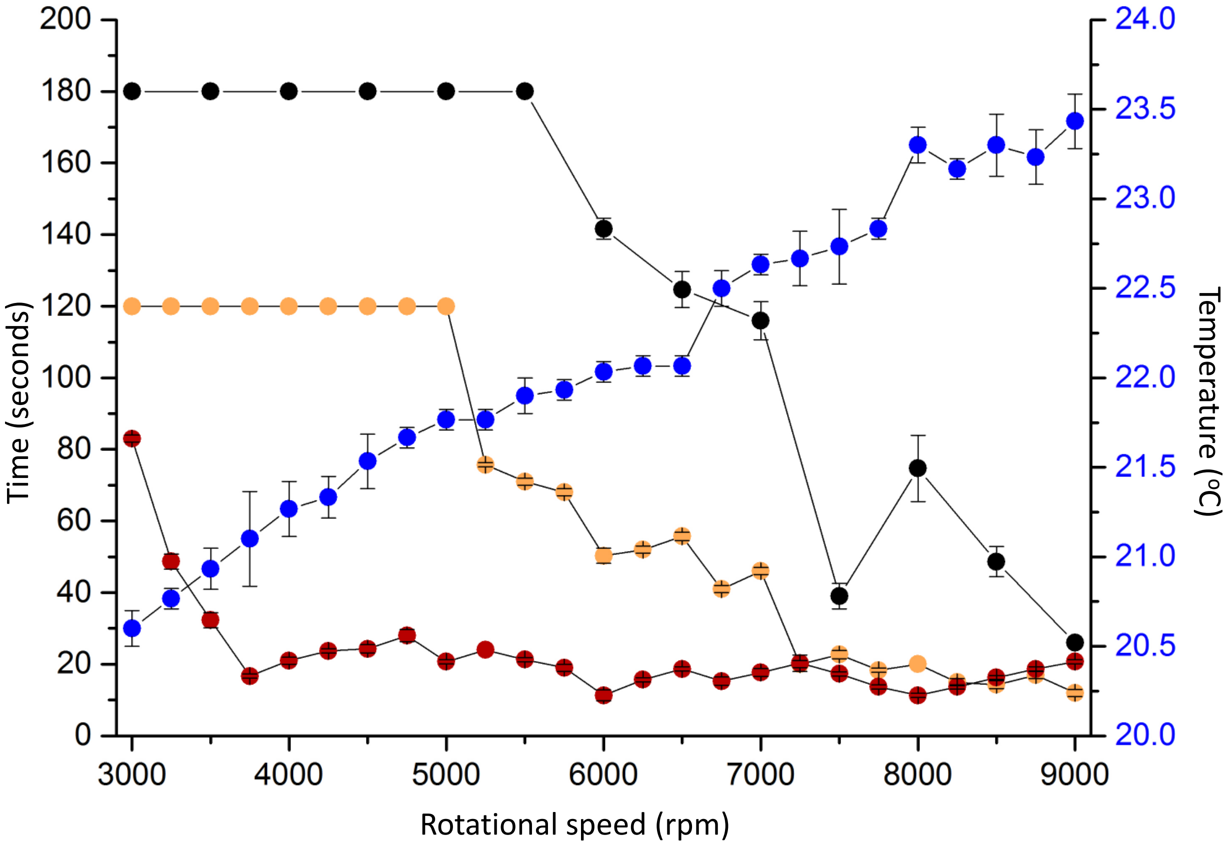

Figure S0.7 Signature of cyclohexene and water.

This analysis presents the mixing times for the aqueous phase (red) and organic phase (orange), along with the thermal response (blue) of a 1:1 mixture, in a hemispherical base quartz tube (20 mm OD, 17.5 mm ID, 18.5 cm in length). These parameters are depicted as functions of rotational speed (ω) at an inclination angle of 45°.

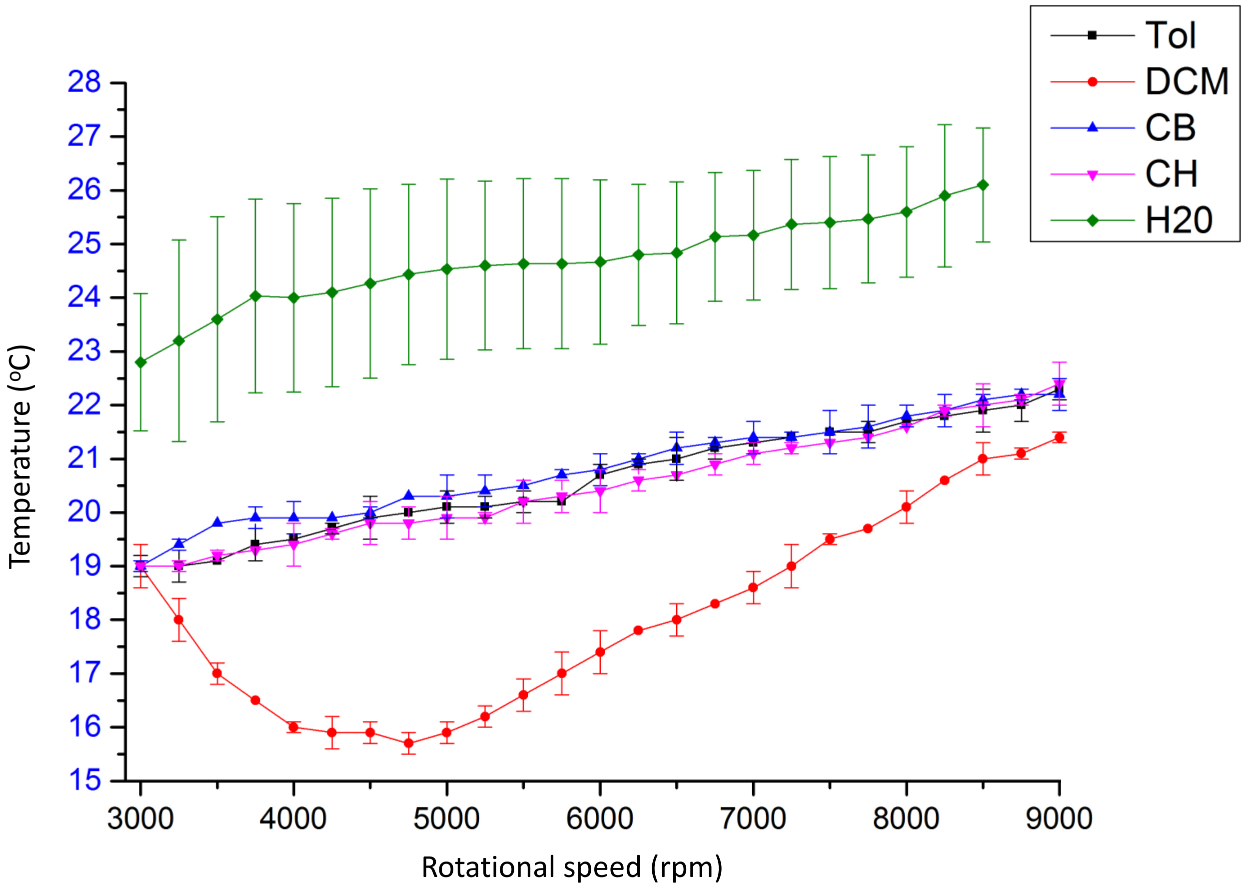

Figure S0.8 Thermal responses.

The thermal responses of different solvents—toluene (Tol), dichloromethane (DCM), chlorobenzene (CB), and cyclohexene (CH)—were measured in a monophasic system using a flat base quartz tube (20 mm OD, 17.5 mm ID, 18.5 cm length). These responses were analysed as functions of rotational speed (ω) at an inclination angle of 45°.

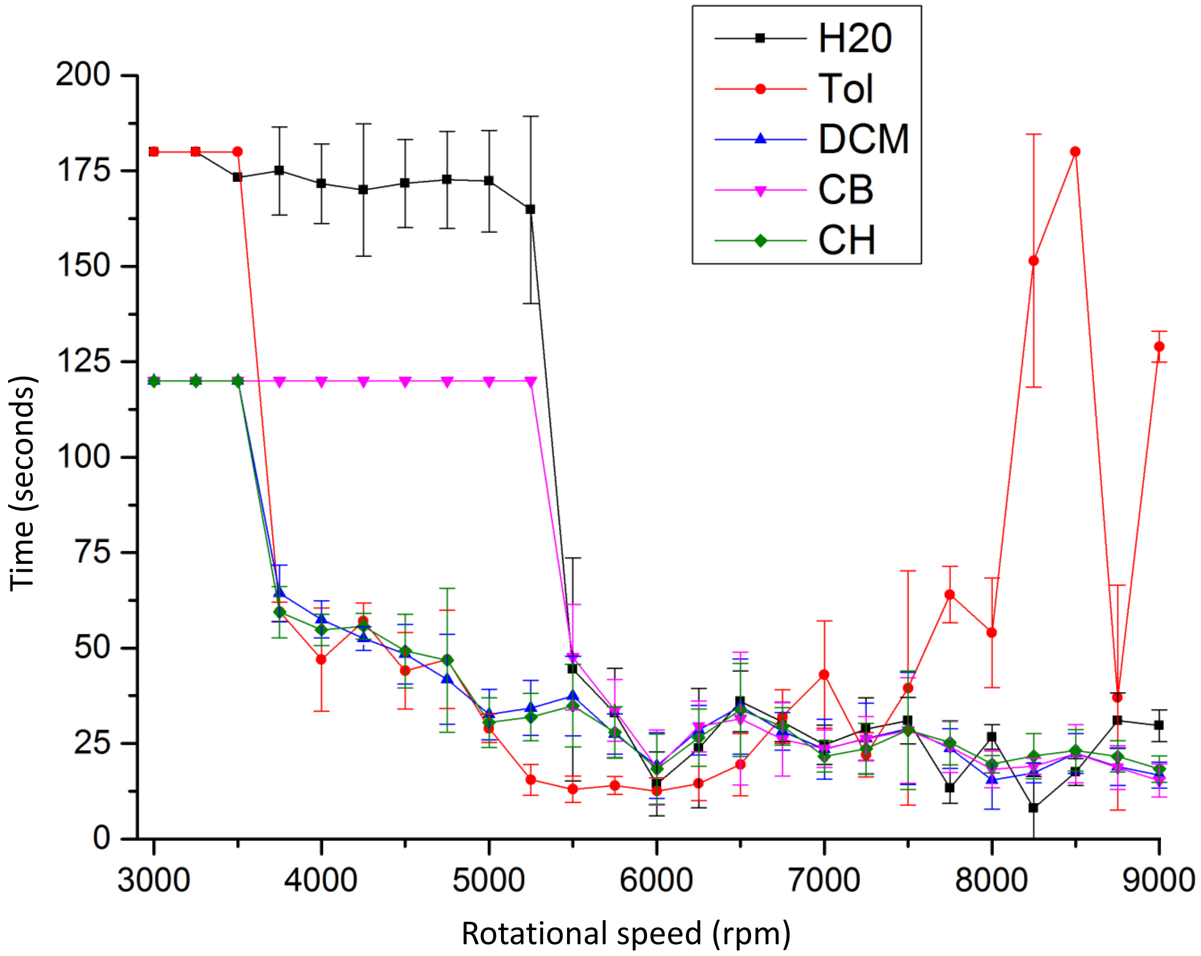

Figure S0.9 Mixing times.

The mixing times of different solvents—toluene (Tol), dichloromethane (DCM), chlorobenzene (CB), and cyclohexene (CH)—were measured in a monophasic system using a flat base quartz tube (20 mm OD, 17.5 mm ID, 18.5 cm length). These responses were analysed as functions of rotational speed (ω) at an inclination angle of 45°.

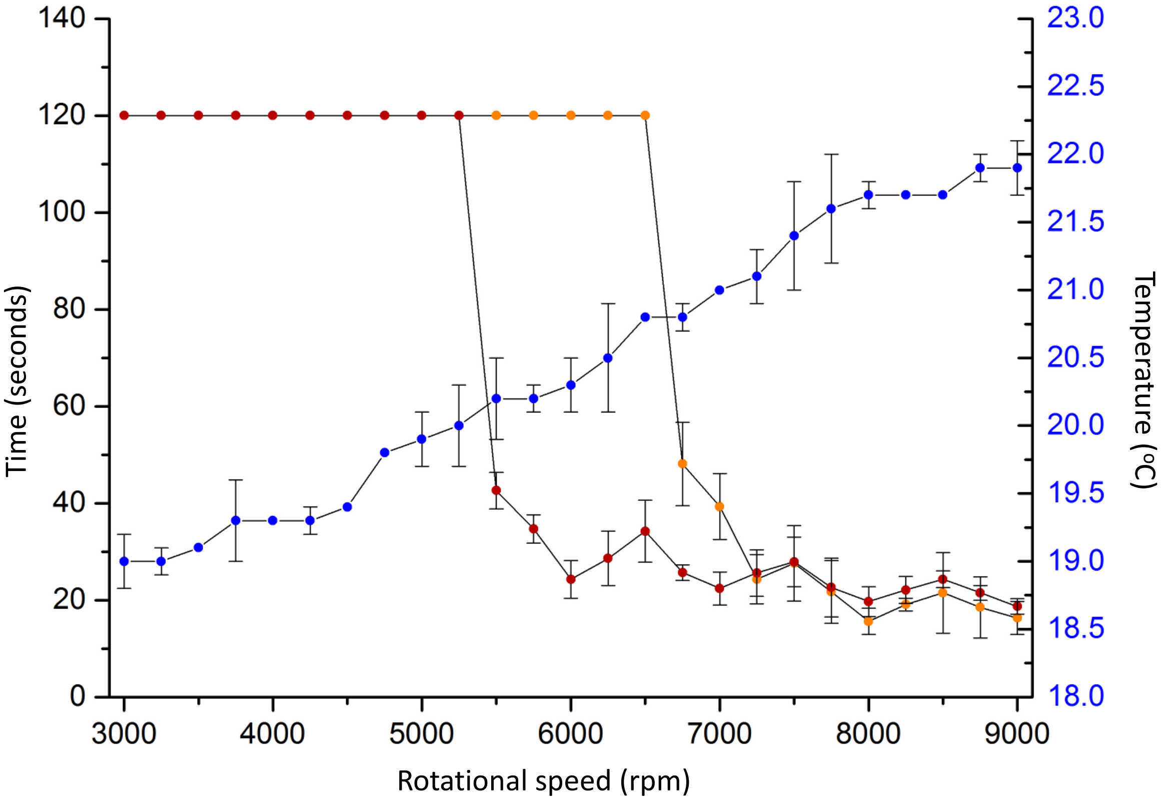

Figure S0.10 Signature of chlorobenzene and water.

This analysis presents the mixing times for the aqueous phase (red) and organic phase (orange), along with the thermal response (blue) of a 1:1 mixture, in a flat base quartz tube (20 mm OD, 17.5 mm ID, 18.5 cm in length). These parameters are depicted as functions of rotational speed (ω) at an inclination angle of 45°.

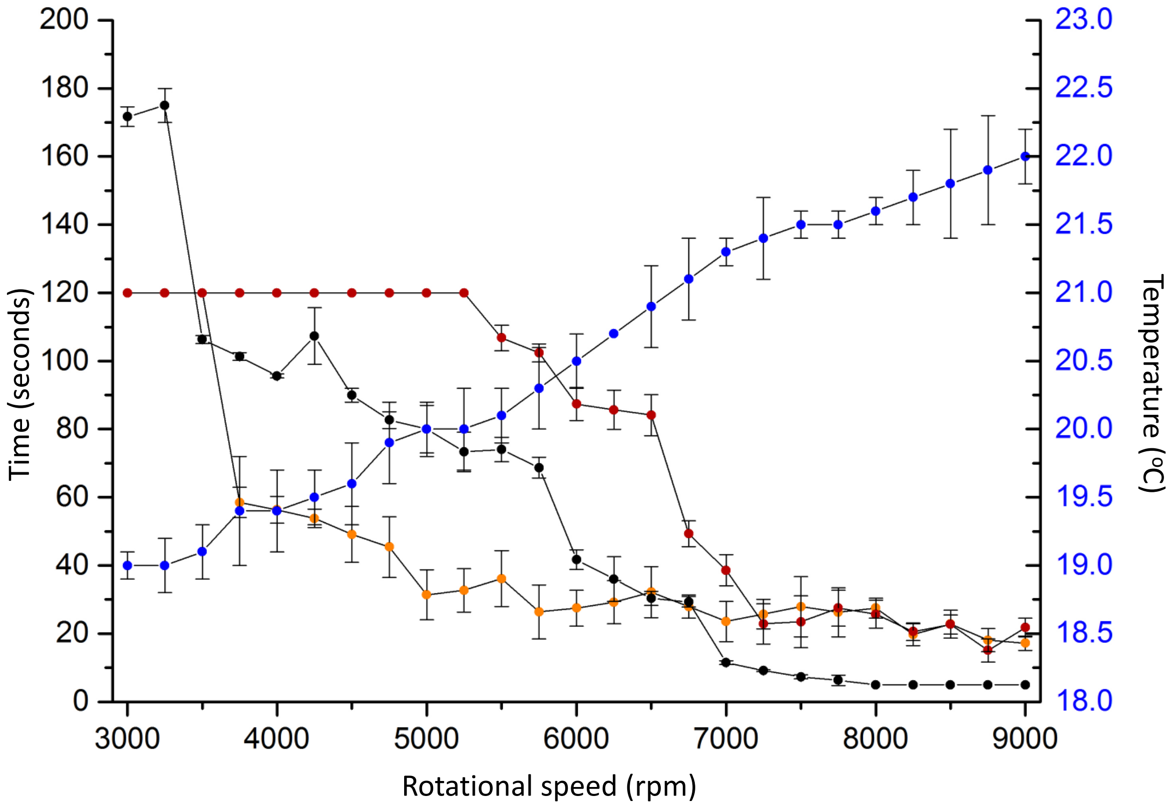

Figure S0.11 Signature of cyclohexene and water.

This analysis presents the mixing times for the aqueous phase (red) and organic phase (orange), along with the thermal response (blue) of a 1:1 mixture, in a flat base quartz tube (20 mm OD, 17.5 mm ID, 18.5 cm in length). These parameters are depicted as functions of rotational speed (ω) at an inclination angle of 45°.

3 Equal Density Immiscible Liquids

To assess the influence of density on the processing of immiscible liquids within the VFD, we examined the behaviour of water and chlorobenzene at rotational speeds ranging from 3000 to 9000 rpm. The mass of the tube post-processing was recorded to calculate the volume of fluid remaining. To match the density of chlorobenzene (1.11 g/mL), calcium chloride was added to the water, thereby increasing its density. Density equalisation was verified by mixing the solutions, as shown in Figure S0.12. This visual confirmation was conducted prior to each experimental run to ensure that the densities were within experimental precision.

To establish the native film volume without a second liquid, experiments were performed with water alone, water with calcium chloride, and chlorobenzene. All experiments were conducted in triplicate, with additional repetitions using a second tube to evaluate the tube's impact on the final volume. Further replication on a separate VFD was carried out to address intermachine variability.

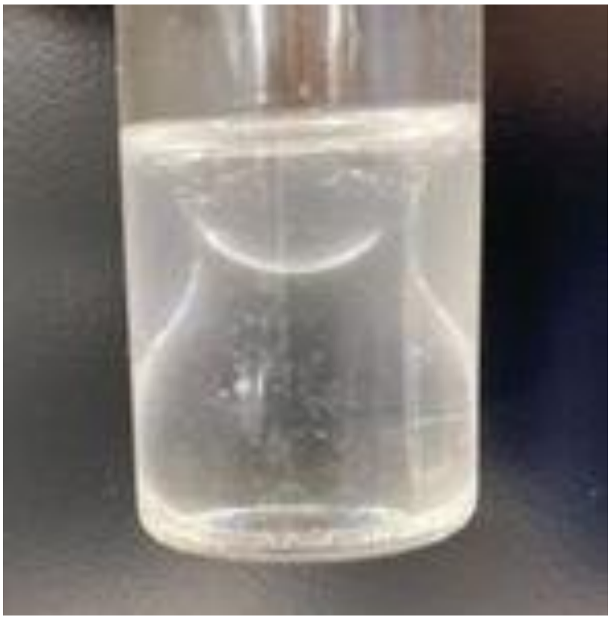

Figure S0.12 Layers of chlorobenzene and $H_2O.CaCl_2$ separated vertically.